Search for Contact Interactions and Finite Quark Radius Using Combined $e^{\pm}p$ Data at HERA

by

O. Turkot

To be sure that your reports and preprints are promptly included in the
HEP literature database
send them to (if possible by air mail):

DESY	DESY
Zentralbibliothek	Bibliothek
Notkestraße 85	Platanenallee 6
22607 Hamburg	15738 Zeuthen
Germany	Germany

Search for contact interactions and finite quark radius using combined $e^{\pm}p$ data at HERA

Dissertation

zur Erlangung des Doktorgrades

des Fachbereichs Physik

der Universität Hamburg

vorgelegt von

Oleksii Turkot

aus Kyiw und Khmelnitsky (Ukraine)

Dissertation submitted to the

University of Hamburg

2017

Gutachter/in der Dissertation:	Prof. Dr. Brian Foster
	Dr. Katarzyna Wichmann
Mitglieder der Prüfungskommission:	Prof. Dr. Brian Foster
	Prof. Dr. Dieter Horns
	Prof. Dr. Gudrid Moortgat-Pick
	Dr. Katarzyna Wichmann
	Prof. Dr. Hab. Aleksander Filip Żarnecki
Datum der Disputation:	29. March 2017
Vorsitzender des Prüfungskommission:	Prof. Dr. Dieter Horns
Vorsitzender des Promotionsausschusses:	Prof. Dr. Wolfgang Hansen
Dekan des MIN-Fakultät:	Prof. Dr. Heinrich Graener

Abstract

A combination is presented of all previously published deep inelastic neutral and charged current $e^{\pm}p$ scattering measurements at HERA for zero beam polarisation. The ZEUS and H1 collaborations have collected data at electron beam energy of 27.5 GeV and proton beam energies of 920, 820, 575 and 460 GeV. The combined data correspond to an integrated luminosity of about 1 fb^{-1} and cover a kinematic range in the negative four-momentum-transfer squared from $Q^2 = 0.045$ GeV^2 to $Q^2 = 50000$ GeV^2 and in Bjorken x from $x_{\mathrm{Bj}} = 6 \times 10^{-7}$ to $x_{\mathrm{Bj}} = 0.65$. The correlations of systematic uncertainties between different sets of data were taken into account, resulting in significantly improved precision.

The combined $e^{\pm}p$ cross sections were used in a QCD analysis at next-to-leading order, providing a set of parton distribution functions, called ZCIPDF. The combined measurements were also used in an analysis beyond the Standard Model using a new approach, performing simultaneous fits on large sets of Monte Carlo replicas of parton distribution functions, PDFs, together with the parameters of "new physics" processes. A simplified approach to reduce the calculation time was developed and extensively tested. It allowed the calculation time to be reduced by about a factor of 50. The resulting 95% C.L. upper limit on the effective quark radius is $0.43 \cdot 10^{-16}$ cm and the limits on the mass scales for different contact interaction scenarios extend up to 10 TeV. The analyses have shown that taking into account the possible influence of processes beyond the Standard Model on the PDF parameters is necessary, since the limits that would be obtained using PDFs from QCD analysis within the Standard Model are too strong by about 10 %.

Studies of the surface quality of 28 Niobium superconducting radio frequency, SRF, cavities and development of a controllable cooling system for Niobium samples are reported. The SRF cavities are the core of the accelerating technology for the future International Linear Collider, ILC; the reported studies are part of an ongoing research and development program.

Zusammenfassung

Die Kombination aller bisher von den HERA Experimenten publizierten Daten zur tief inelastischen ep Streuung ohne Strahlpolarisation werden vorgestellt. Die ZEUS und H1 Kollaborationen haben diese Daten bei einer Energie des Elektronenstrahles von $27,5$ GeV und des Protonenstrahlen vom 920, 820, 575 und 460 GeV aufgezeichnet. Die kombinierten Daten entsprechen einer Luminosität von ungefähr $1\,fb^{-1}$ und decken den kinematischen Bereich des negativen Viererimpulsquadrates $Q^2 = 0,045$ GeV^2 bis $Q^2 = 50000$ GeV^2 und eines Björken-X von 6×10^{-7} bis 0.65 ab. Korrelationen zwischen systematischen Unsicherheiten der verschiedenen Datensätzen wurden berücksichtigt und liefern eine deutlich verbesserte Meßgenauigkeit.

In einer in zweiter Ordnung Stoerungstheorie genauen QCD Analyse (Next-to-leading order) wurde die Kombination aller gemessen ep Wirkungsquerschnitte benutzt, um die Dichtefunktionen der Partonen (genannt ZCIPDF) zu bestimmen. Die kombinierten Messungen wurden ebenfalls für eine Suche nach Physik jenseits des Standardmodels verwendet. Dazu wurden in einem neuen Ansatz Fits von großen Monte Carlo Pseudoexperimenten von Partondichteverteilungen (Parton Distribution Functions - PDFs) zusammen mit Parametern von Prozessen neuer Physik durchgeführt. Um die Berechnungszeiten zu verkürzen wurde ein vereinfachter Ansatz entwickelt und ausführlich getestet. Dadurch konnten die Rechenzeiten um einen Faktor 50 reduziert werden. Als Ergebnis wurde eine obere Grenze des effektiven Quarkradiuses von $0.43 \cdot 10^{-16}$ cm und Ausschlussgrenzen für die Massenskalen verschiedener Kontaktwechselwirkungen bis zu 10 TeV mit einer statistischen Sicherheit von $95\,\%$ ermittelt. Die Analysen haben gezeigt, dass es notwendig ist, Prozesse jenseits des Standardmodels bei den Fits der PDF Parametern zu berücsichtigen, da PDFs aus einer QCD Analyse innerhalb des Standardmodels um etwa $10\,\%$ zu gross sind.

Studien der Oberflächenqualität von 28 supraleitenden Niob Resonatoren und die Entwicklung eines kontrollierbaren Kühlsystems für Niobproben werden beschrieben. Die supraleitenden Resonatoren sind die Herzstücke der Beschleunigertechnologie eines zukünftigen, internationalen Linearbeschleuniger (International Linear Collider - ILC). Diese Studien sind Teil eines laufenden Forschungs- und Entwicklungsprogrammes.

This work is also reported in the following publications:

1. H. Abramowicz et al., *Combination of measurements of inclusive deep inelastic e±p scattering cross sections and QCD analysis of HERA data, Eur. Phys. J.* **C75** (2015), No. 12, 1–98.

2. ZEUS Collaboration, H. Abramowicz et al., *Limits on the effective quark radius from inclusive ep scattering at HERA, Phys. Lett.* **B757** (2016) 468–472, [arXiv:1604.01280].

3. O. Turkot, K. Wichmann, and A. F. Żarnecki, *Simplified QCD fit method for BSM analysis of HERA data,* arXiv:1606.06670.

4. A. F. Żarnecki, *Limits on the effective quark radius from inclusive ep scattering & contact interactions at HERA,* in *Proceedings of Science ICHEP2016,* in press.

5. A. Navitski et al., *Characterization of Surface Defects on EXFEL Series and ILC-Higrade Cavities,* in *Proceedings, 17th International Conference on RF Superconductivity (SRF2015): Whistler, Canada, September 13-18, 2015,* p. MOPB072, 2015.

Contents

Introduction

'In this field, almost everything is already discovered, and all that remains is to fill a few holes.' With these words, Professor Philipp von Jolly tried in 1874 [1] to discourage young Max Plank from learning physics. But instead of filling a few holes within classical physics, the twentieth century began with a theoretical revolution caused by quantum mechanics and special relativity.

Nowadays, in the field of the high energy physics we also have a theoretical model which provides an excellent description for all experimental results - the Standard Model, SM, briefly described in Chapter 1. Despite the fact that the Standard Model has a history full of successes, such as the discovery of the gluon at DESY in 1978 [2–5], $W^{\pm}$ and Z^0 bosons at CERN in 1983 [6,7], the top quark at Fermilab in the 1995 [8,9], and the Higgs boson at CERN in 2012 [10,11], there are a few compelling indications [12,13] that there may be physics beyond the Standard Model (BSM):

Dark matter - according to modern understanding in cosmology, only about $5\,\%$ of the energy-matter density of the Universe is in the form of normal baryonic matter, described by the SM. A further $23\,\%$ is in the form of dark matter and $72\,\%$ in the form of dark energy, which is believed to accelerate the expansion of the Universe. It is suggested that a significant fraction of the dark matter might be in the form of weakly interacting massive particles.

Neutrino oscillations - the SM contains exactly massless and stable neutrinos, participating only in weak interactions mediated by the $W^{\pm}$ bosons. Instead, there are experimental results showing that neutrinos are massive particles and can participate also in the weak interactions mediated by the Z^0 boson.

These and also the large number, 26, of free parameters that have to be measured by experiment suggest that the Standard Model may be an approximation to some more basic theory in the phase space so far studied. Thus it may be that we are standing at the threshold of new revolutionary discoveries, as was the case at the end of the nineteenth century.

The standard model of cosmology, ΛCDM, suggests that a fraction of dark matter consists of weakly interacting massive particles, WIMPs. Such kind of particles are included, for example, in the supersymmetry model, SUSY, which is one of the possible

extensions to the Standard Model. In SUSY, each Standard Model particle has a super-partner with different spin, and searches for the production of such particles are ongoing at the LHC. Among other popular methods to search for physics beyond the Standard Model are precise measurements of the Higgs boson properties, general indirect searches for evidence of the exchange of BSM particles with contact interactions and evaluation of the limits on the compositneteness scale of the fermions.

Not only have the 26 free parameters of the SM to be estimated from the experimental data, but also there are some low-energy effects that have not yet or even cannot be calculated from the theory, such as parton density distributions inside the hadron, PDFs, that are overviewed in Chapter 1. The electron[1]-proton deep inelastic scattering, DIS, measurements by the ZEUS and H1 experiments at the HERA collider, described in Chapter 2, have been an essential ingredient in the estimation of all recent high-precision PDFs. The combination of all final inclusive DIS measurement results from ZEUS and H1, which is a major legacy [14] of HERA, and an example of the QCD global analysis used for PDFs extraction, are presented in Chapters 3 and 4, respectively.

When performing BSM analyses of inelastic hadron scattering, it should be taken into account that PDFs are estimated assuming the validity of the Standard Model and might therefore absorb part of the BSM effects. The procedure for combined BSM and PDFs analysis which allows such effects to be avoided is described in Chapter 5 and the results of such an analysis of the combined HERA data within the contact-interaction models and quark form factor are presented in Chapter 6. The proposed procedure can be used on any set of data suitable for the extraction of PDFs, which may be, for example, a sum of the LHC, Tevatron, HERA and fixed-target experimental data.

One of the possible future facilities for BSM searches and studies of the Higgs boson properties is the International Linear Collider, ILC. Extensive studies of superconducting Niobium cavities, the core of the ILC accelerating technology, are currently ongoing. As a part of these studies, the surface analysis of possible cavity defects and the development of a controllable cooling system for Niobium samples were performed and are described in Chapter 7.

---

[1]Here and later, the word "electron" refers to both electrons and positrons, unless otherwise stated.

Chapter 1

Theoretical Overview

This chapter presents the main aspects of the Standard Model related to the analyses described in Chapters 3 and 4, as well as theories beyond the Standard Model studied in Chapters 5 and 6.

1.1   The Standard Model

The Standard Model [12, 13] is a theory of the fundamental constituents of matter and the interactions among them. It provides a successful description of almost all current experimental data and has proven itself to be "the" theory of modern particle physics.

In terms of the Standard Model, all matter consists of 12 elementary spin–$\frac{1}{2}$ particles - fermions - listed in Table 1.1, and their antiparticles with the same properties except that they have opposite electric charge. All fermions are divided into 3 generations, whose corresponding particles differ only in mass. The Standard Model describes the strong, weak and electromagnetic interactions between fermions via the exchange of spin–1 bosons associated with the $SU_c(3) \times SU_L(2) \times U_Y(1)$ gauged symmetry group. The main parameters of the bosons are listed in Table 1.2.

The electroweak interactions are related to the factors $SU_L(2) \times U_Y(1)$. The subscript "L" indicates that only the left-handed fermions carry the associated quantum number - weak isospin, T_3. As a consequence, the right-handed neutrinos do not participate in the weak interactions and might not even exist. The subscript "Y" is meant to distinguish the group associated with the weak hypercharge $Y = 2(Q - T_3)$ from the electromagnetic group $U_{em}(1)$. Here Q is the electric charge. The invariance of the Lagrangian against $SU_L(2) \times U_Y(1)$ transformations gives rise to three bosons that mediate the weak interactions, $W^\pm$ and Z^0, and one boson that mediates the electromagnetic interactions - the photon γ. The interactions mediated via exchange of the $W^\pm$ bosons are the only ones within the model that connect fermions with different flavours. All twelve fundamental fermions can undergo weak interactions, and nine fermions with non-zero electric charge participate in

	1st generation	2nd generation	3rd generation
Quarks	up $\boldsymbol{u}$ $Q = \frac{2}{3}$ $T_3 = \frac{1}{2}$ $m = 2.2$ MeV ($\overline{\text{MS}}^1$)	charm $\boldsymbol{c}$ $Q = \frac{2}{3}$ $T_3 = \frac{1}{2}$ $m = 1.27$ GeV ($\overline{\text{MS}}^2$)	top $\boldsymbol{t}$ $Q = \frac{2}{3}$ $T_3 = \frac{1}{2}$ $m = 173.21$ GeV (direct)
Quarks	down $\boldsymbol{d}$ $Q = -\frac{1}{3}$ $T_3 = -\frac{1}{2}$ $m = 4.7$ MeV ($\overline{\text{MS}}^1$)	strange $\boldsymbol{s}$ $Q = -\frac{1}{3}$ $T_3 = -\frac{1}{2}$ $m = 96$ MeV ($\overline{\text{MS}}^1$)	bottom $\boldsymbol{b}$ $Q = -\frac{1}{3}$ $T_3 = -\frac{1}{2}$ $m = 4.18$ GeV ($\overline{\text{MS}}^2$)
Leptons	electron $\boldsymbol{e}$ $Q = -1$ $T_3 = -\frac{1}{2}$ $m = 0.51$ MeV	muon $\boldsymbol{\mu}$ $Q = -1$ $T_3 = -\frac{1}{2}$ $m = 105.66$ MeV	tau $\boldsymbol{\tau}$ $Q = -1$ $T_3 = -\frac{1}{2}$ $m = 1.777$ GeV
Leptons	electron neutrino $\boldsymbol{\nu_e}$ $Q = 0$ $T_3 = \frac{1}{2}$ $m < 2$ eV	muon neutrino $\boldsymbol{\nu_\mu}$ $Q = 0$ $T_3 = \frac{1}{2}$ $m < 2$ eV	tau neutrino $\boldsymbol{\nu_\tau}$ $Q = 0$ $T_3 = \frac{1}{2}$ $m < 2$ eV

Table 1.1: Spin–$\frac{1}{2}$ fermions of the Standard Model. Here electric charge Q is given in units of positron charge and m indicates the fermion mass. The weak isospin T_3 is given for the left-handed particles, for all right-handed fermions $T_3 = 0$. The superscript [1] near the $\overline{\text{MS}}$ scheme indicates that the mass is given at a scale $\mu = 2$ GeV, while the superscript [2] indicates that the mass is a "running" mass with $\mu = m_q$. The masses of the fermions are taken from the PDG16 [15].

the electromagnetic interactions.

The strong interactions are related to the $SU_c(3)$ symmetry group with the subscript "c" denoting the "colour" quantum number. They give rise to eight bosons, gluons g, which distinguish the colour states but do not distinguish the other properties. The fermions are divided into quarks, which carry the colour charge and participate in the strong interactions, and leptons, that do not. Since gluons also carry the colour charges they can self-interact, leading to two important consequences:

Colour confinement: The energy stored in the colour field between separated free quarks grows linearly with the distance. As a result, coloured objects can only exist as free particles for an infinitesimally short time and arrange themselves into

	photon $\boldsymbol{\gamma}$ $Q = 0$ $T_3 = 0$ $m = 0$	Z boson $\boldsymbol{Z^0}$ $Q = 0$ $T_3 = 0$ $m = 91.19$ GeV	W bosons $\boldsymbol{W^{\pm}}$ $Q = \pm 1$ $T_3 = \pm 1$ $m = 80.39$ GeV
Spin–1		gluon $\boldsymbol{g}$ $Q = 0$ $m = 0$	
Spin–0		Higgs boson $\boldsymbol{H^0}$ $Q = 0$ $m = 125.09$ GeV	

Table 1.2: Bosons of the Standard Model. The boson masses are taken from the PDG16 [15].

colourless combinations, hadrons, normally of 2 or 3 quarks (mesons and baryons, respectively) but sometimes of 4 quarks (tetraquarks) or, perhaps, 5 quarks (pentaquarks).

Asymptotic freedom: As the length scale becomes smaller, which corresponds to the energy scales becoming larger, the strong coupling becomes weaker. At sufficiently high energy scales the quarks inside hadrons can be treated as quasi-free particles.

The $SU_L(2)$ gauged symmetry with the described interactions would hold for massless fermions, $W^{\pm}$ and Z^0 bosons, which are not seen in nature. To preserve the symmetry, an additional scalar field with a single spinless particle, the Higgs boson H^0, was introduced. The Higgs field has a non-zero vacuum expectation value and, through the mechanism of spontaneous symmetry breaking [12,13], restores the invariance of the fermions and weak interaction boson mass terms in the Lagrangian.

1.2 Deep Inelastic $e^{\pm}p$ Scattering

An inelastic scattering of a point-like particle on a composite massive particle with large momentum transfer is known as Deep Inelastic Scattering or DIS [16]. At the HERA collider, described in Chapter 2, electrons scattered from protons. Depending on the charge of the exchanged particle, two different reactions are recognised:

1. Neutral Current (NC) - the interaction is mediated via exchange of a neutral boson - γ or Z^0, and the lepton does not change charge in the reaction.

2. Charged Current (CC) - the interaction is mediated via exchange of a W^- or W^+ boson and a neutrino is produced in the reaction instead of a scattered electron.

These two types of reactions are schematically displayed in Fig. 1.1. There the four-momentum of the initial and scattered leptons are indicated with l and l', and the four-momentum of the incoming proton with P, respectively.
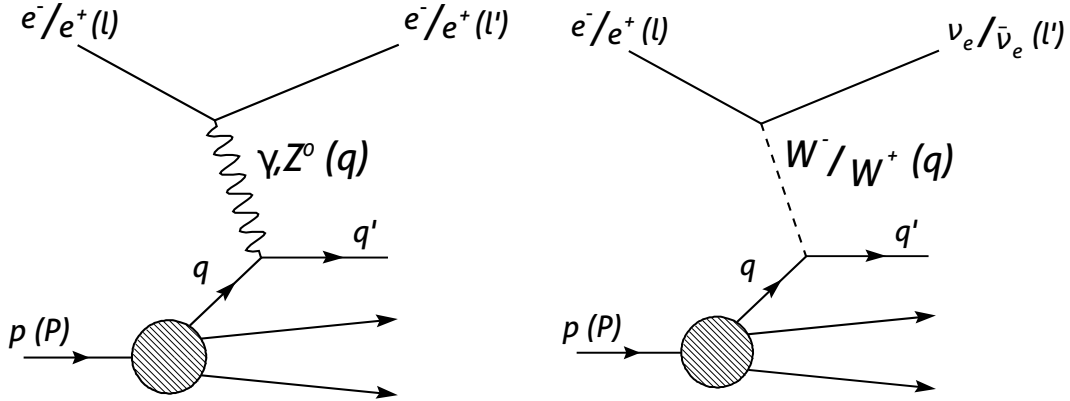
Figure 1.1: Schematic Feynman diagrams describing the deep inelastic neutral current (left) and charged current (right) scattering of a lepton on a proton.

The ep scattering kinematics can be described by the following Lorenz-invariant variables:

1. Centre-of-mass-energy squared of the ep system

$$s = (l + P)^2 \ ; \tag{1.1}$$

2. Negative four-momentum-transfer squared at the electron vertex, also referred to as virtuality

$$Q^2 = -q^2 = (l - l')^2 \ ; \tag{1.2}$$

3. Bjorken scaling variable

$$x_{Bj} = \frac{Q^2}{2P \cdot q} \ ; \tag{1.3}$$

4. Inelasticity

$$y = \frac{P \cdot q}{P \cdot l} \ ; \tag{1.4}$$

5. Centre-of-mass-energy squared of the proton-boson system

$$W^2 = (P + q)^2 \ . \tag{1.5}$$

In the quark-parton model (introduced in Section 1.3.1), the Bjorken scaling variable x_{Bj} can be interpreted as the relative fraction of the proton energy involved in the interaction and the inelasticity y determines the fraction of the electron energy transferred to the proton.

Centre-of-mass-energy squared, virtuality, Bjorken scaling variable and inelasticity are related by

$$s = \frac{Q^2}{x_{Bj} \cdot y} + m_e^2 + m_p^2 \quad, \tag{1.6}$$

where m_e and m_p are masses of the lepton and proton, respectively. For fixed centre-of-mass energy, only two variables are needed to fully describe the kinematics of the event. The masses of the electron and proton are usually neglected. Interactions with virtuality greater than about 1 GeV^2 are classified as DIS.

1.3 Inclusive DIS cross section

In leading order (Feynman diagrams in Fig. 1.1), the differential cross section of deep inelastic scattering of a lepton on a hadron can be expressed by the contraction of the leptonic tensor $L_{\mu\nu}$ with the hadronic tensor $W^{\mu\nu}$:

$$d\sigma \sim L_{\mu\nu} \cdot W^{\mu\nu} \quad. \tag{1.7}$$

The leptonic tensor $L_{\mu\nu}$ represents the coupling of the exchanged boson to the leptons. For photon exchange, γ–Z interference, Z and $W^\pm$ exchange, it has the form [15]:

$$\begin{aligned}
L_{\mu\nu}^\gamma &= 2\left(l_\mu l_\nu' + l_\mu' l_\nu - (l \cdot l' - m_e^2)g_{\mu\nu} - i\lambda\epsilon_{\mu\nu\alpha\beta}l^\alpha l'^\beta\right) \quad, \\
L_{\mu\nu}^{\gamma Z} &= (g_V^e + e\lambda g_A^e)L_{\mu\nu}^\gamma \quad, \\
L_{\mu\nu}^Z &= (g_V^e + e\lambda g_A^e)^2 L_{\mu\nu}^\gamma \quad, \\
L_{\mu\nu}^W &= (1 + e\lambda)^2 L_{\mu\nu}^\gamma \quad,
\end{aligned} \tag{1.8}$$

respectively. The symbols l and l' represent the initial- and final-state lepton four-momentum, as shown in Fig. 1.1, m_e is the lepton mass, which can be neglected at the energy scales of interest, and $\lambda = \pm 1$ and $e = \pm 1$ are lepton helicity and charge, respectively. The vector and axial-vector couplings of the fermions to the Z boson are:

$$\begin{aligned}
g_V^f &= T_3^f - 2Q^f sin^2\theta_W \quad, \\
g_A^f &= T_3^f \quad,
\end{aligned} \tag{1.9}$$

where T_3^f and Q^f are fermions weak isospin and charge, given in Table 1.1, and θ_W is the Weinberg angle.

The hadronic tensor $W^{\mu\nu}$ describes the coupling of the boson to the proton and can be expressed in terms of the generalised structure functions F_i as [15, 16]:

$$W^{\mu\nu} = (-g^{\mu\nu} + \frac{q^\mu q^\nu}{q^2})F_1 + (P^\mu - \frac{P \cdot q}{q^2} q^\mu)(P^\nu - \frac{P \cdot q}{q^2} q^\nu)\frac{F_2}{P \cdot q} - i\epsilon^{\mu\nu\alpha\beta}P_\alpha q_\beta \frac{F_3}{2P \cdot q} \quad . \quad (1.10)$$

By defining the longitudinal structure function $F_L = F_2 - 2x_{\text{Bj}}F_1$, the reduced cross sections for neutral current deep inelastic scattering on unpolarized protons can be written as:

$$\sigma_{r,\text{NC}}^\pm = \frac{\mathrm{d}^2\sigma_{\text{NC}}^{e^\pm p}}{\mathrm{d}x_{\text{Bj}}\mathrm{d}Q^2} \cdot \frac{Q^4 x_{\text{Bj}}}{2\pi\alpha^2 Y_+} = \tilde{F}_2 \mp \frac{Y_-}{Y_+} x\tilde{F}_3 - \frac{y^2}{Y_+}\tilde{F}_{\text{L}} \quad , \quad (1.11)$$

and for charged current DIS:

$$\sigma_{r,\text{CC}}^\pm = \frac{\mathrm{d}^2\sigma_{\text{CC}}^{e^\pm p}}{\mathrm{d}x_{\text{Bj}}\mathrm{d}Q^2} \cdot \frac{2\pi x_{\text{Bj}}}{G_F^2}\left[\frac{M_W^2 + Q^2}{M_W^2}\right]^2 = \frac{Y_+}{2}F_2^{W^\pm} \mp \frac{Y_-}{2}xF_3^{W^\pm} - \frac{y^2}{2}F_{\text{L}}^{W^\pm} \quad . \quad (1.12)$$

Here "$\pm$" corresponds to the sign of the lepton charge, α is the fine-structure constant, $Y_\pm = 1 \pm (1 - y)^2$ and G_F is the Fermi constant. The NC structure functions $\tilde{F}_2$, $\tilde{F}_{\text{L}}$ and $x\tilde{F}_3$ are sums of structure functions related to the photon exchange, γ–Z interference and Z exchange:

$$\tilde{F}_2 = F_2^\gamma - (g_V^e \pm \lambda g_A^e)\kappa_Z F_2^{\gamma Z} + (g_V^{e\,2} + g_A^{e\,2} \pm 2\lambda g_V^e g_A^e)\kappa_Z^2 F_2^Z \quad ,$$
$$\tilde{F}_{\text{L}} = F_{\text{L}}^\gamma - (g_V^e \pm \lambda g_A^e)\kappa_Z F_{\text{L}}^{\gamma Z} + (g_V^{e\,2} + g_A^{e\,2} \pm 2\lambda g_V^e g_A^e)\kappa_Z^2 F_{\text{L}}^Z \quad , \quad (1.13)$$
$$x\tilde{F}_3 = -(g_A^e \pm \lambda g_V^e)\kappa_Z xF_3^{\gamma Z} + \left[2g_V^e g_A^e \pm \lambda(g_V^{e\,2} + g_A^{e\,2})\right]\kappa_Z^2 xF_3^Z \quad .$$

Here $\kappa_Z = \left(\frac{G_F M_Z^2}{2\sqrt{2}\pi\alpha}\right)\left(\frac{Q^2}{Q^2 + M_Z^2}\right)$ is the ratio of the γ–Z interference coupling to the photon exchange coupling.

1.3.1   The quark-parton model

The quark-parton model, QPM, arises from the asymptotic freedom of the strong interactions and describes deep inelastic scattering as the incoherent sum of point-like elastic scatterings of leptons on spin-$\frac{1}{2}$ partons inside the hadron. In this process, the parton is assumed to be a quark and is treated as a free particle with momentum $x_{Bj}P$ in an infinite momentum frame, i.e. for proton energies much larger than its mass, $E_p >> m_p$, so the latter can be neglected.

The elastic scattering of lepton on quark q with a specific value of x_{Bj} mediated by a photon would be [12, 16]:

$$\frac{\mathrm{d}\sigma}{\mathrm{d}Q^2} = \frac{2\pi\alpha^2}{Q^4}Y_+Q^{q2} \quad . \quad (1.14)$$

To obtain a cross section for scattering on a proton, a distribution function $f_i(x)$, which gives the probability that the struck quark i carries a fraction x of the proton's momentum P must be defined. Such functions are called parton number distributions, and momentum distributions $xf_i(x)$ are referred to as parton distribution functions or PDFs. Using $xf_i(x)$, defining PDFs for antiquarks with $x\bar{f}_i(x)$ and taking the sum over all quarks in the proton, the double differential cross section is:

$$\frac{\mathrm{d}^2\sigma_{\mathrm{NC}}^{e^{\pm}p}}{\mathrm{d}x_{\mathrm{Bj}}\mathrm{d}Q^2} = \frac{2\pi\alpha^2}{xQ^4}Y_+ \sum_i^{N_q} Q^{i2}x\left(f_i(x) + \bar{f}_i(x)\right) \quad . \tag{1.15}$$

Comparing Eq. 1.15 to Eq. 1.11:

$$F_2^{\gamma} = x\sum_i^{N_q} Q^{i2}\left(f_i(x) + \bar{f}_i(x)\right) \quad , \tag{1.16}$$

$$F_{\mathrm{L}}^{\gamma} = 0 \quad .$$

Thus, for the region dominated by photon exchange, $\tilde{F}_2$ should not depend on Q^2, $\tilde{F}_2(Q^2, x) \mapsto \tilde{F}_2(x)$. This effect is known as Bjorken scaling and was first observed at the SLAC experiment in 1968 [12,16]. Repeating the procedure also for γ–Z interference and Z exchange, it can be shown that, in the QPM, the generalised structure function $\tilde{F}_{\mathrm{L}} = 0$ and [15]:

$$\left[F_2^{\gamma}, F_2^{\gamma Z}, F_2^{Z}\right] = x\sum_i^{N_q} \left[Q^{i2}, 2Q^i g_V^i, {g_V^i}^2 + {g_A^i}^2\right]\left(f_i(x) + \bar{f}_i(x)\right) \quad ,$$

$$\left[F_3^{\gamma}, F_3^{\gamma Z}, F_3^{Z}\right] = \sum_i^{N_q} \left[0, 2Q^i g_A^i, 2g_V^i g_A^i\right]\left(f_i(x) - \bar{f}_i(x)\right) \quad . \tag{1.17}$$

The generalised structure functions can be rearranged as [17]:

$$\tilde{F}_2 = x\sum_i^{N_q} A_i(Q^2)\left(f_i(x) + \bar{f}_i(x)\right) \quad ,$$

$$x\tilde{F}_3 = x\sum_i^{N_q} B_i(Q^2)\left(f_i(x) - \bar{f}_i(x)\right) \quad . \tag{1.18}$$

The functions A_i and B_i are defined as:

$$A_i(Q^2) = \frac{1}{2}\left[(V_i^L)^2 + (V_i^R)^2 + (A_i^L)^2 + (A_i^R)^2\right] \quad ,$$

$$B_i(Q^2) = (V_i^L)(A_i^L) - (V_i^R)(A_i^R) \quad , \tag{1.19}$$

where the coefficient functions $V_i^{L/R}$ and $A_i^{L/R}$ are:

$$V_i^{L/R} = Q^i - (g_V^e \pm \lambda g_A^e)g_V^i \kappa_Z \quad ,$$
$$A_i^{L/R} = -(g_V^e \pm \lambda g_A^e)g_A^i \kappa_Z \quad , \tag{1.20}$$

where the left (L) and right (R) states are lepton helicity projections, corresponding to $\lambda = -1$ and $\lambda = +1$, respectively, and "$\pm$" corresponds to the sign of the lepton charge.

For the CC process in QPM, $F_L^{W^\pm} = 0$ and $F_2^{W^\pm}$, $xF_3^{W^\pm}$ can be represented by U- and D-type PDFs [14, 15]:

$$F_2^{W^+} = x\bar{U} + xD \quad , \qquad xF_3^{W^+} = xD - x\bar{U} \quad ,$$
$$F_2^{W^-} = x\bar{D} + xU \quad , \qquad xF_3^{W^+} = xU - x\bar{D} \quad , \tag{1.21}$$

$$U = \sum_{i=u,c} f_i(x) \quad , \qquad D = \sum_{i=d,s,b} f_i(x) \quad , \tag{1.22}$$

where only active flavours, i.e. flavours with masses $m^2 < Q^2$, should be kept. The CC reduced cross sections can be expressed as:

$$\sigma_{r,\text{CC}}^+ = x\bar{U} + (1-y)^2 xD \quad ,$$
$$\sigma_{r,\text{CC}}^- = xU + (1-y)^2 x\bar{D} \quad . \tag{1.23}$$

1.3.2 Perturbative Quantum Chromodynamics

Quantum Chromodynamics describes strong interactions between quarks and gluons which are neglected in the QPM. Due to asymptotic freedom at high energies, the coupling constant of QCD, α_s, becomes sufficiently small that perturbation theory can be used. The cross-section predictions can be perturbatively expanded in orders of α_s as:

$$\sigma = \sigma_0 \cdot \alpha_s^0 + \sigma_1 \cdot \alpha_s^1 + \sigma_2 \cdot \alpha_s^2 + \dots \quad . \tag{1.24}$$

The coefficients σ_N are estimated for Feynman diagrams corresponding to order N in the strong coupling. If calculations include only the first non-zero term in the perturbation series, they are called the Leading Order predictions, LO, if the second non-zero term is included - Next-to-Leading Order, NLO, and so on.

1.3.3 Renormalisation

At higher orders, loop diagrams similar to the one shown in Fig. 1.2 are introduced. The integration of such loops, as the momentum tends to infinity, produces divergences. To provide finite results for the calculations, special regularisation methods are used. For the regularisation in the global QCD analyses described in Chapters 3 and 4, the
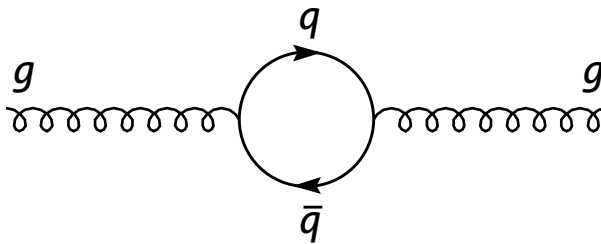
Figure 1.2: Schematic Feynman diagram of the gluon self-energy loop.

modified minimal subtraction scheme [18, 19], $\overline{\text{MS}}$, was used. It is based on the idea of evaluating the loop integrals in a $(4 - \epsilon)$-dimensional space in which they converge and subsequently taking the limit of $\epsilon \to 0$. In this procedure, an arbitrary high momentum cut-off, Λ^2, is introduced, which can be combined with the strong coupling constant by defining the running coupling $\alpha_s(\mu_R^2)$ which depends on the renormalisation scale μ_R^2. For DIS processes, the renormalisation scale is usually set equal to the virtuality, $\mu_R^2 = Q^2$. If the strong coupling constant is defined for some scale μ_0^2, then it can be evaluated for any scale at the chosen order of calculation. For example, at leading order [16]:

$$\alpha_s(Q^2) = \frac{\alpha_s(\mu_0^2)}{1 + \alpha_s(\mu_0^2)\frac{(33-2n_f)}{12\pi}ln\left(\frac{Q^2}{\mu_0^2}\right)} \quad , \tag{1.25}$$

where n_f represents the number of active flavours. Usually the strong coupling is defined for the scale μ_0^2 equal to the Z-boson-mass squared. For the NLO analyses in Chapters 3 and 4, the value of $\alpha_s(M_Z^2) = 0.118$ was used in accordance with PDG14 [20].

1.3.4 Factorisation and evolution of the PDFs

The perturbative expansion of the QCD calculations is applicable only at short distances, where the strong coupling constant is small. Thus the cross-section calculations for DIS should be written as the convolution of two terms [16]: a calculable hard-scattering cross section, $\hat{\sigma}$, and a non-perturbative parton density, f:

$$\sigma = \hat{\sigma} \otimes f \quad . \tag{1.26}$$

This is called factorisation. In the factorisation procedure, part of the gluon interactions corresponding to hard radiative corrections are explicitly included in $\hat{\sigma}$ and the remaining softer interactions are absorbed into the parton density f. The separation is made at a scale known as the factorisation scale μ_F^2. This does not have to be the same as the renormalisation scale, but in the global QCD analyses described in Chapters 3 and 4, they were set equal, $\mu_F^2 = \mu_R^2 = Q^2$.

Because of the factorisation procedure, the PDFs also acquire a dependence on the factorisation scale, $f_i(x) \mapsto f_i(Q^2, x)$. Contrary to the dependence on x, which so far can only be estimated experimentally, the evolution in Q^2 can be evaluated using DGLAP [21–25] evolution. It can be expressed as [15]:

$$\frac{\partial f^{NS}}{\partial ln Q^2} = \frac{\alpha_s(Q^2)}{2\pi} P_{qq} \otimes f^{NS} \quad,$$
$$\frac{\partial}{\partial ln Q^2} \begin{pmatrix} f^S \\ g \end{pmatrix} = \frac{\alpha_s(Q^2)}{2\pi} \begin{pmatrix} P_{qq} & 2n_f P_{qg} \\ P_{gq} & P_{gg} \end{pmatrix} \otimes \begin{pmatrix} f^S \\ g \end{pmatrix} \quad, \tag{1.27}$$

where g is the gluon PDF and the convolution is:

$$[P \otimes f](Q^2, x) = \int_x^1 \frac{1}{z} P(z) f(Q^2, \frac{x}{z}) \mathrm{d}z \quad, \tag{1.28}$$

the f^S term is the singlet quark distribution:

$$f^S(Q^2, x) = \sum_i^{n_f} (f_i(Q^2, x) + \bar{f}_i(Q^2, x)) \quad, \tag{1.29}$$

and the non-singlet f^{NS} distributions are differences of quark distributions:

$$f^{NS}(Q^2, x) = f_i(Q^2, x) - \bar{f}_i(Q^2, x) \quad (\text{or } f_i(Q^2, x) - f_j(Q^2, x)) \quad. \tag{1.30}$$

The splitting functions P_{qq}, P_{qg}, P_{gq} and P_{gg} are summarised graphically in Fig. 1.3. They
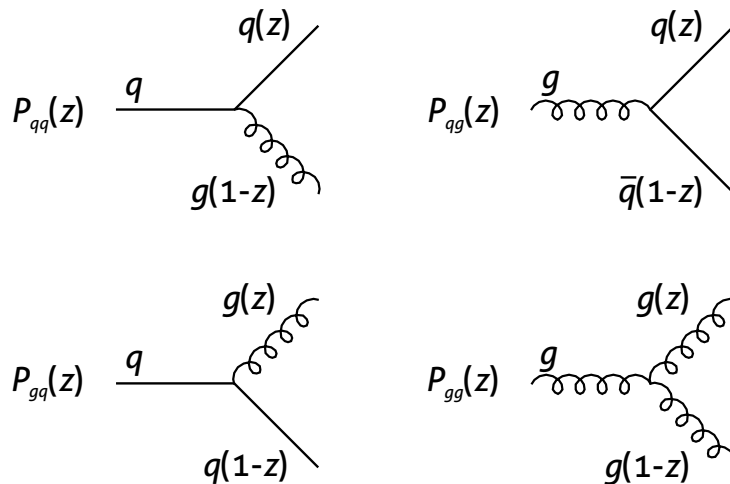
Figure 1.3: The DGLAP splitting functions.

can be expanded as a power series in $\alpha_s(Q^2)$ [16]:

$$
\begin{aligned}
P_{q_i q_j}(z, \alpha_s) &= \delta_{ij} P_{qq}^{(0)}(z) + \frac{\alpha_s}{2\pi} P_{q_i q_j}^{(1)}(z) + ... \\
P_{qg}(z, \alpha_s) &= P_{qg}^{(0)}(z) + \frac{\alpha_s}{2\pi} P_{qg}^{(1)}(z) + ... \\
P_{gq}(z, \alpha_s) &= P_{gq}^{(0)}(z) + \frac{\alpha_s}{2\pi} P_{gq}^{(1)}(z) + ... \\
P_{gg}(z, \alpha_s) &= P_{gg}^{(0)}(z) + \frac{\alpha_s}{2\pi} P_{gg}^{(1)}(z) + ...
\end{aligned}
\tag{1.31}
$$

The leading-order terms are equal to:

$$
\begin{aligned}
P_{qq}^{(0)}(z) &= \frac{4}{3} \left[\frac{1 + z^2}{(1 - z)_+} \right] + 2\delta(1 - z) \quad, \\
P_{qg}^{(0)}(z) &= \frac{1}{2} \left[z^2 + (1 - z)^2 \right] \quad, \\
P_{gq}^{(0)}(z) &= \frac{4}{3} \left[\frac{1 + (1 - z)^2}{z} \right] \quad, \\
P_{gg}^{(0)}(z) &= 6 \left[\frac{1 - z}{z} + z(1 - z) + \frac{z}{(1 - z)_+} \right] + \frac{33 - 2n_f}{6} \delta(1 - z) \quad.
\end{aligned}
\tag{1.32}
$$

The DGLAP equations give a formalism for calculating the parton densities at any scale after they have been estimated for some starting scale Q_0^2.

1.3.5 Treatment of Heavy Flavours

The light quarks (u, d and s) are always considered as active partons in the proton, while the heavy-quark contribution should be taken into account for scales higher than their mass. The most frequently used approaches to the inclusion of heavy quarks are briefly described in the following subsections.

Zero-mass variable-flavour-number scheme

The light quarks are treated as massless in perturbative QCD, which is a good assumption for DIS. For heavy quarks, similar assumption would be valid only for scales much larger than the mass squared of the heavy quark, $Q^2 \gg m_{hq}^2$. Such an approach is implemented in the zero-mass variable-flavour-number scheme, ZM-VFNS. In this factorisation scheme, for $Q^2 < m_{hq}^2$, heavy quarks PDFs are set to zero, $f_{hq}(Q^2, x) = 0$, while for $Q^2 \geq m_{hq}^2$, an additional massless parton is included in the DGLAP equations.

Fixed-flavour-number scheme

In the fixed-flavour-number scheme, FFNS, heavy partons are not included in the PDFs at any scale and are instead generated as massive quarks by boson-gluon-fusion processes. This procedure provides reliable calculations for the region of $Q^2 \sim m_{hq}^2$ but introduces ambiguities in defining the renormalisation and factorisation scales at high values of Q^2.

Variable-flavour-number scheme

The ZM-VFNS and FFNS are interpolated in variable-flavour-number schemes, VFNS, such that the correct features of the FFNS scheme at $Q^2 \sim m_{hq}^2$ are combined with the introduction of heavy-flavour PDFs at large values of Q^2. In the analyses described in Chapters 3 and 4, the optimised Thorne-Roberts [26–28] VFNS, RTOPT, was used. In this scheme, an additional condition, that the derivatives of the heavy-flavour $\tilde{F}_2^{hq}$ structure functions on Q^2 had to match smoothly at the threshold, was introduced.

1.4 Physics beyond the Standard Model

New interactions beyond the Standard Model (BSM) with energy scales much higher than the centre-of-mass energy of the experiment may have an effect on the cross-section measurements. Two BSM models that can influence the DIS cross sections are described in this section.

1.4.1 General contact interactions

The most general method for indirect searches of BSM physics at higher scales is provided by the formalism of contact interactions (CI). In the CI formalism, a virtual exchange of new particles with masses much larger than the centre-of-mass energy is approximated as the four-fermion point-like contact interaction shown in Fig. 1.4. This approach is only
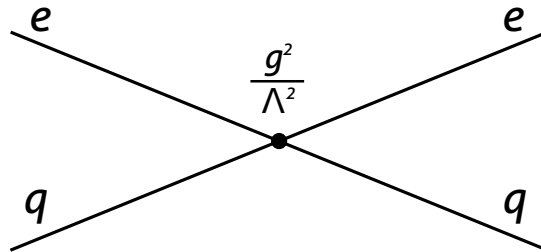
Figure 1.4: Schematic Feynman diagram of the general contact interactions.

valid in the low-energy limit and can be represented as an extra term $\mathcal{L}_{\text{CI}}$ added to the

Standard Model Lagrangian:

$$\mathcal{L}_{\text{CI}} = \sum_{\substack{k,j=L,R \\ q=u,d,s,c,b}} \eta_{kj}^{eq} (\bar{e}_k \gamma^\mu e_k)(\bar{q}_j \gamma_\mu q_j) \quad . \tag{1.33}$$

Here the sum runs over electron and quark helicities and quark flavours, and η_{kj}^{eq} are coupling coefficients. Here only vector-like contact interactions are considered, since for scalar and tensor CI, strong limits have already been placed [29]. The coupling coefficients have the units of inverse square of the mass and describe the helicity and flavour structure of the contact interactions:

$$\eta_{kj}^{eq} = \epsilon_{kj}^{eq} \frac{g^2}{\Lambda^2} \quad . \tag{1.34}$$

The coefficients ϵ_{kj}^{eq} can be equal to ± 1 or 0, g is the coupling strength and Λ is the mass scale of the contact interactions. Any specific CI model with a particular configuration of ϵ_{kj}^{eq} coefficients can be parameterised with one parameter, $\eta = \frac{g^2}{\Lambda^2}$. For simplicity and since, at HERA, the contribution from the first generation of quarks is dominant, flavour symmetry was assumed:

$$\begin{aligned} \eta_{kj}^{eu} &= \eta_{kj}^{ec} \quad , \\ \eta_{kj}^{ed} &= \eta_{kj}^{es} = \eta_{kj}^{eb} \quad . \end{aligned} \tag{1.35}$$

Modification of the model Lagrangian influences the NC DIS e^-p cross sections by changing the coefficient functions $V_i^{L/R}$ and $A_i^{L/R}$ of Eq. 1.20 to [29]:

$$\begin{aligned} V_i^m &= Q^i - (g_V^e - \lambda g_A^e) g_V^i \kappa_Z + \frac{Q^2}{2\alpha}(\eta_{mL}^{ei} + \eta_{mR}^{ei}) \quad , \\ A_i^m &= -(g_V^e - \lambda g_A^e) g_A^i \kappa_Z + \frac{Q^2}{2\alpha}(\eta_{mL}^{ei} - \eta_{mR}^{ei}) \quad . \end{aligned} \tag{1.36}$$

For NC DIS e^+p, the coefficient functions of Eq. 1.36 should be changed by $V_i^{L,R} \Rightarrow V_i^{R,L}$ and $A_i^{L,R} \Rightarrow A_i^{R,L}$.

In CC DIS, only η_{LR}^{eq} and η_{LL}^{eq} can contribute, since right-handed neutrinos cannot be produced. Effects of η_{LR}^{eq} for CC scattering are excluded by the pion-decay data [30], and η_{LL}^{eq} coupling coefficients modify the CC reduced cross sections of Eq. 1.23 as:

$$\sigma_{r,\text{CC}}^{\pm} \Rightarrow \left[1 - \frac{sin^2\theta_W(M_W^2 + Q^2)}{2\pi\alpha}(\eta_{LL}^{ed} - \eta_{LL}^{eu})\right]^2 \cdot \sigma_{r,\text{CC}}^{\pm} \quad . \tag{1.37}$$

1.4.2 Quark form factor

In the Standard Model, all fermions and gauge bosons are assumed to be point-like particles; any non-zero spatial distribution would lead to deviations of the data from the

SM predictions. One of the possible scenarios is to assign an effective finite radius to electrons and/or quarks and to assume the SM bosons remain point-like. If the expected deviations are small, the predictions for such scenarios can be calculated by modifying the SM cross-section predictions with a semi-classical form-factor [31]:

$$\frac{d\sigma}{dQ^2} = \frac{d\sigma^{\mathrm{SM}}}{dQ^2} \left(1 - \frac{R_e^2}{6}Q^2\right)^2 \left(1 - \frac{R_q^2}{6}Q^2\right)^2 , \tag{1.38}$$

where R_e^2 and R_q^2 are the mean-square radii of the electron and the quark, respectively. In the analysis described in Chapters 5 and 6, the electron was assumed to be point-like, $R_e^2 \equiv 0$, and only quarks were allowed to have finite spatial distribution. Neutral current and charged current DIS cross sections are modified by Eq. 1.38 in a similar way. The mean-square radii R_q^2 have units of GeV^{-2} and the form factor can be parameterised with $\eta = R_q^2$. To maintain the generality of the approach, both positive and negative values of η were considered. Negative quark-radius squared is assigned when the quark charge changes sign as a function of radius.

Chapter 2

The HERA collider

In this chapter the HERA collider and parts of the ZEUS and H1 experiments relevant to the inclusive DIS analyses are described.

2.1 HERA

The Hadron Elektron Ring Anlage (HERA) [32, 33] was the first in the world and so far the only high-energy electron-proton collider. It was operated at Deutsches Elektronen-Synchrotron (DESY), national research centre at Hamburg, between 1992-2007.

A schematic view of HERA is given in Fig 2.1. The main accelerator ring is 6336 metres long and consists of four $90°$ bends and four staight sections with areas for the following experiments:

H1 [**34, 35**] - general-purpose electron-proton-scattering detector located at the north interaction point; described in Section 2.3.

HERMES [**36**] - fixed-target spectrometer at the east hall for studies of deep inelastic scattering of longitudinaly polarised electrons on a polarised hadron target. It ran from 1995 till 2007.

ZEUS [**37**] - general-purpose electron-proton-scattering detector located at the south interaction point; described in Section 2.2.

HERA-B [**38, 39**] - fixed-target experiment at the west hall, designed to produce B mesons in the interactions of the proton beam with an internal wire target. It was designed primarily for searches for CP violation and operated from 1997 till 2003.

The HERA collider operated in two phases: HERA I, from 1992 to 2000, and HERA II, from 2002 to 2007. From 1994 and until the last beam in 2007 the electron beam energy was 27.5 GeV. The proton beam energy until 1998 was 820 GeV and afterwards was
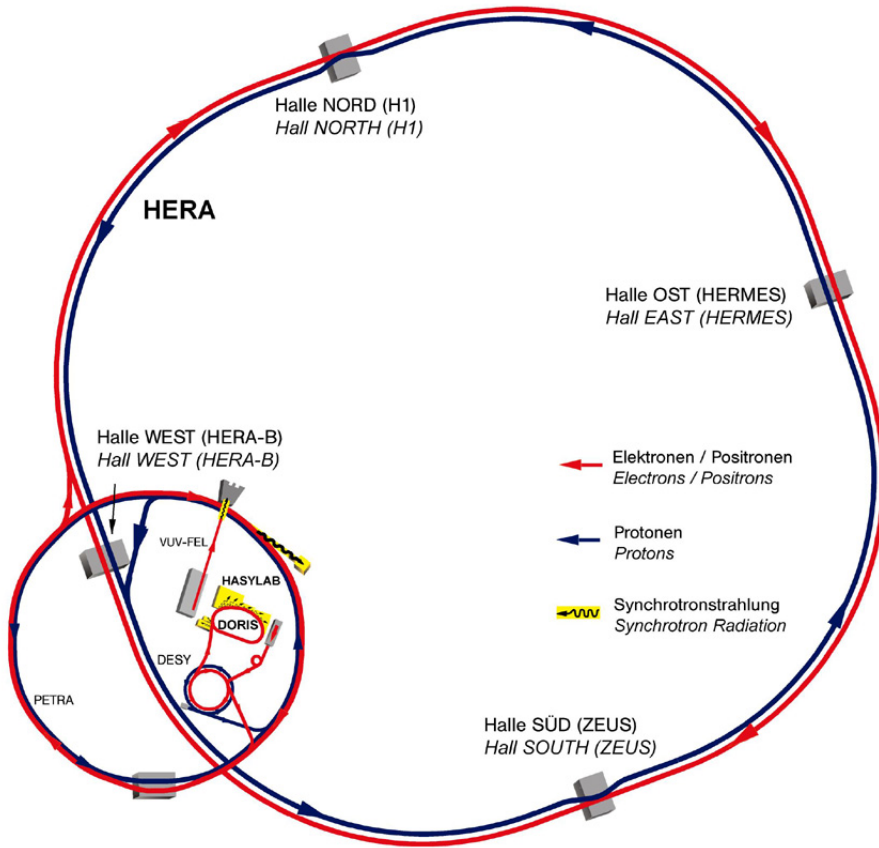
Figure 2.1: Schematic view of the HERA ring and the preaccelerating facilities.

increased to 920 GeV. During the last three months before the shutdown the proton beam energy was decreased to 575 GeV and 460 GeV. These provided the two experiments, ZEUS and H1, with data for four different centre-of-mass energies of about 300, 318, 251 and 225 GeV, and allowed a model-independent estimation of the longitudinal structure function F_L [40, 41].

In the period of 2000-2002 the HERA collider was upgraded [42]. New separator magnets, almost three times stronger and three times smaller than before, were used at the interaction point for the separation of the electron and proton beams and new quadrupole magnets increased the beam focusing. This allowed the maximum of the instantaneous luminosity to be increased from $1.5 \times 10^{31} \text{cm}^{-2}\text{s}^{-1}$ to $5 \times 10^{31} \text{cm}^{-2}\text{s}^{-1}$ and to deliver to the experiments about three times more integrated luminosity during the HERA II period compared to HERA I. Spin rotators were installed in the electron accelerating ring around the ZEUS and H1 interaction points to produce longitudinal polarisation.

2.2 ZEUS detector

The ZEUS detector [37] was one of the two general purpose detectors at HERA designed for studies of electron-proton interactions. It had a solid angle coverage of 99.8% in the proton-direction hemisphere and 99.5% in the electron-direction hemisphere. The layout of the detector is shown in Fig. 2.2.
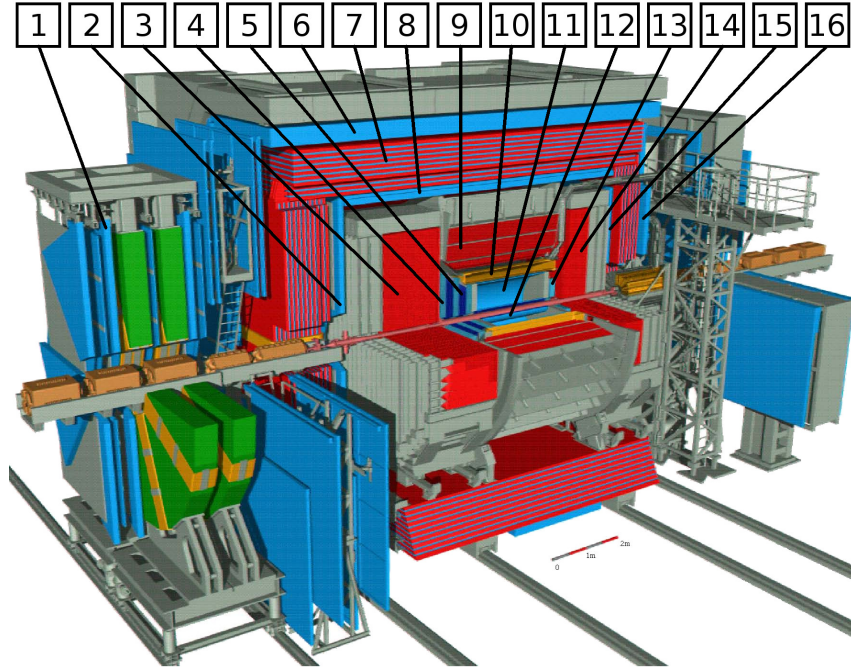
Figure 2.2: Schematic view of the ZEUS detector. The labeled subdetector components are: 1 - outer forward muon spectrometer FMUON; 2 - inner forward muon spectrometer FMUI; 3 - forward calorimeter FCAL; 4 - forward tracking detector FTD; 5 - transition radiation detector TRD; 6 - outer barrel muon spectrometer BMUON; 7 - iron yoke and compensating solenoid; 8 - inner barrel muon spectrometer BMUI; 9 - barrel calorimeter BCAL; 10 - superconducting solenoid; 11 - central tracking detector CTD; 12 - vertex detector VXD or MVD; 13 - rear tracking detector RTD; 14 - rear calorimeter RCAL; 15 - inner rear muon spectrometer RMUI; 16 - outer rear muon spectrometer RMUON.

The coordinate system at ZEUS has its origin at the nominal interaction point, the x axis was chosen to point to the centre of the HERA ring, the y axis points upwards and the z axis is in the direction of the proton beam. The direction of the proton beam is often referred to as the forward direction. The polar angle θ and the azimuthal angle ϕ are defined with respect to the z and x axis, respectively.

Due to the large momentum imbalance between incident protons and electrons, most of the final-state particles were boosted in the proton beam direction. To take this into

account the ZEUS detector was designed to be asymmetric. Starting from the interaction
point, the essential elements of the detector are: a vertex detector (VXD before 1996 or
MVD from 2001; labeled as "12" in Fig. 2.2); forward (FTD, "4"), central (CTD, "11")
and rear (RTD, "13") tracking detectors plus transition radiation detector (TRD, "5");
a thin magnetic solenoid ("10"); forward (FCAL, "3"), central (BCAL, "9") and rear
(RCAL, "14") calorimeters; and muon spectrometers before (FMUI "2", BMUI "8" and
RMUI "15") and after (FMUON "1", BMUON "6" and RMUON "16") the iron yoke
("7"). To catch electrons scattered through the hole in RCAL near the beam pipe, a
beam-pipe calorimeter BPC [43] was built and operated from 1995 to 2000. For six weeks
in 1997 a beam pipe tracker BPT [44] was installed in front of BPC. The region near the
beam pipe in the proton direction from 1993 to 2000 was covered by the leading proton
spectrometer LPS [45]. The luminosity measurement systems were installed downstream
in the electron beam direction, outside the detector, at a distance from 8 to 107 m from the
interaction point. The parts of the detector most crucial for inclusive DIS measurements
are described in detail in the following.

2.2.1 Tracking system

The ZEUS tracking system [46] was designed to reconstruct tracks over the polar angle
range $7.5^{\circ} < \theta < 170^{\circ}$, provide dE/dx information for electron identification and locate
the interaction point, known as the primary vertex. The superconducting coil provided a
high magnetic field of $B = 1.43\,\mathrm{T}$ [47] for separation and better momentum reconstruction
of charged particles. The layout of the main elements of the tracking system is shown in
Fig. 2.3.
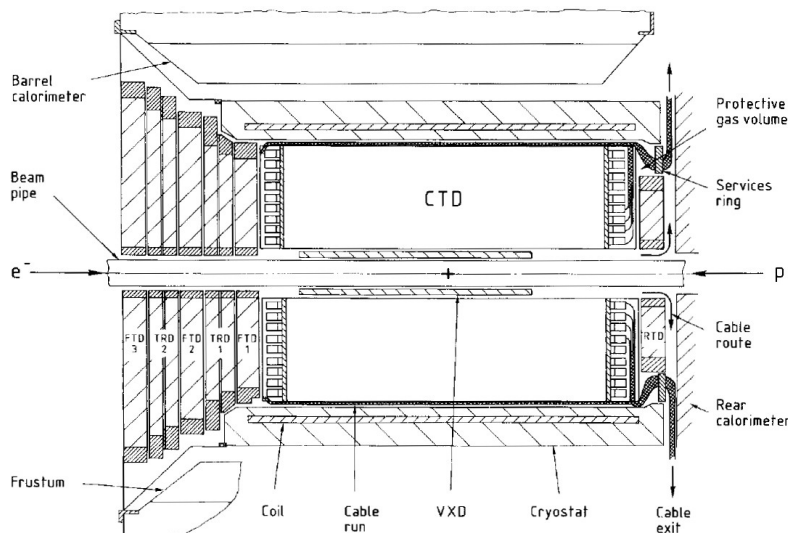
Figure 2.3: Schematic view of the ZEUS tracking system.

Tracking Detectors

Vector drift chambers with maximum drift times of 500 ns were used as tracking detectors. Trajectories at polar angles from 15° to 164° were reconstructed in the central tracking detector CTD, and from 7.5° to 28° in the forward tracking detector FTD. Scattered electrons from low-Q^2 events at polar angles from 160° to 170° were measured in a small rear tracking detector, RTD.

The CTD [37, 46, 47] was a 2 m long, 1.6 m diameter cylindrical drift chamber with nine superlayers, each with eight sense-wire layers. The five odd-numbered superlayers had wires parallel to the chamber axis and four even-numbered superlayers were tilted at stereo angles close to 5°. The stereo angles were chosen such that the angular resolution in polar and azimuthal angles were roughly equal. The superlayers were subdivided by the wires into "cells", tilted at 45° with respect to the radius vector. The layout of wires at the chamber endplates in a 45° sector is shown in Fig. 2.4.
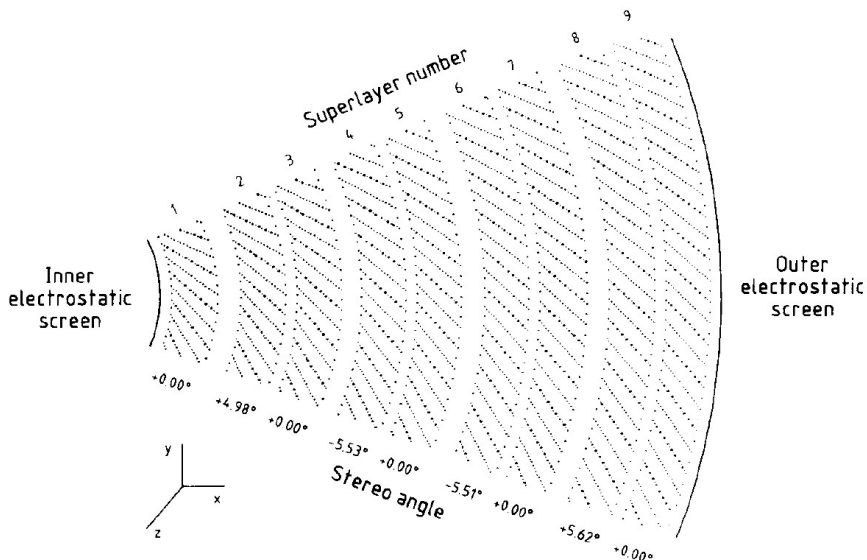
Figure 2.4: The layout of wires in one octant of the ZEUS central tracking detector CTD. The sense wires are indicated by the large dots. The wire positions are shown at the end plates.

The resolution on transverse momentum, p_T, for tracks with hits in all nine CTD superlayers was [48]:

$$\sigma(p_T)/p_T = 0.0058 p_T \otimes 0.0065 \otimes 0.0014/p_T \quad , \qquad (2.1)$$

where p_T is in GeV. Here the first term represents the resolution of the hit position measurement, the second term arises from the scattering within the CTD and the last term corresponds to the scattering before the CTD.

The FTD consisted of three drift chambers, each with six sense layers arranged at $60°$ stereo. The FTD chambers were interleaved by four layers of transition radiation detectors for electron identification. The RTD consisted of one planar drift chamber of the FTD type.

Vertex Detectors

The main purpose of the vertex detector VXD [49] was the detection of short-lived particles and improvement of the momentum and angular resolution of charged tracks. The VXD consisted of 120 cells, each with 12 sense wires, located between the outer radius of the beampipe and the inner wall of the CTD. It covered the polar angle region from $8.6°$ to $165°$. Due to technical problems, the VXD stopped operation in 1993 and was removed from the detector during maintenance in 1996.
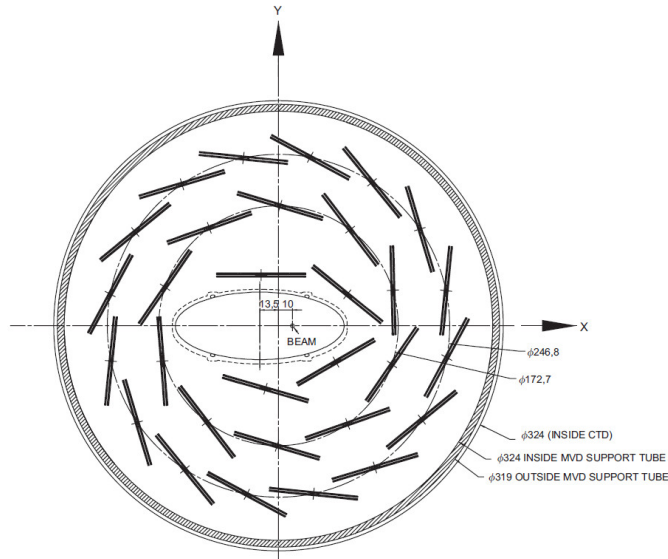
Figure 2.5: The layout of the silicon sensors in the transverse plane of the ZEUS barrel MVD. The direction of the z axis points out of the paper.

A micro vertex detector MVD [50] was developed to replace the VXD and was installed in the detector during the HERA upgrade in 2001. The MVD consisted of a barrel (BMVD) and a forward (FMVD) section. The barrel section contained three layers of silicon sensors placed as shown in Fig. 2.5, and provided polar-angle coverage for tracks from $30°$ to $150°$. The forward section was composed of four vertical planes and extended the polar-angle coverage to $7°$. The MVD improved the transverse momentum resolution of the CTD to [51]:

$$\sigma(p_T)/p_T = 0.0029p_T \otimes 0.0081 \otimes 0.0012/p_T \quad . \tag{2.2}$$

2.2.2   Calorimeter

The calorimeter [37, 52, 53] at ZEUS was a sampling calorimeter composed of cells with 3.3 mm-thick depleted uranium (DU) plates as an absorber and 2.6 mm-thick scintillator plates as a detector. The thickness of the DU plates corresponds to one radiation length, X_0, the mean distance over which the energy of a relativistic electron decreases to a factor of $\frac{1}{e}$ by bremsstrahlung, or $\frac{7}{9}$ of the mean free path for a high-energy photon before producing the e^+e^- pair. The thickness of the scintillator plates was optimised to give equal signals for electrons and hadrons of equal energy ($e/h = 1.00 \pm 0.02$ [52]), which makes the ZEUS calorimeter a compensating calorimeter.
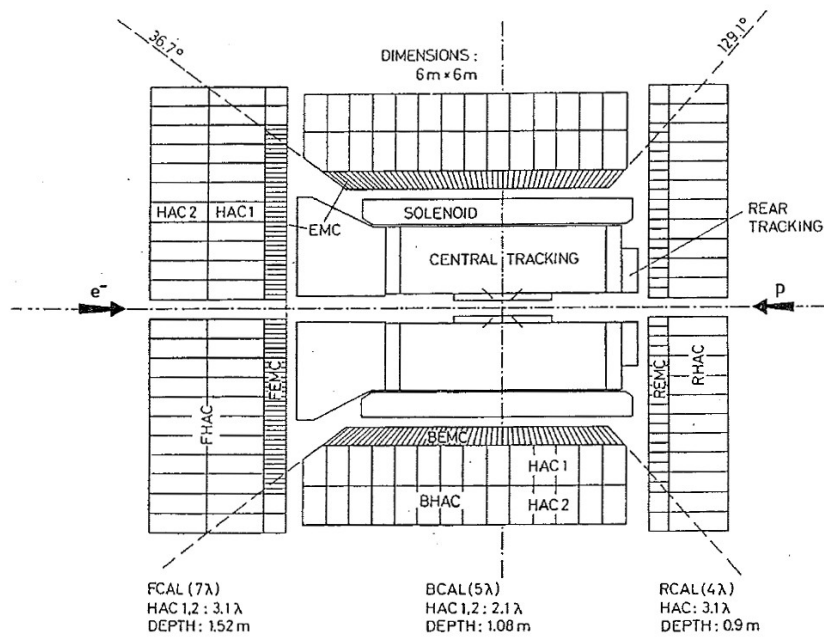
Figure 2.6: The layout of the ZEUS calorimeter system.

The ZEUS calorimeter system consisted of:

FCAL - forward calorimeter covering polar angles from $2.2°$ to $39.9°$;

BCAL - barrel calorimeter extending from $36.7°$ to $129.2°$;

RCAL - rear calorimeter extending from $128.1°$ to $176.5°$;

BPC - beam pipe calorimeter in the hole between the RCAL and beam pipe;

FPC - forward plug calorimeter installed in the beam hole of the FCAL.

FNC - forward neutron calorimeter located downstream of the interaction point at $Z = 105$ m;

The FCAL, BCAL and RCAL had a similar structure and their layout is shown in Fig. 2.6. Each component was longitudinaly segmented into electromagnetic (EMC) and one (RCAL) or two (FCAL and BCAL) hadronic sections (HAC1,2). The depth of the electromagnetic sections was about $25X_0$ or 1 interaction length, λ, which is the mean distance travelled by a relativistic hadronic particle before undergoing an inelastic nuclear interaction. The depth of the hadronic sections was $2 \times 3.1\,\lambda$ in the FCAL, $2 \times 2.1\,\lambda$ in the BCAL and $1 \times 3.1\,\lambda$ in the RCAL.

The silicon pad detectors of the hadron-electron separator (HES) were installed after the fourth and seventh scintillator layers of the FCAL and after the fourth scintillator layer of the BCAL and RCAL. They were used for electron identification and provided a hadron rejection by about a factor of 125 in the FCAL and 25 in the BCAL and RCAL at 90% electron efficiency for energies between 2 and 100 GeV.

The energy resolution of the ZEUS calorimeter for hadrons was:

$$\sigma(E)/E = \frac{35\%}{\sqrt{E}} \otimes 2\% \quad , \tag{2.3}$$

and for electrons:

$$\sigma(E)/E = \frac{18\%}{\sqrt{E}} \otimes 1\% \quad . \tag{2.4}$$

2.2.3   Luminosity measurement system

At ZEUS the luminosity was evaluated [54, 55] by measuring the rate of the electron-photon bremsstrahlung, $ep \rightarrow ep\gamma$. The advantage of this process is that it has a sufficiently high cross section that can be precisely calculated from Bethe-Heitler [56] theory. It also has a clear experimental signature - the bremsstrahlung photon and electron emerge from the interaction point at very small angles with respect to the electron beam direction. The integrated luminosity for a certain data taking period was calculated as:

$$L = \frac{N_\gamma}{A\sigma} \quad . \tag{2.5}$$

Here N_γ is the number of bremsstrahlung photons selected in a certain solid angle and energy range over the period, A is the probability for such photons to be observed in this solid angle, and σ is the bremsstrahlung cross-section integrated over the same energy range.

The general layout of the ZEUS luminosity monitor detectors [54] used during the HERA I period is displayed in Fig. 2.7 a. The electron detectors were installed at $Z = -8$, -35 and -45 m near the electron beam pipe, and the photon detector was positioned at $Z = -107$ m close to the proton beam pipe. Due to the excellent background conditions and large photon acceptance, only photons were used for the precise luminosity determination and scattered electrons were used for systematic checks. The electrons
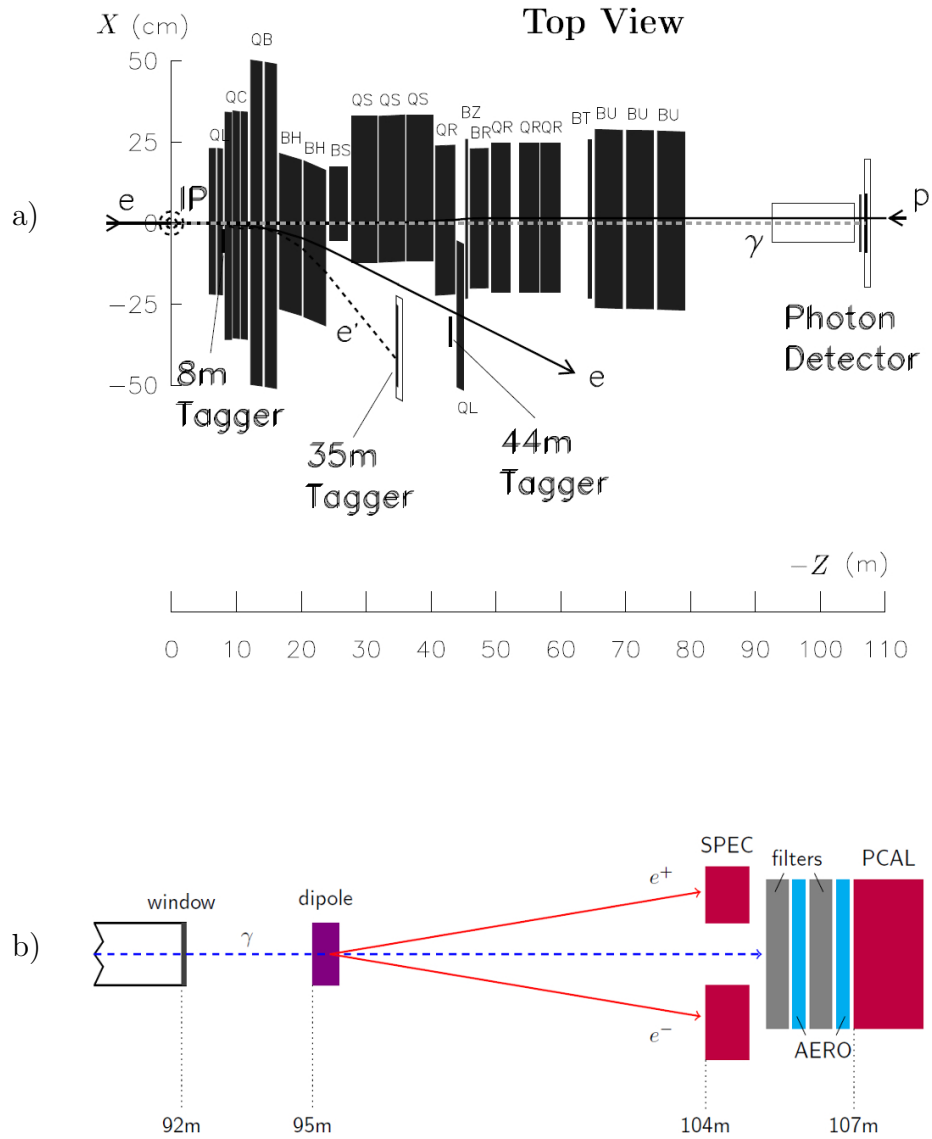
Figure 2.7: The layout of the ZEUS luminosity measurement system for the HERA I (a) and HERA II (b) data-taking periods. The PCAL in b) denotes the same photon detector as in a).

measured in the electron detectors in the absence of a detected photon were used to identify photoproduction events. The photon detector also allowed photons from initial- and final-state radiation to be measured. The beam-related backgrounds were estimated from non-colliding beams, which were electron or proton beams without counter-rotating partners.

After the HERA upgrade, the instantaneous luminosity was increased by more than a factor of 3. This was achieved by a stronger beam focusing and slightly larger beam currents and led to more synchrotron radiation and a larger rate of bremsstrahlung events. The effect of the synchrotron radiation on the photon detector was reduced by installing thicker carbon absorber blocks in front of it. As an additional luminometer [55], two spectrometers with a dipole magnet were installed outside the exit window, as shown in Fig. 2.7 b. They measured electron pairs converted from the bremsstrahlung photons and split by the magnetic field of the dipole. Two independent luminosity measurements allowed an independent comparison and therefore, in principle, a reduction of the systematic uncertainties.

2.2.4   Trigger system

At HERA, proton and electron bunches crossed every 96 ns, which corresponds to a 10.4 MHz rate. The interesting physics events at the designed instantaneous luminosity were expected [57] at a rate of below 1 Hz, while background events were predicted to have a rate of about 100 KHz. The maximum possible rate to write events to tape was about 10 Hz at an average event size of about 100 KByte. To cope with the high frequency collisions and high background rates at ZEUS, a three-level trigger system [57, 58] was built.

At the first-level trigger (FLT), data were first processed separately in each detector system with dedicated hardware processors, then sent to the global first-level trigger box (GFLTB), where the final trigger decision was made. The subdetector data were stored in either analogue or digital pipelines until the decision of the GFLTB arrived, which on average took $4.4\,\mu$s. The subdetector data from the collision selected by the GFLTB were digitalized and sent to the second-level trigger (SLT). The design output rate for the FLT was set to 1 kHz.

At the SLT, more precise trigger information was calculated and sent to the global second-level trigger box (GSLTB). In the GSLTB the data from the subdetectors were combined and used for the iterative calculations required for the trigger decision. The data selected by the GSLTB were transfered to the event builder (EVB), which combined it into an event. The SLT reduced the collision data rate to a maximum of 100 Hz.

The complete event information from the EVB was sent to the third-level trigger (TLT). There events were fully analysed to make the trigger decisions. After the TLT, the selected events were stored on a tape for future offline analyses at a rate of about 5 Hz.

2.3   H1 detector

The H1 detector [34, 35] was another general-purpose detector at HERA with almost 4π solid-angle coverage. The general layout of the detector is shown in Fig. 2.8. The coordinate system in H1 was defined in the similar way as in ZEUS.
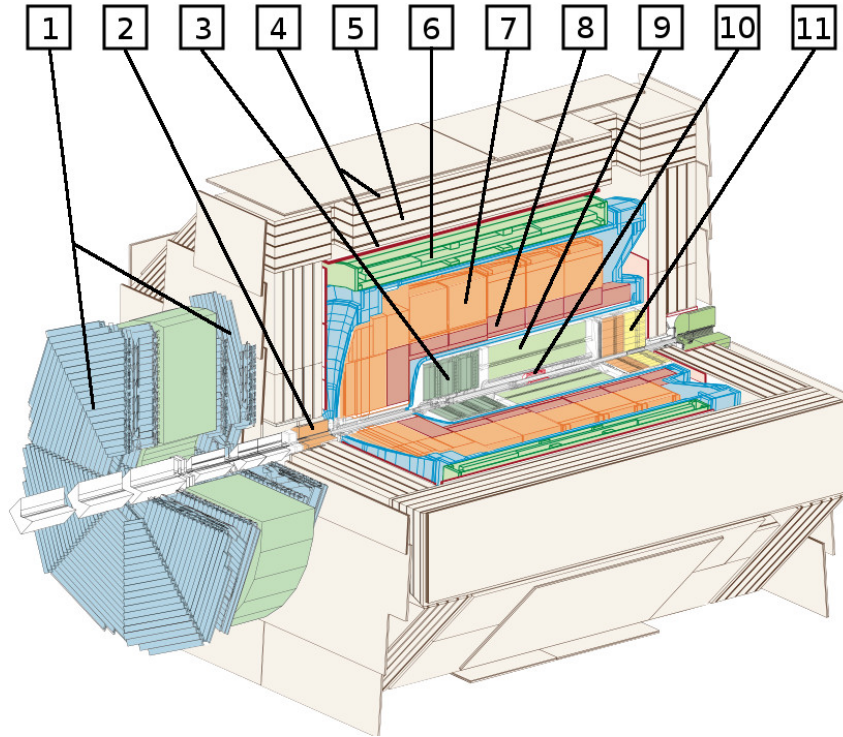
Figure 2.8: Schematic view of the H1 detector. The labeled subdetector components are: 1 - forward muon spectrometer; 2 - PLUG calorimeter; 3 - forward tracking device; 4 - central muon chamber; 5 - instrumented iron yoke; 6 - superconducting coil; 7 - hadronic LAr calorimeter; 8 - electromagnetic LAr calorimeter; 9 - central tracking device; 10 - silicon tracker; 11 - backward electromagnetic calorimeter BEMC.

The H1 detector was even more asymmetric in the longitudinal plane than ZEUS. Starting from the interaction vertex, the detector consisted of: silicon (labeled as "10" in Fig. 2.8), central ("9") and forward ("3") tracking systems; electromagnetic ("8") and hadronic ("7") sections of the liquid argon (LAr) cryostat; backward electromagnetic calorimeter (BEMC, "11"); a superconducting cylindrical coil ("6"); a silicon-copper plug (PLUG, "2"); central ("4") and forward ("1") muon spectrometers; and an iron yoke ("5"). An electron tagger and photon detector for luminosity monitoring were installed along the beam pipe in the backward direction at $Z = -33$ m and $Z = -103$ m, respectively.

2.3.1   Tracking system

The H1 tracking system [35, 59] provided simultaneous track triggering, reconstruction and identification of charged particles over the polar angle range $7° < \theta < 175°$. It was placed in a liquid-argon calorimeter, surounded by a superconducting solenoid that provided 1.15 T magnetic field parallel to the z axis. The layout of the main components of the tracking system is displayed in Fig. 2.9.
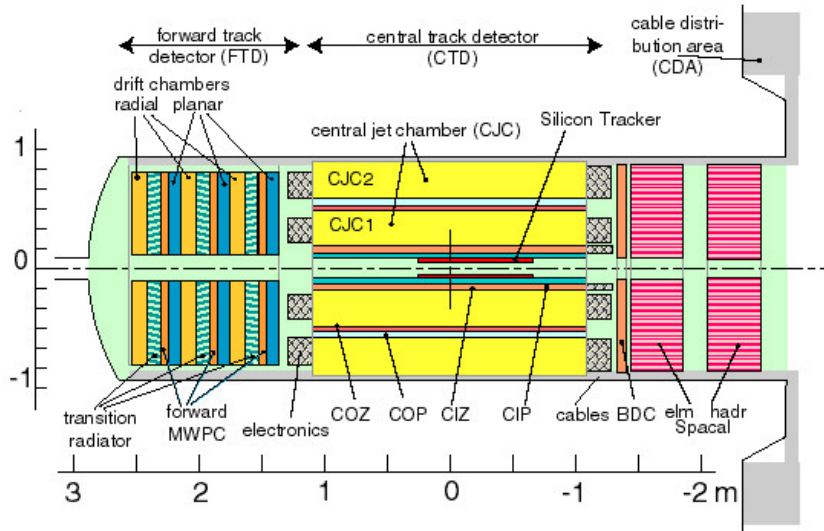
Figure 2.9: Schematic view of the H1 tracking system.

Tracking Detectors

The tracking detectors consisted of two mechanically distinct parts, the central (CTD) and forward (FTD) tracking devices. Tracks with polar angles in the range from $7°$ to $25°$ were measured in the FTD, and from $25°$ to $155°$ in the CTD. Scattered electrons at polar angles from $155°$ to $175°$ were detected in the backward proportional chamber BWPC.

The CTD was constructed of two concentric 220 cm long central jet chambers, CJC1 and CJC2, which had respectively 24 and 32 layers of wires parallel to the z axis separated into drift cells. The inner chamber (CJC1) was divided into 30 cells in the azimuthal direction, the outer chamber (CJC2) into 60 cells. The cells were tilted at $30°$ with respect to the radius vector, as shown in Fig. 2.10. The central jet chambers were suplemented by the central inner (CIZ) and central outer (COZ) drift chambers with the wires perpendicular to the z axis for precise measurements of the z coordinate. The CIZ chambers

were installed inside CJC1, and the COZ chambers fitted in between CJC1 and CJC2. For triggering purposes, the central inner (CIP) and central outer (COP) proportional chambers were installed inside the CIZ and between the COZ and CJC2, respectively.
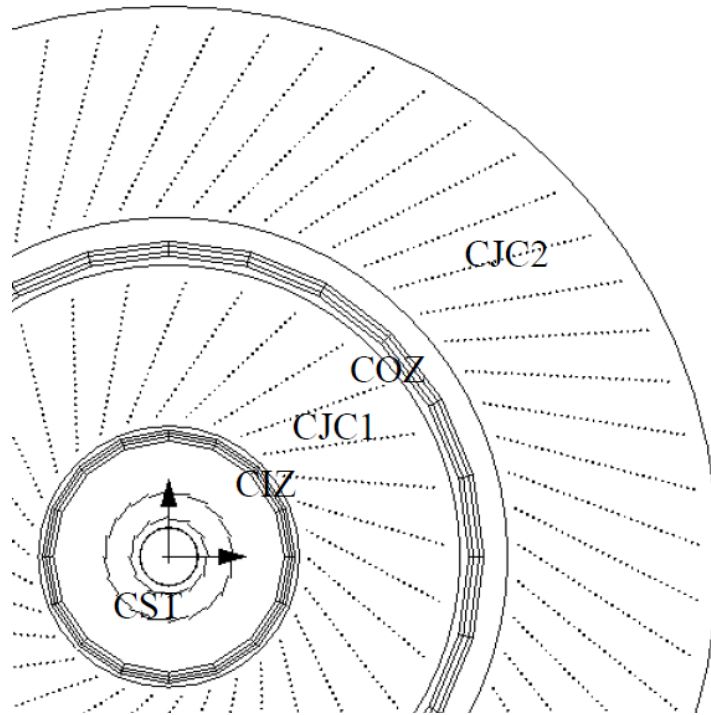
Figure 2.10: The layout of the H1 central tracker.

The FTD consisted of three supermodules, each including three planar wire drift chambers with different orientations for accurate θ measurements, a multiwire proportional chamber, FWPC, for fast triggering, a passive transition radiator and a radial wire drift chamber for electron identification and accurate $r\phi$ determination.

Silicon Trackers

The silicon vertex detector [59–61] was built to provide vertex information on the tracks close to the interaction point. It consisted of the central (CST), backward (BST) and forward (FST) silicon trackers. The CST and BST were operational from the beginning of 1997; during the HERA upgrade, the BST was redesigned and the FST [61] was installed.

The CST consisted of two layers of double-sided silicon-strip detectors around the beam axis at radii of 5.75 cm and 9.75 cm, as shown in Fig. 2.11. It provided polar-angle coverage from $30°$ to $150°$. Both FST and BST consisted of 12 silicon-sensor layers in the

transverse plane. The FST provided the detection of the particles in the angular region from 7° to 19° and BST from 163° to 174°.
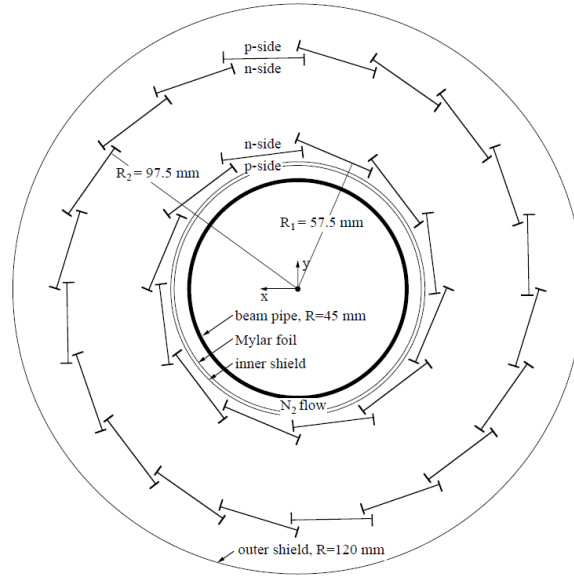
Figure 2.11: The layout of the silicon sensors in the transverse plane of the H1 CST. The direction of the z axis points in to the paper.

The resolution of transverse momentum p_T from the hit position measurement for tracks with $p_T > 10$ GeV was [59] :

$$\sigma(p_T)/p_T = 0.0043 p_T \quad , \tag{2.6}$$

where p_T is in GeV.

2.3.2 Calorimeter

The H1 calorimeter system [35, 62–64] consisted of:

LAr calorimeter - a liquid argon calorimeter covering polar angles from 4° to 154°;

PLUG - a small calorimeter in the proton direction with copper absorber and silicon pad readout covering the region between the liquid-argon cryostat and beam-pipe, $0.7^\circ < \theta < 3.3^\circ$;

SpaCal - a lead/scintillator-fibre calorimeter extending from $153°$ to $177.5°$;

FNC - forward neutron calorimeter located downstream of the interaction point at $Z = 107$ m;

VLQ - special spectrometer designed to cover vary small momentum transfers with polar angles from $178°$ to values close to $180°$;

BEMC - a lead scintillator backward electromagnetic calorimeter built for electron triggering from $151°$ to $176°$;

Tail Catcher - a tail-catcher system which provided a rough calorimetric measurement of hadronic particles leaking out of the LAr calorimeter.

The layout of these components is schematically displayed in Fig. 2.12.
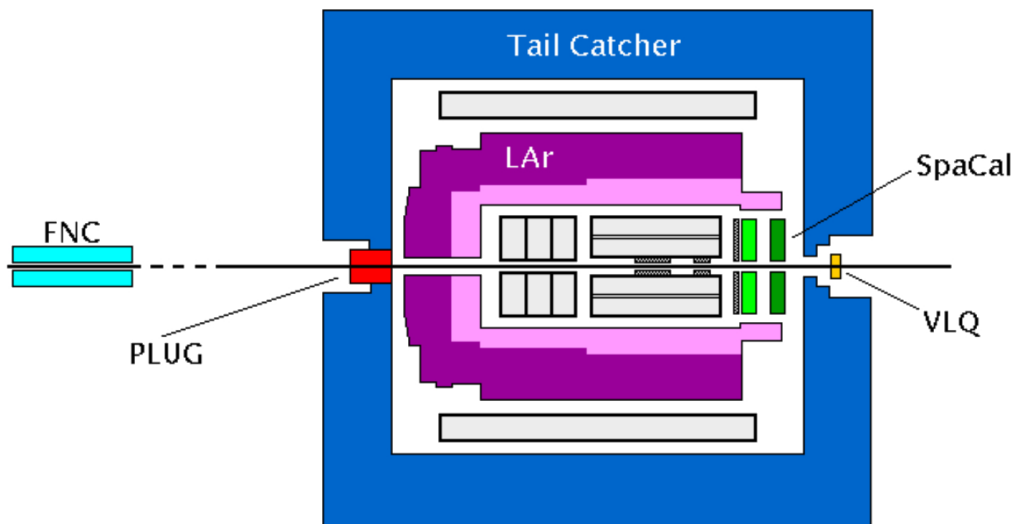
Figure 2.12: The layout of the H1 calorimeter system.

The LAr calorimeter [35, 62] was a sampling calorimeter constructed of cells with lead or stainless steel as an absorber and liquid argon as a detector. The liquid argon technique [35] for the calorimeter was chosen because of the good stability, fine granularity for electron-pion separation and ease of calibration. The LAr calorimeter was non-compensating; the signal for hadrons was about $30\,\%$ smaller than for electrons. Therefore, the fine segmentation of the calorimeter was exploited to distinguish the hadronic component of the jets from the electromagnetic component and a correction was applied to the hadronic signal. The calorimeter modules were divided into inner electromagnetic (EMC) and outer hadronic (HAC) stacks. The EMC cells consisted of 2.4 mm lead absorber and

2.35 mm liquid-argon active material and HAC cells of 16 mm steel absorber and 2.4 mm liquid-argon active material. The depth of the EMC varied between $30X_0$ in the forward and $20X_0$ in the central region, which corresponds to 1.4λ and 1λ, respectively. The total depth of EMC and HAD varied between 8λ in the forward and 5λ in the central region. The energy resolution of the LAr calorimeter for hadrons was:

$$\sigma(E)/E = \frac{50\%}{\sqrt{E}} \otimes 2\% \quad , \tag{2.7}$$

and for electrons:

$$\sigma(E)/E = \frac{12\%}{\sqrt{E}} \otimes 1\% \quad . \tag{2.8}$$

A spaghetti calorimeter SpaCal [63,64] also consisted of electromagnetic and hadronic sections. Both sections had scintillating plastic fibres embedded in a lead matrix. The inner electromagnetic section was made of 0.5 mm fibres with lead-to-fibre ratio of $2.3 : 1$ and the outer hadronic section of 1.0 mm fibres with lead-to-fibre ratio of $3.4 : 1$. The SpaCal provided an energy resolution for hadrons of

$$\sigma(E)/E = \frac{13\%}{\sqrt{E}} \otimes 4\% \quad , \tag{2.9}$$

and for electrons of

$$\sigma(E)/E = \frac{7\%}{\sqrt{E}} \otimes 1\% \quad . \tag{2.10}$$

2.3.3   Luminosity measurement system

The luminosity for all HERA I analyses and low-Q^2 or low-energy HERA II analyses was evaluated with the Bethe-Heitler process [34,65], similar to the procedure described in Section 2.2.3. Electrons and photons originating from this process were detected in the luminosity system schematically shown in Fig. 2.13 a. The electron tagger, ET, was located at $Z = -33.4$ m and the photon detector at $Z = -102.9$ m. The photon detector had a $22\,X_0$ depth and was shielded by a $2\,X_0$ lead filter and $1\,X_0$ Cherenkov counter. The filter protected the photon detector against synchrotron radiation and Cherenkov counter was used for rejection of early photon showers and to give a first rough energy measurement [65].

Along with the bremsstrahlung process, QED Compton (QEDC) scattering [65,66] was used for evaluation of the luminosity. It was used in the H1 inclusive DIS analysis [67] of the high-energy HERA II data, which provides more than half of all H1 integrated luminosity. The electron and photon emitted in the QEDC process have a significant transverse momentum and can be detected in the BEMC or in the LAr calorimeter. An example of a QEDC event candidate is schematically displayed in Fig. 2.13 b. The QEDC
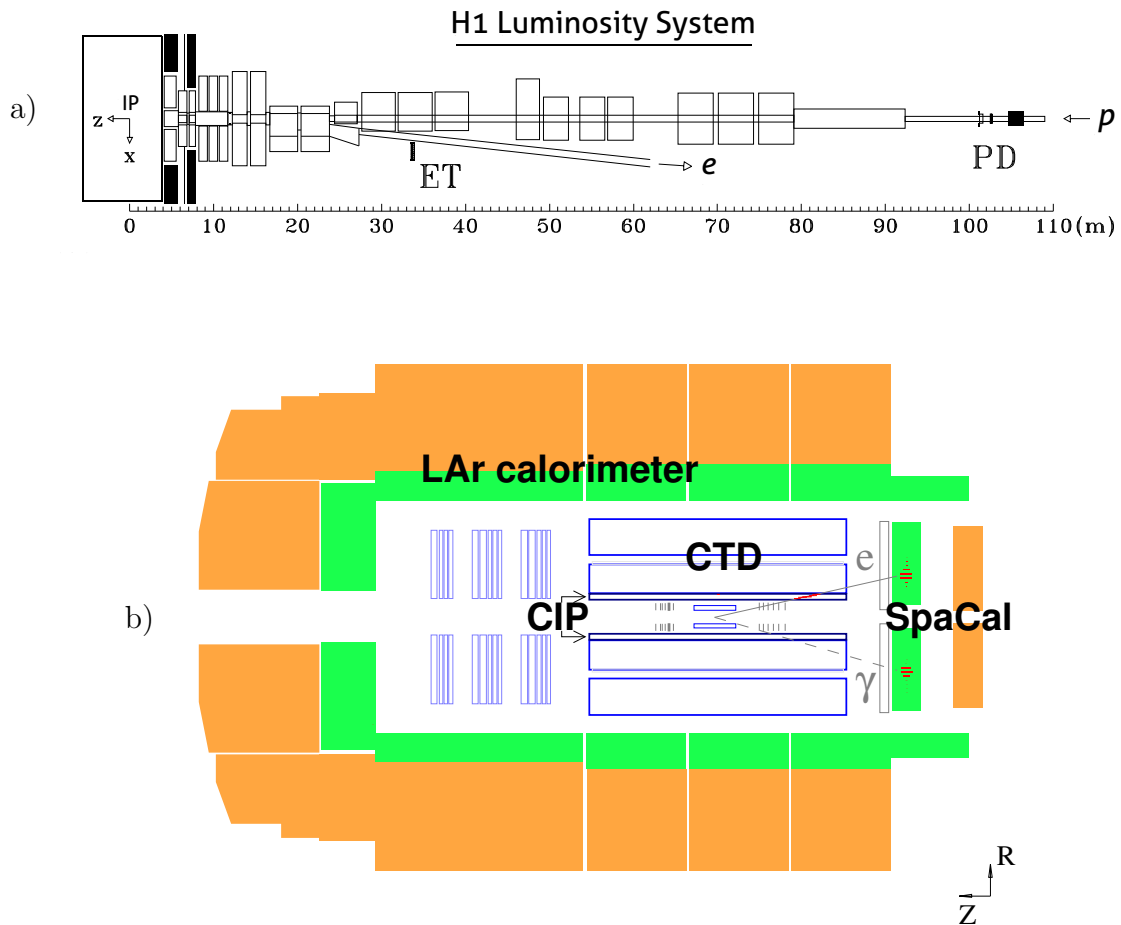
Figure 2.13: The layout of the H1 system for luminosity measurement from the bremsstrahlung process (a) and an example of the elastic QED Compton scattering candidate event observed in the H1 detector (b).

method is insensitive to details of the beam optics but has a smaller cross section then the bremsstrahlung process. The luminosity measured with this method was in agreement with the result obtained using the Bethe-Heitler process [66].

2.3.4   Trigger system

The H1 trigger system [34, 68–70] faced a similar task to that of ZEUS of selecting not more than 10 events per second from a 10.4 MHz bunch crossings rate. For this purpose, five levels L1-L5 of trigger system were developed such that each higher level had a lower input frequency and could use a more complex detector data.

The L1 trigger provided a decision for each bunch crossing after about $2.5\,\mu$s. During this time the detector data were stored in the pipelines and decisions from the trigger elements of the detector subsystems were sent to the central trigger logic. If the L1 central trigger made a decision to keep the event, the data were sent to the second level. The output rate of L1 was designed to be 1 kHz.

At L2, the decision was derived in about $20\,\mu$s from a combination of two independent hardware systems, a complex topological correlator L2TT and a neural network trigger L2NN, which exploited the correlations between the trigger quantities from the various subsystems in a multidimensional space. The L2 system reduced the signal rate to about 100 - 200 Hz.

The L3 was a software trigger starting in parallel with L2 and using more complex matching of the information from different detector components. It further reduced the signal rate to 50 Hz.

An additional Fast Track Trigger FTT [69,70] was built for the H1 experiment during the HERA luminosity upgrade. It provided information to the first three trigger levels and allowed a full three-dimensional reconstruction of all charged tracks detected in 12 selected layers of the CTD within $25\,\mu$s. At the first trigger level, FTT reconstructed tracks in two dimensions, at the second level in three dimensions and at the third level it calculated the invariant mass sums of the charged particles, which allowed particle resonances to be identified.

On the fourth and fifth trigger levels, the raw data of the full event was available and used for event reconstruction and classification. At this level, about 5 events per second were selected to be stored on tapes.

Chapter 3

Combination of the inclusive cross sections

In this chapter, a combination of all previously published ZEUS and H1 inclusive DIS cross-section measurements for neutral and charged current $e^\pm p$ scattering is described. The techniques of the DIS kinematics reconstruction used in inclusive DIS analyses are also listed. The combined data have been used for the determination of the parton density functions HERAPDF2.0 [14] as well as ZCIPDF (described in Chapter 4) and the evaluation of the limits on scenarios beyond the Standard Model (Chapters 5 and 6).

3.1   Inclusive data samples

The data for the combination were taken at electron beam energy of 27.5 GeV and proton beam energies of 920, 820, 575 and 460 GeV during two data-taking periods, HERA I (from 1994 to 2000) and HERA II (from 2002 to 2007). In total, 41 data sets from 22 publications corresponding to an integrated luminosity of about 1 fb^{-1} were used in the combination procedure and are summarised in Table 3.1.

During the HERA I period, until 1997, the HERA collider was operated with a proton beam energy of 820 GeV. In 1995, special runs were performed with the interaction-vertex position shifted forward, which allowed backward-scattered electrons with small angles to be detected and covered the Q^2 range down to $Q^2 = 0.2\,\mathrm{GeV}^2$. To measure the energy of the final-state electrons at even smaller scattering angles, ZEUS in 1995 installed a beam-pipe calorimeter (BPC) [43, 76]. For a period of six weeks in 1997, a beam-pipe tracker (BPT) [44, 77] was installed in addition in front of the BPC. This allowed the inclusive cross sections for Q^2 down to $Q^2 = 0.045\,\mathrm{GeV}^2$ to be measured. In 1998, the proton beam energy was increased to 920 GeV. In total during the HERA I period, each of the two experiments collected about 100 pb^{-1} of e^+p and 16 pb^{-1} of e^-p data.

During the HERA II period, the data were collected with a longitudinally polarised

Data Set		e^+/e^-	$\sqrt{s}$ GeV	x_{Bj} Grid from	to	$Q^2[\mathrm{GeV}^2]$ Grid from	to	$\mathcal{L}$ pb^{-1}	Method of x_{Bj},Q^2 rec.	Ref.
HERA I $E_p = 820\,\mathrm{GeV}$ and $E_p = 920\,\mathrm{GeV}$ data sets										
H1 svx-mb [2]	95-00	e^+p	301, 319	0.000005	0.02	0.2	12	2.1	El., Σ^1	[71]
H1 low-Q^2 [2]	96-00	e^+p	301, 319	0.0002	0.1	12	150	22	El., Σ^1	[72]
H1 NC	94-97	e^+p	301	0.0032	0.65	150	30000	35.6	e-Σ	[73]
H1 CC	94-97	e^+p	301	0.013	0.40	300	15000	35.6	JB	[73]
H1 NC	98-99	e^-p	319	0.0032	0.65	150	30000	16.4	e-Σ	[74]
H1 CC	98-99	e^-p	319	0.013	0.40	300	15000	16.4	JB	[74]
H1 NC HY	98-99	e^-p	319	0.0013	0.01	100	800	16.4	El.	[75]
H1 NC	99-00	e^+p	319	0.0013	0.65	100	30000	65.2	e-Σ	[75]
H1 CC	99-00	e^+p	319	0.013	0.40	300	15000	65.2	JB	[75]
ZEUS BPC	95	e^+p	300	0.000002	0.00006	0.11	0.65	1.65	El.	[76]
ZEUS BPT	97	e^+p	300	0.0000006	0.001	0.045	0.65	3.9	El., e-Σ	[77]
ZEUS SVX	95	e^+p	300	0.000012	0.0019	0.6	17	0.2	El.	[78]
ZEUS NC [2] high/low-Q^2	96-97	e^+p	300	0.00006	0.65	2.7	30000	30.0	PT	[79]
ZEUS CC	94-97	e^+p	300	0.015	0.42	280	17000	47.7	JB	[80]
ZEUS NC	98-99	e^-p	318	0.005	0.65	200	30000	15.9	DA	[81]
ZEUS CC	98-99	e^-p	318	0.015	0.42	280	30000	16.4	JB	[82]
ZEUS NC	99-00	e^+p	318	0.005	0.65	200	30000	63.2	DA	[83]
ZEUS CC	99-00	e^+p	318	0.008	0.42	280	17000	60.9	JB	[84]
HERA II $E_p = 920\,\mathrm{GeV}$ data sets										
H1 NC	03-07	e^+p	319	0.0008	0.65	60	30000	182	El., e-Σ	[67]^2
H1 CC	03-07	e^+p	319	0.008	0.40	300	15000	182	JB	[67]^2
H1 NC	03-07	e^-p	319	0.0008	0.65	60	50000	151.7	El., e-Σ	[67]^2
H1 CC	03-07	e^-p	319	0.008	0.40	300	30000	151.7	JB	[67]^2
H1 NC med-Q^2 $^{*y.5}$	03-07	e^+p	319	0.0000986	0.005	8.5	90	97.6	El.	[85]
H1 NC low-Q^2 $^{*y.5}$	03-07	e^+p	319	0.000029	0.00032	2.5	12	5.9	El.	[85]
ZEUS NC	06-07	e^+p	318	0.005	0.65	200	30000	135.5	El., JB, DA	[86]
ZEUS CC	06-07	e^+p	318	0.0078	0.42	280	30000	132	JB	[87]
ZEUS NC	05-06	e^-p	318	0.005	0.65	200	30000	169.9	DA	[88]
ZEUS CC	04-06	e^-p	318	0.015	0.65	280	30000	175	JB	[89]
ZEUS NC nominal ^{*y}	06-07	e^+p	318	0.000092	0.008343	7	110	44.5	El.	[90]
ZEUS NC satellite ^{*y}	06-07	e^+p	318	0.000071	0.008343	5	110	44.5	El.	[90]
HERA II $E_p = 575\,\mathrm{GeV}$ data sets										
H1 NC high-Q^2	07	e^+p	252	0.00065	0.65	35	800	5.4	El., e-Σ	[41]
H1 NC low-Q^2	07	e^+p	252	0.0000279	0.0148	1.5	90	5.9	El.	[85]
ZEUS NC nominal	07	e^+p	251	0.000147	0.013349	7	110	7.1	El.	[90]
ZEUS NC satellite	07	e^+p	251	0.000125	0.013349	5	110	7.1	El.	[90]
HERA II $E_p = 460\,\mathrm{GeV}$ data sets										
H1 NC high-Q^2	07	e^+p	225	0.00081	0.65	35	800	11.8	El., e-Σ	[41]
H1 NC low-Q^2	07	e^+p	225	0.0000348	0.0148	1.5	90	12.2	El.	[85]
ZEUS NC nominal	07	e^+p	225	0.000184	0.016686	7	110	13.9	El.	[90]
ZEUS NC satellite	07	e^+p	225	0.000143	0.016686	5	110	13.9	El.	[90]

Table 3.1: The 41 data sets from H1 and ZEUS used for the combination. The notation [2] in the column "Data Set" indicates that the data were treated as two data sets in the analysis. The notations $^{*y.5}$ and ^{*y} are explained in the text. The notation ^{2} for the H1 HERA II paper [67] indicates that published cross sections were scaled by a factor of 1.018 as prescribed in the H1 HERA II luminosity determination paper [66]. Integrated luminosities are quoted as given by the collaborations. Methods used for the reconstruction of x_{Bj} and Q^2 are described in Section 3.2. The notation ^{1} indicates that the extended sigma method was used. The table was taken from the HERAPDF2.0 paper [14].

electron beam; the corresponding cross sections were corrected to zero beam polarisation. With proton beam energy of 920 GeV, H1 measured about 182 pb^{-1} of e^+p and 152 pb^{-1} of e^-p data and ZEUS about 134 pb^{-1} of e^+p and 172 pb^{-1} of e^-p data. In 2007, the proton beam energy was lowered to 575 GeV and 460 GeV, providing about 6 pb^{-1} and 13 pb^{-1} of e^+p data for each of the experiments, respectively. The data with lowered centre-of-mass energies were used to determine the F_{L} structure function.

3.2 Reconstruction of kinematics

The DIS kinematic variables introduced in Section 1.2 can be reconstructed from the parameters of the scattered electron, e, from the hadronic final state, h, or from a combination of the two. The choice of the most appropriate reconstruction method in each analysis was based on the type of the scattering process, resolution of the detector components in the considered phase-space region and possible biases of the measurements or photon radiation in the initial or final state.

3.2.1 Electron method

The "electron method" [91] (El.) relies on the incoming electron energy, E_e, scattered electron energy, E_e', its angle with respect to the electron beam, θ_e, and transverse momentum, $P_{T,e}$. It can be applied only to NC events and kinematics are reconstructed via

$$
\begin{aligned}
y_e &= 1 - \frac{\Sigma_e}{2E_e} \quad, \\
Q_e^2 &= \frac{P_{T,e}^2}{1 - y_e} \quad, \\
x_e &= \frac{Q_e^2}{sy_e} \quad,
\end{aligned}
\tag{3.1}
$$

where $\Sigma_e = E_e'(1 - \cos\theta_e)$. This method provides an accurate reconstruction of Q^2 but poor accuracy of x_{Bj} for low values of y [91, 92].

3.2.2 Hadron method

Due to the neutrino produced in the final state, the kinematics of CC scattering events can be reconstructed only from the hadronic final state. The main problem of the "hadron method" is that some particles may leave the apparatus undetected in the forward or backward directions through the beam-pipe. Most of such loses are in the proton direction; to reduce their effect on the determined kinematics, the Jacquet-Blondel method [93] (JB)

was developed:

$$y_h = \frac{\Sigma_h}{2E_e} \quad ,$$

$$Q_h^2 = \frac{P_{T,h}^2}{1 - y_h} \quad , \tag{3.2}$$

$$x_h = \frac{Q_h^2}{sy_h} \quad .$$

Here $\Sigma_h = (E - P_Z)_h = \sum_i (E_i - p_{Z,i})$, E_i and $p_{Z,i}$ are the energy and longitudinal component of the momentum of particle i, respectively, and $P_{T,h} = |\sum_i \boldsymbol{p}_{T,i}|$ is the total transverse momentum of the final-state hadrons. A hadronic scattering angle

$$\tan \frac{\theta_h}{2} = \frac{\Sigma_h}{P_{T,h}} \tag{3.3}$$

corresponds to the angle of a scattered quark in the framework of the QPM.

The main uncertainties of the Jacquet-Blondel method originate from particles with small transverse momentum escaping the apparatus undetected and the uncertainty of the calorimeter energy calibration. It provides a rather precise reconstruction at low and medium values of y ($y < 0.2$) but the accuracy degrades at high y [92].

3.2.3   Sigma method

In NC events, a combination of information from the scattered electron and hadronic final state can be used to achieve a better precision of kinematics reconstruction. One such combined approach is the "sigma method" [92] (Σ) in which a total $E - P_Z$ variable,

$$E - P_Z = E_e'(1 - \cos \theta_e) + \sum_i (E_i - p_{Z,i}) = \Sigma_e + \Sigma_h \quad , \tag{3.4}$$

was introduced and used in conjunction with the relation $E - P_Z = 2E_e$, which holds for events without initial- or final-state radiation,

$$y_\Sigma = \frac{\Sigma_h}{E - P_Z} \quad ,$$

$$Q_\Sigma^2 = \frac{P_{T,e}^2}{1 - y_\Sigma} \quad , \tag{3.5}$$

$$x_\Sigma = \frac{Q_\Sigma^2}{sy_\Sigma} \quad .$$

The sigma method provides the reconstruction of kinematics independently of initial-state QED radiation and has the highest precision in the low x_{Bj} - low Q^2 region [92]. It

is the only method which covers the complete HERA kinematic region without significant precision degradation.

In two H1 analyses [71, 72], the sigma method was further extended by replacing the centre-of-mass energy in the Eq. 3.5 for x_{Bj} with $2E_p(E - P_Z)$,

$$
\begin{aligned}
y_{\Sigma'} &= y_\Sigma \quad, \\
Q^2_{\Sigma'} &= Q^2_\Sigma \quad, \\
x_{\Sigma'} &= \frac{Q^2_\Sigma}{2E_p(E - P_Z)y_\Sigma} = \frac{Q^2_\Sigma}{2E_p\Sigma_h} \quad.
\end{aligned}
\tag{3.6}
$$

3.2.4 Electron-sigma method

The electron method has the most stable reconstruction of Q^2 and the sigma method of x_{Bj} over the HERA kinematic region. These two quantities, Q^2_e and x_Σ, were used in a hybrid "e-sigma method" [92] (e-Σ) via

$$
\begin{aligned}
y_{e\Sigma} &= \frac{Q^2_e}{sx_\Sigma} = \frac{2E_e}{E - P_Z} y_\Sigma \quad, \\
Q^2_{e\Sigma} &= Q^2_e \quad, \\
x_{e\Sigma} &= x_\Sigma \quad.
\end{aligned}
\tag{3.7}
$$

Such a combined method optimises the reconstruction quality of the sigma method but has enlarged sensitivy to radiative corrections [92].

3.2.5 Double-angle method

In the "double-angle method" [91, 94] (DA), Q^2 and x_{Bj} are reconstructed from the polar angle of the scattered electron, θ_e, and the hadronic final state, θ_h, via

$$
\begin{aligned}
y_{DA} &= \frac{\tan(\theta_h/2)}{\tan(\theta_e/2) + \tan(\theta_h/2)} \quad, \\
Q^2_{DA} &= 4E_e^2 \cdot \frac{\cot(\theta_e/2)}{\tan(\theta_e/2) + \tan(\theta_h/2)} \quad, \\
x_{DA} &= \frac{Q^2_{DA}}{sy_{DA}} \quad.
\end{aligned}
\tag{3.8}
$$

This method has small radiative corrections and is independent of the calorimeter absolute energy calibration [92]. It provides high precision at high values of Q^2 ($Q^2 > 100$ GeV^2) but has poor resolution in the low x_{Bj} - low Q^2 region.

3.2.6   PT method

In the "PT method" [95] (PT), deviations of the measured hadronic transverse energy from the true values are compensated individually for each event by using a functional form, C, derived from the MC simulation. It depends on θ_h, $P_{T,h}$ and $\delta_{PT} = P_{T,h}/P_{T,e}$. Next, the hadronic scattering angle θ_{PT} is evaluated via

$$\tan\frac{\theta_{PT}}{2} = \frac{\Sigma_{PT}}{P_{T,e}} \quad , \quad \text{where} \quad \Sigma_{PT} = 2E_e \frac{C(\theta_h, P_{T,h}, \delta_{PT}) \cdot \Sigma_h}{\Sigma_e + C(\theta_h, P_{T,h}, \delta_{PT}) \cdot \Sigma_h} \quad . \quad (3.9)$$

It is used in conjunction with θ_e in the equations for the double-angle method to determine x_{Bj}, y and Q^2.

The PT method thus makes an optimum combination of all the information from the measurements of both the hadronic system and the scattered electron, and optimises the resolution of reconstructed kinematics over the entire kinematic range measured.

3.3   Combination procedure

The combination procedure of the 41 inclusive HERA data sets was performed in two steps: translation of the data samples onto common grids and averaging in an iterative procedure based on minimisation of a χ^2 function.

3.3.1   Common (x_{Bj}, Q^2) grids and centre-of-mass energies

The double-differential cross sections were published by the two experiments for different sets of (x_{Bj}, Q^2) points and slightly different centre-of-mass energies, $\sqrt{s}$. The difference in the centre-of-mass energies arose due to different values of the electron beam energy measured by the collaborations; H1 obtained the value of 27.6 GeV and ZEUS measured 27.5 GeV. Thus, before performing the averaging, data points were translated to common $(x_{Bj\,grid}, Q^2_{grid})$ grids and $\sqrt{s_{com}}$ values.

All of the data taken at proton beam energy of 920 GeV and the data for $E_p = 820$ GeV with $y < 0.35$ were translated to $\sqrt{s_{com\,1}} = 318$ GeV and (x_{Bj}, Q^2) grid-1, depicted with open circles in Fig. 3.1. The $E_p = 820$ GeV data with $y \geq 0.35$ were translated to $\sqrt{s_{com\,2}} = 300$ GeV and grid-1. The data from the runs with proton beam energy lowered to 575 GeV and 460 GeV were translated to $\sqrt{s_{com\,3}} = 251$ GeV and $\sqrt{s_{com\,4}} = 225$ GeV, respectively, and $(x_{Bj\,grid}, Q^2_{grid})$ grid-2, which has a finer structure in y, designed for the F_{L} measurements, which is shown by dots in Fig. 3.1.

The two grids were chosen such that the translation factors are small, of the order of a few percent. For each data point with $\sqrt{s_{com\,1}}$ or $\sqrt{s_{com\,2}}$, the grid-1 point closest in Q^2 and then in x_{Bj} was chosen. For all points from the datasets marked with ^{*y} in Table 3.1 and points with $y > 0.5$ from the datasets marked with $^{*y.5}$, grid-1 points were chosen in Q^2

H1 and ZEUS
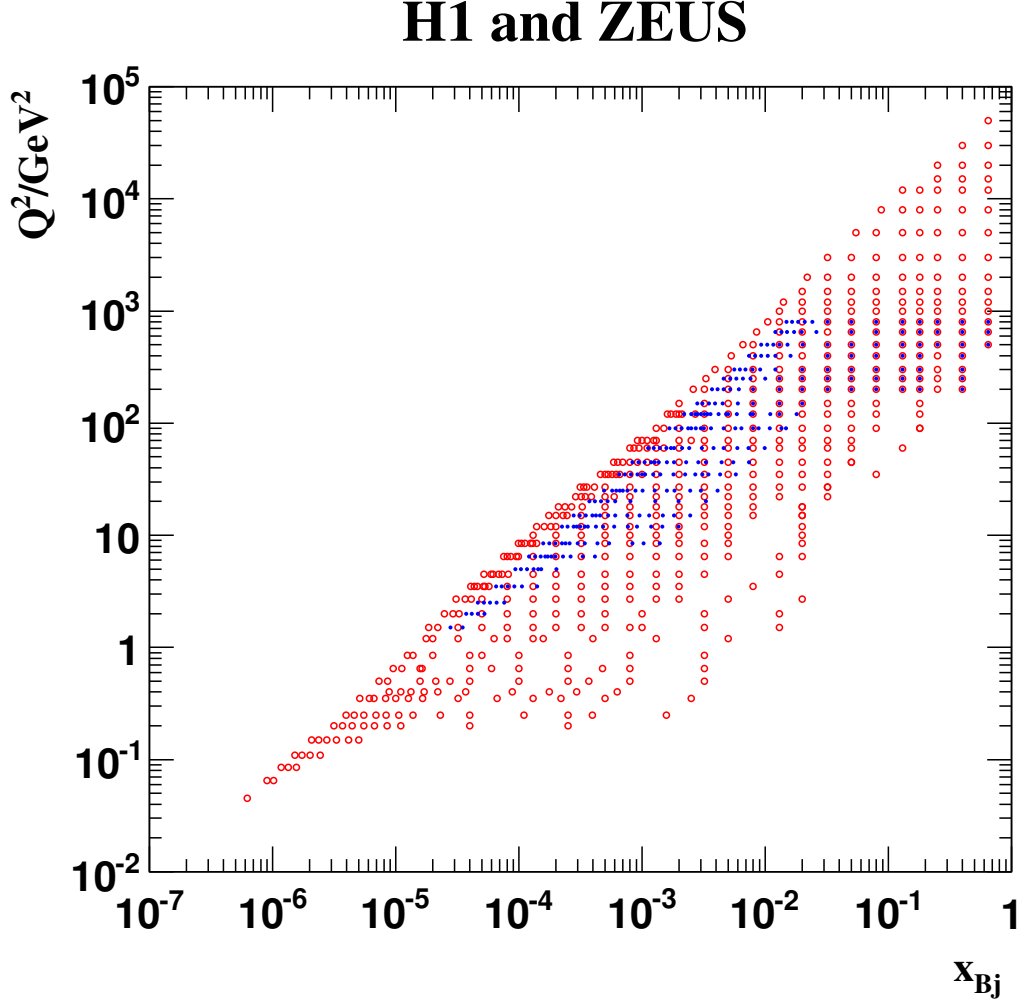
Figure 3.1: The points of the two grids used for the combination. Grid-1 (red open circles) was used for data with $\sqrt{s_{\mathrm{com},1}} = 318\,\mathrm{GeV}$ or $\sqrt{s_{\mathrm{com},2}} = 300\,\mathrm{GeV}$. Grid-2 (blue dots) was used for data with $\sqrt{s_{\mathrm{com},2}} = 251\,\mathrm{GeV}$ or $\sqrt{s_{\mathrm{com},3}} = 225\,\mathrm{GeV}$. The figure was taken from the HERAPDF2.0 paper [14].

and then in y. For all data with $\sqrt{s_{com\,3}}$ or $\sqrt{s_{com\,4}}$, the grid-2 points were always chosen in Q^2 and then in y. In total there are 1307 $(x_{Bj\,grid}, Q^2_{grid})$ points for the new combined cross sections. For only nine of these points were the two different $(x_{Bj\,grid}, Q^2_{grid})$ measurements from one data set translated into the same combined $(x_{Bj\,grid}, Q^2_{grid})$ point and for only one were the three different measurements from one data set translated into one combined

point.

For this translation, the cross-section values were multiplied by the ratios, T_{grid}, of the QCD predictions for $\sqrt{s_{com}}$ and $(x_{Bj\,grid}, Q^2_{grid})$ to predictions for $\sqrt{s}$ and (x_{Bj}, Q^2) where the measurements took place. The QCD predictions were obtained from QCD global fits performed using the HERAFitter framework [96, 97]. For $Q^2 > 3\,\text{GeV}^2$, a next-to-leading-order QCD fit within the DGLAP formalism was performed and factors $T_{\text{grid\,DGLAP}}$ evaluated. In addition, for $Q^2 < 4.9\,\text{GeV}^2$, a fractal-model fit [98] was used and factors $T_{\text{grid\,FM}}$ calculated. For data in the range $3 \leq Q^2 \leq 4.9\,\text{GeV}^2$, the ratios were averaged to give

$$T_{\text{grid\,ave}} = T_{\text{grid,FM}}(1 - (Q^2 - 3)/1.9) + T_{\text{grid\,DGLAP}}(Q^2 - 3)/1.9 \ , \qquad (3.10)$$

where Q^2 is in GeV^2. The range for the transition between the fractal and DGLAP QCD fits was varied within $2 \leq Q^2 \leq 7.5$; the effect on the final combined cross sections was found to be negligible.

3.3.2   Cross-section averaging

The double-differential cross sections were published with their statistical, correlated and uncorrelated systematic uncertainties. For each data set, all uncorrelated systematic uncertainties were added in quadrature and the correlated uncertainties were kept separate. Some of the systematic uncertainties were originally published as asymmetric; these were symmetrised before the averaging procedure [14].

The averaging of the data was performed using the HERAverager [99] tool. It is based on the χ^2 minimisation method [71], assuming that the data points are statistically uncorrelated between data sets and imposing that there is only one correct value for the cross section of each process at each grid point. These values, denoted as $\boldsymbol{m}_t$ for averaging iteration t, were estimated by minimising the χ^2 function defined as

$$\chi^2\left(\boldsymbol{m}_t, \boldsymbol{b}\right) = \sum_{i=1}^{N_M} \sum_{ds_i} \frac{\left[m_t^i - \sum_j \gamma_j^{i,ds} m_t^i b_j - \mu^{i,ds}\right]^2}{\delta^2_{i,ds,\text{stat}}\, \mu^{i,ds}\left(m_{t-1}^i - \sum_j \gamma_j^{i,ds} m_{t-1}^i b_j\right) + \left(\delta_{i,ds,\text{uncor}}\, m_{t-1}^i\right)^2} + \sum_j b_j^2 ,$$

(3.11)

where the summation $\sum_{i=1}^{N_M}$ runs over all points of two grids which accumulated at least one measurement, $\sum_{ds_i}$ extends over the data sets ds contributing to the point i, $\mu^{i,ds}$ is the measured value at the point i from set ds and $\gamma_j^{i,ds}$, $\delta_{i,ds,\text{stat}}$ and $\delta_{i,ds,\text{uncor}}$ are the relative correlated systematic, relative statistical and relative uncorrelated systematic uncertainties, respectively. The components m_{t-1}^i denote the averaged cross sections from the previous iteration. For the first iteration, $t = 1$, they are set equal to $m_0^i = \mu^{i,ds}$. The procedure converges after two iterations. The vector $\boldsymbol{b}$ represents correlated shifts of the cross sections in units of the respective relative correlated systematic uncertainties $\gamma_j^{i,ds}$;

for the first iteration it is set to zero. The summations over j extend over all correlated systematic uncertainties.

All the NC and CC cross-section values from H1 and ZEUS were combined in one simultaneous averaging procedure. Some systematic uncertainties were correlated between data sets and the two experiments and the resulting shifts propagated coherently to all data sets. Thus, even in case of only one cross-section value contributing to the grid point, it was shifted due to the correlation of the systematic uncertainties. A list of correlated systematic uncertainties is given in Table 3.2 and their correlations across the data sets are presented in Table 3.3.

3.3.3   Iterative procedure

The fractal and DGLAP QCD fits used for the translation of data sets to common $(x_{Bj\,grid}, Q^2_{grid})$ grids were performed on the limited kinematic space of the available data; in the combination procedure all of the data were used simultaneously and data from different Q^2 regions influence the shifts of correlated systematic uncertainties. Therefore similar fits on the subsets of the combined data and subsets of the separate data sets provided slightly different results. To avoid possible inaccuracies arising from this, the combination procedure was performed in three iterations. Each iteration had two steps:

1. the data were translated to the common $\sqrt{s}_{\mathrm{com}}$ values and $(x_{\mathrm{Bj,grid}}, Q^2_{\mathrm{grid}})$ grids as described in Section 3.3.1;

2. the data were averaged as described in Section 3.3.2.

In the first iteration, the fits were performed on the uncombined data and in the subsequent iterations the combined data resulting from the previous step were used. It was found that after the third iteration no significant variation of the results could be observed and thus the procedure was stopped.

3.4   Procedural uncertainties

The treatment of some systematic uncertainties included ambiguities and the two collaborations had to make choices for the combination. The influence of these choices on the resulting cross sections was checked and included as an additional procedural uncertainty.

3.4.1   Multiplicative treatment of systematic uncertainties

By convention, all correlated systematic uncertainties were considered to be proportional to the averaged cross-section values $\boldsymbol{m}$. Such a treatment is called "multiplicative" and is certainly a valid assumption for normalisation uncertainties, but for other uncertainties

Index	Source of the uncertainty	Ref.
1	Luminosity for ZEUS NC 96-97 and CC 94-97 data	[79, 80]
2	Diagonalised systematic uncertainty γ_2^{ave} from H1 svx-mb 95-00 data combination	[71]
3	Electron and positron energy scale in H1 NC 94-00 analyses	[73–75]
4	Diagonalised systematic uncertainty γ_3^{ave} from H1 svx-mb 95-00 data combination	[71]
5	Positron polar angle in H1 NC 94-97 analysis	[73]
6	Electron and positron polar angle in H1 NC 98-00 analyses	[74, 75]
7	Diagonalised systematic uncertainty γ_4^{ave} from H1 svx-mb 95-00 data combination	[71]
8	Hadronic energy scale for LAr calorimeter in H1 HERA I analyses	[73–75]
9	Energy identified as noise in the LAr calorimeter in H1 HERA I analyses	[73–75]
10	Diagonalised systematic uncertainty γ_5^{ave} from H1 svx-mb 95-00 data combination	[71]
11	Photoproduction background subtraction in H1 analyses	[67, 73–75]
12	Efficiency of the anti-photoproduction cut in H1 CC 94-97 analysis	[73]
13	Efficiency of the anti-photoproduction cut in H1 CC 98-00 analyses	[74, 75]
14	Background subtraction with the charge asymmetry method in H1 NC 98-00 analyses	[75]
15	Diagonalised systematic uncertainty γ_1^{ave} from H1 low-Q^2 96-00 data combination	[72]
16	Diagonalised systematic uncertainty γ_1^{ave} from H1 svx-mb 95-00 data combination	[71]
17	Luminosity for H1 94-97 data	[73]
18	Luminosity for H1 98-99 data	[74, 75]
19	Luminosity for H1 99-00 data	[75]
20	The positron identification efficiency in ZEUS NC 96-97 analysis	[79]
21	Effect of detector elements alignment on positron angle in ZEUS NC 96-97 analysis	[79]
22	Positron polar angle measured with tracking detector in ZEUS NC 96-97 analysis	[79]
23	Positron energy scale from calorimeter calibration in ZEUS NC 96-97 analysis	[79]
24	Hadronic energy scale for the FCAL in ZEUS NC 96-97 and CC 94-97 analyses	[79, 80]
25	Hadronic energy scale for the BCAL in ZEUS NC 96-97 and CC 94-97 analyses	[79, 80]
26	Hadronic energy scale for the RCAL in ZEUS NC 96-97 analysis	[79]
27	Effect of diffractive component in MC on kinematics in ZEUS NC 96-97 analysis	[79]
28	Photoproduction background subtraction in ZEUS NC 96-97 analysis	[79]
29	Polar angle of the hadronic system from hadronic clusters in ZEUS NC 96-97 analysis	[79]
30	Additional normalisation uncertainty of 1% for ZEUS low-Q^2 NC 96-97 data	[79]
31	Electron and positron energy scale in ZEUS NC 98-00 analyses	[81, 83]
32	Photoproduction background subtraction in ZEUS NC 98-00 analyses	[81, 83]
33	Electron and positron isolation requirements in ZEUS NC 98-00 analyses	[81, 83]
34	Electron and positron momentum requirements in ZEUS NC 98-00 analyses	[81, 83]
35	Distribution in the Z coordinate of the event vertex in ZEUS NC 98-99 analysis	[81]
36	Choice of the parton-shower scheme in ZEUS NC 98-00 and CC 94-00 analyses	[80–84]
37	Hadronic energy scale in ZEUS CC 98-00 analyses	[82, 84]
38	Polar angle of the hadronic system in ZEUS CC 98-00 analyses	[82, 84]
39	Luminosity for ZEUS 98-99 data	[81, 82]
40	Distribution in the Z coordinate of the event vertex in ZEUS NC 99-00 analysis	[83]
41	Hadronic-energy flow in MC near the FCAL beamhole in ZEUS NC 99-00 analysis	[83]
42	Choice of the parton distribution functions in ZEUS NC 99-00 analysis	[83]
43	Luminosity for ZEUS 99-00 data	[83, 84]
44	Diagonalised systematic uncertainty γ_2^{ave} from H1 low-Q^2 96-00 data combination	[72]
45	Diagonalised systematic uncertainty γ_3^{ave} from H1 low-Q^2 96-00 data combination	[72]
46	Diagonalised systematic uncertainty γ_4^{ave} from H1 low-Q^2 96-00 data combination	[72]
47	Diagonalised systematic uncertainty γ_5^{ave} from H1 low-Q^2 96-00 data combination	[72]
48	Diagonalised systematic uncertainty γ_6^{ave} from H1 low-Q^2 96-00 data combination	[72]
49	Diagonalised systematic uncertainty γ_7^{ave} from H1 low-Q^2 96-00 data combination	[72]
50	Diagonalised systematic uncertainty γ_8^{ave} from H1 low-Q^2 96-00 data combination	[72]
51	Diagonalised systematic uncertainty γ_9^{ave} from H1 low-Q^2 96-00 data combination	[72]
52	Diagonalised systematic uncertainty γ_{10}^{ave} from H1 low-Q^2 96-00 data combination	[72]
53	Diagonalised systematic uncertainty γ_{11}^{ave} from H1 low-Q^2 96-00 data combination	[72]
54	Diagonalised systematic uncertainty γ_{12}^{ave} from H1 low-Q^2 96-00 data combination	[72]

Table 3.2:   Description of the correlated systematic uncertainties used in the data sets for combination.

Index	Source of the uncertainty	Ref.
55	Diagonalised systematic uncertainty γ_{13}^{ave} from H1 low-Q^2 96-00 data combination	[72]
56	Diagonalised systematic uncertainty γ_{14}^{ave} from H1 low-Q^2 96-00 data combination	[72]
57	Diagonalised systematic uncertainty γ_6^{ave} from H1 svx-mb 95-00 data combination	[71]
58	Diagonalised systematic uncertainty γ_7^{ave} from H1 svx-mb 95-00 data combination	[71]
59	Diagonalised systematic uncertainty γ_8^{ave} from H1 svx-mb 95-00 data combination	[71]
60	Diagonalised systematic uncertainty γ_9^{ave} from H1 svx-mb 95-00 data combination	[71]
61	Diagonalised systematic uncertainty γ_{10}^{ave} from H1 svx-mb 95-00 data combination	[71]
62	Diagonalised systematic uncertainty γ_{11}^{ave} from H1 svx-mb 95-00 data combination	[71]
63	Diagonalised systematic uncertainty γ_{12}^{ave} from H1 svx-mb 95-00 data combination	[71]
64	Diagonalised systematic uncertainty γ_{13}^{ave} from H1 svx-mb 95-00 data combination	[71]
65	Diagonalised systematic uncertainty γ_{14}^{ave} from H1 svx-mb 95-00 data combination	[71]
66	Diagonalised systematic uncertainty γ_{15}^{ave} from H1 svx-mb 95-00 data combination	[71]
67	Diagonalised systematic uncertainty γ_{16}^{ave} from H1 svx-mb 95-00 data combination	[71]
68	Diagonalised systematic uncertainty γ_{17}^{ave} from H1 svx-mb 95-00 data combination	[71]
69	Diagonalised systematic uncertainty γ_{18}^{ave} from H1 svx-mb 95-00 data combination	[71]
70	Diagonalised systematic uncertainty γ_{19}^{ave} from H1 svx-mb 95-00 data combination	[71]
71	Diagonalised systematic uncertainty γ_{20}^{ave} from H1 svx-mb 95-00 data combination	[71]
72	Diagonalised systematic uncertainty γ_{21}^{ave} from H1 svx-mb 95-00 data combination	[71]
73	Diagonalised systematic uncertainty γ_{22}^{ave} from H1 svx-mb 95-00 data combination	[71]
74	Diagonalised systematic uncertainty γ_{23}^{ave} from H1 svx-mb 95-00 data combination	[71]
75	Diagonalised systematic uncertainty γ_{24}^{ave} from H1 svx-mb 95-00 data combination	[71]
76	Diagonalised systematic uncertainty γ_{25}^{ave} from H1 svx-mb 95-00 data combination	[71]
77	Diagonalised systematic uncertainty γ_{26}^{ave} from H1 svx-mb 95-00 data combination	[71]
78	Cut on the total $E - P_Z$ variable in ZEUS BPC and BPT analyses	[76, 77]
79	Cut on y_{JB} variable in ZEUS BPC and BPT analyses	[76, 77]
80	Cut on shower-width in BPC for positron identification in ZEUS BPC and BPT analyses	[76, 77]
81	Cut on matching the BPT tracks to BPC shower in ZEUS BPT analysis	[77]
82	Cut on Z coordinate of the BPT tracks vertices in ZEUS BPT analysis	[77]
83	Fiducial cut along the X axes in ZEUS BPT analysis	[77]
84	Fiducial cut along the Y axes in ZEUS BPT analysis	[77]
85	Positron energy scale for the BPC in ZEUS BPT analysis	[77]
86	BPC energy response in ZEUS BPC and BPT analyses	[76, 77]
87	Absolute BPC/BPT position along X axis in ZEUS BPT analysis	[77]
88	Luminosity for ZEUS BPT data	[77]
89	Hadronic energy scale in ZEUS SVX, BPC and BPT analyses	[76–78, 100]
90	Fractions of DJANGO and RAPGAP events in the MC in ZEUS BPT analysis	[77]
91	Photoproduction background subtraction in ZEUS SVX, BPC and BPT analyses	[76–78, 100]
92	Re-weighting of the MC outside the measurement region in ZEUS BPT analysis	[77]
93	Luminosity for ZEUS BPC data	[76]
94	Positron energy scale for the BPC in ZEUS BPC analysis	[76]
95	Position alignment of the BPC in ZEUS BPC analysis	[76]
96	Energy identified as noise in CAL in ZEUS BPC analysis	[76]
97	Fraction of the diffractive events in ZEUS BPC analysis	[76]
98	Acceptance estimated from the MC in ZEUS BPC analysis	[76]
99	Radiative corrections in ZEUS BPC analysis	[76]
100	Luminosity and trigger efficiency for ZEUS SVX data	[78, 100]
101	Horizontal position of the SRTD in ZEUS SVX analysis	[78, 100]
102	Vertical position of the SRTD in ZEUS SVX analysis	[78, 100]
103	Distribution in the Z coordinate of the event vertex in ZEUS SVX analysis	[78, 100]
104	Positron energy calibration in ZEUS SVX analysis	[78, 100]
105	Horizontal position of the two halves of the SRTD in ZEUS SVX analysis	[78, 100]
106	Vertical position of the two halves of the SRTD in ZEUS SVX analysis	[78, 100]
107	Photoproduction background subtraction in ZEUS SVX analysis	[78, 100]
108	The number of MC events in satellite bunches in ZEUS SVX analysis	[78, 100]

Table 3.2: Continued.

Index	Source of the uncertainty	Ref.
109	Box cut at the RCAL in ZEUS SVX analysis	[78, 100]
110	Additional 2% uncertainty for data with $Q^2 < 2.5$ GeV^2 in ZEUS SVX analysis	[78, 100]
111	Theoretical uncertainty on luminosity measured with Bethe-Heitler process	[101]
112	Electron and positron energy scale in LAr calorimeter in H1 NC 03-07 analyses	[41, 67]
113	Electron and positron polar angle in H1 NC 03-07 analyses	[41, 67]
114	Hadronic energy scale in H1 03-07 analyses	[41, 67]
115	Energy identified as noise in LAr calorimeter in H1 NC 03-07 analyses	[41, 67]
116	Energy identified as noise in LAr calorimeter in H1 CC 03-07 analyses	[67]
117	Efficiency of the anti-photoproduction cut in H1 CC 03-07 analyses	[67]
118	Photoproduction background from charge asymmetry in H1 NC 03-07 analyses	[67]
119	Luminosity for H1 e^+p 03-07data	[67]
120	Luminosity for H1 e^-p 03-07data	[67]
121	Theoretical uncertainty on luminosity measured with elastic QED Compton events	[67]
122	Positron energy scale in the SpaCal in H1 med/low-Q^2 NC 03-07 analyses	[85]
123	Positron polar angle in H1 med/low-Q^2 NC 03-07 analyses	[85]
124	Hadronic energy scale in H1 med/low-Q^2 NC 03-07 analyses	[85]
125	Energy identified as noise in LAr calorimeter in H1 med/low-Q^2 NC 03-07 analyses	[85]
126	Electron tagger acceptance in H1 med/low-Q^2 NC 03-07 analyses	[85]
127	Luminosity, trigger and reconstruction efficiencies in H1 med/low-Q^2 NC 03-07 analyses	[85]
128	Electron finding algorithm in ZEUS NC 05-06 analysis	[88]
129	Electron and positron energy scale in ZEUS NC 05-07 analyses	[86, 88]
130	Electron polar angle in ZEUS NC 05-06 analysis	[88]
131	Choice of the parton-shower scheme in ZEUS NC 05-07 analyses	[86, 88]
132	Box cut at the FCAL in ZEUS NC 05-06 analysis	[88]
133	Cut on the total $E - P_Z$ variable in ZEUS NC 05-06 analysis	[88]
134	Normalisation of photoproduction background in MC in ZEUS NC 05-07 analyses	[86, 88]
135	Hadronic energy scale in ZEUS CC 04-06 analysis	[89]
136	CTD tracking efficiency at the first-level trigger in ZEUS CC 06-07 analysis	[87]
137	Hadronic energy scale in ZEUS CC 06-07 analysis	[87]
138	Part of luminosity uncertainty correlated between ZEUS 04-06 data	[88, 89]
139	Part of luminosity uncertainty correlated between ZEUS 06-07 data	[86, 87, 90]
140	Part of luminosity uncertainty correlated between all ZEUS HERA II data	[86–90]
141	Cut on the total $E - P_Z$ variable in ZEUS NC 06-07 analysis	[86]
142	Electron finding algorithm in ZEUS NC 06-07 analysis	[86]
143	Electron isolation requirements in ZEUS NC 06-07 analysis	[86]
144	Electron energy resolution in MC in ZEUS NC 06-07 analysis	[86]
145	Box cut at the FCAL in ZEUS NC 06-07 analysis	[86]
146	Hadronic energy scale in MC in ZEUS NC 06-07 analysis	[86]
147	Additional luminosity normalisation for ZEUS 06-07 data	[86, 87]
148	Additional luminosity normalisation for ZEUS NC 96-97 data	[79]
149	Background subtraction with charge asymmetry in H1 low-Q^2 MER and LER analyses	[85]
150	Luminosity, trigger and reconstruction efficiencies for H1 LER data	[41, 85]
151	Background suppression with positron discriminator in H1 high-Q^2 MER and LER analyses	[41]
152	Background subtraction with charge asymmetry in H1 high-Q^2 MER and LER analyses	[41]
153	Luminosity for H1 MER data	[41]
154	Normalisation of photoproduction background in MC in ZEUS HER, MER and LER analyses	[90]
155	Hadronic energy scale in MC in ZEUS HER, MER and LER analyses	[90]
156	Scale factors applied to the diffractive MC in ZEUS HER, MER and LER analyses	[90]
157	Electrom validation with MVD and CTD in ZEUS HER, MER and LER analyses	[90]
158	Part of luminosity uncertainty for ZEUS shifted-vertex HER data	[90]
159	Part of luminosity uncertainty for ZEUS central-vertex LER data	[90]
160	Part of luminosity uncertainty for ZEUS shifted-vertex LER data	[90]
161	Part of luminosity uncertainty for ZEUS central-vertex MER data	[90]
162	Part of luminosity uncertainty for ZEUS shifted-vertex MER data	[90]

Table 3.2: Continued.

Systematic uncertainty index

Data Set	1	2	3	4	5	6	7	8	9	10	11	12	13	14	15	16	17	18	19	20	21	22	23	24	25	26	27
HERA I $E_p = 820\,\mathrm{GeV}$ and $E_p = 920\,\mathrm{GeV}$ data sets																											
H1 svx-mb [2] e^+p 95-00		+					+			+																	
H1 low-Q^2 [2] e^+p 96-00				+			+			+																	
H1 NC e^+p 94-97			+		+			+	+		+																
H1 CC e^+p 94-97								+	+		+																
H1 NC e^-p 98-99			+					+	+		+																
H1 CC e^-p 98-99					+	+		+	+		+																
H1 NC HY e^+p 98-99			+			+		+	+		+																
H1 NC e^+p 99-00			+			+		+	+		+																
H1 CC e^+p 99-00								+	+		+																
ZEUS BPC e^+p 95																+											
ZEUS BPT e^+p 97															+												
ZEUS SVX e^+p 95																											
ZEUS NC high-Q^2 e^+p 96-97	+												+							+	+	+	+	+	+	+	+
ZEUS NC low-Q^2 e^+p 96-97	+											+		+						+	+		+	+	+	+	+
ZEUS CC e^+p 94-97	+																							+	+		
ZEUS NC e^-p 98-99													+				+	+									
ZEUS CC e^-p 98-99														+				+									
ZEUS NC e^+p 99-00																	+	+	+								
ZEUS CC e^+p 99-00																			+								
HERA II $E_p = 920\,\mathrm{GeV}$ data sets																											
H1 NC e^+p 03-07											+																
H1 CC e^+p 03-07											+																
H1 NC e^-p 03-07											+																
H1 CC e^-p 03-07											+																
H1 NC med-Q^2 e^+p 03-07																											
H1 NC low-Q^2 e^+p 03-07																											
ZEUS NC e^+p 06-07																											
ZEUS CC e^+p 06-07																											
ZEUS NC e^-p 05-06																											
ZEUS CC e^-p 04-06																											
ZEUS NC nominal e^+p 06-07																											
ZEUS NC satellite e^+p 06-07																											
HERA II $E_p = 575\,\mathrm{GeV}$ data sets																											
H1 NC high-Q^2 e^+p 07																											
H1 NC low-Q^2 e^+p 07																											
ZEUS NC nominal e^+p 07																											
ZEUS NC satellite e^+p 07																											
HERA II $E_p = 460\,\mathrm{GeV}$ data sets																											
H1 NC high-Q^2 e^+p 07																											
H1 NC low-Q^2 e^+p 07																											
ZEUS NC nominal e^+p 07																											
ZEUS NC satellite e^+p 07																											

Table 3.3: Correlations of the systematic uncertainties between data sets used for the combination. The notation [2] in the column Data Set indicates that the data were treated in the analysis as two data sets with the same systematic uncertainties.

Data Set		Systematic uncertainty index																									
		28	29	30	31	32	33	34	35	36	37	38	39	40	41	42	43	44	45	46	47	48	49	50	51	52	53	54
HERA I $E_p = 820$ GeV and $E_p = 920$ GeV data sets																												
H1 svx-mb [2]	e^+p 95-00																											
H1 low-Q^2 [2]	e^+p 96-00																	+	+	+	+	+	+	+	+	+	+	+
H1 NC	e^+p 94-97																											
H1 CC	e^+p 94-97																											
H1 NC	e^-p 98-99																											
H1 CC	e^-p 98-99																											
H1 NC HY	e^-p 98-99																											
H1 NC	e^+p 99-00																											
H1 CC	e^+p 99-00																											
ZEUS BPC	95																											
ZEUS BPT	97																											
ZEUS SVX	95																											
ZEUS NC high-Q^2	e^+p 96-97	+																										
ZEUS NC low-Q^2	e^+p 96-97	+	+																									
ZEUS CC	e^+p 94-97			+	+	+	+	+																				
ZEUS NC	e^-p 98-99					+	+		+	+																		
ZEUS CC	e^-p 98-99				+	+	+	+		+	+	+																
ZEUS NC	e^+p 99-00									+			+				+											
ZEUS CC	e^+p 99-00									+	+	+	+	+	+	+	+											
HERA II $E_p = 920$ GeV data sets																												
H1 NC	e^+p 03-07																											
H1 CC	e^+p 03-07																											
H1 NC	e^-p 03-07																											
H1 CC	e^-p 03-07																											
H1 NC med-Q^2	e^+p 03-07																											
H1 NC low-Q^2	e^+p 03-07																											
ZEUS NC	e^+p 06-07																											
ZEUS CC	e^+p 06-07																											
ZEUS NC	e^-p 05-06																											
ZEUS CC	e^-p 04-06																											
ZEUS NC nominal	e^+p 06-07																											
ZEUS NC satellite	e^+p 06-07																											
HERA II $E_p = 575$ GeV data sets																												
H1 NC high-Q^2	e^+p 07																											
H1 NC low-Q^2	e^+p 07																											
ZEUS NC nominal	e^+p 07																											
ZEUS NC satellite	e^+p 07																											
HERA II $E_p = 460$ GeV data sets																												
H1 NC high-Q^2	e^+p 07																											
H1 NC low-Q^2	e^+p 07																											
ZEUS NC nominal	e^+p 07																											
ZEUS NC satellite	e^+p 07																											

Table 3.3: Continued.

Data Set		Systematic uncertainty index																									
		55	56	57	58	59	60	61	62	63	64	65	66	67	68	69	70	71	72	73	74	75	76	77	78	79	80	81
HERA I $E_p = 820$ GeV and $E_p = 920$ GeV data sets																												
H1 svx-mb [2]	e^+p 95-00			+																								
H1 low-Q^2 [2]	e^+p 96-00		+																									
H1 NC	e^+p 94-97			+	+	+	+	+	+	+	+	+	+	+	+	+	+	+	+	+	+	+	+	+				
H1 CC	e^+p 94-97																												
H1 NC	e^-p 98-99																												
H1 CC	e^-p 98-99																												
H1 NC HY	e^+p 98-99																												
H1 NC	e^+p 99-00																												
H1 CC	e^+p 99-00																												
ZEUS BPC	95																									+	+	+	+
ZEUS BPT	97																									+	+	+	
ZEUS SVX	95																												
ZEUS NC high-Q^2	e^+p 96-97																												
ZEUS NC low-Q^2	e^+p 96-97																												
ZEUS CC	e^+p 94-97																												
ZEUS NC	e^-p 98-99																												
ZEUS CC	e^-p 98-99																												
ZEUS NC	e^+p 99-00																												
ZEUS CC	e^+p 99-00																												
HERA II $E_p = 920$ GeV data sets																												
H1 NC	e^+p 03-07																												
H1 CC	e^+p 03-07																												
H1 NC	e^-p 03-07																												
H1 CC	e^-p 03-07																												
H1 NC med-Q^2	e^+p 03-07																												
H1 NC low-Q^2	e^+p 03-07																												
ZEUS NC	e^+p 06-07																												
ZEUS CC	e^+p 06-07																												
ZEUS NC	05-06																												
ZEUS CC	e^-p 04-06																												
ZEUS NC nominal	e^+p 06-07																												
ZEUS NC satellite	e^+p 06-07																												
HERA II $E_p = 575$ GeV data sets																												
H1 NC high-Q^2	07																												
H1 NC low-Q^2	07																												
ZEUS NC nominal	e^+p 07																												
ZEUS NC satellite	e^+p 07																												
HERA II $E_p = 460$ GeV data sets																												
H1 NC high-Q^2	07																												
H1 NC low-Q^2	07																												
ZEUS NC nominal	e^+p 07																												
ZEUS NC satellite	e^+p 07																												

Table 3.3: Continued.

Systematic uncertainty index

Data Set	82	83	84	85	86	87	88	89	90	91	92	93	94	95	96	97	98	99	100	101	102	103	104	105	106	107	108
HERA I $E_p = 820$ GeV and $E_p = 920$ GeV data sets																											
H1 svx-mb [2] e^+p 95-00																											
H1 low-Q^2 [2] e^+p 96-00																											
H1 NC e^+p 94-97																											
H1 CC e^+p 94-97																											
H1 NC e^+p 98-99																											
H1 CC e^-p 98-99																											
H1 NC HY e^-p 98-99																											
H1 NC e^+p 99-00																											
H1 CC e^+p 99-00																											
ZEUS BPC e^+p 95	+				+			+		+																	
ZEUS BPT e^+p 97		+	+	+	+	+	+	+	+	+	+																
ZEUS SVX e^+p 95								+		+																	
ZEUS NC high-Q^2 e^+p 96-97												+	+	+	+	+	+	+	+	+	+	+	+	+	+	+	+
ZEUS NC low-Q^2 e^+p 96-97																			+	+	+	+	+	+	+	+	+
ZEUS CC e^+p 94-97																											
ZEUS NC e^-p 98-99																											
ZEUS CC e^-p 98-99																											
ZEUS NC e^+p 99-00																											
ZEUS CC e^+p 99-00																											
HERA II $E_p = 920$ GeV data sets																											
H1 NC e^+p 03-07																											
H1 CC e^+p 03-07																											
H1 NC e^-p 03-07																											
H1 CC e^-p 03-07																											
H1 NC med-Q^2 e^+p 03-07																											
H1 NC low-Q^2 e^+p 03-07																											
ZEUS NC e^+p 06-07																											
ZEUS CC e^+p 06-07																											
ZEUS NC e^-p 05-06																											
ZEUS CC e^-p 04-06																											
ZEUS NC nominal e^+p 06-07																											
ZEUS NC satellite e^+p 06-07																											
HERA II $E_p = 575$ GeV data sets																											
H1 NC high-Q^2 e^+p 07																											
H1 NC low-Q^2 e^+p 07																											
ZEUS NC nominal e^+p 07																											
ZEUS NC satellite e^+p 07																											
HERA II $E_p = 460$ GeV data sets																											
H1 NC high-Q^2 e^+p 07																											
H1 NC low-Q^2 e^+p 07																											
ZEUS NC nominal e^+p 07																											
ZEUS NC satellite e^+p 07																											

Table 3.3: Continued.

Data Set		109	110	111	112	113	114	115	116	117	118	119	120	121	122	123	124	125	126	127	128	129	130	131	132	133	134	135
HERA I $E_p = 820$ GeV and $E_p = 920$ GeV data sets																												
H1 svx-mb [2]	e^+p 95-00		+																									
H1 low-Q^2 [2]	e^+p 96-00		+																									
H1 NC	e^+p 94-97		+																									
H1 CC	e^+p 94-97		+																									
H1 NC	e^-p 98-99		+																									
H1 CC	e^-p 98-99		+																									
H1 NC HY	e^-p 98-99		+																									
H1 NC	e^+p 99-00		+																									
H1 CC	e^+p 99-00		+																									
ZEUS BPC	95		+																									
ZEUS BPT	97		+																									
ZEUS SVX	95		+	+																								
ZEUS NC high-Q^2	e^+p 96-97		+																									
ZEUS NC low-Q^2	e^+p 96-97		+																									
ZEUS CC	e^+p 94-97		+																									
ZEUS NC	e^-p 98-99		+																									
ZEUS CC	e^-p 98-99		+																									
ZEUS NC	e^+p 99-00		+																									
ZEUS CC	e^+p 99-00		+																									
HERA II $E_p = 920$ GeV data sets																												
H1 NC	e^+p 03-07				+	+		+		+		+		+														
H1 CC	e^+p 03-07					+		+	+		+		+	+														
H1 NC	e^-p 03-07				+	+			+	+			+	+														
H1 CC	e^-p 03-07					+	+							+														
H1 NC med-Q^2	e^+p 03-07			+		+							+		+	+	+	+	+	+								
H1 NC low-Q^2	e^+p 03-07			+		+							+		+	+	+	+	+	+								
ZEUS NC	e^+p 06-07			+											+		+	+				+		+			+	
ZEUS CC	e^+p 06-07			+											+	+	+	+	+		+	+	+	+	+	+		+
ZEUS NC	e^+p 05-06			+																								
ZEUS CC	e^-p 04-06			+																								
ZEUS NC nominal	e^+p 06-07			+																								
ZEUS NC satellite	e^+p 06-07			+																								
HERA II $E_p = 575$ GeV data sets																												
H1 NC high-Q^2	e^+p 07			+	+	+	+	+							+		+	+										
H1 NC low-Q^2	e^+p 07			+	+	+																						
ZEUS NC nominal	e^+p 07			+															+									
ZEUS NC satellite	e^+p 07			+																								
HERA II $E_p = 460$ GeV data sets																												
H1 NC high-Q^2	e^+p 07			+	+	+	+	+							+		+	+										
H1 NC low-Q^2	e^+p 07			+	+	+																						
ZEUS NC nominal	e^+p 07			+															+									
ZEUS NC satellite	e^+p 07			+																								

Systematic uncertainty index

Table 3.3: Continued.

Data Set	136	137	138	139	140	141	142	143	144	145	146	147	148	149	150	151	152	153	154	155	156	157	158	159	160	161	162
HERA I $E_p = 820$ GeV and $E_p = 920$ GeV data sets																											
H1 svx-mb [2] e^+p 95-00																											
H1 low-Q^2 [2] e^+p 96-00																											
H1 NC e^+p 94-97																											
H1 CC e^+p 94-97																											
H1 NC e^-p 98-99																											
H1 CC e^-p 98-99																											
H1 NC HY e^-p 98-99																											
H1 NC e^+p 99-00																											
H1 CC e^+p 99-00																											
ZEUS BPC 95																											
ZEUS BPT 97																											
ZEUS SVX 95																											
ZEUS NC high-Q^2 e^+p 96-97													+														
ZEUS NC low-Q^2 e^+p 96-97													+														
ZEUS CC e^+p 94-97																											
ZEUS NC e^-p 98-99																											
ZEUS CC e^-p 98-99																											
ZEUS NC e^+p 99-00																											
ZEUS CC e^+p 99-00																											
HERA II $E_p = 920$ GeV data sets																											
H1 NC e^+p 03-07						+	+	+	+	+	+	+	+														
H1 CC e^+p 03-07		+																									
H1 NC e^-p 03-07		+																									
H1 CC e^-p 03-07			+																								
H1 NC med-Q^2 e^+p 03-07			+																								
H1 NC low-Q^2 e^+p 03-07																											
ZEUS NC e^+p 06-07				+	+							+	+														
ZEUS CC e^+p 06-07				+	+																						
ZEUS NC e^-p 05-06					+																						
ZEUS CC e^-p 04-06					+																						
ZEUS NC nominal e^+p 06-07					+														+	+	+	+					
ZEUS NC satellite e^+p 06-07					+														+	+	+	+	+				
HERA II $E_p = 575$ GeV data sets																											
H1 NC high-Q^2 e^+p 07														+		+		+									
H1 NC low-Q^2 e^+p 07															+	+	+										
ZEUS NC nominal e^+p 07																			+	+	+	+			+		
ZEUS NC satellite e^+p 07																			+	+	+	+				+	
HERA II $E_p = 460$ GeV data sets																											
H1 NC high-Q^2 e^+p 07														+		+											
H1 NC low-Q^2 e^+p 07															+		+										
ZEUS NC nominal e^+p 07																			+	+	+			+			
ZEUS NC satellite e^+p 07																			+	+	+				+		

Table 3.3: Continued.

an "additive" approach, when absolute values of the uncertainties are not scaled, might be correct. To check the effect of changing the treatment of systematic uncertainties, an alternative combination was performed with all uncertainties treated as "additive" in the combination procedure except the following 29 normalisation uncertainties:

1, 15, 16, 17, 18, 19, 30, 39, 43, 88, 93, 100, 111, 119, 120, 121, 127, 138, 139, 140, 147, 148, 150, 153, 158, 159, 160, 161, 162.

The differences between cross sections obtained in this alternative combination and in the nominal combination were defined as the correlated procedural uncertainties, $\delta_{\rm rel}$, and are typically below 1 % for medium-Q^2 and x_{Bj} data and a few percent for low- and high-Q^2 or x_{Bj} data. Absolute values of the procedural uncertainties $\delta_{\rm rel}$ for a few selected (x_{Bj}, Q^2) grid points at $\sqrt{s_{com\,1}} = 318$ GeV are presented together with the total uncertainties in Fig. 3.2.

3.4.2 Correlations between systematic uncertainties on different data sets

In the nominal combination procedure, only the theoretical luminosity uncertainty number 111 in Table 3.2 was correlated between H1 and ZEUS data sets, and only the H1 photoproduction background uncertainty 11 was correlated between the data from the HERA I and HERA II periods. More systematic uncertainties might have correlations between different data sets since the same Monte Carlo simulation packages and similar calibration methods were used in different analyses. A detailed analysis of such correlations was performed for the combination of HERA I data [102] and revealed that only correlations of the photoproduction background and hadronic energy-scale uncertainties have a noticeable effect on the combination results. In the combination of all HERA data, a similar check was performed for HERA I data. For the data from the HERA II period, correlations between the experiments were considered less important [14]. Two alternative combinations in which systematic sources for the photoproduction background and hadronic energy scale were taken as correlated across data sets were prepared. Instead of the combined H1 HERA I svx-mb 95-00 [71] and low-Q^2 96-00 [72] data, separate data sets were used. Their photoproduction-background uncertainties were taken as correlated to the systematic errors 11, 28, and 91 and their hadronic energy-scale uncertainties were correlated to the systematic errors 8, 24, 25, 26, 89, 114, and 124. The differences between the nominal combination and alternative combinations were defined as correlated procedural uncertainties, $\delta_{\gamma p}$ and $\delta_{\rm had}$. They are typically below 1% for NC and below 0.5% for CC scattering and reach the few percent level for the low-Q^2 data. Absolute values of the procedural uncertainties $\delta_{\gamma p}$ and $\delta_{\rm had}$ for a few selected (x_{Bj}, Q^2) grid points at $\sqrt{s_{com\,1}} = 318$ GeV are compared to the total uncertainties in Fig. 3.3 and Fig. 3.4, respectively.
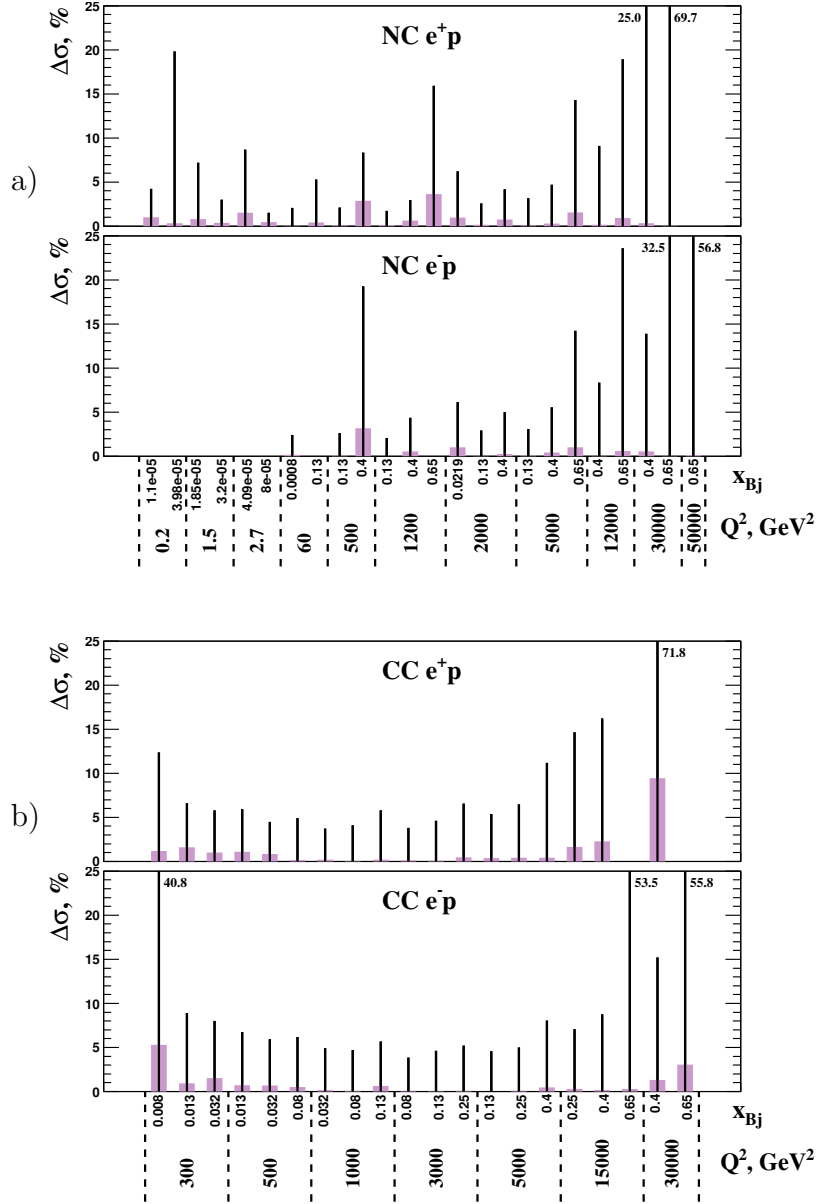
Figure 3.2: Absolute values of the procedural uncertainties δ_{rel} (wide purple error bars) and the total uncertainties excluding procedural uncertainties (thin error bars) from combined inclusive NC (a) and CC (b) data at $\sqrt{s_{com\,1}} = 318$ GeV for selected values of Q^2 and x_{Bj}. Values of the total uncertainties that exceed the histogram ranges are also given next to the bars.
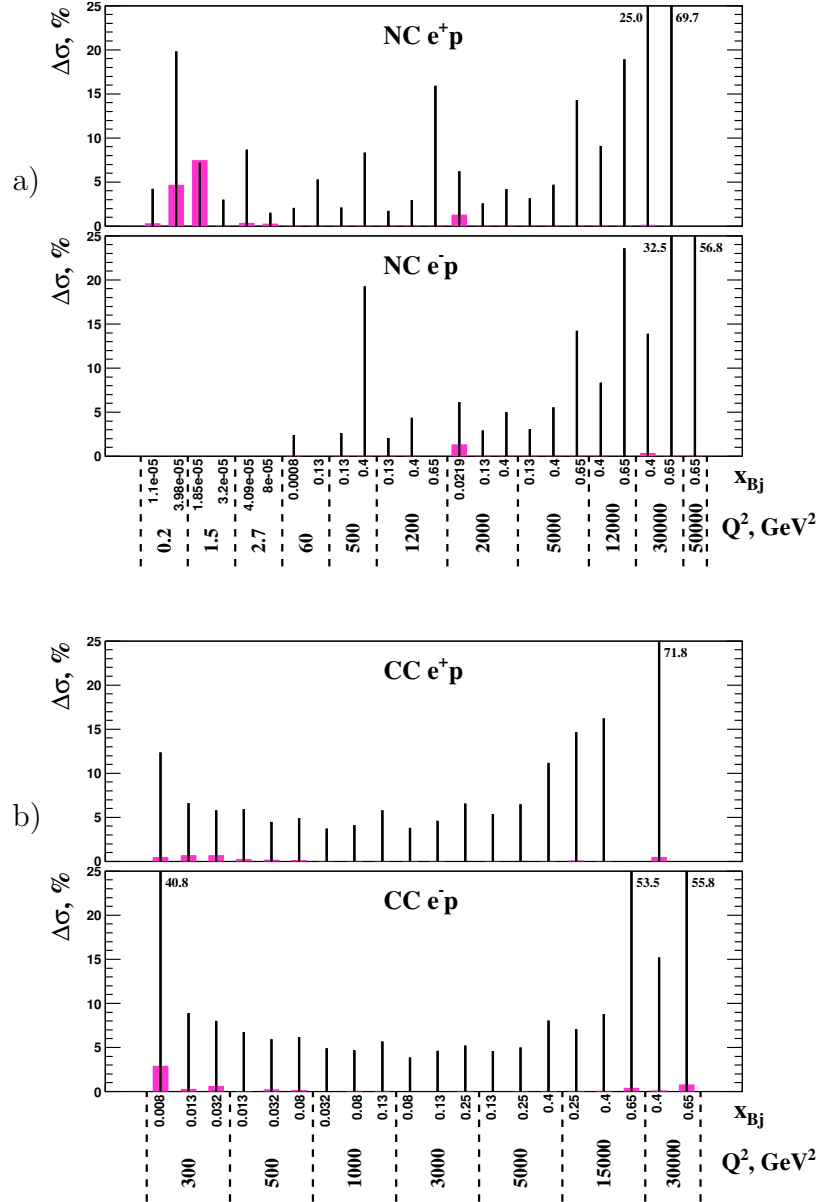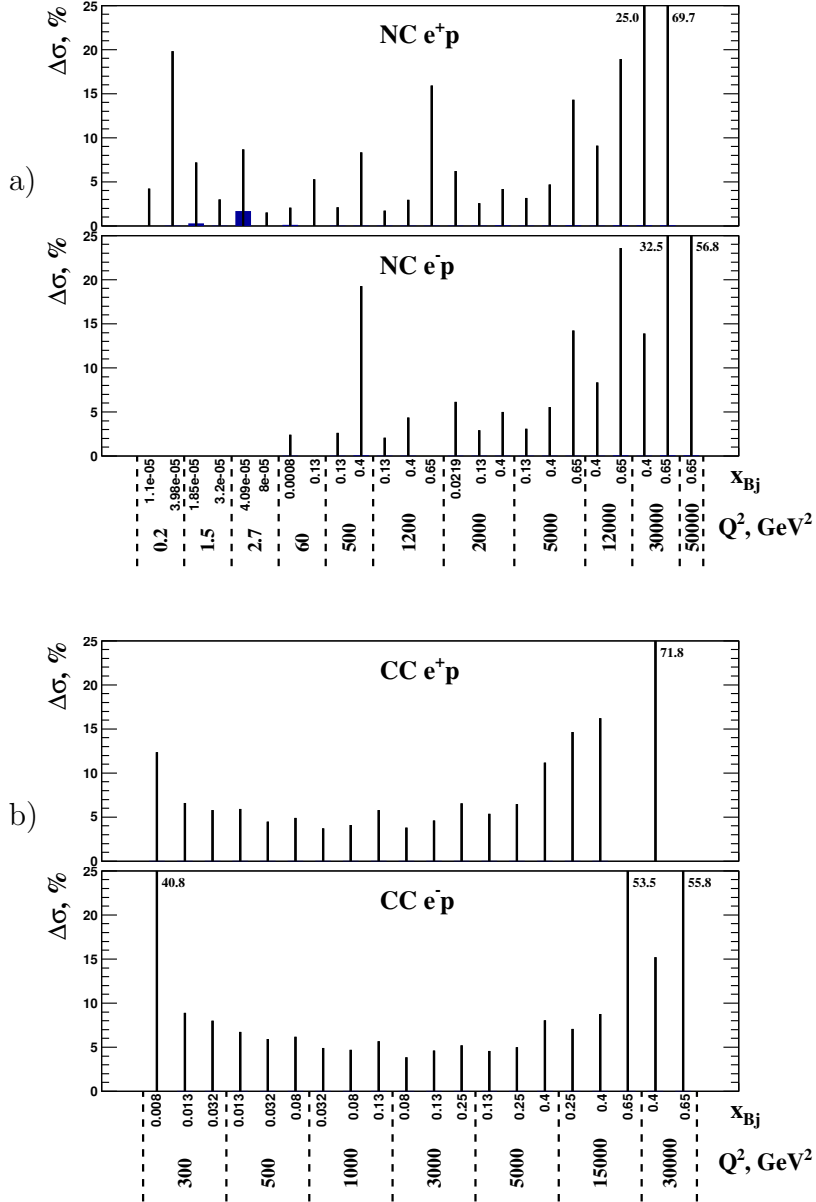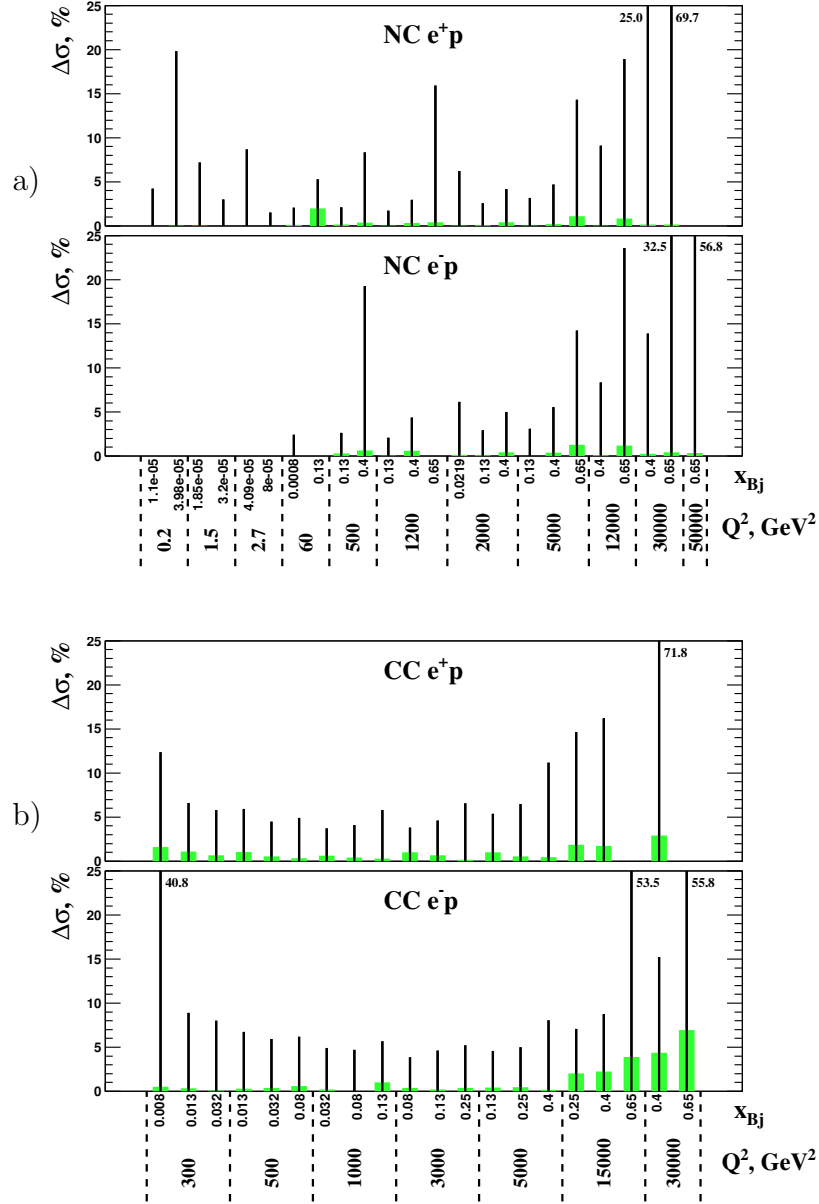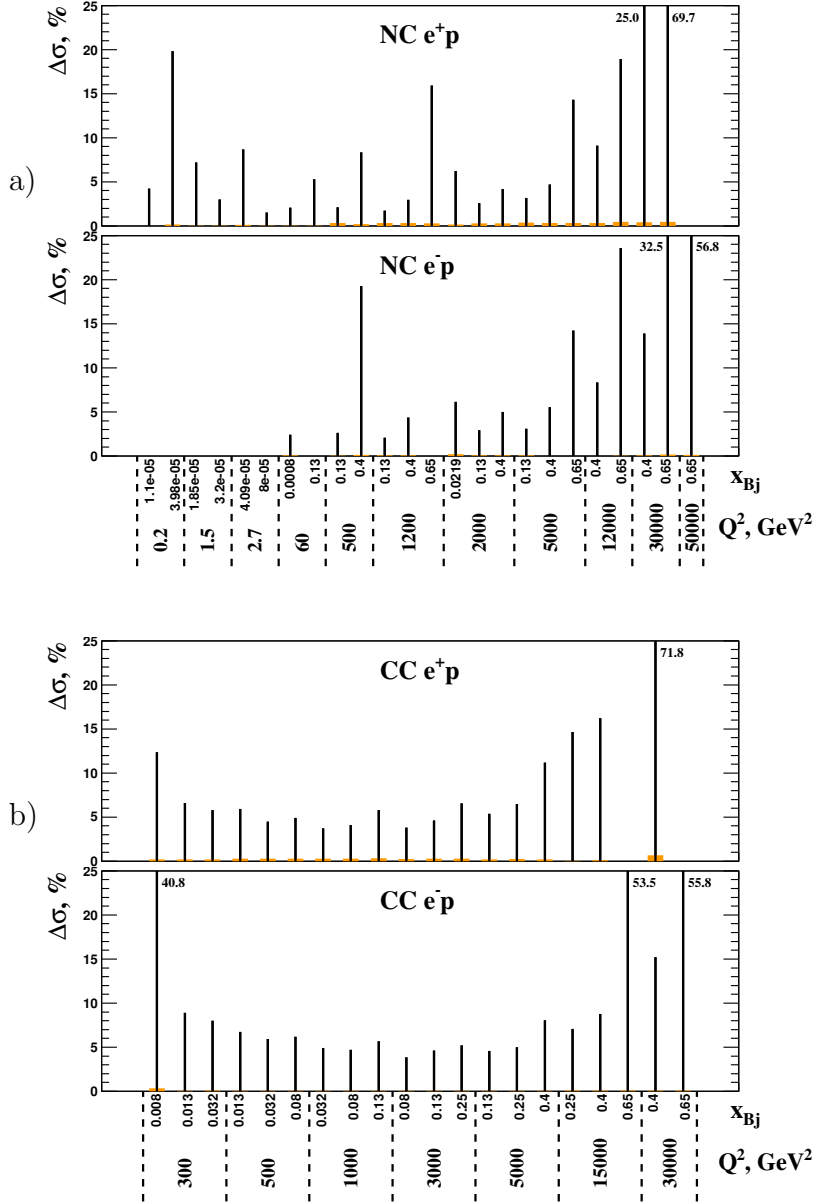
Figure 3.3: Absolute values of the procedural uncertainties $\delta_{\gamma p}$ (wide pink error bars) and the total uncertainties excluding procedural uncertainties (thin error bars) from combined inclusive NC (a) and CC (b) data at $\sqrt{s_{com\,1}} = 318$ GeV for selected values of Q^2 and x_{Bj}. Values of the total uncertainties that exceed the histogram ranges are also given next to the bars.
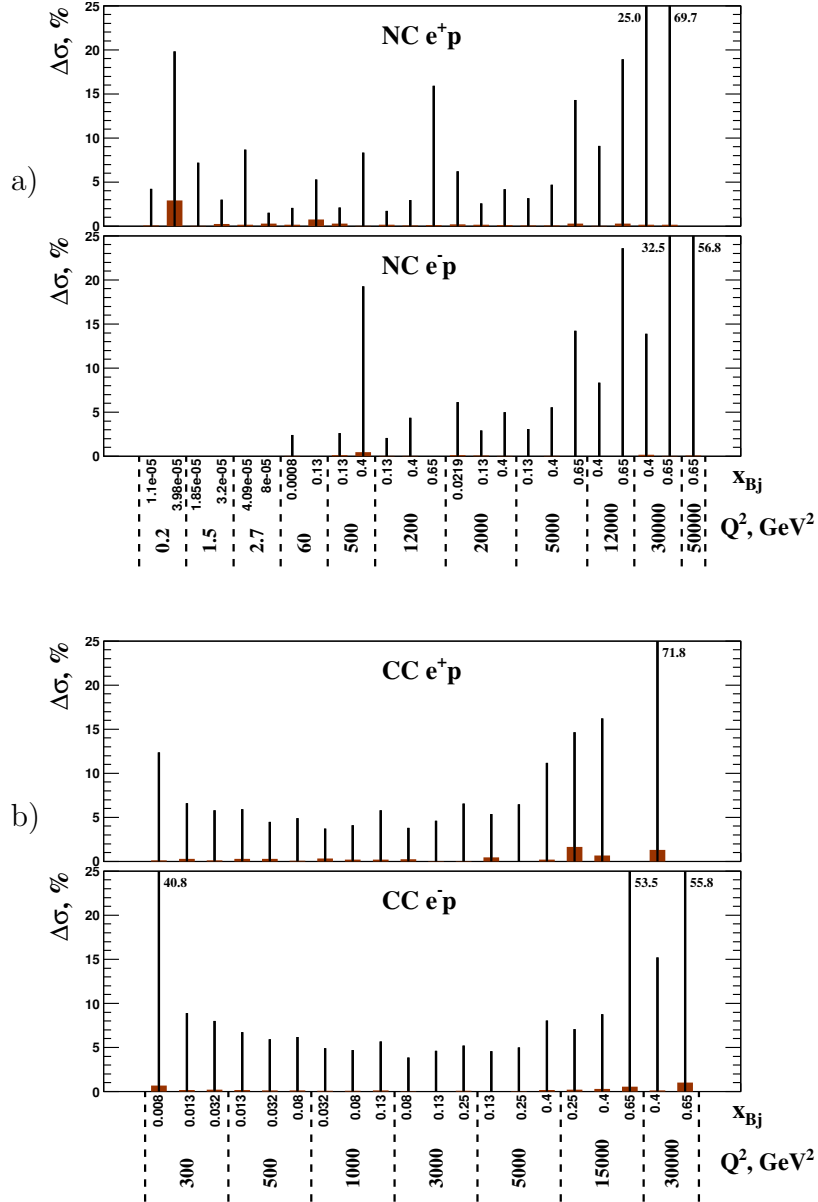
Figure 3.4: Absolute values of the procedural uncertainties δ_{had} (wide brown error bars) and the total uncertainties excluding procedural uncertainties (thin error bars) from combined inclusive NC (a) and CC (b) data at $\sqrt{s_{com\,1}} = 318$ GeV for selected values of Q^2 and x_{Bj}. Values of the total uncertainties that exceed the histogram ranges are also given next to the bars.

3.4.3 Large pulls of correlated systematic uncertainties

All 162 correlated systematic uncertainties from the separate data sets were treated as fully point-to-point correlated. During the averaging, none of the sources was shifted by more than $2.4\,\sigma$ and pulls were defined as

$$p_j = b_j/(1 - \Delta_{b_j}^2)^{1/2} \quad , \tag{3.12}$$

where Δ_{b_j} is the uncertainty on the source j after the averaging. The distribution of pulls p_j is displayed in Fig. 3.5 a. It has a root-mean-square value of 1.34 due to some large values of pulls. These large pulls originate from small relative uncertainties, with typical values below 1%, for which there is only a small reduction of the uncertainty in the averaging procedure. Forty sources of systematic uncertainties were found to have pulls $p_j > 1.3$. In order to investigate this, an additional combination was prepared with these uncertainties scaled by a factor of two. The distribution of pulls for the alternative combination is shown in Fig. 3.5 b and has a root-mean-square value of 1.03, which indicates that it is closer to the Normal distribution than the distribution of pulls from the nominal combination.

Scaling of each of the selected 40 systematic uncertainties separately could have been used to produce an individual procedural uncertainty. Instead the correlations between these uncertainties were studied and are shown in Fig. 3.6. According to them, the selected uncertainties were divided into four groups by their relation to:

1. very low-Q^2 data from HERA I: 7, 62, 64, 67, 69, 72, 74, 76, 84, 90, 101, 102, 105, 109;

2. low- and medium-Q^2 data from HERA II with lowered proton beam energies: 122, 124, 125, 149, 151, 152, 154, 156, 157, 160;

3. medium- and high-Q^2 data from HERA I and II: 8, 48, 53, 55, 112, 114, 116, 129, 136, 144, 145;

4. normalisation issues from HERA I and II: 15, 30, 139, 140, 147.

For each group, an alternative combination with corresponding uncertainties scaled by a factor of two was prepared and the difference between the results of such combinations and that of the nominal combination were defined as additional procedural uncertainties δ_1, δ_2, δ_3 and δ_4. The distributions of pulls for each of the alternative combinations are presented in Fig. 3.7. Evaluated procedural uncertainties are typically below 0.1%, reaching the few percent level for some low-Q^2 NC and medium-Q^2 CC data points. Absolute values of the procedural uncertainties δ_1–δ_4 for a few selected (x_{Bj}, Q^2) grid points of NC and CC data at $\sqrt{s_{com\,1}} = 318$ GeV are shown in Fig. 3.8–3.11.
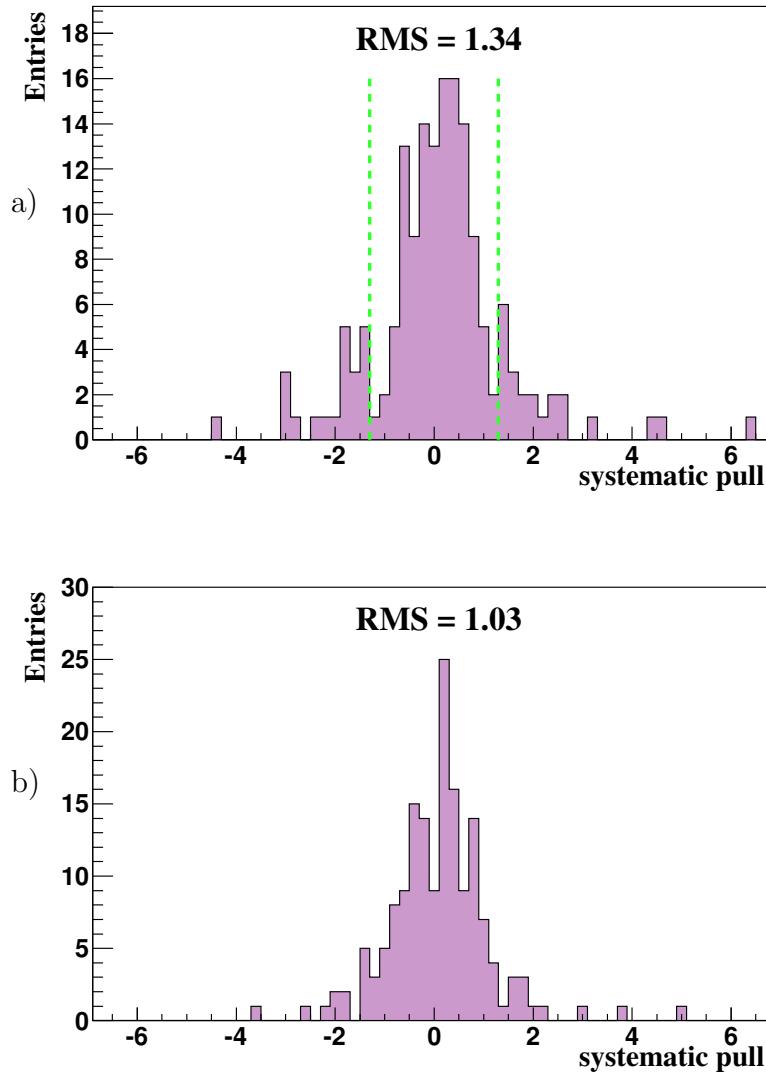
Figure 3.5: Distributions of pulls p_j for the correlated systematic uncertainties including global normalisations from nominal inclusive data combination (a) and from an alternative combination with 40 selected systematic uncertainties scaled by a factor of two (b). The vertical dashed lines in Fig. 3.5 a indicate pull values of -1.3 and 1.3. There are no entries outside the histogram ranges. The root mean squares, RMS, of the distributions are given on each figure.
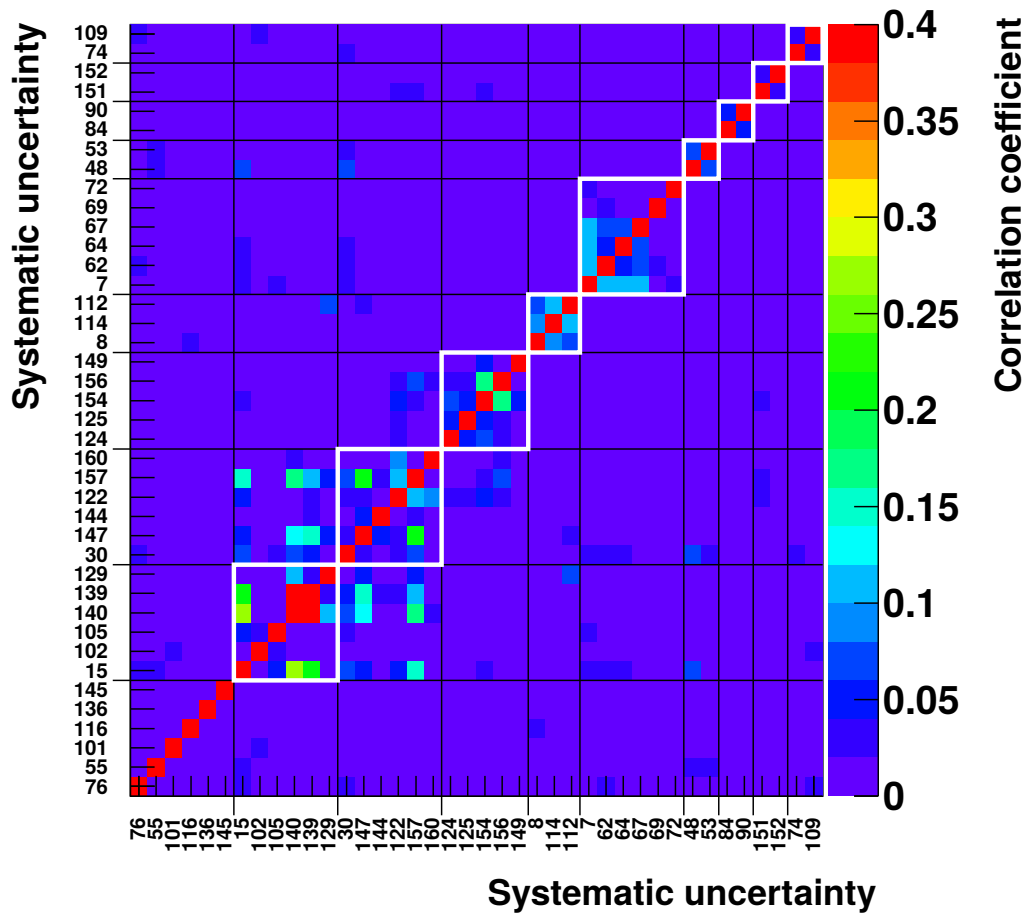
Figure 3.6: Correlation coefficients between systematic uncertainties with pulls p_j larger than 1.3.
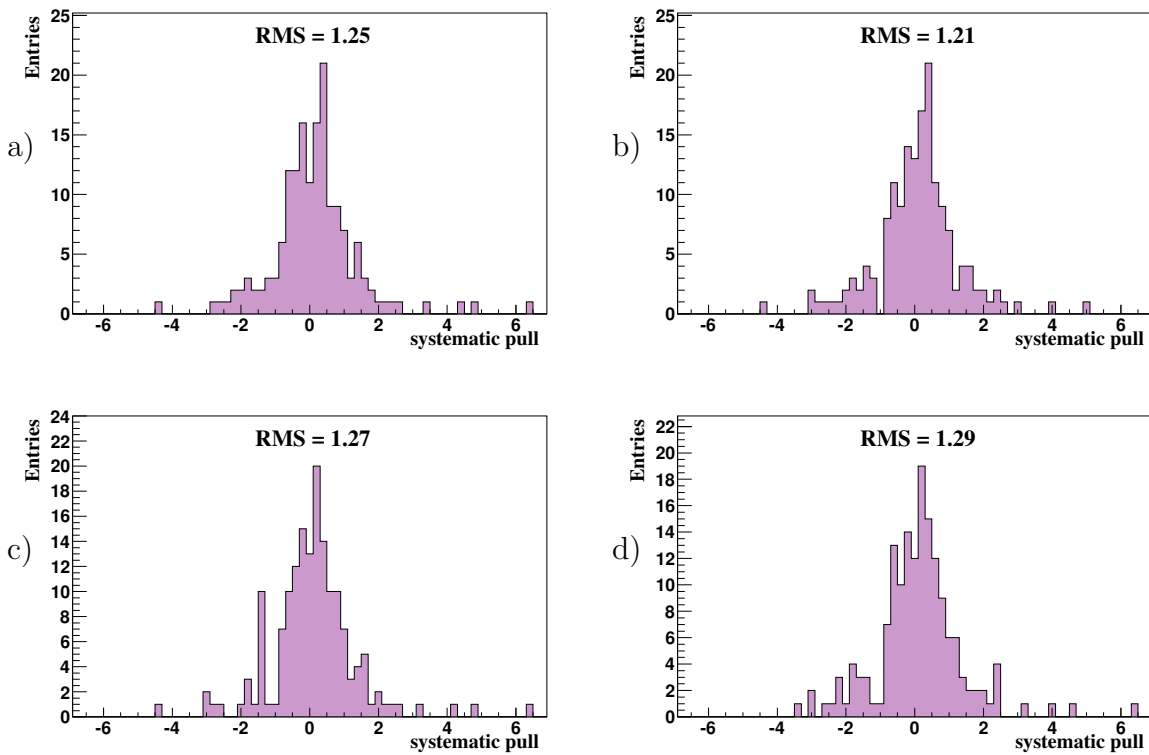
Figure 3.7: Distributions of pulls p_j for the correlated systematic uncertainties including global normalisations from the alternative combinations with systematic uncertainties from group 1 (a), 2 (b), 3 (c) or 4 (d) scaled by a factor of two. There are no entries outside the histogram ranges. The root mean squares, RMS, of the distributions are given on each figure.
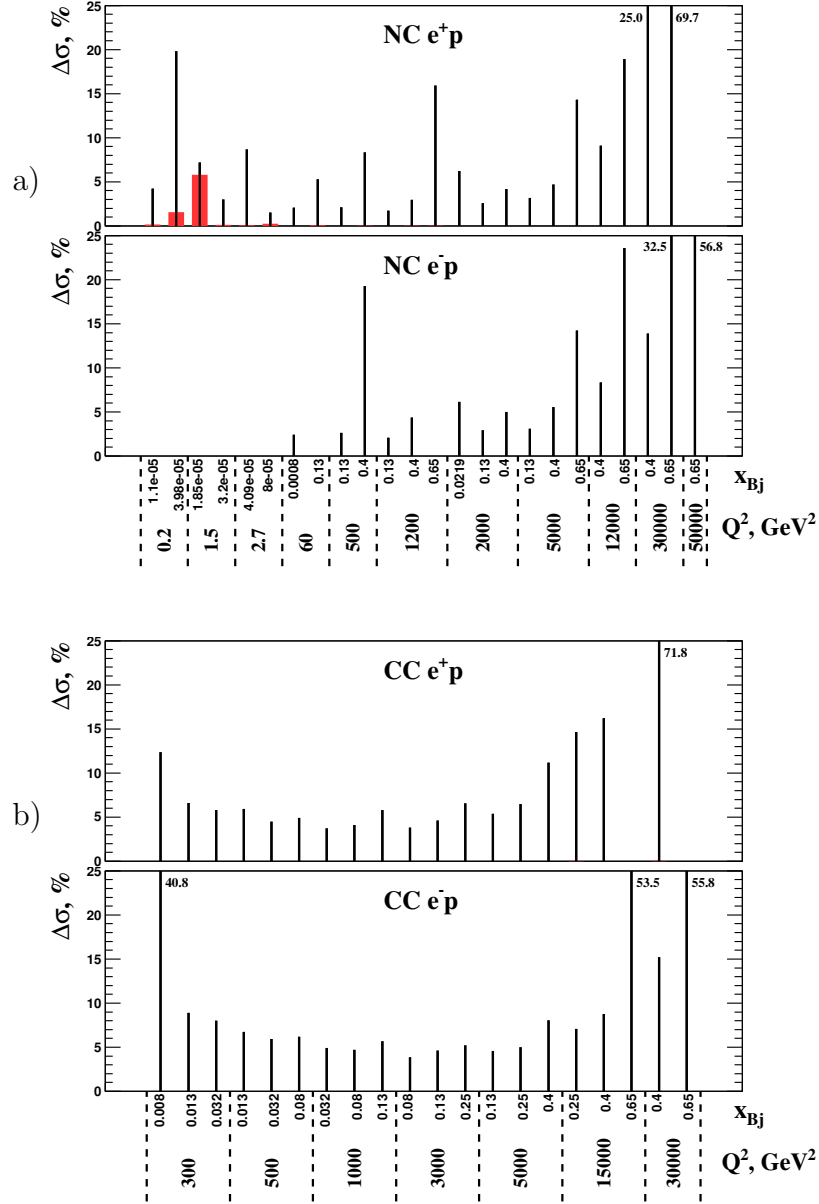
Figure 3.8: Absolute values of the procedural uncertainties δ_1 (wide red error bars) and the total uncertainties excluding procedural uncertainties (thin error bars) from combined inclusive NC (a) and CC (b) data at $\sqrt{s_{com\,1}} = 318$ GeV for selected values of Q^2 and x_{Bj}. Values of the total uncertainties that exceed the histogram ranges are also given next to the bars.

Figure 3.9: Absolute values of the procedural uncertainties δ_2 (wide blue error bars) and the total uncertainties excluding procedural uncertainties (thin error bars) from combined inclusive NC (a) and CC (b) data at $\sqrt{s_{com\,1}} = 318$ GeV for selected values of Q^2 and x_{Bj}. Values of the total uncertainties that exceed the histogram ranges are also given next to the bars.

Figure 3.10: Absolute values of the procedural uncertainties δ_3 (wide green error bars) and the total uncertainties excluding procedural uncertainties (thin error bars) from combined inclusive NC (a) and CC (b) data at $\sqrt{s_{com\,1}} = 318$ GeV for selected values of Q^2 and x_{Bj}. Values of the total uncertainties that exceed the histogram ranges are also given next to the bars.

Figure 3.11: Absolute values of the procedural uncertainties δ_4 (wide orange error bars) and the total uncertainties excluding procedural uncertainties (thin error bars) from combined inclusive NC (a) and CC (b) data at $\sqrt{s_{com\,1}} = 318$ GeV for selected values of Q^2 and x_{Bj}. Values of the total uncertainties that exceed the histogram ranges are also given next to the bars.

3.5 Result of the HERA data combination

The 2927 data points from 41 separate datasets were averaged into 1307 combined cross-sections measurements. This resulted in a number of degrees of freedom $ndf = 2927 - 1307 = 1620$. A full list of the combined reduced cross-section values with their statistical, uncorrelated and all point-to-point correlated systematic and procedural uncertainties is given at the combination web page [103].

3.5.1 Distribution of data pulls

In the averaging procedure, a value of $\chi^2/ndf = 1686.75/1620 = 1.04$ was obtained, indicating good consistency of the data from the two experiments. For points from data sets ds, contributing to the (x_{Bj}, Q^2) grids point i the pulls $\mathrm{p}^{i,ds}$ were defined as

$$\mathrm{p}^{i,ds} = \frac{\mu^{i,ds} - m^i \left(1 - \sum_j \gamma_j^{i,ds} b_j\right)}{\sqrt{\Delta_{i,ds}^2 - \Delta_i^2}} \quad . \tag{3.13}$$

Here $\Delta_{i,ds}$ and Δ_i are the statistical and uncorrelated systematic uncertainties added in quadrature for the data point i, ds and the combined cross-section value i, respectively. Distributions of the pulls of the data are displayed in Fig. 3.12. The root-mean-square values of these distributions are close to unity, also showing good consistency of the separate data sets.

3.5.2 Combined inclusive $e^\pm p$ cross sections

The individual and the combined reduced cross sections for NC e^+p and e^-p as a function of Q^2 for selected values of x_{Bj} are presented in Fig. 3.13 a and Fig. 3.14 a, and are compared to the results of the HERA I data combination [102] in Fig. 3.13 b and Fig. 3.14 b, respectively. As shown in Fig. 3.13 a, up to 8 separate data points contribute to some combined measurements, providing a remarkable improvement in precision. Since, for e^-p scattering, about ten times more data were collected during the HERA II period than HERA I, the improvements due to the new combination displayed in Fig. 3.14 b are the most prominent.

The averaged data with lowered proton beam energies for low and high values of Q^2 are shown in Fig. 3.15 and Fig. 3.16 together with predictions from HERAPDF2.0 NLO [14]. The low-, medium- and high-Q^2 regions of the NC e^+p data with $\sqrt{s_{com\,2}} = 300$ GeV and $\sqrt{s_{com\,1}} = 318$ GeV are presented in Fig. 3.17, Fig. 3.18 and Fig. 3.19. It includes the data with the lowest measured Q^2 values, down to $Q^2 = 0.045$ GeV^2. The NC e^-p data have the cross section with the highest measured Q^2 value of 50000 GeV^2 and are displayed in Fig. 3.20. The CC measurements of e^+p and e^-p are shown in Fig. 3.21 a and b, respectively.

H1 and ZEUS
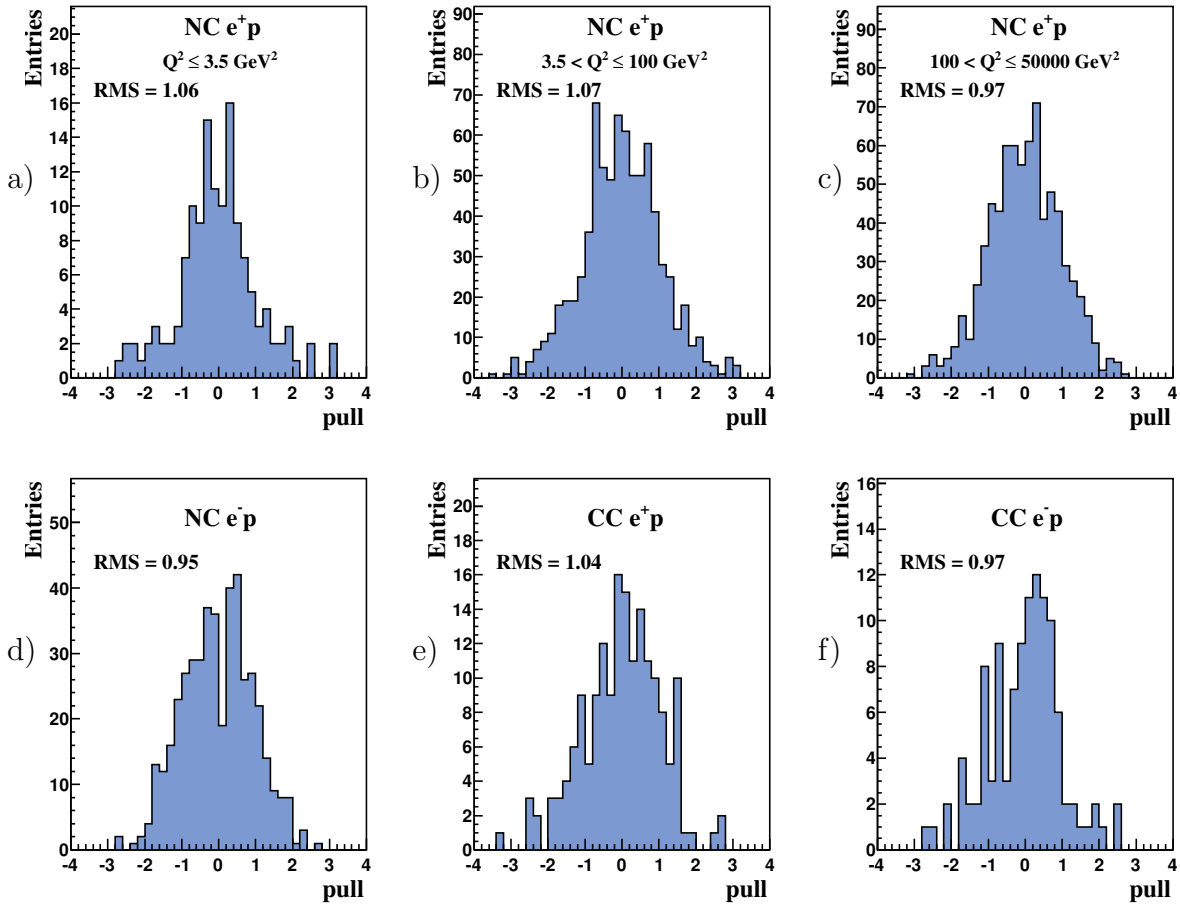
Figure 3.12: Distributions of pulls $p^{i,ds}$ from inclusive DIS data combination for: a) NC e^+p for $Q^2 \leq 3.5\,\mathrm{GeV}^2$; b) NC e^+p for $3.5 < Q^2 \leq 100\,\mathrm{GeV}^2$; c) NC e^+p for $100 < Q^2 \leq 50000\,\mathrm{GeV}^2$; d) NC e^-p for $60 \leq Q^2 \leq 50000\,\mathrm{GeV}^2$; e) CC e^+p for $300 \leq Q^2 \leq 30000\,\mathrm{GeV}^2$; and f) CC e^-p for $300 \leq Q^2 \leq 30000\,\mathrm{GeV}^2$. There are no entries outside the histogram ranges. The root mean square, RMS, of each distribution is given. The figures were taken from the HERAPDF2.0 paper [14].

The combined inclusive NC e^+p and e^-p HERA data together with fixed-target data [104, 105] and the predictions of HERAPDF2.0 NLO [14] for more than four orders of magnitude in Q^2 and x_{Bj} are shown in Fig. 3.22 a. There, for approximately $0.02 < x_{Bj} < 0.2$, QCD scaling, i.e. the relative independence of the structure functions on Q^2 at fixed x_{Bj}, is clearly visible, as are scaling violations for $x_{Bj} \leq 0.02$ and $x_{Bj} \geq 0.2$ and the difference between NC e^+p and e^-p scattering in the high-Q^2 region due to photon–Z interference. The first similar results obtained by the ZEUS [106] and H1 [107] collaborations are presented in Fig. 3.22 b and c, respectively. The new combined measurements show a spectacular increase in precision and the phase-space covered.

The NC and CC combined double-differential reduced cross sections were integrated over x_{Bj} for $y < 0.9$ using the cross-section predictions from HERAPDF2.0 NLO. The single-differential cross-sections $d\sigma/dQ^2$ thus obtained are displayed in Fig. 3.23. At low Q^2, NC cross sections are a few orders of magnitude larger than CC values since they are dominated by virtual photon exchange but CC and NC cross sections become similar in magnitude as Q^2 approaches the mass-scale squared of the electroweak bosons, $W^\pm$ and Z^0, demonstrating the effects of electroweak unification.

In the HERAPDF2.0 analysis [14], part of the NC e^+p data was used for the extraction of the $\tilde{F}_2$ structure function, as displayed in Fig. 3.24. The function $\tilde{F}_2$ shows a rise toward low values of x_{Bj}. This rise becomes steeper for higher values of Q^2, which corresponds to the scaling violation. The $\tilde{F}_2$ structure functions first obtained by the ZEUS [106] and H1 [107] collaborations are shown in Fig. 3.24 b and c, respectively. The $\tilde{F}_2$ values evaluated with the combined HERA data demonstrate a dramatic reduction of the uncertainties.

The high-precision inclusive cross-section measurements produced in this combination span six orders of magnitude in both Q^2 and x_{Bj}, and form the major legacy of the HERA experiments.
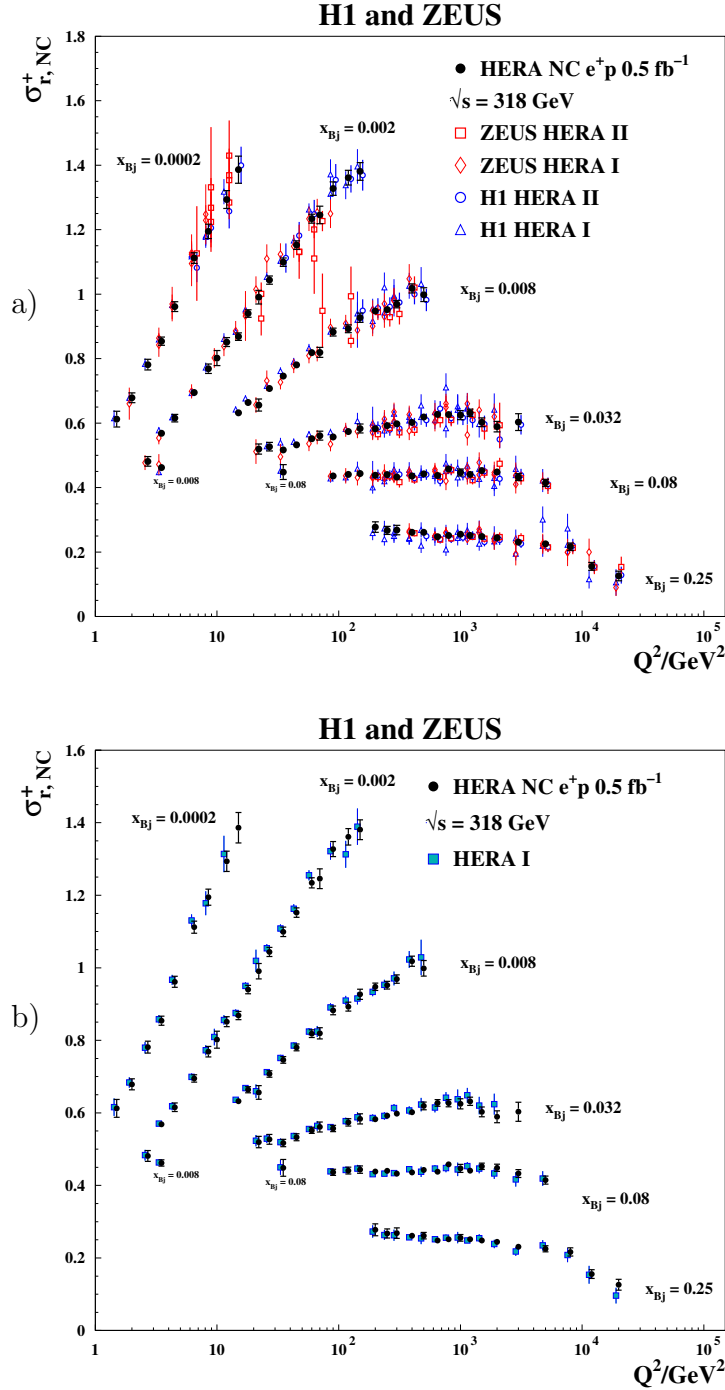
Figure 3.13: The combined HERA data for the inclusive NC e^+p reduced cross sections as a function of Q^2 for selected values of x_{Bj} compared to the individual H1 and ZEUS data (a) and to the results from HERA I alone [102] (b). The individual measurements are displaced horizontally for better visibility. The error bars represent the total uncertainties. The figures were taken from the HERAPDF2.0 paper [14].
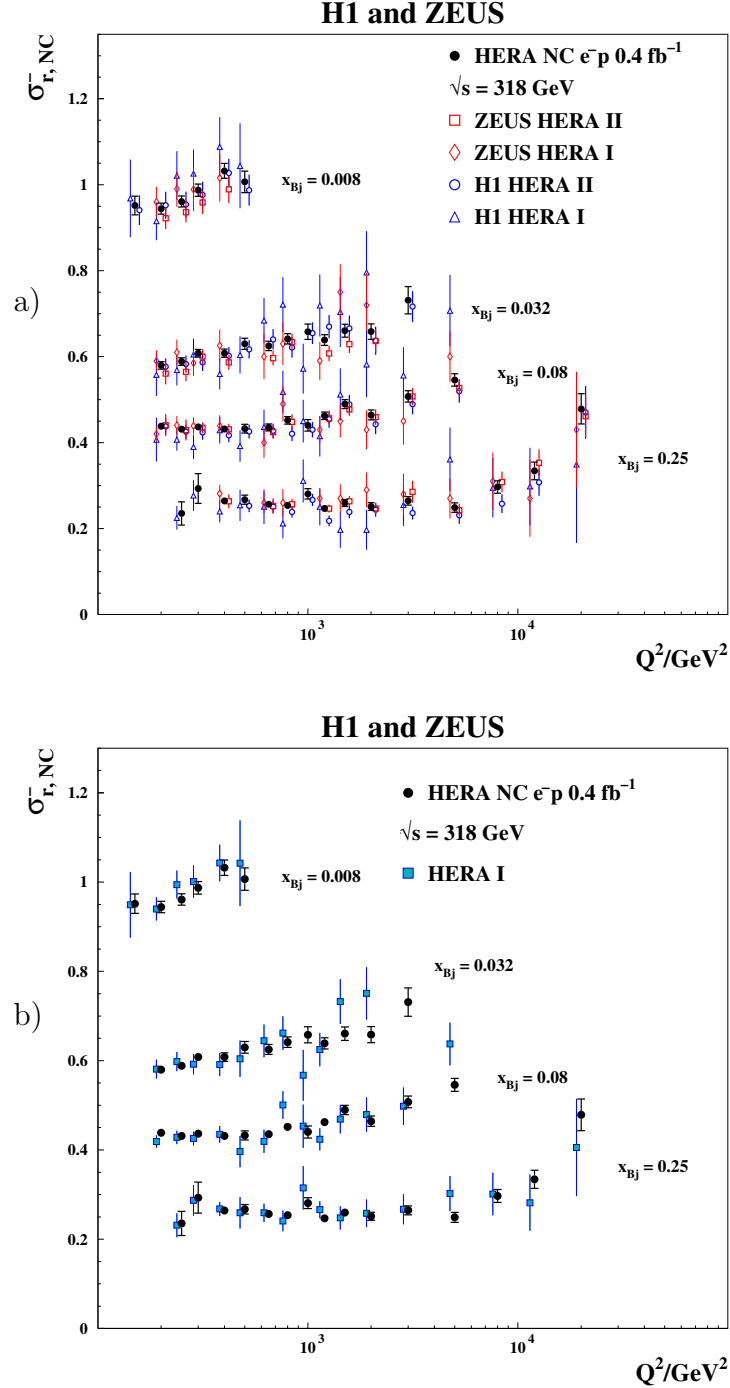
Figure 3.14: The combined HERA data for the inclusive NC e^-p reduced cross sections as a function of Q^2 for selected values of x_{Bj} compared to the individual H1 and ZEUS data (a) and to the results from HERA I alone [102] (b). The individual measurements are displaced horizontally for better visibility. The error bars represent the total uncertainties. The figures were taken from the HERAPDF2.0 paper [14].
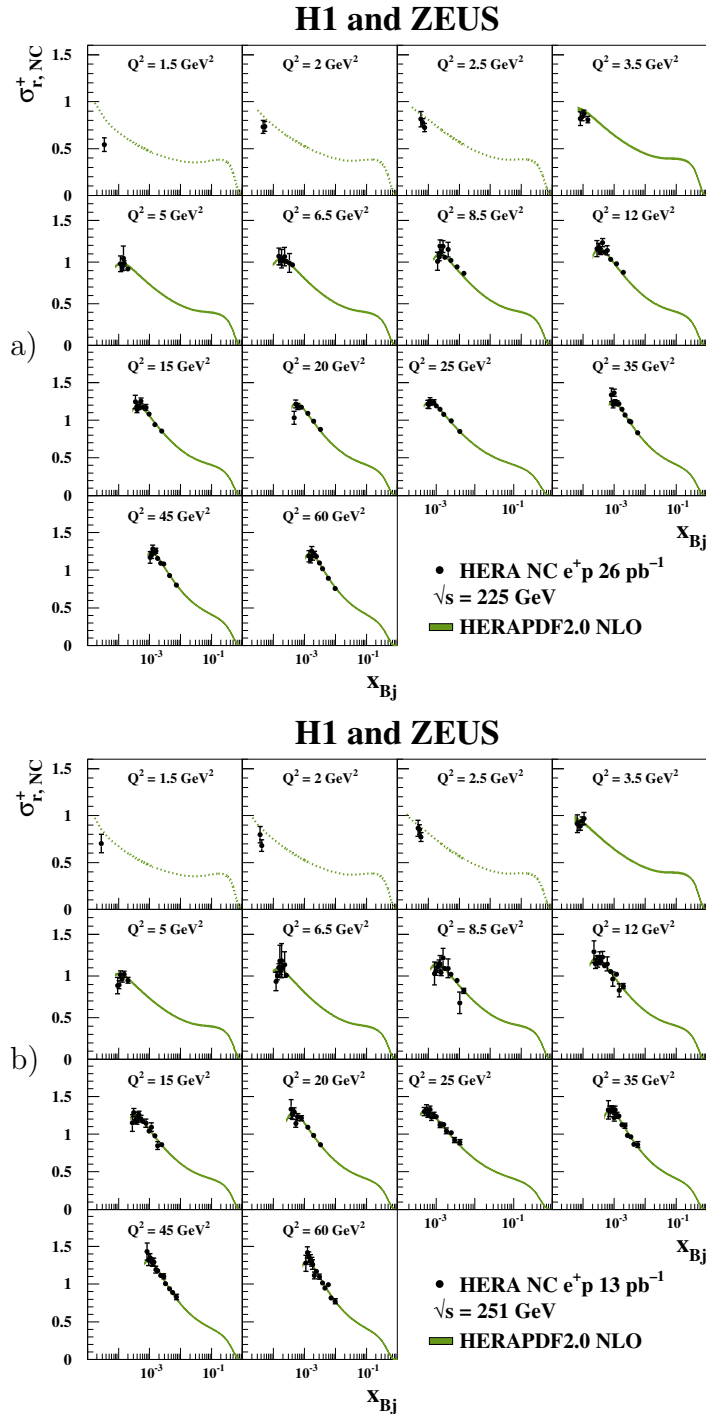
Figure 3.15: The combined HERA data for the inclusive NC e^+p reduced cross sections as a function of x_{Bj} for low values of Q^2 at $\sqrt{s_{com\,4}} = 225$ GeV (a) and $\sqrt{s_{com\,3}} = 251$ GeV (b) with overlaid predictions of HERAPDF2.0 NLO [14]. The error bars represent the total uncertainties on data and bands represent the total uncertainties on predictions. The figures were taken from the HERAPDF2.0 paper [14].
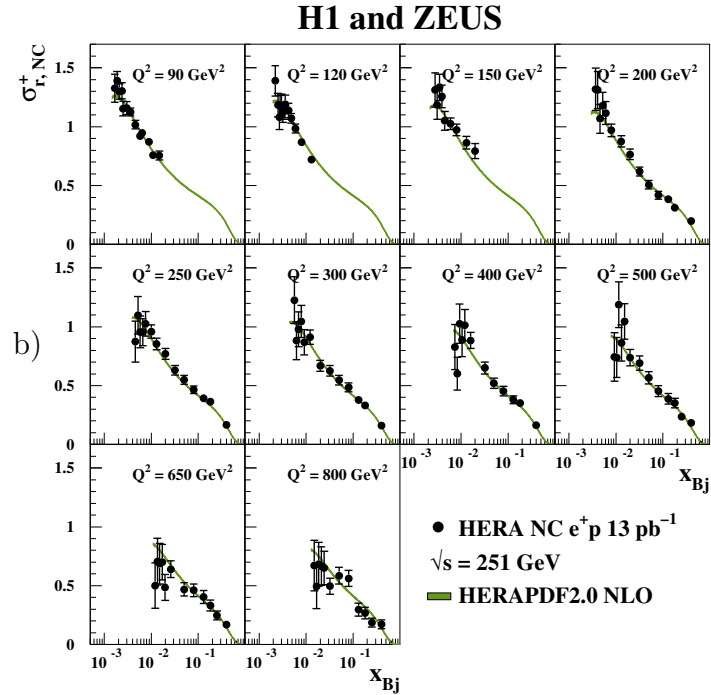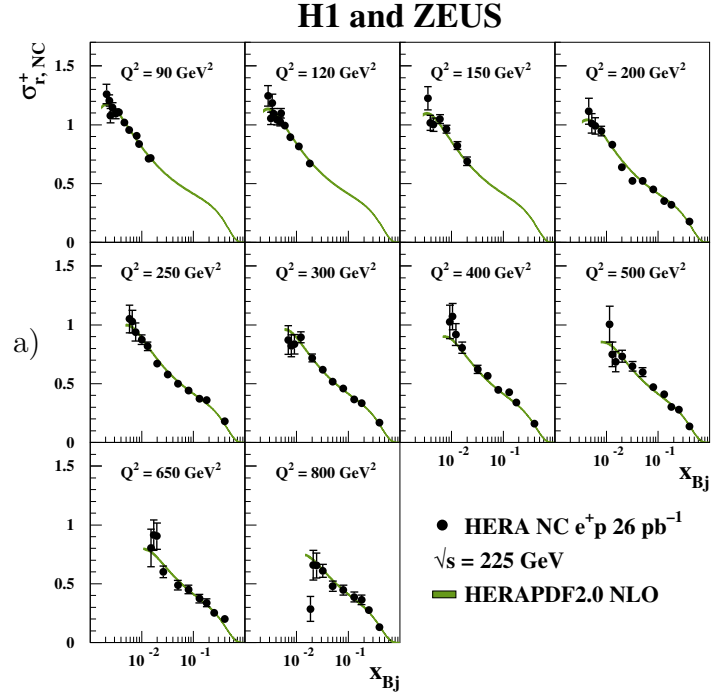
Figure 3.16: The combined HERA data for the inclusive NC e^+p reduced cross sections as a function of x_{Bj} for high values of Q^2 at $\sqrt{s_{com\,4}} = 225$ GeV (a) and $\sqrt{s_{com\,3}} = 251$ GeV (b) with overlaid predictions of HERAPDF2.0 NLO [14]. The error bars represent the total uncertainties on data and bands represent the total uncertainties on predictions. The figures were taken from the HERAPDF2.0 paper [14].
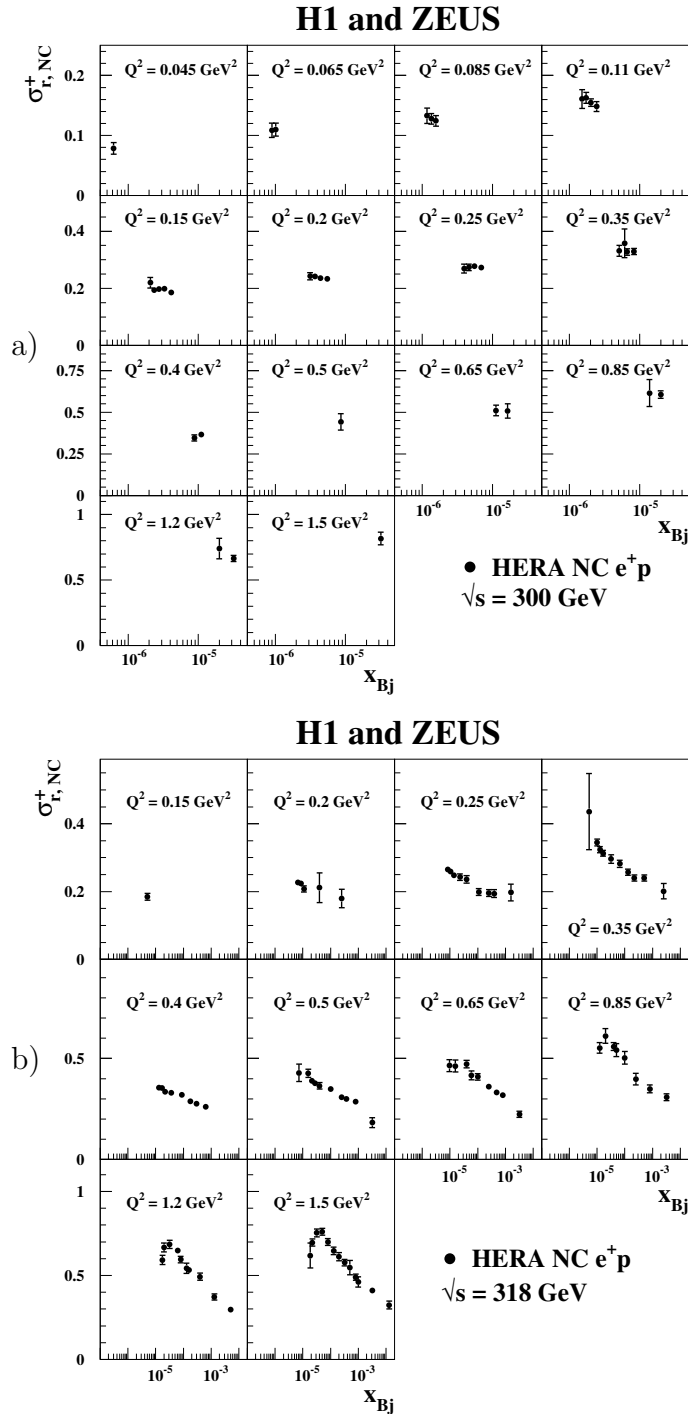
Figure 3.17: The combined HERA data for the inclusive NC e^+p reduced cross sections as a function of x_{Bj} for low values of Q^2 at $\sqrt{s_{com\,2}} = 300$ GeV (a) and $\sqrt{s_{com\,1}} = 318$ GeV (b). The error bars represent the total uncertainties. The figures were taken from the HERAPDF2.0 paper [14].
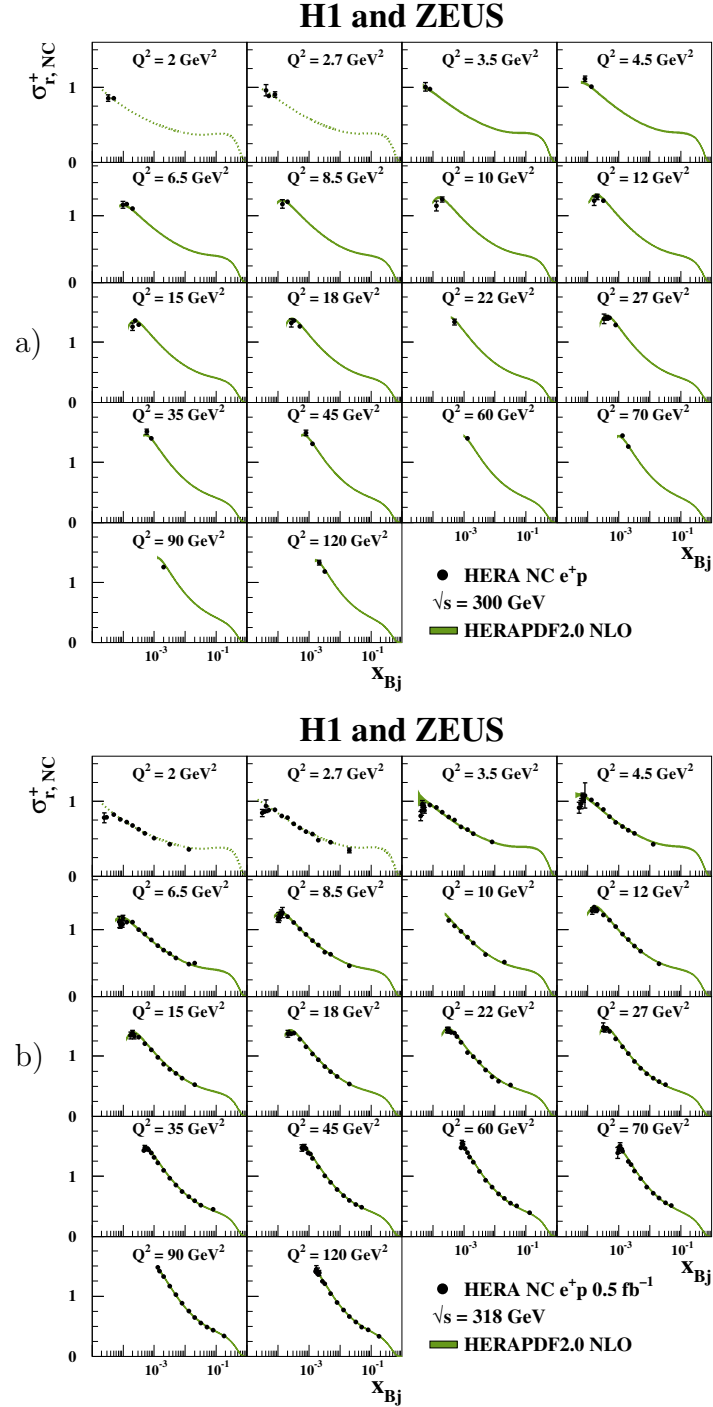
Figure 3.18: The combined HERA data for the inclusive NC e^+p reduced cross sections as a function of x_{Bj} for medium values of Q^2 at $\sqrt{s_{com\,2}} = 300$ GeV (a) and $\sqrt{s_{com\,1}} = 318$ GeV (b) with overlaid predictions of HERAPDF2.0 NLO [14]. The error bars represent the total uncertainties on data and bands represent the total uncertainties on predictions. The figures were taken from the HERAPDF2.0 paper [14].
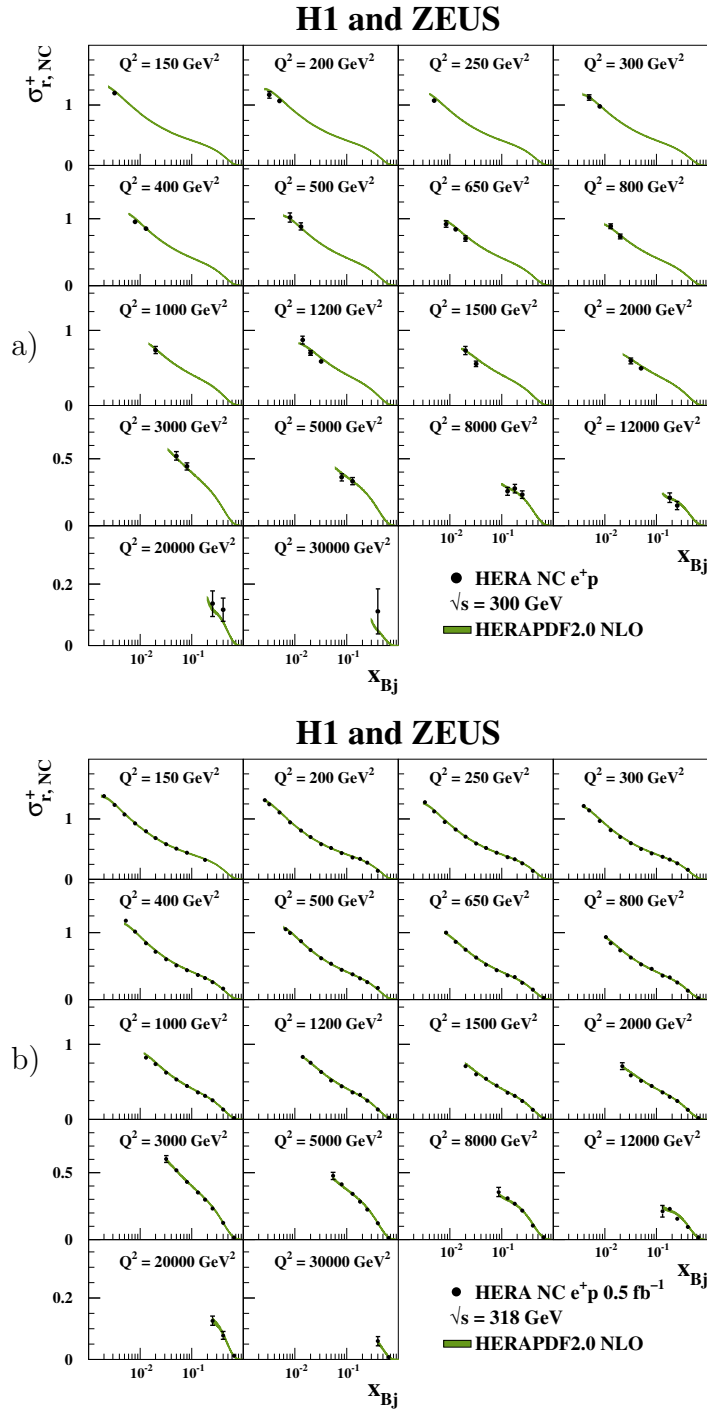
Figure 3.19: The combined HERA data for the inclusive NC e^+p reduced cross sections as a function of x_{Bj} for high values of Q^2 at $\sqrt{s_{com\,2}} = 300$ GeV (a) and $\sqrt{s_{com\,1}} = 318$ GeV (b) with overlaid predictions of HERAPDF2.0 NLO [14]. The error bars represent the total uncertainties on data and bands represent the total uncertainties on predictions. The figures were taken from the HERAPDF2.0 paper [14].
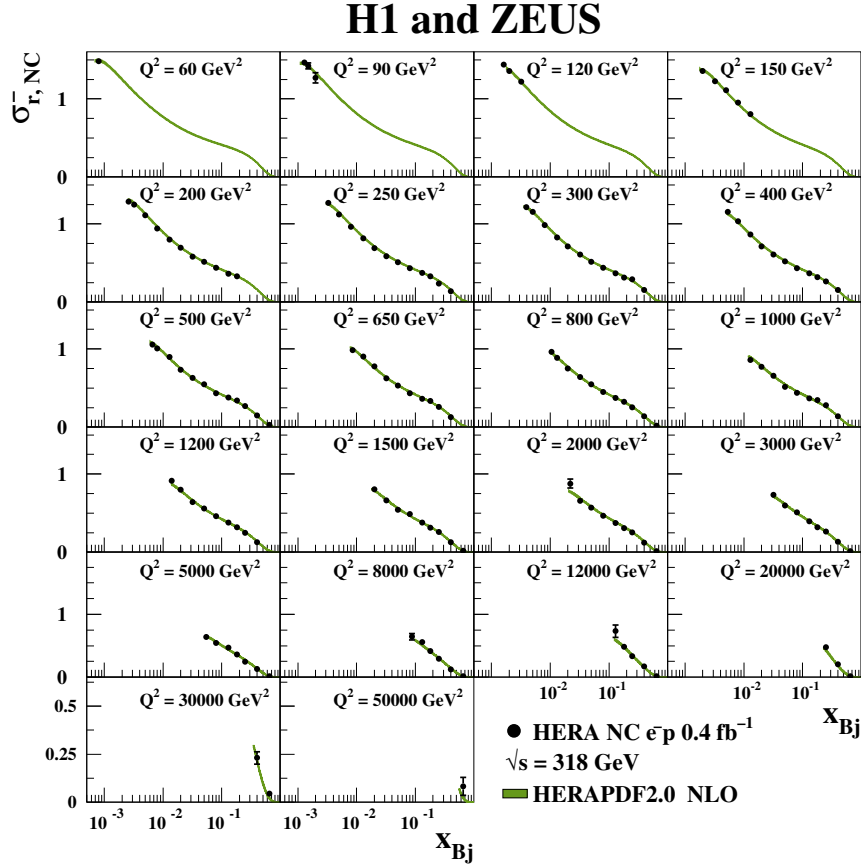
Figure 3.20: The combined HERA data for the inclusive NC e^-p reduced cross sections as a function of x_{Bj} for different values of Q^2 at $\sqrt{s_{com1}} = 318$ GeV with overlaid predictions of HERAPDF2.0 NLO [14]. The error bars represent the total uncertainties on data and bands represent the total uncertainties on predictions. The figure was taken from the HERAPDF2.0 paper [14].
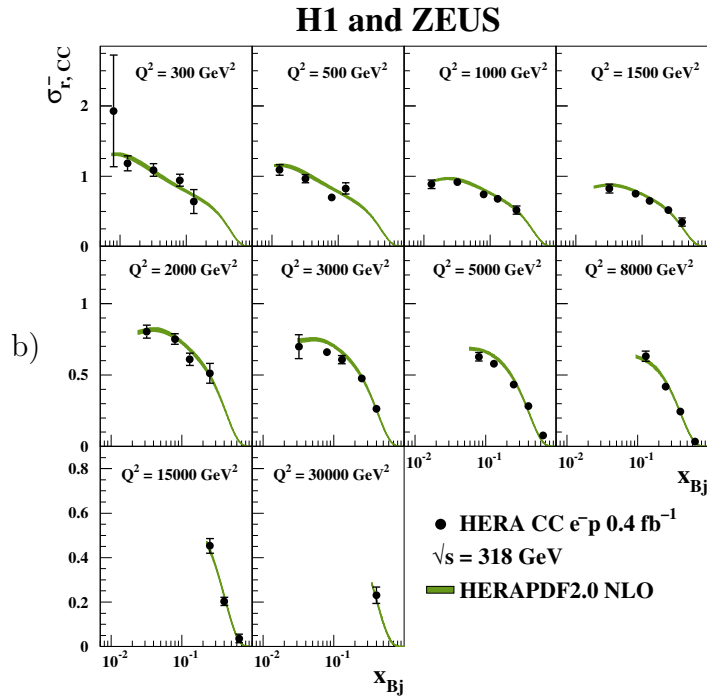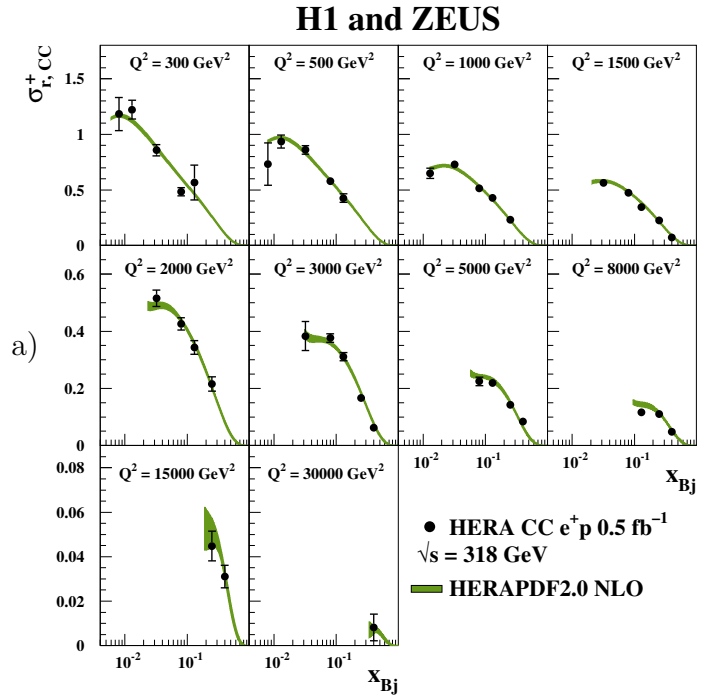
Figure 3.21: The combined HERA data for the inclusive CC e^+p (a) and e^-p (b) reduced cross sections as a function of x_{Bj} for different values of Q^2 at $\sqrt{s_{com\,1}} = 318$ GeV with overlaid predictions of HERAPDF2.0 NLO [14]. The error bars represent the total uncertainties on data and bands represent the total uncertainties on predictions. The figures were taken from the HERAPDF2.0 paper [14].
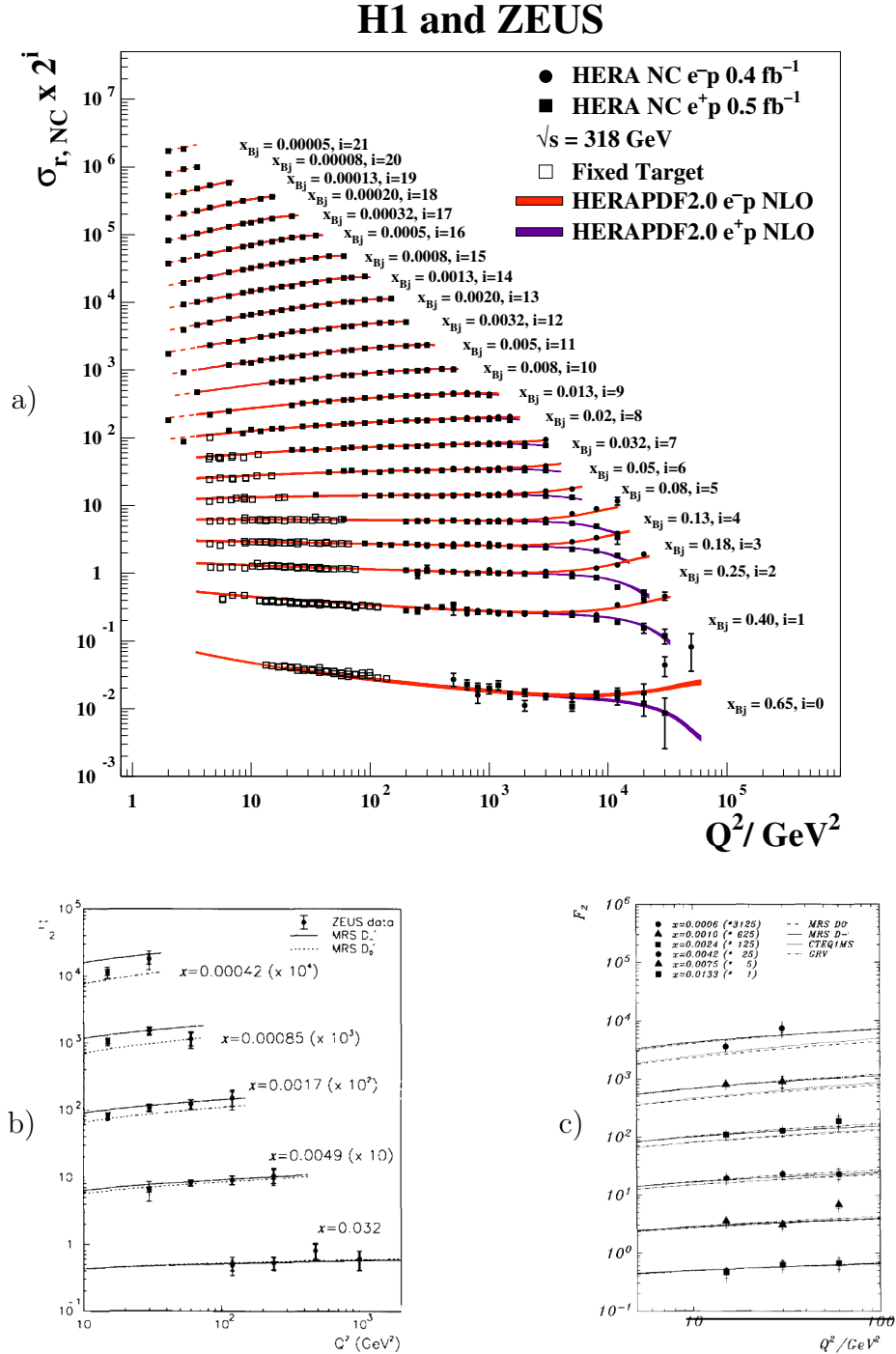
Figure 3.22: Figure a - the combined HERA data for the inclusive NC e^+p and e^-p reduced cross sections together with fixed-target data [104, 105] and the predictions of HERAPDF2.0 NLO [14]. The bands represent the total uncertainties on the predictions. The figure was taken from the HERAPDF2.0 paper [14]. Figures b and c - the structure function $\tilde{F}_2$ as a function of Q^2 for different values of x_{Bj} measured by ZEUS [106] and H1 [107] collaborations in 1992, respectively.
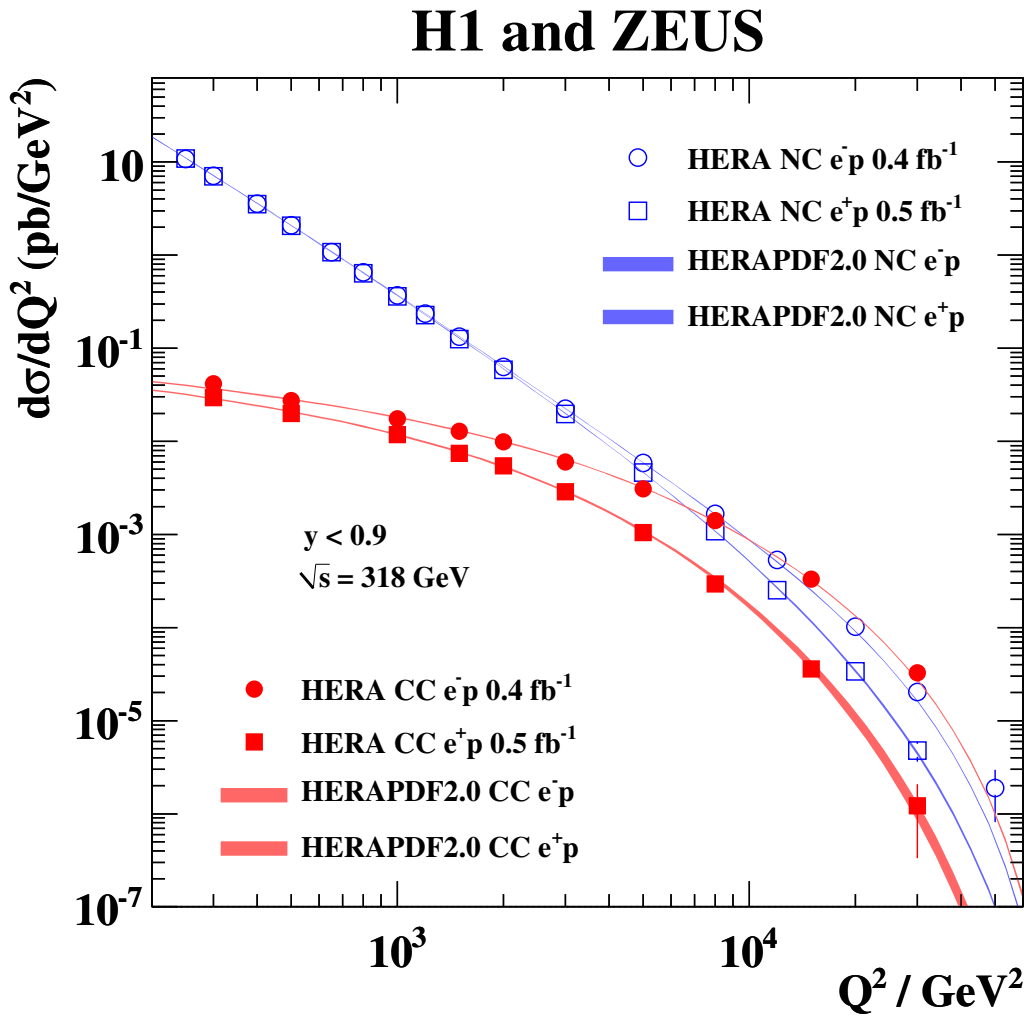
Figure 3.23: The combined HERA NC and CC e^+p and e^-p cross sections integrated over x_{Bj} for $y < 0.9$ together with predictions from HERAPDF2.0 NLO [14]. The bands represent the total uncertainty on the predictions. The figure was taken from the HERAPDF2.0 paper [14].
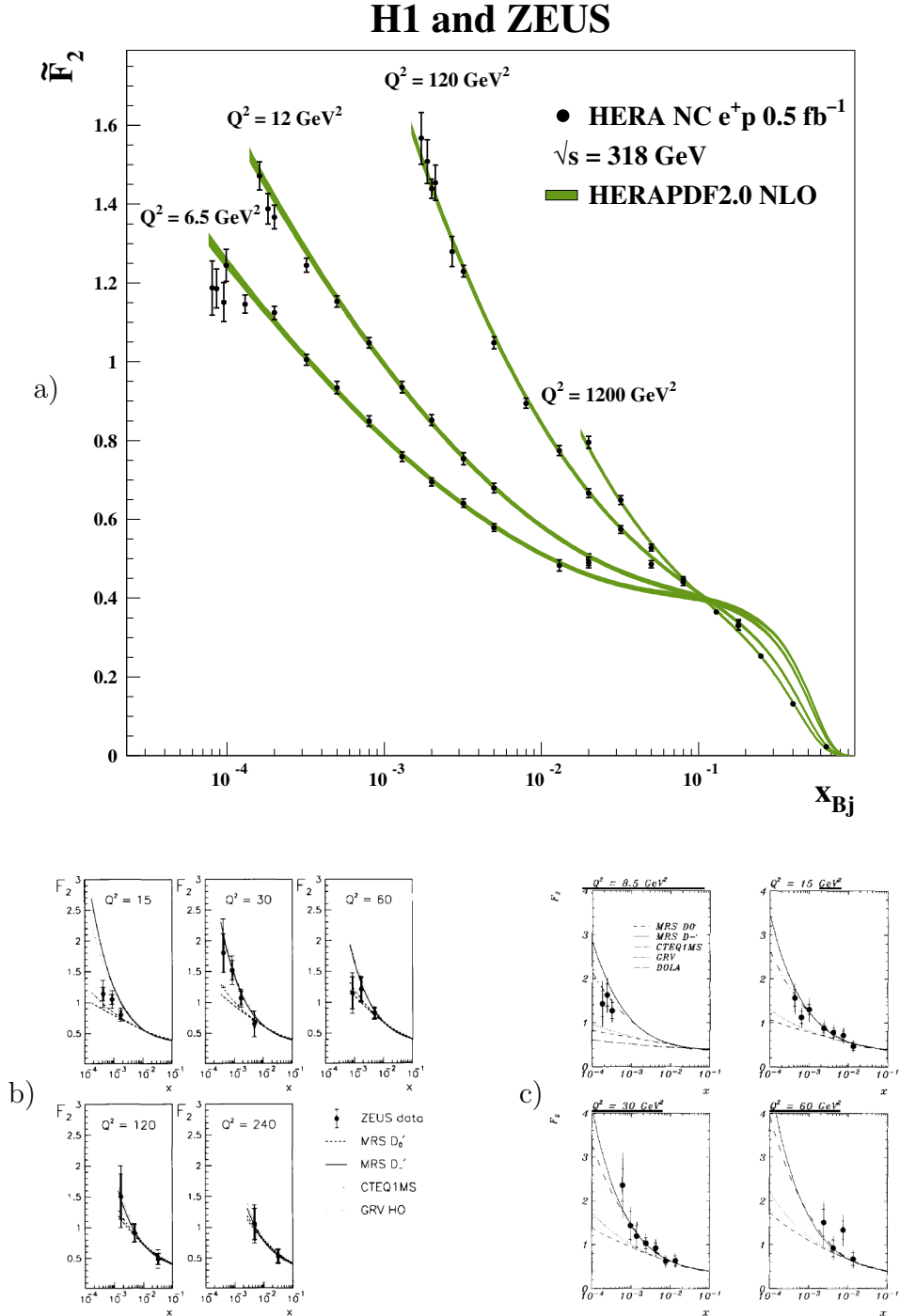
Figure 3.24: Figure a - the structure function $\tilde{F}_2$ as extracted from the measured reduced cross sections for four values of Q^2 together with predictions from HERAPDF2.0 NLO [14]. The bands represent the total uncertainty on the predictions. The figure was taken from the HERAPDF2.0 paper [14]. Figures b and c - the structure function $\tilde{F}_2$ as a function of x_{Bj} for different values of Q^2 measured by ZEUS [106] and H1 [107] collaborations in 1992, respectively.

Chapter 4

QCD analysis and determination of ZCIPDFs

This chapter describes the Standard Model perturbative QCD analysis within the DGLAP formalism used to determine the ZCIPDF parton distribution functions. The combined DIS data from HERA (see Chapter 3) has been used. The framework established for HERAPDF2.0 [14] has been followed with a few differences that are explained in detail in the following sections. This analysis resulted in the parton distribution functions ZCIPDF which were used for SM predictions in the Monte Carlo generation of replicas as presented in Section 5.1.3 and have been a basis for the BSM and the simultaneous PDFs+BSM fits described in Sections 5.1.1 and 5.2.1, respectively.

4.1 QCD fit settings

Predictions for the double-differential DIS cross sections were evaluated using the convolution of proton PDFs and perturbative QCD cross sections. PDFs at any scale μ_{f}^2 can be obtained by solving the DGLAP evolution equations but for this they need to be provided as functions of x at some starting scale, $\mu_{\mathrm{f}_0}^2$.

In the presented analysis, the factorisation and renormalisation scales were set to $\mu_{\mathrm{r}}^2 = \mu_{\mathrm{f}}^2 = Q^2$ and the starting scale was chosen to be $Q_0^2 = 1.9\,\mathrm{GeV}^2$. Perturbative QCD is expected to be applicable for $Q^2 > 1\,\mathrm{GeV}^2$ and to stay safely in this kinematic region, only cross sections starting from $Q_{\min}^2 = 3.5\,\mathrm{GeV}^2$ were used. This provided 1145 data point with $3.5 \leq Q^2 \leq 50000\,\mathrm{GeV}^2$ and $0.651 \times 10^{-4} \leq x_{\mathrm{Bj}} \leq 0.65$. Since the highest x_{Bj} in the data considered is 0.65, higher-twist corrections are expected to be negligible. Target-mass corrections are also expected to be negligible as the centre-of-mass energy at the γp-vertex is above $15\,\mathrm{GeV}$ for all kinematic region.

The cross-section predictions were calculated in the HERAFitter framework [96, 97] from structure functions (as shown in Eq. 1.11) that were obtained from PDFs convoluted

with quark coefficient functions. Next-to-leading-order (NLO) calculations in the $\overline{\text{MS}}$ renormalisation scheme were used for the DGLAP evolution and evaluation of quark coefficient functions within the QCDNUM [108] programme. The value of the strong coupling constant used was $\alpha_s(M_Z^2) = 0.118$ as for HERAPDF2.0 [14]. The charged-current cross sections start from $Q^2 = 300\,\text{GeV}^2$, which is much higher than the mass of the bottom quark[1] and thus coefficient functions for them were calculated in the zero-mass variable-flavour-number scheme (ZMVFNS). In the neutral-current structure function, the same scheme has been used for the light quarks while the coefficient functions for the heavy quarks were evaluated in the general-mass variable-flavour-number scheme (GMVFNS) RTOPT [26–28] developed by R. Thorne and R. Roberts. Mass parameters for the charm and beauty quarks were chosen to be the same as in the determination of NLO PDFs in the HERAPDF2.0 analysis [14], $M_c = 1.47\,\text{GeV}$ and $M_b = 4.5\,\text{GeV}$. In the GMVFNS scheme, M_c^2 and M_b^2 have to be higher than the starting scale; this condition is fulfilled with $Q_0^2 = 1.9\,\text{GeV}^2$.

4.2 Parameterisation

The PDF distributions of the proton were parameterised at the starting scale with the functional form of

$$xf(x) = Ax^B(1-x)^C(1 + Dx + Ex^2) \ , \tag{4.1}$$

where x corresponds to the fraction of the proton's momentum taken by the struck parton in the quark-parton model, parameter A represents the normalisation, B describes the shape for low values of x, C is responsible for $xf(x) \to 0$ at $x \to 1$ and the polynomial term in the end provides the additional freedom for the parametrisation.

Following the HERAPDF2.0 appoach, the parameterised PDFs were the gluon distribution, xg, the valence-quark distributions, xu_v, xd_v, and the u-type and d-type antiquark distributions, $x\bar{U} = x\bar{u}$, $x\bar{D} = x\bar{d} + x\bar{s}$:

$$xg(x) = A_g x^{B_g}(1-x)^{C_g} - A_g' x^{B_g'}(1-x)^{C_g'} \ , \tag{4.2}$$

$$xu_v(x) = A_{u_v} x^{B_{u_v}}(1-x)^{C_{u_v}}\left(1 + E_{u_v}x^2\right) \ , \tag{4.3}$$

$$xd_v(x) = A_{d_v} x^{B_{d_v}}(1-x)^{C_{d_v}} \ , \tag{4.4}$$

$$x\bar{U}(x) = A_{\bar{U}} x^{B_{\bar{U}}}(1-x)^{C_{\bar{U}}}\left(1 + D_{\bar{U}}x\right) \ , \tag{4.5}$$

$$x\bar{D}(x) = A_{\bar{D}} x^{B_{\bar{D}}}(1-x)^{C_{\bar{D}}} \ . \tag{4.6}$$

An addition term $A_g' x^{B_g'}(1-x)^{C_g'}$ was subtracted from the gluon distribution, xg, with C_g' fixed to $C_g' = 25$ [14, 109], to make it more flexible at low x, such that it is not controlled by the single power B_g as x approaches zero. This produces a requirement on parameters

---

[1]Since the mass of the top quark is high in comparison to the Q^2 range of the HERA data its contribution is expected to be negligible.

B_g and B'_g to be different which was not set during the fit procedure but was checked in the results. The parameters A_{u_v}, A_{d_v}, A_g were constrained by the quark number- (Eq. 4.7) and momentum-sum rules (Eq. 4.8):

$$\int\limits_0^1 u_v(x)dx = 2 \quad , \quad \int\limits_0^1 d_v(x)dx = 1 \tag{4.7}$$

and

$$\int\limits_0^1 \left[\sum_i (q_i(x) + \bar{q}_i(x)) + g(x) \right] x dx = 1 \quad . \tag{4.8}$$

The strange-quark distribution is expressed as an x-independent fraction, f_s, of the d-type sea, $x\bar{s} = f_s x\bar{D}$ with $f_s = 0.4$ [14] at the starting scale Q_0^2. To ensure the SU(2) symmetry at $x \to 0$, the $A_{\bar{U}}$ was set to $A_{\bar{U}} = A_{\bar{D}}(1 - f_s)$ and the $B_{\bar{U}}$ and $B_{\bar{D}}$ were set as equal, $B_{\bar{U}} = B_{\bar{D}}$. With all these constraints, 14 parameters were left as free in the fit.

4.3 Definition of the least-squares function

The PDF distributions for the optimal description of data can be estimated using the method of least squares [20, 110]. For this, a χ^2 function which depends on the PDF parameters $\boldsymbol{p}$ should be built such that its minimum would define the least-squares estimators $\widehat{\boldsymbol{p}}$. In the ZCIPDF fit, the measured inclusive DIS cross-section values μ_0^i (where i denotes the data point index) were assumed to have a Gaussian distribution of statistical, uncorrelated and systematic uncertainties and the following χ^2 formula was used:

$$\chi^2(\boldsymbol{m}, \boldsymbol{s}) = \sum_i \frac{\left[m^i + \sum_j \gamma_j^i m^i s_j - \mu_0^i \right]^2}{\left(\delta_{i,\text{stat}}^2 + \delta_{i,\text{uncor}}^2 \right) (\mu_0^i)^2} + \sum_j s_j^2 \quad . \tag{4.9}$$

There γ_j^i, $\delta_{i,\text{stat}}$ and $\delta_{i,\text{uncor}}$ are the relative correlated systematic, relative statistical and relative uncorrelated systematic uncertainties of the input data, respectively. The vector $\boldsymbol{m}$ represents the set of pQCD cross-section predictions m^i which depends on the PDF parameters $\boldsymbol{p}$ at the starting scale, and the components s_j of the vector $\boldsymbol{s}$ represent the correlated systematic shifts of the cross sections in units of the relative correlated systematic uncertainties γ_j^i. The summations extend over all data points i and all correlated systematic uncertainties j.

The definition of χ^2 for the ZCIPDF fit differs from the one used for the HERA-PDF2.0 [14] study due to different assumptions on the uncertainty distributions. Despite the large statistical uncertainties on some high-Q^2 data points, it was verified that changing to the Poisson statistic for them does not change the result of PDF or BSM fits

significantly (for details see Section 5.3). This, together with the fact that information required for analysis with Poisson statistics cannot be used after the data combination, motivated the change of the χ^2 function.

4.4   Result of the ZCIPDF fit

The parameters of the ZCIPDF fit are presented in Table 4.1 and correlations between them in Table 4.2. The global correlation coefficients ρ_i were evaluated in accordance with James' statistical methods [110] using the correlation matrix V as

$$\rho_i = \sqrt{1 - \frac{1}{V_{ii} \cdot (V^{-1})_{ii}}} \quad , \tag{4.10}$$

where $V_{ii} \equiv 1$ and $(V^{-1})_{ii}$ are diagonal elements of the correlation matrix and its inverse, respectively. The gluon, valence quarks and sea distributions at the scale of $Q^2 = 10 \, \text{GeV}^2$ are presented and compared to the distributions of HERAPDF2.0 in Fig. 4.1, which was also used as addition material for the quark-radius paper [111]. Despite the difference in the definition of the χ^2 function, the PDFs show very good agreement.

	A	B	C	D	E	A'	B'	C'
xg	5.03	0.0270	8.47			0.600	-0.178	25
xu_v	4.01	0.709	4.95		14.7			
xd_v	3.40	0.830	4.15					
$x\bar{U}$	0.107	-0.170	8.03	11.3				
$x\bar{D}$	0.179	-0.170	5.74					

Table 4.1: Central values of the ZCIPDF parameters.

The minimum value of the χ^2, χ^2_{min}, together with information on the number of degrees of freedom, ndf, which is equal to the number of measurements minus the number of fitted parameters, provides a useful test of the goodness-of-fit [20]. For the ZCIPDF fit, $\chi^2/ndf = 1361.62/1131 = 1.20$, which is close to the value of $\chi^2/ndf = 1357/1131$ obtained in the HERAPDF2.0 analysis and shows that the data is reasonably described by the fit predictions. The χ^2 values for the individual datasets of the combined HERA data are summarised in Table 4.3 and for different ranges of Q^2 in Table 4.4. These values do not include the correlated part of the χ^2, χ^2_{corr}, which corresponds to the second sum in Eq. 4.9. In ZCIPDF fit it was $\chi^2_{corr} = 85.5$.

In order to quantify the results of the fit and size of the shifts of 169 correlated systematic uncertainties, pull variables were introduced in the same way as for the combination
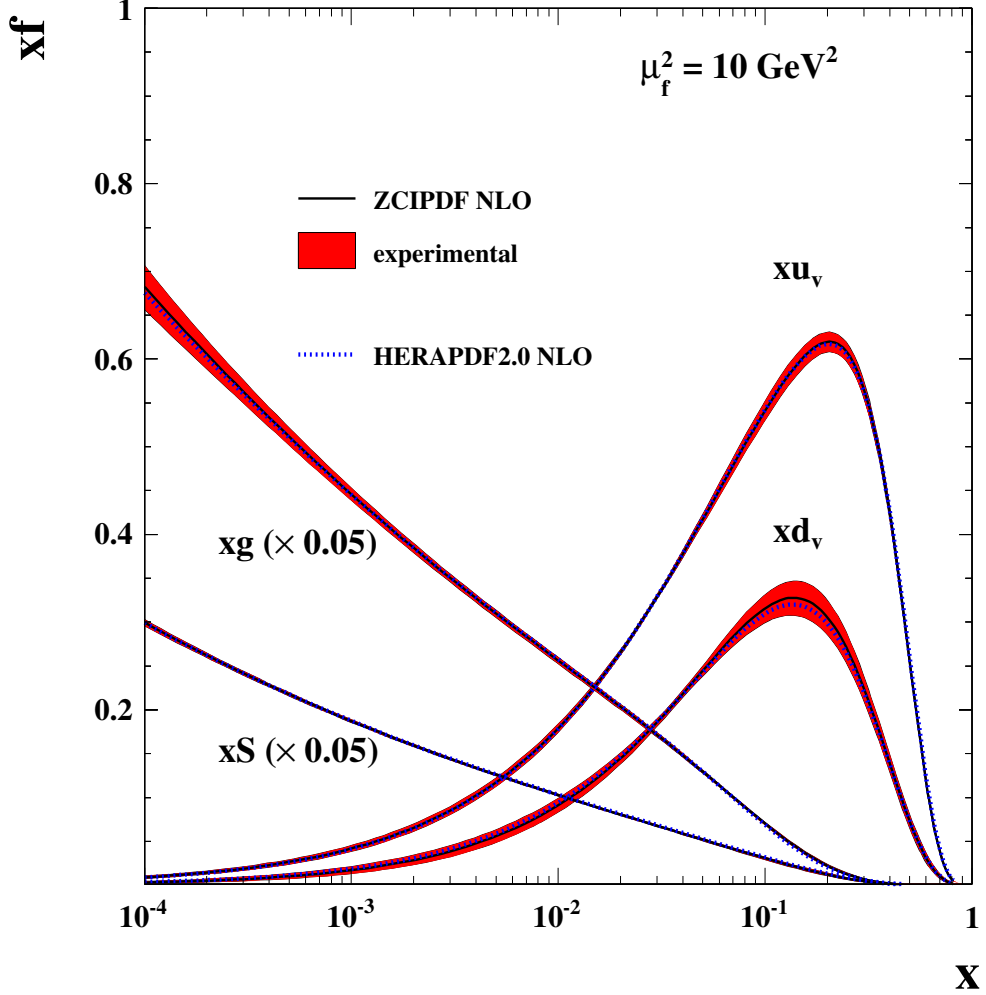
Figure 4.1: The PDF set ZCIPDF with experimental uncertainty at the factorisation scale $\mu_f^2 = Q^2 = 10\,\mathrm{GeV}^2$. Also shown are the central values of HERAPDF2.0 NLO. A similar plot has been used as addition material for the quark-radius paper [111].

of HERA data, according to Eq. 3.13[2] and Eq. 3.12. Distributions of the pulls of the data $p^{i,1}$ are displayed in Fig. 4.2. The root-mean-square values, RMS, of these distributions are close to unity, showing that the data is well described by the ZCIPDF predictions. The pulls of the systematic uncertainties p_j are presented in Fig. 4.3. Their distribution

---

[2]The cross section and uncorrelated uncertainty of the combined data points in Eq. 3.13 were replaced with the prediction of the fit and its experimental uncertainty. Data used in the fit has only one cross-section value at any (Q^2,x) grid point for each process and thus $k = 1$.
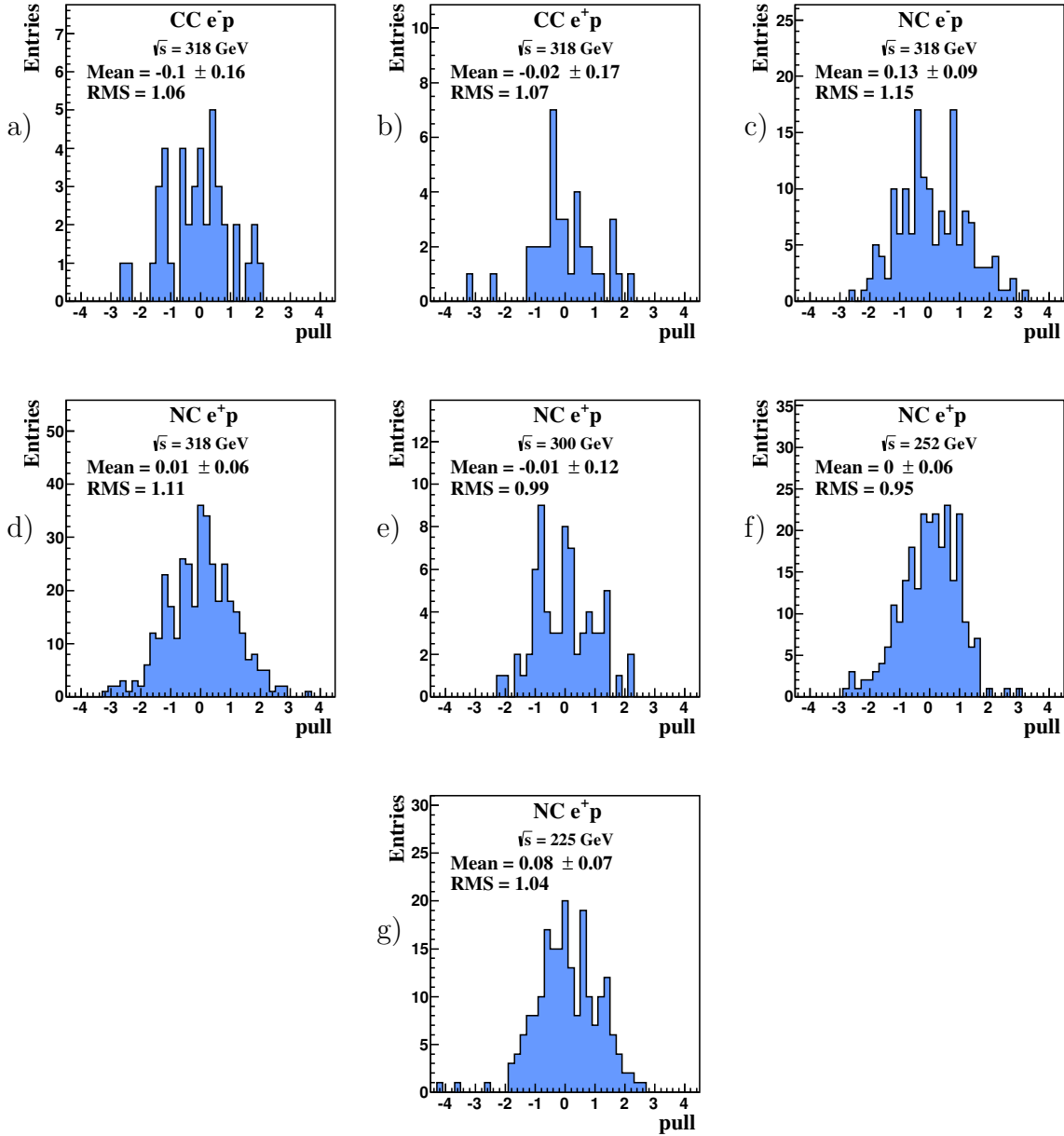
Figure 4.2: Distributions of pulls $p^{i,1}$ from ZCIPDF fit for: a) CC e^-p for $\sqrt{s} = 318$ GeV; b) CC e^+p for $\sqrt{s} = 318$ GeV; c) NC e^-p for $\sqrt{s} = 318$ GeV; d) NC e^+p for $\sqrt{s} = 318$ GeV; e) NC e^+p for $\sqrt{s} = 300$ GeV; f) NC e^+p for $\sqrt{s} = 252$ GeV; and g) NC e^+p for $\sqrt{s} = 225$ GeV. There are no entries outside the histogram ranges. The root mean square, RMS, of each distribution is given.

has a RMS of 1.64, which might indicate that some of the systematic uncertainties in the data were underestimated or may be partially correlated.
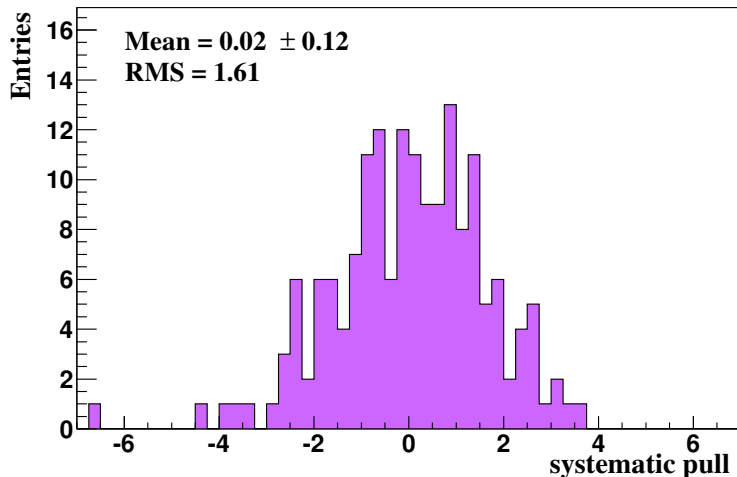
Figure 4.3: Distribution of pulls p_j from the ZCIPDF fit for the correlated systematic uncertainties including global normalisations and procedural uncertainties. There are no entries outside the histogram range. The root mean square, RMS, of the distribution is given.

The predictions of the ZCIPDF fit are compared to the high-Q^2 HERA inclusive NC e^+p and e^-p reduced cross sections in Fig. 4.4 and Fig. 4.5, respectively. In both cases the data are well described by the predictions.

4.5 Uncertainties on ZCIPDFs

The experimental uncertainties of the ZCIPDF were estimated using the Hessian method [112] on fitted parameters with the criterion $\Delta\chi^2 = 1$.

The uncertainties due to the choice of model parameters were evaluated by varying the minimum value of Q^2 in the data, $Q^2_{\min}$, the mass parameters of the charm and beauty quarks M_c and M_b, the strangeness fraction f_s and the strong coupling $\alpha_s(M_Z^2)$. All of these variations, except for $\alpha_s(M_Z^2)$, are taken to be the same as for the model uncertainty on the NLO fit of HERAPDF2.0 [14]. The strong coupling constant, $\alpha_s(M_Z^2)$, was varied within its full uncertainty, including the scale uncertainty, as determined in the HERAPDF2.0 analysis. The differences between the central distributions of the PDFs and the distributions corresponding to the variations were added in quadrature, separately for positive and negative deviations.
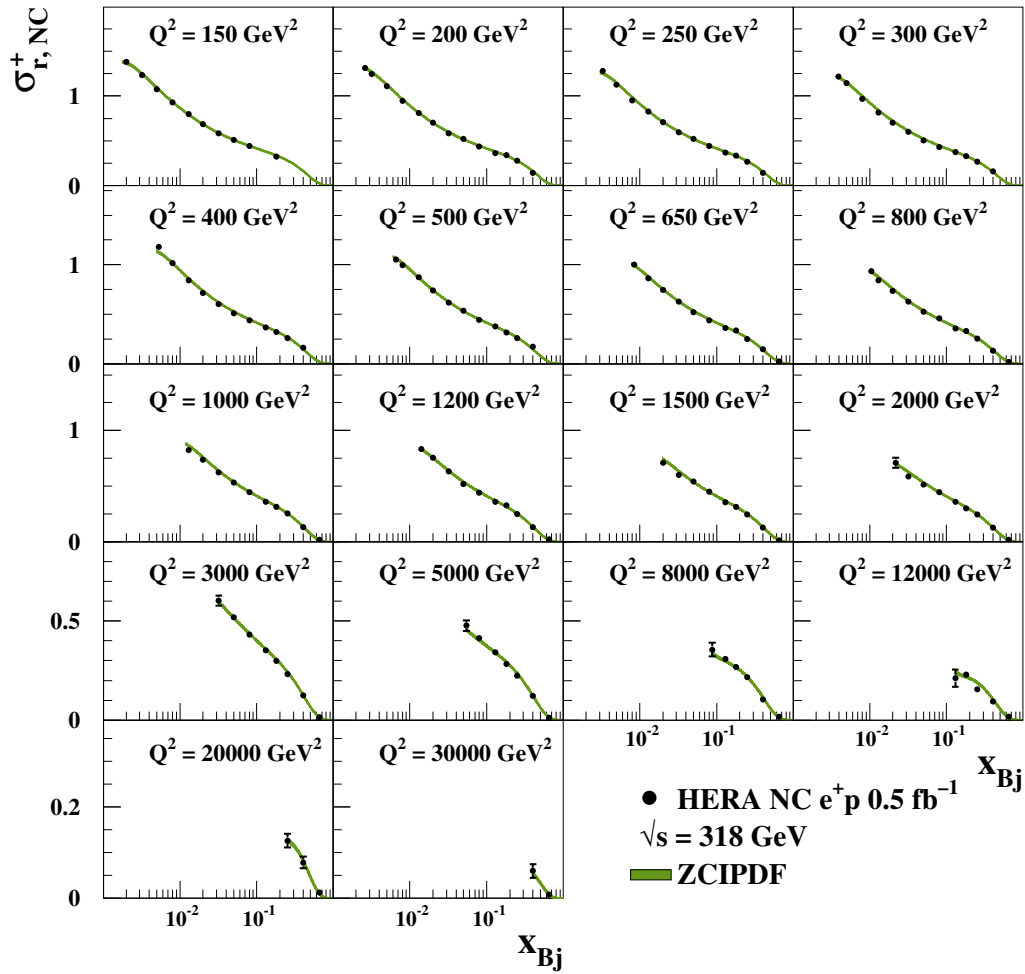
Figure 4.4: The predictions of the ZCIPDF fit compared to part of the combined HERA inclusive NC e^+p reduced cross sections with $Q^2 \geq 150\,\mathrm{GeV}^2$. The bands represent the experimental uncertainties on the predictions.
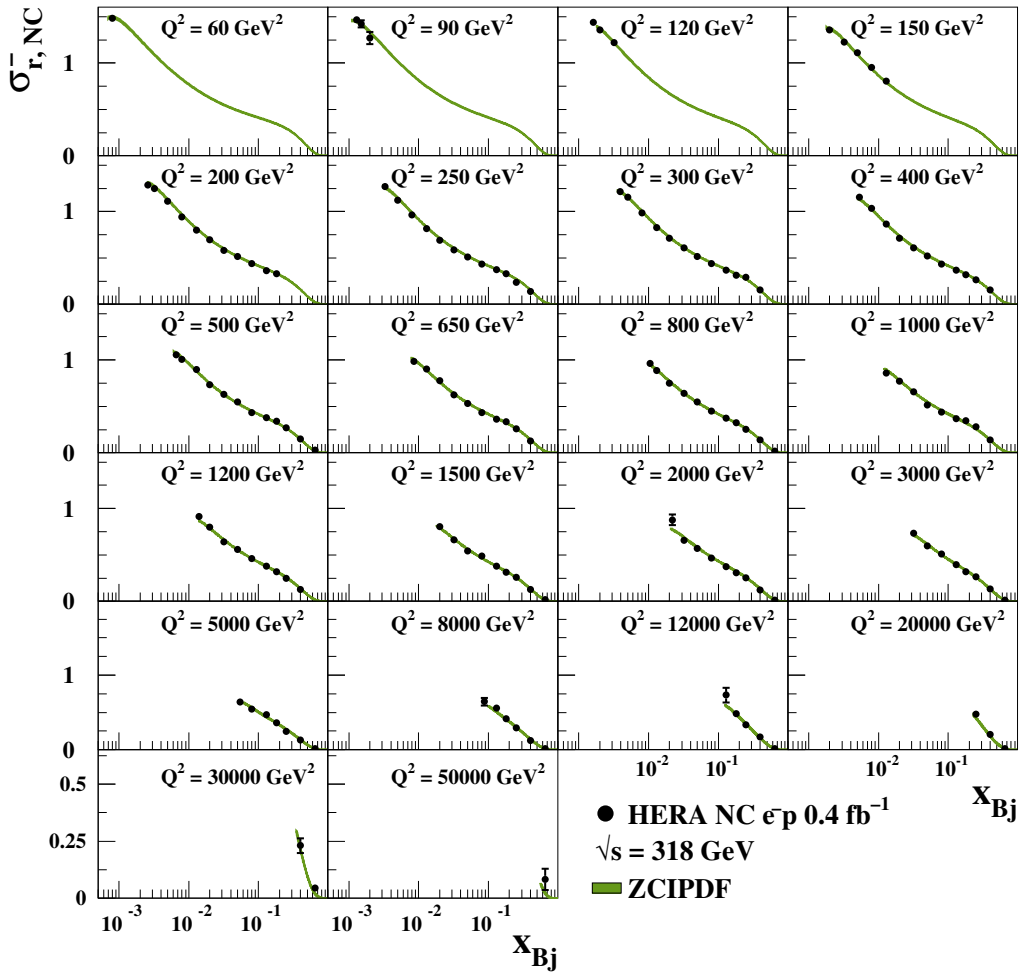
Figure 4.5: The predictions of the ZCIPDF fit compared to part of the combined HERA inclusive NC e^-p reduced cross sections with $Q^2 \geq 60\,\mathrm{GeV}^2$. The bands represent the experimental uncertainties on the predictions.
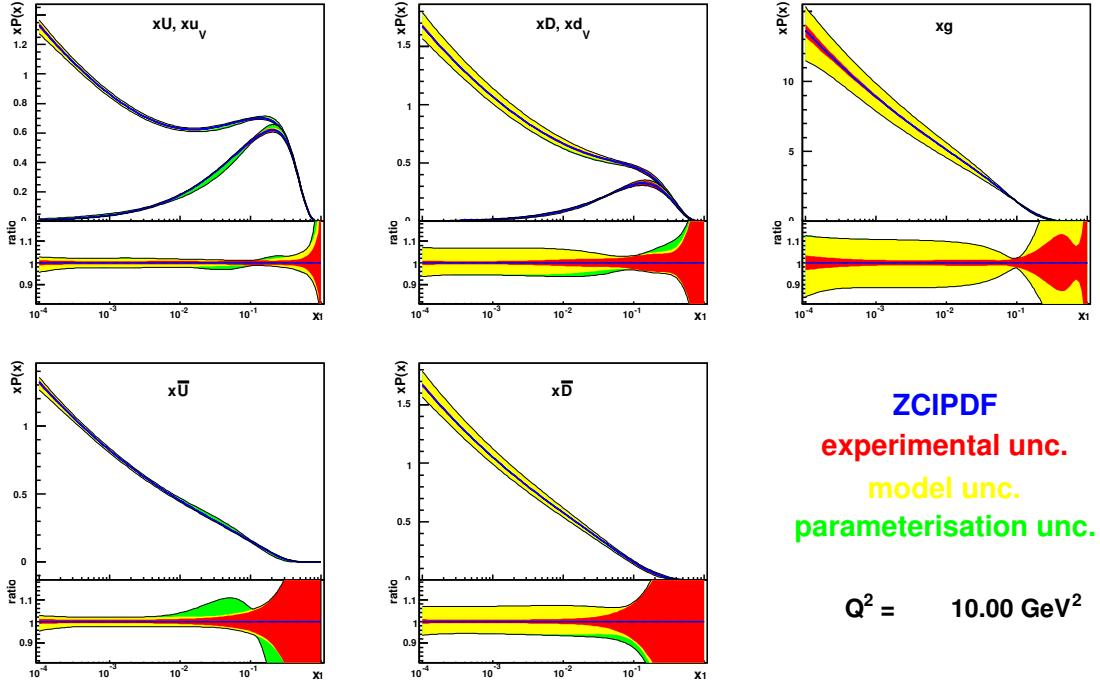
Figure 4.6: The parton distribution functions xU, xu_v, xD, xd_v, xg, $x\bar{U}$ and $x\bar{D}$ of ZCIPDF at $Q^2 = 10\,\mathrm{GeV}^2$ with the experimental, model and parameterisation uncertainties. The plots have been generated using the DrawResults package of the HERAFitter framework.

To evaluate the uncertainties due to the choice of parameterisation, the variation of the starting scale Q_0^2 and fits with an additional D or E parameter in every parameterised PDF were made. The only significant difference from the central fit among the fits with an additional parameter was in the D_{u_v} parameter. The final parameterisation uncertainty of the fit was taken to be the largest difference of these fits from the central value.

The total uncertainty on ZCIPDF was obtained by adding the experimental, model and parameterisation uncertainties in quadrature. Evaluation and representation of these uncertainties have been implemented in the DrawResults and DrawPdfs packages of the HERAFitter framework [96, 97]. Fig. 4.6 was obtained with DrawResults and shows the ZCIPDF with uncertainties at the scale of $Q_0^2 = 10\,\mathrm{GeV}^2$. The ZCIPDF fit has significantly larger model uncertainty of the gluon distribution than HERAPDF2.0 due to the variations of the strong coupling $\alpha_s(M_Z^2)$.

Param	Global	B_g	C_g	A'_g	B'_g	B_{u_v}	C_{u_v}	E_{u_v}	B_{d_v}	C_{d_v}	$C_{\bar{U}}$	$D_{\bar{U}}$	$A_{\bar{D}}$	$B_{\bar{D}}$	$C_{\bar{D}}$
B_g	0.99	1	0.36	-0.48	0.43	0.057	-0.012	-0.051	0.034	0.033	-0.021	-0.006	-0.047	-0.066	0.008
C_g	0.99	0.36	1	0.32	0.40	0.086	-0.081	-0.099	-0.10	-0.075	0.18	0.42	-0.22	-0.26	-0.40
A'_g	0.99	-0.48	0.32	1	0.50	0.12	-0.051	-0.12	0.044	0.055	-0.05	-0.007	-0.03	-0.037	-0.054
B'_g	0.99	0.43	0.40	0.50	1	0.092	-0.025	-0.088	0.064	0.068	-0.11	-0.17	0.16	0.18	0.027
B_{u_v}	0.99	0.057	0.086	0.12	0.092	1	0.13	-0.66	0.23	0.10	0.39	-0.099	0.26	0.19	0.21
C_{u_v}	0.97	-0.012	-0.081	-0.051	-0.025	0.13	1	0.58	-0.088	-0.22	0.38	0.22	0.072	0.071	0.037
E_{u_v}	0.99	-0.051	-0.099	-0.12	-0.088	-0.66	0.58	1	-0.14	-0.11	0.12	0.38	-0.10	-0.062	-0.038
B_{d_v}	0.99	0.034	-0.10	0.044	0.064	0.23	-0.088	-0.14	1	0.83	0.24	0.054	0.13	0.092	0.53
C_{d_v}	0.97	0.033	-0.075	0.055	0.068	0.10	-0.22	-0.11	0.83	1	0.088	-0.064	0.056	0.028	0.23
$C_{\bar{U}}$	0.99	-0.021	0.18	-0.05	-0.11	0.39	0.38	0.12	0.24	0.088	1	0.64	0.037	0.043	-0.11
$D_{\bar{U}}$	0.99	-0.006	0.42	-0.007	-0.17	-0.099	0.22	0.38	0.054	-0.064	0.64	1	-0.44	-0.42	-0.021
$A_{\bar{D}}$	0.96	-0.047	-0.22	-0.03	0.16	0.26	0.072	-0.10	0.13	0.056	0.037	-0.44	1	0.95	0.20
$B_{\bar{D}}$	0.97	-0.066	-0.26	-0.037	0.18	0.19	0.071	-0.062	0.092	0.028	0.043	-0.42	0.95	1	0.17
$C_{\bar{D}}$	0.99	0.008	-0.40	-0.054	0.027	0.21	0.037	-0.038	0.53	0.23	-0.11	-0.021	0.20	0.17	1

Table 4.2: The correlation matrix of PDF parameters of the ZCIPDF fit and global correlation coefficients defined in Eq. 4.10.

Dataset	χ^2/ N_{data}
CC e^-p 318 GeV	47.3 / 42
CC e^+p 318 GeV	44.6 / 39
NC e^-p 318 GeV	211.4 / 159
NC e^+p 318 GeV	453.3 / 377
NC e^+p 300 GeV	67.8 / 70
NC e^+p 252 GeV	229.6 / 254
NC e^+p 225 GeV	222.1 / 204

Table 4.3: The χ^2 values of ZCIPDF fit for the individual datasets of the combined HERA data.

Dataset	χ^2/ N_{data}
$3.5 \leq Q^2 < 10\,\mathrm{GeV}^2$	162.2 / 129
$10 \leq Q^2 < 100\,\mathrm{GeV}^2$	350.4 / 356
$100 \leq Q^2 < 1000\,\mathrm{GeV}^2$	514.6 / 441
$1000 \leq Q^2 < 10000\,\mathrm{GeV}^2$	216.0 / 185
$10000 \leq Q^2 \leq 50000\,\mathrm{GeV}^2$	32.9 / 34

Table 4.4: The χ^2 values of ZCIPDF fit for five different regions in Q^2.

Variation	Standard Value	Lower Limit	Upper Limit
$Q^2_{\min}$ [GeV^2]	3.5	2.5	5.0
M_c [GeV]	1.47	1.41	1.53
M_b [GeV]	4.5	4.25	4.75
f_s	0.4	0.3	0.5
$\alpha_s(M_Z^2)$	0.118	0.1146	0.122
Q_0^2 [GeV^2]	1.9	1.6	2.2

Table 4.5: Input parameters for ZCIPDF fit and the variations considered to evaluate model and parameterisation (Q_0^2) uncertainties.

Chapter 5

Beyond-the-Standard-Model analysis

The ZCIPDF fit, as well as HERAPDF2.0, have shown a reasonable description of the inclusive DIS data with $\chi^2/ndf = 1.2$. This leaves a small parameter space for possible scenarios of physics beyond the Standard Model and motivates the determination of exclusion limits on them. This chapter describes the least squares and frequentist approaches of setting such limits. Both approaches were used for two different methods of contact interactions analysis - separate and combined with parton-density-functions fits.

5.1 Beyond-the-Standard-Model analysis with fixed PDFs

Beyond-the-Standard-Model scenarios described in Section 1.4 are expected to modify the cross-section predictions for $Q^2 \geq 10000 \, \text{GeV}^2$, while PDFs are mostly constrained by data with lower values of Q^2. Thus, for a first check, PDF parameters may be fixed to the values obtained in ZCIPDF fit.

5.1.1 BSM fits with fixed PDFs

Each considered BSM model was parameterised with one parameter η in the units of GeV^{-2} as shown in Section 1.4. The parameter η was included as an additional fit parameter to the private modification of the HERAFitter framework [96, 97] and the predictions on the cross-section values were modified with

$$\sigma_{\text{NLO}}^{\text{SM+CI}} = \sigma_{\text{NLO}}^{\text{SM}} \times \frac{\sigma_{\text{LO EW}}^{\text{SM+CI}}}{\sigma_{\text{LO EW}}^{\text{SM}}} \quad . \tag{5.1}$$

There $\sigma_{\text{NLO}}^{\text{SM+CI}}$ is the resulting cross-section value at NLO, $\sigma_{\text{NLO}}^{\text{SM}}$ is the cross-section prediction without BSM at NLO, $\sigma_{\text{LO EW}}^{\text{SM+CI}}$ and $\sigma_{\text{LO EW}}^{\text{SM}}$ are cross sections calculated with

and without BSM modification in leading order of the electroweak theory [29]. The BSM parameters fitted to the data with PDFs fixed to the ZCIPDF are denoted as $\eta_{\text{CI-only}}^{\text{Data}}$. For example, in the effective quark-radius model, $\eta = R_{\text{q}}^2$ and the value of $\eta_{\text{CI-only}}^{\text{Data}} \equiv R_{\text{q CI-only}}^{2 \text{ Data}} = -0.35 \times 10^{-6} \, \text{GeV}^{-2}$ was obtained.

5.1.2   Limits setting with the least-squares method

The method of least squares can be used not only for the estimation of model parameters, but also for the evaluation of limits on these parameters within a certain confidence level, C.L. The limits on the parameter η can be derived from the dependence of the χ^2 value on this parameter. For this, the value of η is varied near its estimator $\eta_{\text{CI-only}}^{\text{Data}}$ and for each of these variations η_i^{True}, the value of η is fixed to η_i^{True} and a fit of the shifts of systematic uncertainties is performed resulting in some value of $\chi_i^2 = \chi^2(\eta_i^{\text{True}})$. In the case of linear dependence of the cross sections on η, the distribution of $\chi^2(\eta^{\text{True}})$ is expected to have the form of a second-order polynomial with the minima $\chi_{\text{min}}^2 = \chi^2(\eta_{\text{CI-only}}^{\text{Data}})$. Values of η_j with $\chi^2(\eta_j) - \chi_{\text{min}}^2 > 2.71$ are excluded at 95% C.L. [20].

As an example, a distribution of χ^2 for different values of $R_{\text{q}}^{2 \text{ True}}$ with PDFs fixed to ZCIPDF is presented in Fig. 5.1. The 95% C.L. limits on R_{q}^2 estimated with this distribution are:

$$-4.74 \times 10^{-6} \, \text{GeV}^{-2} < R_{\text{q}}^2 < 4.07 \times 10^{-6} \, \text{GeV}^{-2} \quad . \tag{5.2}$$

They are represented with dashed lines in Fig. 5.1.

Some contact interaction models have nonlinear dependence of the cross-section predictions on the η parameter, which leads to a different shape of the $\chi^2(\eta^{\text{True}})$ distribution, sometimes with more than one minimum. This was the case for the VA model of general contact interactions, as presented in Fig. 5.2. For such BSM models, no meaningful limits can be evaluated with the least-squares method and an alternative method must be used.

5.1.3   Limits setting with the technique of Monte Carlo replicas

The method of least squares described in the previous section provides a fast calculation of the exclusion limits on the BSM models but due to the limitations described there cannot be used for all of the considered models. Thus a more time-consuming but universal frequentist approach [113] based on fits to large sets of Monte Carlo replicas was chosen as the main method for this analysis.

Monte Carlo (MC) replicas are sets of cross-section values in the same (Q^2, x) grid as data, generated by randomly varying cross-section predictions according to the data uncertainties. A set of replicas was created for some assumed true value of the contact interactions parameter, η^{True}. The reduced-cross-section predictions calculated from the ZCIPDF were scaled according to Eq. 5.1, resulting in a set of cross-section values m_0^i,
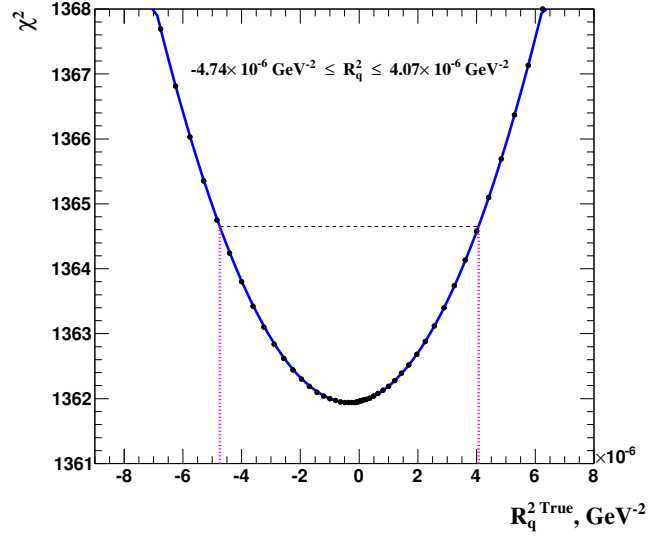
Figure 5.1: χ^2 as a function of $R_q^{2 \text{ True}}$ in the procedure with PDFs fixed to ZCIPDF. The interval of R_q^2 and dashed lines represent the limits for 95% C.L.
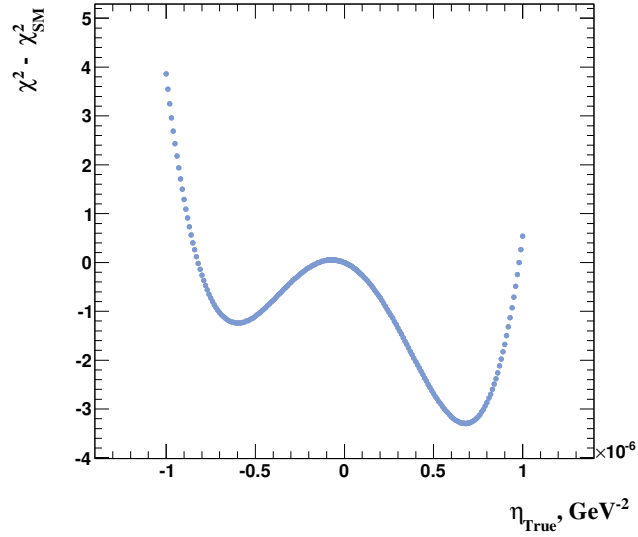
Figure 5.2: χ^2 as a function of η^{True} for the VA model of contact interactions.

where i denotes the index of the point in the (Q^2, x) grid. Next, the values of m_0^i were varied randomly within statistical and systematic uncertainties taken from the data, assuming that they follow a Gaussian distribution and taking into account the correlations of systematic uncertainties:

$$\mu^i = \left[m_0^i + \sqrt{\delta_{i,\text{stat}}^2 + \delta_{i,\text{uncor}}^2} \cdot \mu_0^i \cdot r_i \right] \cdot \left(1 + \sum_j \gamma_j^i \cdot r_j \right) \quad . \tag{5.3}$$

There, μ^i is the resulting cross-section replica, μ_0^i, $\delta_{i,\text{stat}}^2$, $\delta_{i,\text{uncor}}^2$ and γ_j^i are the same data cross section, relative statistical, uncorrelated and correlated systematic uncertainties as in Eq. 4.9, respectively, and r_i and r_j represent random numbers taken from a normal distribution.

Up to 5000 sets of replicas μ^i were generated for each value of η^{True} and used for a QCD fit with PDFs fixed to ZCIPDF and η and shifts of systematic uncertainties as free parameters, resulting in a distribution of fitted values η^{Fit}. The value of $\eta_{\text{CI−only}}^{\text{Data}}$ was taken as a test statistic, to which the values of η^{Fit} were compared and probability P to obtain $\eta^{\text{Fit}} < \eta_{\text{CI−only}}^{\text{Data}}$ (for a limit in a positive direction) or $\eta^{\text{Fit}} > \eta_{\text{CI−only}}^{\text{Data}}$ (for a limit in the negative direction) was evaluated. As an example, a distribution of values $R_q^{2\,\text{Fit}}$ fitted to MC replicas with $R_q^{2\,\text{True}} = 6 \times 10^{-6}\,\text{GeV}^{-2}$ are compared to $R_{\text{q CI−only}}^{2\,\text{Data}}$ in Fig. 5.3. The probability to obtain $R_q^{2\,\text{Fit}} < R_{\text{q CI−only}}^{2\,\text{Data}}$ for this distribution is $P(R_q^{2\,\text{Fit}} < R_{\text{q}}^{2\,\text{Data}}) = 0.96\%$.
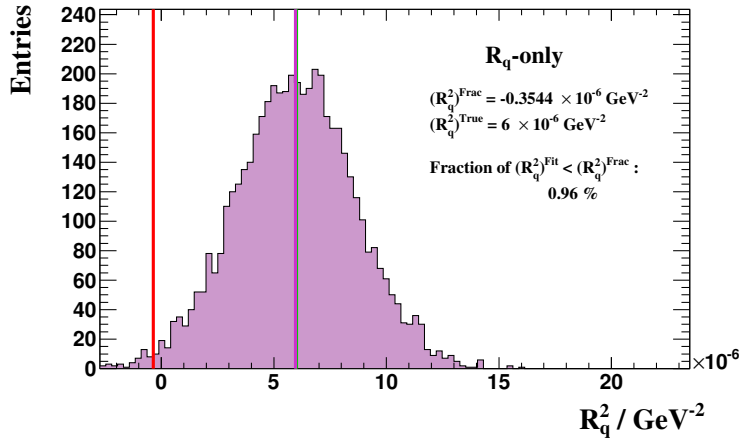
Figure 5.3: A distribution of $R_q^{2\,\text{Fit}}$ fitted to the Monte Carlo replicas with $R_q^{2\,\text{True}} = 6 \times 10^{-6}\,\text{GeV}^{-2}$ in the procedure with PDFs fixed to ZCIPDF [2]. Vertical lines represent (from left to right) $R_{\text{q CI−only}}^{2\,\text{Data}}$, the mean of the distribution and $R_q^{2\,\text{True}}$ (the last two overlap since the mean value is very close to the $R_q^{2\,\text{True}}$).

The procedure was repeated for different values of η^{True}, providing the values of probability $P(\eta^{\text{Fit}} < \eta^{\text{Data}})$. The probability $P(R_q^{2\,\text{Fit}} < R_q^{2\,\text{Data}})$ as a function of $R_q^{2\,\text{True}}$ obtained in the analysis of quark radius [111] is displayed in Fig. 5.4.

ZEUS
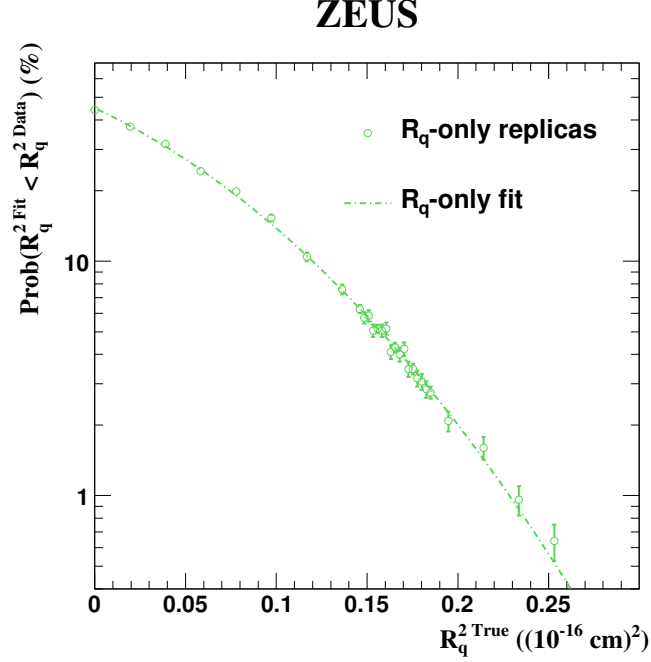
Figure 5.4: The probability of obtaining $R_q^{2\,\text{Fit}}$ values smaller than that obtained for the actual data, $R_q^{2\,Data}$, calculated from Monte Carlo replicas with PDF parameters fixed to the ZCIPDF values, as a function of the assumed value for the quark-radius squared, $R_q^{2\,True}$. Points with statistical error bars represent Monte Carlo replica sets generated for different values of $R_q^{2\,True}$.

The values of probability in the region of $0.025 \leq P \leq 0.1$ were fitted with

$$f(x) = 0.05 \cdot exp((x - A) \cdot B) \quad , \tag{5.4}$$

such that the fit parameter A provides the 95% C.L. limit on η, since $f(x) = 0.05$ for $x = A$. A fit to the values obtained in the quark radius analysis is presented in Fig. 5.5. A similar procedure was used for the estimation of the lower boundary; 95% C.L. limits on R_q^2 for the frequentist approach with fixed PDF parameters are found to be

$$-4.62 \times 10^{-6} \text{ GeV}^{-2} < R_q^2 < 4.04 \times 10^{-6} \text{ GeV}^{-2} \quad . \tag{5.5}$$

These are well consistent with the results obtained by the least-squares method (Eq. 5.2).

---

[2]Figures 5.3, 5.4, 5.5 and 5.9 were added as an additional material to the quark-radius analysis paper [111].

ZEUS
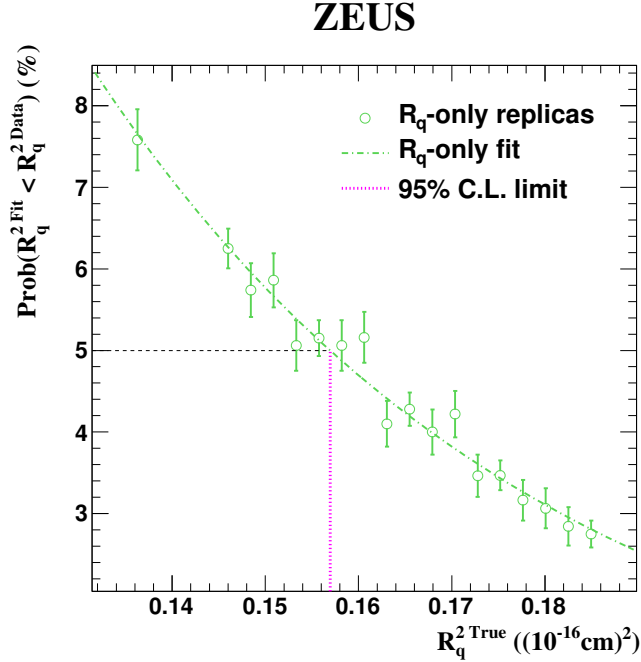
Figure 5.5: The probability of obtaining $R_q^{2\,\mathrm{Fit}}$ values smaller than that obtained for the actual data, $R_q^{2\,Data}$, calculated from the Monte Carlo replicas with the PDF parameters fixed to the ZCIPDF values, as a function of the assumed value for the quark-radius squared, $R_q^{2\,True}$. Points with statistical error bars represent Monte Carlo replica sets generated for different values of $R_q^{2\,True}$. Shown are the results selected for the final limit evaluation. The dash-dotted line represents the fitted exponential dependence used to interpolate simulation results to a probability of 5%. The resulting 95% C.L. limit on the R_q^2 value is indicated by the vertical dotted line.

5.2 Beyond-the-Standard-Model analysis combined with PDF fit

The main disadvantage of the analysis procedure described in the previous section is that the same data are used first in the determination of PDFs within the Standard Model and afterwards in the contact-interactions parameter-limit evaluation. A possible contribution from BSM processes to the high-Q^2 DIS data could affect the PDF fit and result in biased PDF distributions. The Standard Model predictions obtained from such a fit would include some BSM contribution, providing good agreement with the data but thereby overestimating CI limits.

Such a bias cannot be avoided in the analysis of HERA data by using another available PDF set since HERA inclusive DIS cross sections are the backbone of all recent high-

precision PDFs. For example, the CT14 [114] and JR14 [115] PDF fits used the HERA I combination, and MMHT2014 [116] and NNPDF3.0 [117] additionaly included HERA II data from the H1 and ZEUS experiments.

The proper procedure for a BSM analysis of the HERA data would be a global QCD analysis which simultaneously includes a possible contribution from BSM processes in the QCD fit.

5.2.1 Combined BSM+PDFs fits

In the global QCD fit, the CI parameter η can be estimated simultaneously with PDFs as an additional fit parameter. To check if such a fit would prevent biases in the fitted CI parameter values, a test on the generated pseudodata has been performed. The pseudodata sets were prepared in the same (Q^2, x) grid as the data for different values of the quark radius parameter $R_q^{2\;\text{True}}$ from the predictions of ZCIPDF, modified according to Eq. 1.38. The uncertainties for the resulting cross-section values were taken to be the same as for the data. This procedure differs from the generation of MC replicas in that the cross-section predictions were not varied within uncertainties. The QCD fit simultaneously estimated PDF parameters and $R_q^{2\;\text{Fit}}$ on the obtained sets of pseudodata. The results are displayed in Fig. 5.6 as solid blue circles. For comparison, a two-step fit was also performed on the same pseudodata sets, first estimating PDF parameters within the Standard Model and afterwards fitting $R_q^{2\;\text{Fit}}$ with PDF parameters fixed to the results of the first fit. Results of the two-step fit are presented in Fig. 5.6 with open red circles. They show a bias in the CI parameter values that is not present in the case of the combined fit.

The CI parameters obtained in the fit to data combined with the estimation of the PDF parameters is denoted as $\eta_{\text{CI+PDF}}^{\text{Data}}$. For the fit of PDFs and quark radius, the χ^2 was $\chi^2/ndf = 1361.60/1130 = 1.20$ and the value of $R_{q\;\text{CI+PDF}}^{2\;\text{Data}} = -0.47 \times 10^{-6}\,\text{GeV}^{-2}$ was estimated. The global correlation coefficient for the R_q^2 parameter was $\rho_{R_q^2} = 0.49$.

5.2.2 Combined procedure for the least-squares method

Similar to the procedure described in Section 5.1.2, limits on the BSM parameters can be evaluated with the least-squares method for the combined approach. In this analysis, for each fixed value of η_i^{True} the full PDF parameters fit is performed and the resulting value of $\chi^2(\eta_i^{\text{True}})$ is recorded. The limits are evaluated from the distribution of $\chi^2(\eta_i^{\text{True}})$ in the same way as for the procedure with fixed PDFs.

To compare the least-squares method with the combined procedure and the procedure with fixed PDFs, the distributions of $\chi^2(R_q^{2\;\text{True}})$ were calculated using the pseudodata set generated with $R_q^{2\;\text{True}} = 0$; the results are shown in Fig. 5.7. The distribution for the procedure with fixed PDFs can be described with a narrower parabola and thus would result in stronger limits than the combined procedure.
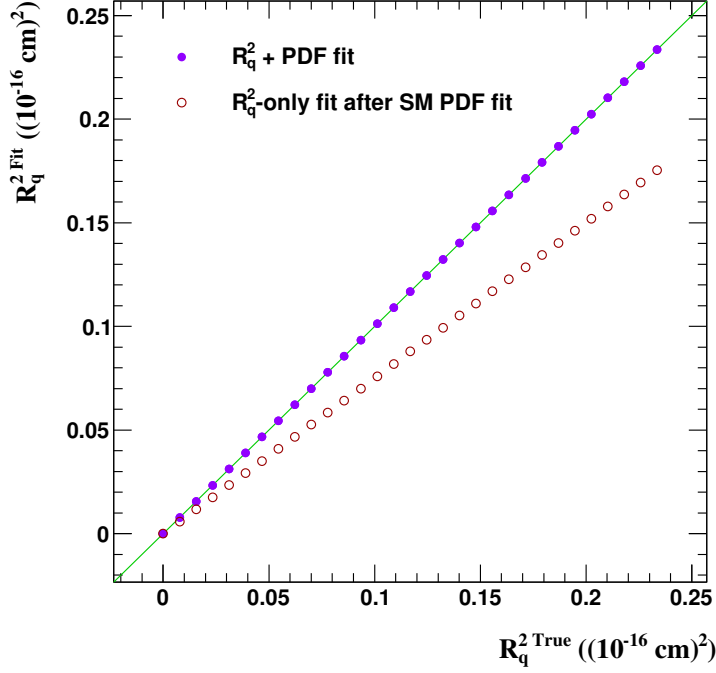
Figure 5.6: Results of the combined fit of PDF parameters and $R_q^{2\ \mathrm{Fit}}$ (solid blue circles) and the two-step fit first estimating PDF parameters assuming the validity of the Standard Model, fixing them and evaluating $R_q^{2\ \mathrm{Fit}}$ (open red circles). The pseudodata for the fits are obtained by modifying SM cross-section predictions with the quark-radius form-factor $R_q^{2\ \mathrm{True}}$.

A distribution of χ^2 estimated with data with the combined procedure is presented in Fig. 5.8. The 95% C.L. limits on R_q^2 evaluated with this procedure are:

$$-5.59 \times 10^{-6}\ \mathrm{GeV}^{-2} < R_q^2 < 4.64 \times 10^{-6}\ \mathrm{GeV}^{-2}\ \ . \tag{5.6}$$

They are by about 8% weaker than the limits obtained in the procedure with PDFs fixed to ZCIPDF (Eq. 5.2) and show that the possible influence of quark radii or any other contact-interactions model on the PDF parameters should be taken into account in the BSM analysis.
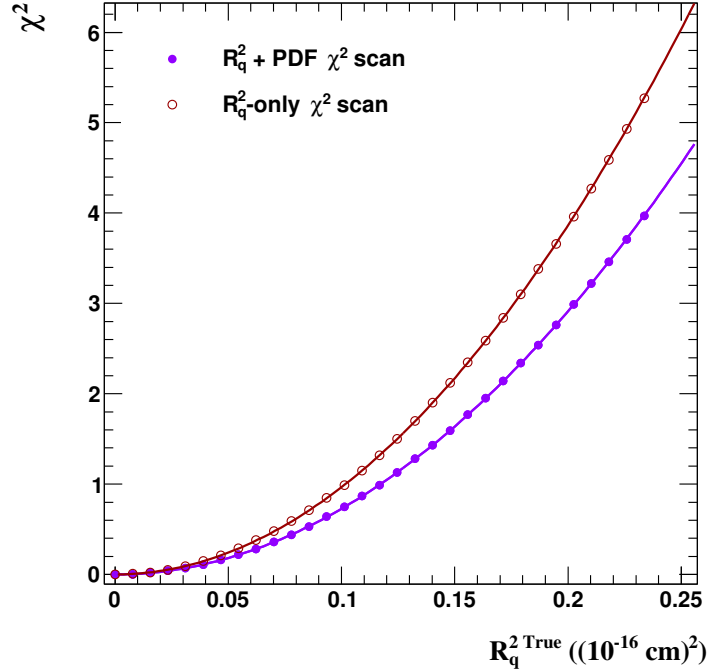
Figure 5.7: χ^2 distributions for the least-squares method with the combined procedure (solid blue circles) and the procedure with fixed PDFs (open red circles). Both distributions are estimated on the pseudodata generated from the Standard Model cross-section predictions.

5.2.3 Combined procedure for the Monte Carlo replicas method

The combined procedure can also be applied to the Monte Carlo replicas method of limit evaluation. For this, each of the Monte Carlo replica sets prepared for some η^{True} using Eq. 5.3 has to be fitted using the combined QCD fit simultaneously estimating PDF parameters and the BSM parameter η^{Fit}. The η^{Fit} values are compared to $\eta^{\text{Data}}_{\text{CI+PDF}}$ and the probability of obtaining $\eta^{\text{Fit}} < \eta^{\text{Data}}_{\text{CI+PDF}}$ is estimated. The limits are derived from the probability values calculated for different η^{True} as described in Section 5.1.3.

The distribution of $R_q^{2\,\text{Fit}}$ fitted simultaneously with PDF parameters to MC replicas with $R_q^{2\,\text{True}} = 6 \times 10^{-6}$ GeV^{-2} is compared to $R_{\text{q}\,\text{CI+PDF}}^{2\,\text{Data}}$ in Fig. 5.9. This distribution has about 18% larger root-mean-square value than the distribution displayed in Fig. 5.3 and a probability value of $P(R_q^{2\,\text{Fit}} < R_{\text{q}}^{2\,\text{Data}}) = 1.84\%$. The distribution of probability $P(R_q^{2\,\text{Fit}} < R_{\text{q}}^{2\,\text{Data}})$ as a function of $R_q^{2\,\text{True}}$ obtained with the combined procedure in
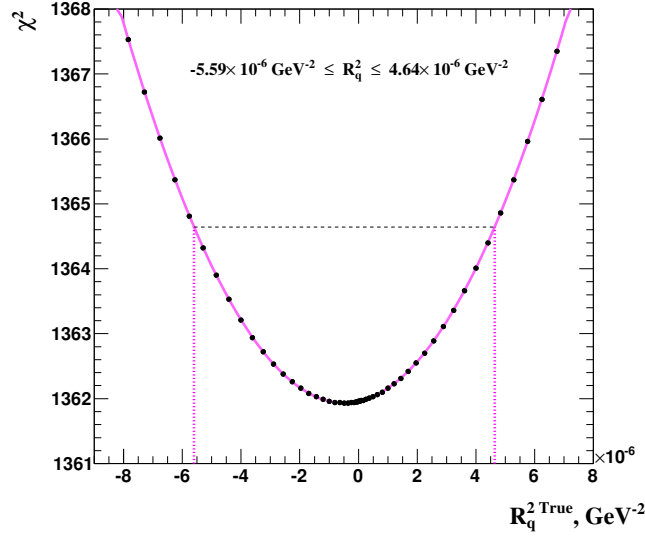
Figure 5.8: χ^2 as a function of $R_q^{2\,\text{True}}$ in the combined procedure. The interval of R_q^2 and dashed lines represent the limits for 95% C.L.
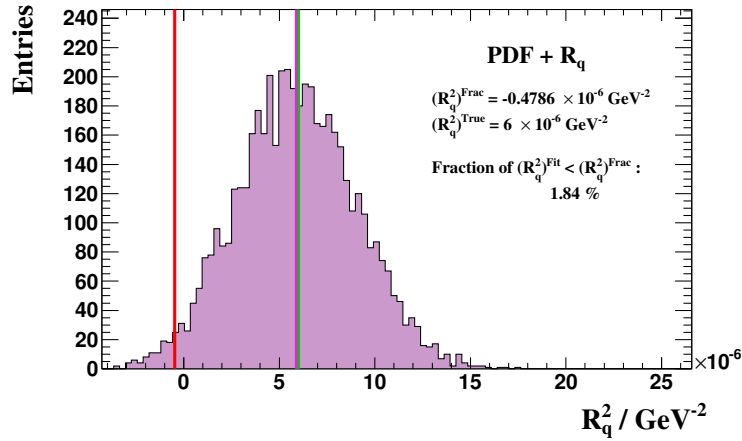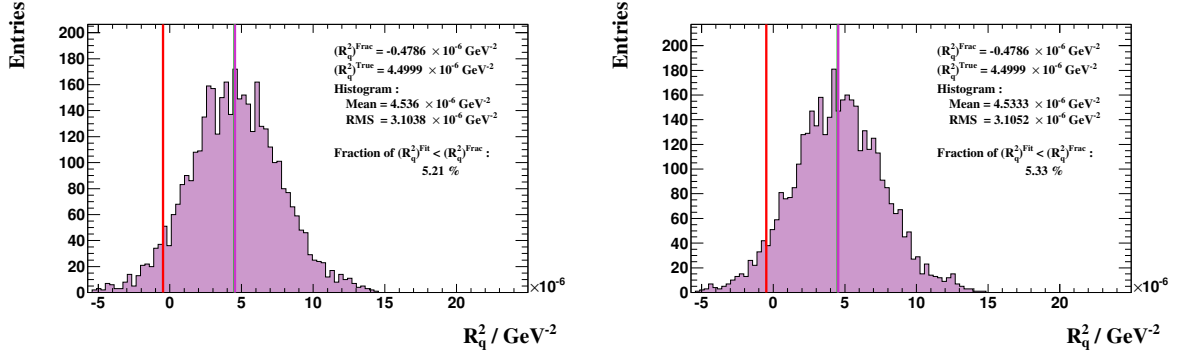

Figure 5.9: A distribution of $R_q^{2\,\text{Fit}}$ fitted on Monte Carlo replicas for $R_q^{2\,\text{True}} = 6 \times 10^{-6}\,\text{GeV}^{-2}$ in the combined procedure. Vertical lines represent (from left to right) $R_{q\;\text{CI+PDF}}^{2\;\text{Data}}$, the mean of the distribution and $R_q^{2\,\text{True}}$ (the last two overlap since the mean value is very close to the $R_q^{2\,\text{True}}$).

the quark-radius analysis [111] is compared to the probability distribution evaluated in the procedure with fixed PDFs in Fig. 5.10. The 95% C.L. limits on the quark radius evaluated with the combined procedure using the frequentist approach are

$$-5.51 \times 10^{-6} \ \text{GeV}^{-2} < R_\text{q}^2 < 4.64 \times 10^{-6} \ \text{GeV}^{-2} \quad . \tag{5.7}$$

These are in good agreement with the limits obtained with the least-squares method (Eq. 5.6) and are around 8% weaker than the limits obtained with the procedure with PDFs fixed to ZCIPDF (Eq. 5.5), showing that the limits evaluated with fixed PDFs are overestimated.
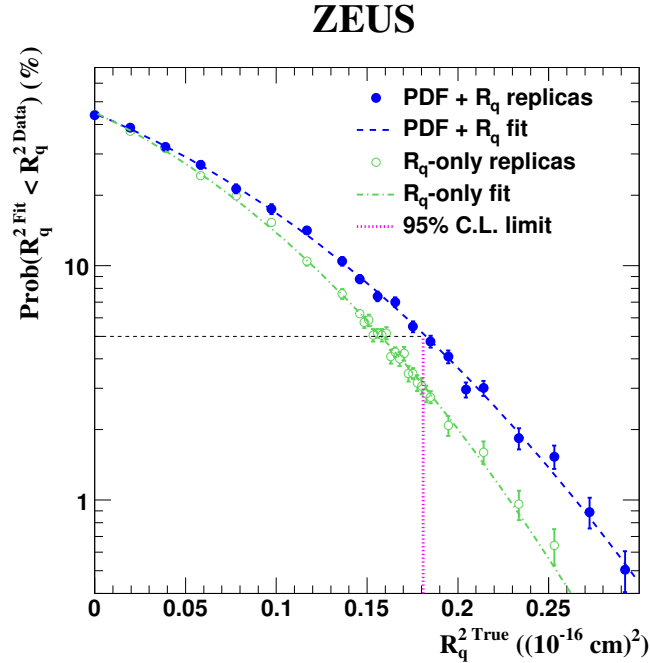
Figure 5.10: The probability of obtaining $R_q^{2\,\text{Fit}}$ values smaller than that obtained for the actual data, $R_q^{2\,Data}$, calculated from the Monte Carlo replicas, as a function of the assumed value for the quark-radius squared, $R_q^{2\,True}$. Points with statistical error bars represent the Monte Carlo replica sets generated for different values of $R_q^{2\,True}$. The solid blue circles correspond to the results obtained from the simultaneous fit of R_q^2 and PDF parameters (PDF+R_q). For comparison, the open green circles represent the dependence obtained when fixing the PDF parameters to the ZCIPDF values (R_q-only). The plot has been taken from the quark-radius analysis paper [111].

5.3 Gaussian and Poisson statistics

The statistical uncertainties of all data points of the HERA inclusive DIS combination were assumed to follow Gaussian statistics. This assumption was used in the χ^2 definition of PDFs fits (Eq. 4.9) and in the calculations of Monte Carlo replicas (Eq. 5.3). In the region of $Q^2 \geq 10000\,\mathrm{GeV}^2$, 14 data points have statistical uncertainties greater than 20% and thus Poisson statistics might constitute a more appropriate treatment.

In the combination of the data [14], all cross-section uncertainties from the two experiments were treated according to Gaussian statistics, while all H1 [41, 67, 71–75, 85] and half of ZEUS [76–78, 83, 87, 89, 90] publications of the inclusive data lack information on the number of observed events, N_{data}. This makes a full analysis within Poisson statistics impossible. Instead a test using a Poisson probability distribution for producing and fitting replicas of 14 selected data points with $Q^2 \geq 10000\,\mathrm{GeV}^2$ and statistical uncertainties $\delta^2_{i,\mathrm{stat}} > 0.2$ was performed. For each of these points, N_{data} was approximately evaluated as

$$\epsilon^i = \frac{A \cdot L^i}{\sigma^i_{\mathrm{SM}}} \cdot \iint \sigma_{\mathrm{SM}} dQ^2 dx, \tag{5.8}$$

$$N^i_{\mathrm{data}} = \lfloor \sigma^i_{\mathrm{data}} \cdot \epsilon^i \rceil, \tag{5.9}$$

where A is the acceptance, L^i is luminosity, σ^i_{SM} and σ^i_{data} are the ZCIPDF fit predictions and the data values of the double-differential cross section, respectively. Bin boundaries for the integration were taken similar to those of the ZEUS HERA II NC [86, 88] and CC [87, 89] publications:

$$\begin{aligned}
\mathrm{NC}: \ & Q^2 = [9000, 15000, 25000, 42000, 70000]\ \mathrm{GeV}^2 \\
& x = [0.09, 0.15, 0.23, 0.35, 0.53, 0.75] \\
\mathrm{CC}: \ & Q^2 = [12600, 22500, 60000]\ \mathrm{GeV}^2 \\
& x = [0.18, 0.32, 0.56, 1.00] \ .
\end{aligned} \tag{5.10}$$

The acceptance was assumed to be $A = 0.95$ for all considered points, close to the acceptance values given in ZEUS NC e^-p and CC e^+p publications [80, 81]. The luminosity for different sets was taken as a sum of corresponding luminosities from ZEUS and H1:

$$\begin{aligned}
L_{\mathrm{NC}e^-p} &= 353.9\ pb^{-1} \ ; \\
L_{\mathrm{NC}e^+p,\ \sqrt{s}=300\ \mathrm{GeV}} &= 65.6\ pb^{-1} \ ; \\
L_{\mathrm{NC}e^+p,\ \sqrt{s}=318\ \mathrm{GeV}} &= 445.9\ pb^{-1} \ ; \\
L_{\mathrm{CC}e^-p} &= 359.5\ pb^{-1} \ ; \\
L_{\mathrm{CC}e^+p} &= 523.4\ pb^{-1} \ .
\end{aligned} \tag{5.11}$$

The expected number of events, N_{exp}, was calculated as

$$N^i_{\mathrm{exp}} = \lfloor \sigma^i_{\mathrm{exp}} \cdot \epsilon^i \rceil \ , \tag{5.12}$$

Figure 5.11: A distribution of $R_q^{2\,\text{Fit}}$ fitted to the Monte Carlo replicas for $R_q^{2\,\text{True}} = 4.5 \times 10^{-6}\,\text{GeV}^{-2}$ in the procedure combined with PDFs fit with 14 selected data points with high statistical uncertainties treated according to Gaussian (left figure) and Poisson (right figure) statistics. Vertical lines represent (from left to right) $R_{q\,\text{CI+PDF}}^{2\,\text{Data}}$, $R_q^{2\,\text{True}}$ and the mean of the distribution (the last two overlap since the mean value is very close to the $R_q^{2\,\text{True}}$).

where σ_{exp}^i is the cross-section prediction modified with some contact-interaction model.

In every MC replica set for each of the 14 selected points, the number of observed events N_{obs}^i was calculated from a Poisson distribution with N_{exp}^i and the cross section was evaluated as

$$\mu^i = \left(\frac{N_{\text{obs}}^i}{\epsilon^i}\right) \cdot (1 + \delta_{i,\text{uncor}} \cdot r_i) \cdot \left(1 + \sum_j \gamma_j^i \cdot r_j\right) \quad, \tag{5.13}$$

with statistical uncertainty

$$\delta_{i,\text{stat}} = \sqrt{\left(\frac{\mu^i}{\epsilon^i}\right)} \quad. \tag{5.14}$$

For all other data points, replicas were calculated according to Eq. 5.3.

A comparison of the Gaussian and Poisson treatment of the selected 14 data points was performed on the model with quark radius $R_q^2 = 4.5 \times 10^{-6}\,\text{GeV}^{-2}$. Monte Carlo replicas for all other than the selected points in the Poisson sample were taken to be the same as in the Gaussian sample. Parameter $R_q^{2\,\text{Fit}}$ was fitted on 5000 replicas simultaneously with PDFs. The distributions thereby obtained are presented in Fig. 5.11. The main parameters of these distributions are listed in Table 5.1. Since distributions of fitted $R_q^{2\,\text{Fit}}$ from the two samples agree well, Gaussian statistics can be used for modelling the statistical fluctuations of all data points.

	Gaussian	Poisson	Uncertainty
Mean $[\text{TeV}^{-2}]$	4.536	4.533	0.049
RMS $[\text{TeV}^{-2}]$	3.104	3.105	0.035
$P(R_q^{2\,\text{Fit}} < R_\text{q}^{2\,\text{Data}})$ [%]	5.21	5.33	0.35

Table 5.1: Parameters of distributions presented in Fig. 5.11.

Chapter 6

Limits on new physics

This chapter summarises the results of a global (QCD + beyond the Standard Model) analysis performed using the combined HERA inclusive $e^\pm p$ DIS cross sections. The limit-setting procedure with global QCD fits in the frequentist approach has been found to be very time consuming, so that, to reduce the calculation time, a simplified approach, based on the Taylor expansion of the cross section predictions, has been developed and is presented here.

6.1 Quark form factor

The analysis of quark radius based on simultaneous fits of PDF parameters and R_q^2 using the sets of Monte Carlo replicas as described in the preceding section yields the 95% C.L. limits of

$$-(0.47 \cdot 10^{-16} \text{ cm})^2 < R_q^2 < (0.43 \cdot 10^{-16} \text{ cm})^2 \quad . \tag{6.1}$$

These limits are about 8% weaker than the limits that would be obtained for fixed PDF parameters, as demonstrated in Fig. 5.10. This shows that it is important to take into account the possible influence of quark radii or any other contact-interactions parameter on the PDF-parameters extraction.

The experimental sensitivity of the data to R_q^2 was calculated from the median of the limit distribution for the SM replicas providing the value of $R_{q\ \text{sens}} = 0.45 \cdot 10^{-16}$ cm for both positive and negative values of R_q^2. The limits on R_q^2 are in a good agreement with this estimated sensitivity.

Deviations of the cross sections corresponding to the 95% C.L. exclusion limits on R_q^2 are compared to the combined HERA high-Q^2 NC and CC DIS data integrated over x in Fig. 6.1 and Fig. 6.2, respectively. The rise of the NC $e^- p$ cross-section values in the last two bins visually demonstrates the reason for the negative values of $R_{q\ \text{CI-only}}^{2\ \text{Data}}$ and $R_{q\ \text{CI+PDF}}^{2\ \text{Data}}$.
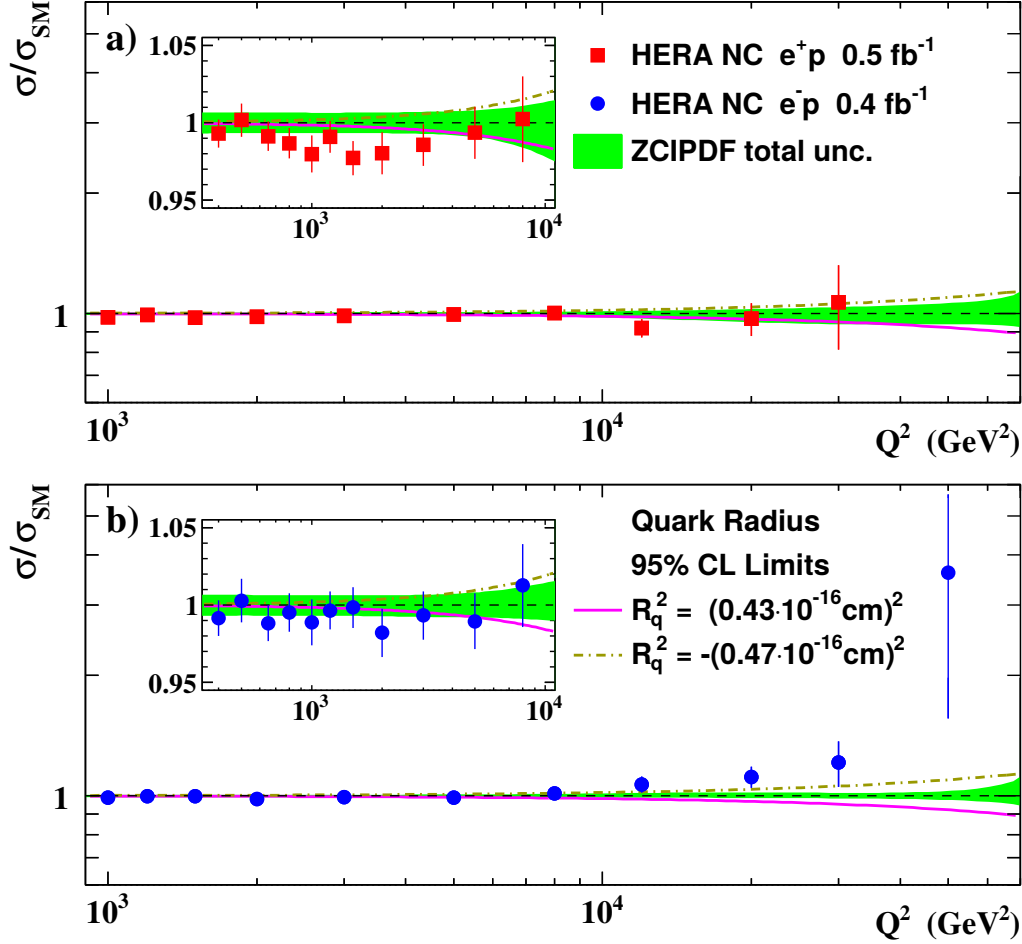
Figure 6.1: Combined HERA (a) e^+p and (b) e^-p NC DIS data divided by the cross-section expectations from ZCIPDF and compared to the 95% C.L. exclusion limits on the effective mean-square radius of quarks. The bands on the ZCIPDF predictions represent the total uncertainty. The insets show the comparison in the $Q^2 < 10^4$ GeV^2 region with a linear ordinate scale. A similar plot was used in the quark-radius analysis paper [111].

The 95% C.L. limits for the quark radius presented here are more than a factor of two better than the previous ZEUS limits of $-(1.06 \cdot 10^{-16} \text{ cm})^2 < R_q^2 < (0.85 \cdot 10^{-16} \text{ cm})^2$, based on the HERA I data [118]. The upper limit also improves the result published by the H1 collaboration [119], $R_q < 0.65 \cdot 10^{-16}$ cm, and is similar to the limit from quark-pair production at LEP2 [120], $R_q < 0.42 \cdot 10^{-16}$ cm. It is important to note that the possible BSM physics parameterised by the form factors at LEP and HERA might be different and limits on them are largely complementary.
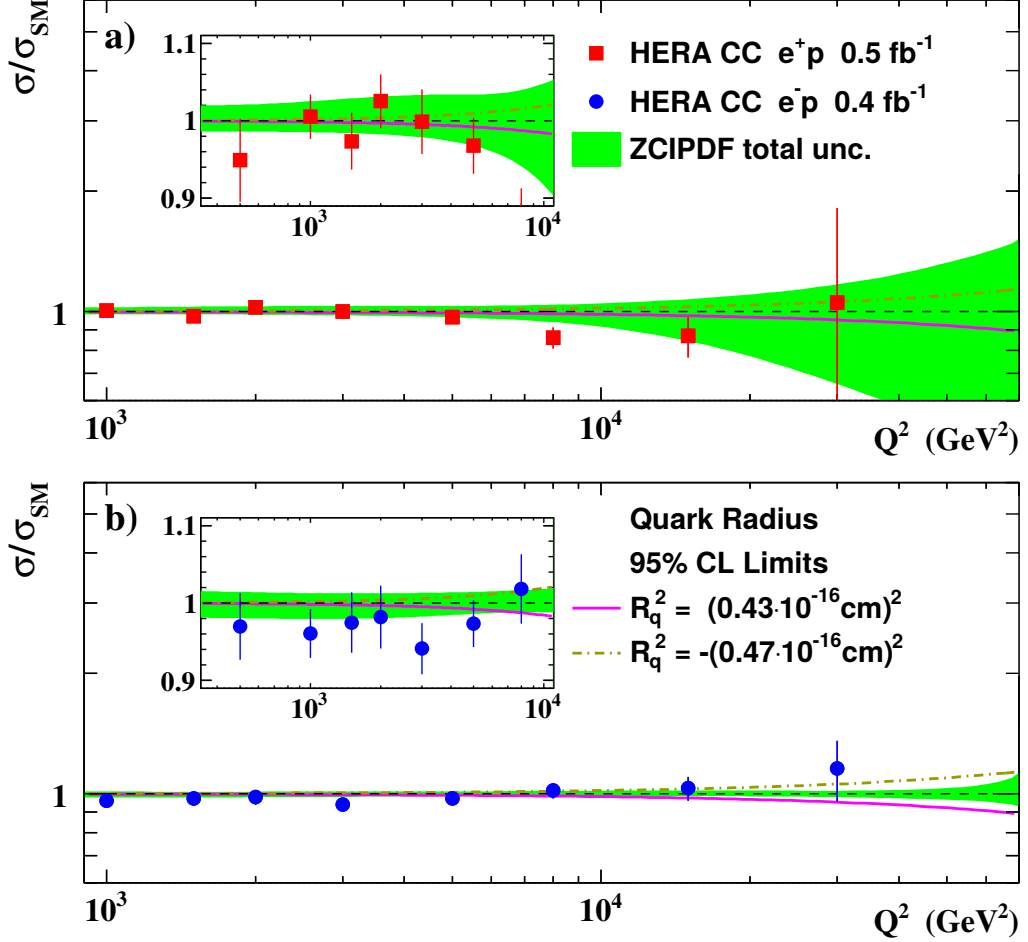
Figure 6.2: Combined HERA (a) e^+p and (b) e^-p CC DIS data divided by the cross-section expectations from ZCIPDF and compared to the 95% C.L. exclusion limits on the effective mean-square radius of quarks. Other details as for Fig. 6.1.

6.2 Simplified fit procedure

In the quark-radius analysis, about 5000 Monte Carlo replicas were generated and fitted for each value of the true quark-radius squared, $R_q^{2\,\mathrm{True}}$. In total about 200 000 combined fits of PDF parameters and $R_q^{2\,\mathrm{Fit}}$ were performed, each taking on average about 1.5 hour of processing (CPU) time. Thus, more than 30 years of CPU time were used for setting the final limits in the single BSM scenario, making the processing time a limiting factor for the extension of the analysis to other models.

To reduce the calculation time of each QCD fit a simplified procedure was devel-

oped [121] for estimating the cross-section predictions $\boldsymbol{m}$ used in the χ^2 formula (Eq. 4.9). The 14 PDF parameters, denoted $\boldsymbol{p}$ in the following (or p^k for the separate parameter with index k), fitted on Monte Carlo replicas for $\eta^{\text{True}} = 0$ were assumed to fluctuate only within relatively small uncertainties from the ZCIPDF parameters, denoted $\boldsymbol{p_0}$. The dependence of the cross-section predictions on these parameters $m(x_i, Q_i^2, \boldsymbol{p}, \eta = 0)$ was approximated by a first-order Taylor expansion as

$$m(x_i, Q_i^2, \boldsymbol{p}, 0) = m_0^i + \sum_k \theta_{0\,k}^i \cdot \Delta p^k \quad . \tag{6.2}$$

There $m_0^i = m(x_i, Q_i^2, \boldsymbol{p_0}, 0)$ are cross-section predictions from ZCIPDF, $\theta_{0\,k}^i$ are the vectors of derivatives:

$$\theta_{0\,k}^i = \left. \frac{\partial m(x_i, Q_i^2, \boldsymbol{p}, 0)}{\partial p_k} \right|_{\boldsymbol{p}=\boldsymbol{p_0}} \quad , \tag{6.3}$$

with $k = 1, \ldots N_{par}, N_{par} = 14$ and Δp^k is the shift of the PDF parameter p^k from the nominal fit result, $\Delta p^k = p^k - p_0^k$. The derivatives were evaluated on ZCIPDF fit results with the linear approximation as

$$\theta_{0\,k}^i \approx \frac{m(x_i, Q_i^2, \boldsymbol{p_0^{+k}}, 0) - m(x_i, Q_i^2, \boldsymbol{p_0^{-k}}, 0)}{\sigma_k} \quad . \tag{6.4}$$

Here σ_k is the uncertainty of the fitted PDF parameter p_0^k and the two parameter sets $\boldsymbol{p_0^{+k}}$ and $\boldsymbol{p_0^{-k}}$ are defined as

$$\boldsymbol{p_0^{+k}} = \left(p_0^1, \ldots, p_0^k + \frac{\sigma_k}{2}, \ldots, p_0^{N_{par}} \right) \quad , \tag{6.5}$$

$$\boldsymbol{p_0^{-k}} = \left(p_0^1, \ldots, p_0^k - \frac{\sigma_k}{2}, \ldots, p_0^{N_{par}} \right) \quad . \tag{6.6}$$

The described procedure was tested by comparing its results with the results of the full PDF fit on MC replicas for $\eta^{\text{True}} = 0$, with the η parameter fixed to $\eta = 0$. The reduced cross-section predictions for NC and CC $e^{\pm}p$ DIS at $Q^2 = 8000$ GeV^2 and $x = 0.25$ are compared in Fig. 6.3. The predictions of the simplified procedure agree well with the predictions of the full fit which results in the good agreement of the final χ^2 values, as shown in the left plot in Fig. 6.4. The simplified method reduces the processing time of the fits almost by a factor of 50, as can be seen in the right plot in Fig. 6.4.

The cross-section predictions approximation (Eq. 6.2) was extended to include the dependence on the coupling η with

$$m(x_i, Q_i^2, \boldsymbol{p}, \eta) = m_0^i + \sum_k \theta_{0\,k}^i \Delta p^k + \left(m_1^i + \sum_{k'} \theta_{1\,k'}^i \Delta p^{k'} \right) \eta$$

$$+ \left(m_2^i + \sum_{k''} \theta_{2\,k''}^i \Delta p^{k''} \right) \eta^2 \quad . \tag{6.7}$$
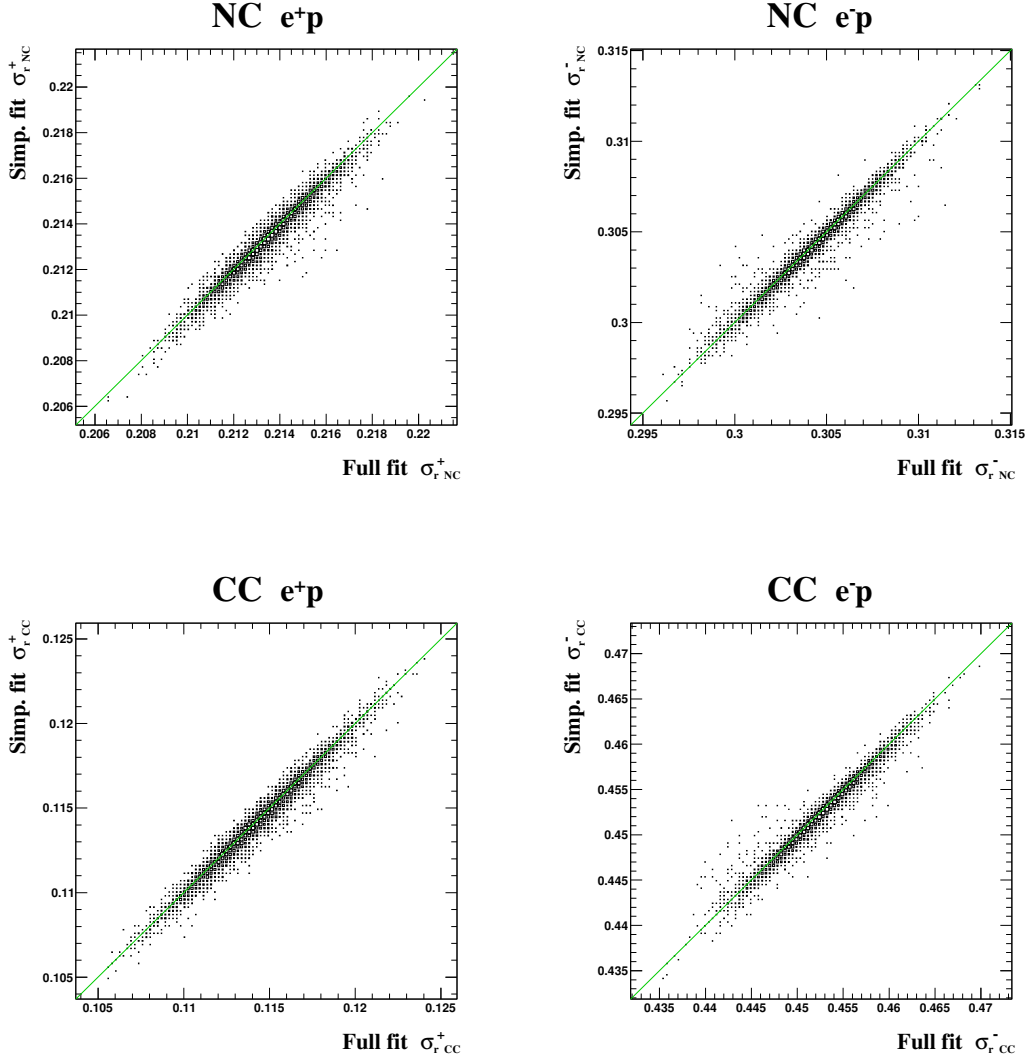
Figure 6.3: Comparison of the reduced cross-section predictions for NC and CC $e^{\pm}p$ DIS (as indicated in the plot labels) at $Q^2 = 8000$ GeV^2 and $x = 0.25$ from the full QCD fit and from the simplified fit on the large set of Standard Model replicas. The plots have been taken from the note on the simplified procedure for QCD fits [121].

The cross-section terms m_1^i and m_2^i are defined as

$$m_1^i \;=\; \frac{m(x_i, Q_i^2, \boldsymbol{p_0}, +\Delta\eta) - m(x_i, Q_i^2, \boldsymbol{p_0}, -\Delta\eta)}{2\,\Delta\eta} \quad, \tag{6.8}$$

$$m_2^i \;=\; \frac{m(x_i, Q_i^2, \boldsymbol{p_0}, +\Delta\eta) + m(x_i, Q_i^2, \boldsymbol{p_0}, -\Delta\eta) - 2\,m_0^i}{2\,(\Delta\eta)^2} \quad, \tag{6.9}$$
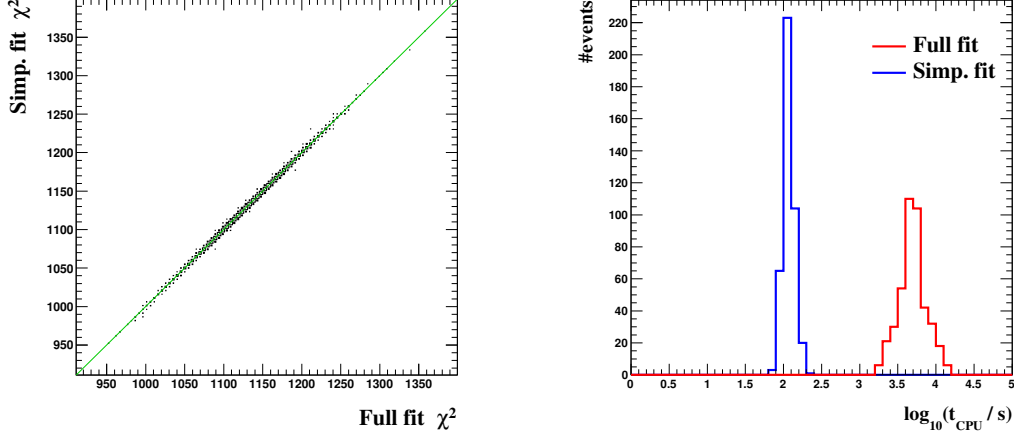
Figure 6.4: Comparison of the χ^2 values (left) and processing time (right) of the full QCD and simplified fit procedure used on the set of the Standard Model replicas. The plots have been taken from the note on the simplified procedure for QCD fits [121].

and additional combinations of derivatives are

$$\theta^i_{1\,k} \quad = \quad \frac{\theta^i_{+\,k} - \theta^i_{-\,k}}{2\,\Delta\eta} \quad , \tag{6.10}$$

$$\theta^i_{2\,k} \quad = \quad \frac{\theta^i_{+\,k} + \theta^i_{-\,k} - 2\,\theta^i_{0\,k}}{2\,(\Delta\eta)^2} \quad , \tag{6.11}$$

$$\theta^i_{+\,k} \quad = \quad \left.\frac{\partial m(x_i, Q_i^2, \boldsymbol{p}, +\Delta\eta)}{\partial p_k}\right|_{\boldsymbol{p}=\boldsymbol{p_0}} \quad , \tag{6.12}$$

$$\theta^i_{-\,k} \quad = \quad \left.\frac{\partial m(x_i, Q_i^2, \boldsymbol{p}, -\Delta\eta)}{\partial p_k}\right|_{\boldsymbol{p}=\boldsymbol{p_0}} \quad . \tag{6.13}$$

There $\Delta\eta$ is a fixed, but otherwise arbitrary, step value. It was taken equal to the uncertainty on η obtained in the fit with PDF parameters fixed to the values of ZCIPDF.

The presented approach was tested on the combined PDFs and quark-radii form-factor fits of the Monte Carlo replicas generated for the Standard Model ($R_q^{\text{True}} \equiv 0$) and the quark-radius limit of $R_q^{\text{True}} = 0.43 \cdot 10^{-16}$ cm. The fitted value of $R_q^{2\ \text{Fit}}$ and the final χ^2 from each of the MC replica fits were compared to the result of the full fit, as shown in Fig. 6.5 and Fig. 6.6. Both values show good agreement between the two approaches. As an additional check, the simplified method was used to reproduce the limit-setting
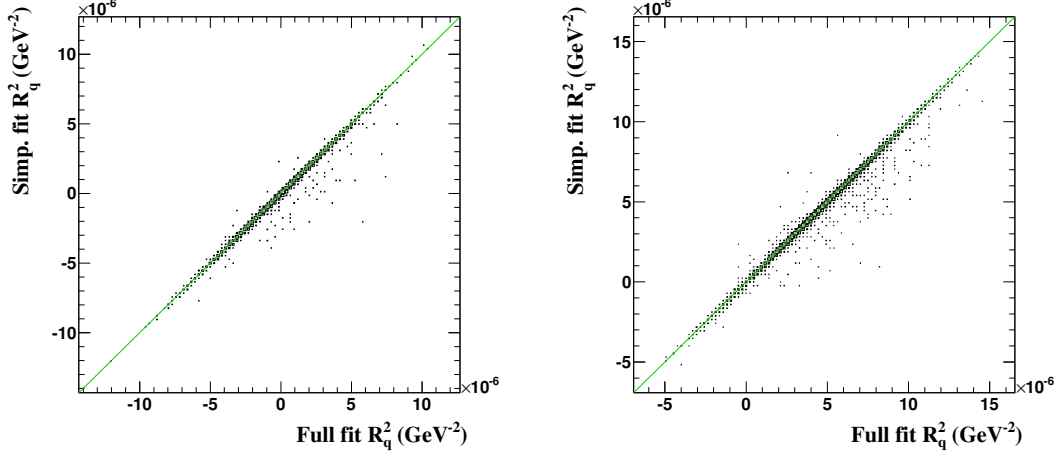
Figure 6.5: Comparison of the quark-radius squared, $R_q^{2\ \text{Fit}}$, resulting from the simplified and full combined PDFs and R_q^2 fits on Monte Carlo replicas generated for $R_q^{\text{True}} = 0$ (left) and $R_q^{\text{True}} = 0.43 \cdot 10^{-16}$ cm (right). The plots have been taken from the note on the simplified procedure for QCD fits [121].
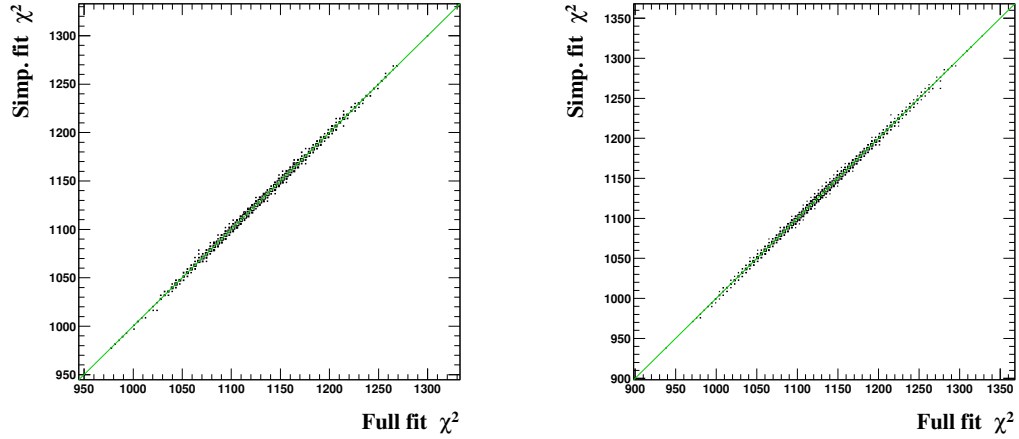
Figure 6.6: Comparison of the χ^2 values resulting from the simplified and full combined PDFs and R_q^2 fits on Monte Carlo replicas generated for $R_q^{\text{True}} = 0$ (left) and $R_q^{\text{True}} = 0.43 \cdot 10^{-16}$ cm (right). The plots have been taken from the note on the simplified procedure for QCD fits [121].

procedure from the quark-radius analysis paper [111]. The probability values evaluated for different R_q^{True} are compared to the results from the paper in Fig. 6.7. The limits that would be obtained with the simplified procedure perfectly agree with the limits evaluated in the full analysis, which verifies that the developed method can be safely used to shorten the computation time of the limits for other contact interactions models.
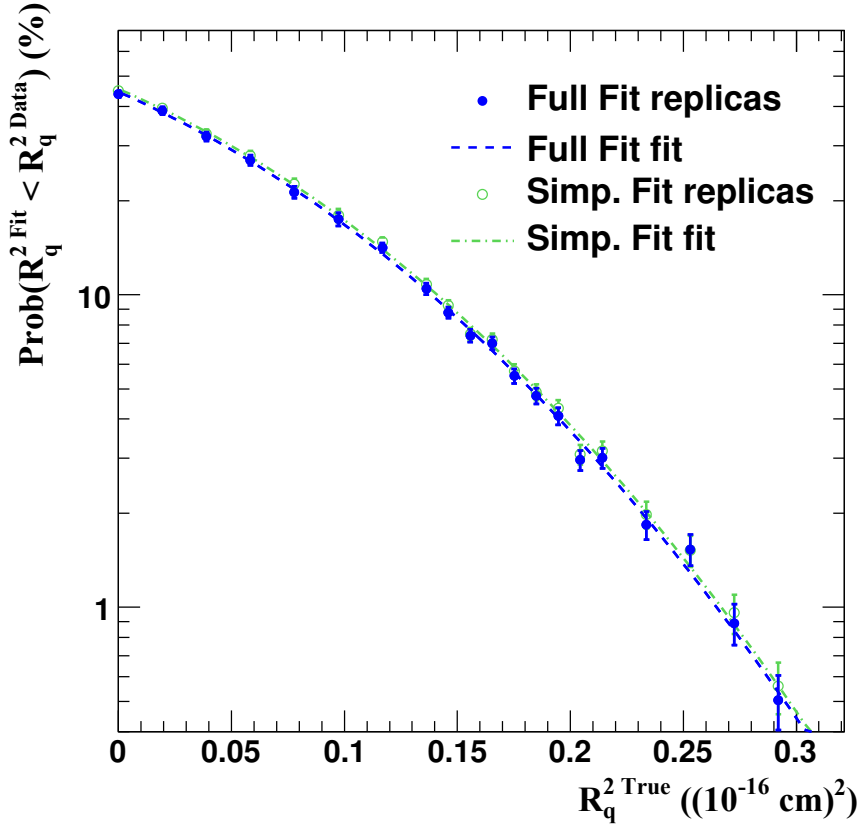
Figure 6.7: The probability of obtaining $R_q^{2\,Fit}$ values smaller than that obtained for the actual data, $R_q^{2\,Data}$, as a function of the $R_q^{2\,True}$ obtained with the simplified (open green circles) and full (solid blue circles) fit approaches. Probabilities of the full fit approach correspond to the published ZEUS results [111]. The plots have been taken from the note on the simplified procedure for QCD fits [121].

6.3 General contact interactions

The simplified fit procedure has been used for the combined QCD+BSM analysis of the general contact interactions described in Section 1.4.1. The coupling strength g was assumed to be $g = 2\sqrt{\pi}$ and the fitted BSM parameter was defined by

$$\eta = \frac{4\pi}{\Lambda^2} \quad , \tag{6.14}$$

changing Eq. 1.34 to

$$\eta_{ij}^{eq} = \epsilon_{ij}^{eq}\eta \quad . \tag{6.15}$$

The sets of parameters ϵ_{ij}^{eq} for the considered models are listed in the first column of the Table 6.1.

HERA $e^{\pm}p$ 1994-2007 data

		95% **C.L. limits (TeV)**				$\eta_{\mathrm{CI+PDF}}^{\mathrm{Data}}$	p_{SM}
Coupling structure		Measured		Expected			
Model	$[\epsilon_{LL},\epsilon_{LR},\epsilon_{RL},\epsilon_{RR}]$	Λ^-	Λ^+	Λ^-	Λ^+	(TeV^{-2})	(%)
LL	$[+1,\ 0,\ 0,\ 0]$	22.0	4.5	5.9	6.2	0.308	6.5
RR	$[\ 0,\ 0,\ 0,+1]$	32.9	4.4	5.7	6.1	0.341	5.6
VV	$[+1,+1,+1,+1]$	14.7	9.5	11.0	11.4	0.043	24.8
AA	$[+1,-1,-1,+1]$	-	4.8 - 10.4	7.9	7.8	0.324	0.7
VA	$[+1,-1,+1,-1]$	-	3.6 - 10.1	4.1	4.1	0.679	2.1
X1	$[+1,-1,\ 0,\ 0]$	-	3.5 - 6.6	5.7	5.6	0.680	0.3
X2	$[+1,\ 0,+1,\ 0]$	10.8	6.8	7.8	8.2	0.091	23.1
X4	$[\ 0,+1,+1,\ 0]$	7.6	9.2	8.0	8.6	-0.026	60.3

Table 6.1: Coupling structure parameters ϵ_{ij}^{eq} and 95% C.L. limits on the compositeness scale, Λ, for the considered general contact-interactions models. Also listed are the expected limits, values of $\eta_{\mathrm{CI+PDF}}^{\mathrm{Data}}$ fitted on data and probabilities p_{SM} of the Standard Model to result in the best-fit coupling value greater than (or less than, in case of the negative value) $\eta_{\mathrm{CI+PDF}}^{\mathrm{Data}}$. The compositeness scale Λ^+ corresponds to positive and Λ^- to negative values of the coupling η. The same coupling structure applies to all quarks.

The same analysis procedure as for the quark radius has been followed for each model evaluating $\eta_{\mathrm{CI+PDF}}^{\mathrm{Data}}$ in the combined fit on data, calculating the probability P of obtaining $\eta^{\mathrm{Fit}} < \eta_{\mathrm{CI+PDF}}^{\mathrm{Data}}$ (for limits on Λ^+) or $\eta^{\mathrm{Fit}} > \eta_{\mathrm{CI+PDF}}^{\mathrm{Data}}$ (for limits on Λ^-) and estimating the 95% C.L. limits with the criterion of $P = 5\%$. As an example, the probability distributions $P(\eta^{\mathrm{Fit}} < \eta_{\mathrm{CI+PDF}}^{\mathrm{Data}})$ and $P(\eta^{\mathrm{Fit}} > \eta_{\mathrm{CI+PDF}}^{\mathrm{Data}})$ for the VV model are presented in Fig. 6.8 with solid and open blue circles, respectively. For comparison, a distribution of $P(\eta^{\mathrm{Fit}} > 0)$

which was used for the evaluation of the Standard Model limit expectation is shown in Fig. 6.8 with open green squares. Estimated 95% C.L. limits on the compositeness scales Λ^+ and Λ^- are presented in Fig. 6.9 and Table 6.1 [122]. Also listed in the table are the values of $\eta_{\mathrm{CI+PDF}}^{\mathrm{Data}}$ and probabilities p_{SM} that an experiment, assuming validity of the Standard Model, would produce a value of $\eta^{\mathrm{Fit}} > \eta_{\mathrm{CI+PDF}}^{\mathrm{Data}}$ for $\eta_{\mathrm{CI+PDF}}^{\mathrm{Data}} \geq 0$ or $\eta^{\mathrm{Fit}} < \eta_{\mathrm{CI+PDF}}^{\mathrm{Data}}$ for $\eta_{\mathrm{CI+PDF}}^{\mathrm{Data}} < 0$.
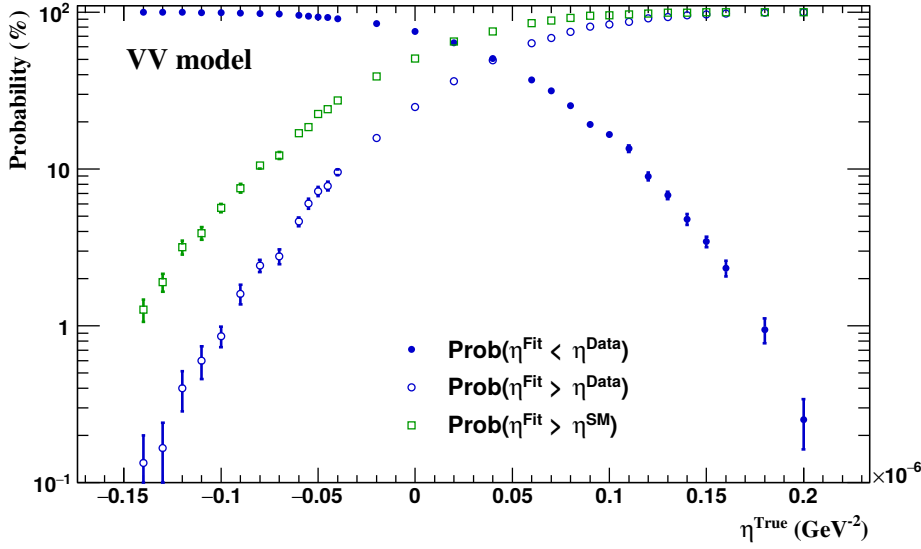
Figure 6.8: The probability P of obtaining the η^{Fit} value smaller (solid blue circles) or greater (open blue circles) than the best-fit coupling value for data, $\eta_{\mathrm{CI+PDF}}^{\mathrm{Data}}$, calculated from multiple Monte Carlo replicas for different assumed values of the CI coupling, η^{True}, for the VV contact-interaction scenario. Expected probability values, calculated by comparing the fitted couplings to $\eta^{SM} \equiv 0$, are presented with open green squares for comparison.

For the VV, X2 and X4 models, no significant deviation from the Standard Model has been observed. The probabilities p_{SM} for these scenarios range from 23.1 to 60.3% and measured limits are close to the expected values. The LL and RR models show larger differences of $\eta_{\mathrm{CI+PDF}}^{\mathrm{Data}}$ from the SM value of 0, with p_{SM} equal to 6.5 and 5.6, respectively, leading to large values of the compositeness scale in the negative direction of the CI coupling. The AA model, as well as VA and X1, have negative coupling values excluded at 95% C.L. The probability distributions for this BSM scenario are displayed in Fig. 6.10. The best-fit value for it corresponds to a compositeness scale of about 6.2 TeV and $p_{SM} = 0.7\%$, which means a 2.5 σ deviation from the Standard Model.
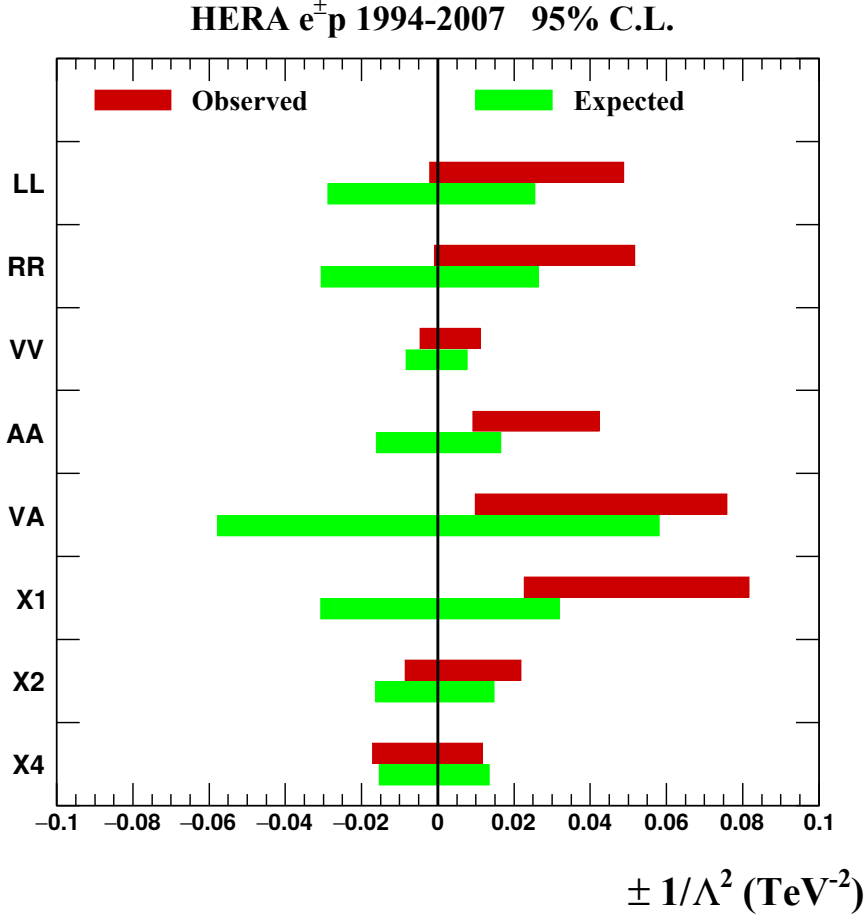
Figure 6.9: Confidence intervals (red bars) and the expected limits (green bars) of $\pm 1/\Lambda^2$ for 95% C.L. of the considered general contact-interaction scenarios.

The presented $eeqq$ contact interaction limits are compared to the recent published results from Atlas [123], CMS [124], and ALEPH [125], as well as previous results from the ZEUS [17] and H1 [126] collaborations in Table 6.2. The results from the DELPHI [127] collaboration on $eebb$ contact interactions are also given for reference. The limits estimated using the combined HERA inclusive $e^{\pm}p$ DIS cross sections are significantly stronger than limits previously evaluated by ZEUS and H1, are generally comparable to the results from the LEP2 experiments and are overall weaker than the limits obtained in the analyses of LHC $\sqrt{s} = 8$ TeV data. In the Atlas and CMS analyses only models with $\eta_{LR} = \eta_{RL}$ were considered. This condition does not necessarily have to hold for contact interactions among the different fermion species, such as $eeqq$. Therefore the limits presented here for the VA, X1 and X2 models are currently the strongest existing limits.
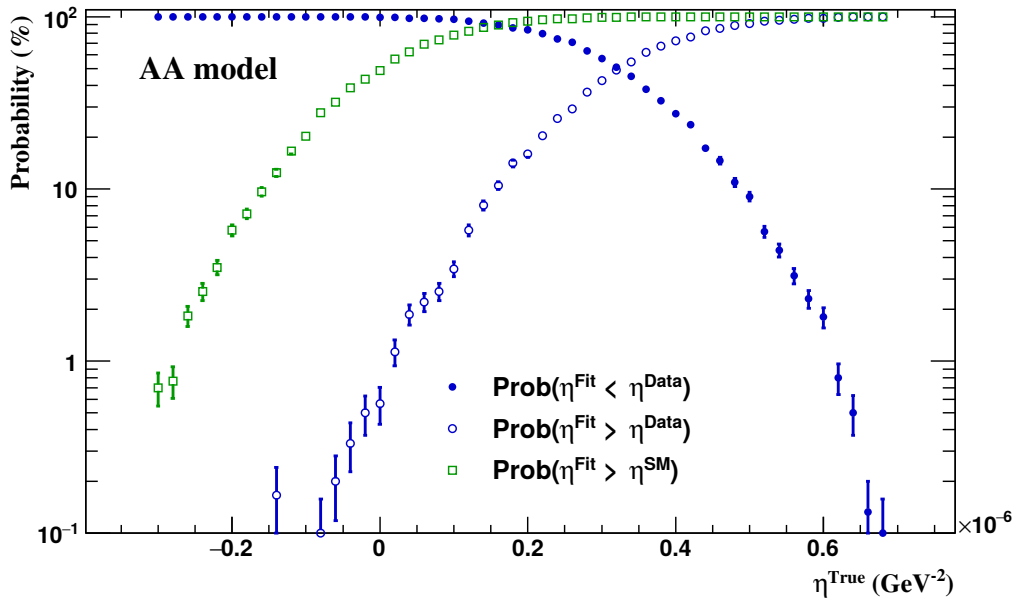
Figure 6.10: The probability P of obtaining the η^{Fit} value smaller (solid blue circles) or greater (open blue circles) than the best-fit coupling value for data, $\eta_{\text{CI+PDF}}^{\text{Data}}$, calculated from multiple Monte Carlo replicas for different assumed values of the CI coupling, η^{True}, for the AA contact interaction scenario. The expected probability values, calculated by comparing the fitted couplings to $\eta^{SM} \equiv 0$, are presented with open green squares for comparison.

	Measured 95% C.L. limits (TeV)													
Model	HERA combined (this analysis)		Atlas		CMS		ALEPH		DELPHI		ZEUS 2004		H1 2011	
Model	Λ^-	Λ^+	Λ^-	Λ^+	Λ^-	Λ^+	Λ^-	Λ^+	Λ^-	Λ^+	Λ^-	Λ^+	Λ^-	Λ^+
LL	22.0	4.5	20.7	16.4	18.3	13.5	7.2	12.9	10.2	8.4	1.7	2.7	4.0	4.2
RR	32.9	4.4	20.2	16.6			5.3	10.2	2.2	5.7	1.8	2.7	3.9	4.4
VV	14.7	9.5					8.3	16.9	10.6	9.5	6.2	5.4	7.2	5.6
AA	-	4.8 - 10.4					9.6	15.9	12.9	10.7	4.7	4.4	5.1	4.4
VA	-	3.6 - 10.1									3.3	3.2	3.6	3.8
X1	-	3.5 - 6.6									3.6	2.6		
X2	10.8	6.8									3.9	4.0		
X4	7.6	9.2	25.2	19.2			6.8	3.7			5.1	4.8	4.8	5.4

Table 6.2: The 95% C.L. limits on the compositeness scale, Λ, for the considered $eeqq$ general contact-interactions models estimated in the presented analysis and measured by the Atlas [123], CMS [124], ALEPH [125], ZEUS [17] and H1 [126] collaborations. Also shown are DELPHI [127] results for $eebb$ general CI. The compositeness scale Λ^+ corresponds to positive and Λ^- to negative values of the coupling η.

Chapter 7

Study of the SCRF cavities for the ILC-HiGrade project

The International Linear Collider is a possible future facility that can constrain or discover physics beyond the Standard Model in indirect searches at scales up to 60 TeV [128]. In this chapter, studies of the quality limitation factors of superconducting radio-frequency cavities, the core of the ILC accelerating technology, are described. In particular, the development and assembly of the cooling system for studies of hydride growth on Niobium and optical inspections of the cavity defects are presented.

7.1 Superconducting radio-frequency cavities

A large variety of particle accelerators, such as storage rings, light sources and linear colliders, operate superconducting radio frequency (SCRF) cavities for acceleration of the particle beams. Starting from studies at the TESLA Test Facility (TTF) [129], 9-cell 1.3 GHz Niobium cavities have been developed over the past 18 years and achieved the highest gradients to date for multi-cell cavities [130]. They have been used in the FLASH [131] and XFEL [132] projects and are planned as the baseline design for the International Linear Collider (ILC) [130], the possible next big HEP machine.

The fundamental advantages of superconducting cavities over normal-conducting are high conversion efficiency from primary electric power to beam power (about 20%), small beam emittance growth, low surface resistance of about 10 nΩ at 2 K and around 5 to 6 orders of magnitude higher quality factor (see 7.1.1). This makes the superconducting option an ideal choice for a high-luminosity collider or high-brilliance light source.

Most of the SCRF cavities worldwide are formed from Niobium, since it is chemically inert and has the highest critical temperature and critical magnetic field of all pure metals [132]. There exist compound superconductors with a higher critical temperature and field, but cavities based on them have shown lower performance [132].

The ILC-HiGrade project [133] and laboratory [134, 135] have been founded at DESY to study and develop the mass-production procedure of SCRF cavities providing at least 31.5 MV/m gradient with a production yield higher than 90 % to meet the ILC requirements. For this project, the manufacturing contracts for the 800 XFEL cavities included an additional 24 cavities that now are available for treatment studies [130]. One of those cavities is shown in Fig. 7.1. The ILC-HiGrade laboratory is equipped with an **O**ptical **B**ench for **A**utomated **C**avity inspection with **H**igh resolution on short **T**imescales (OBACHT) and non-destructive cavity inner-surface study (by surface imprinting with a hardened rubber, known as a "replica") system for optical and profilometry inspections [136], a centrifugal barrel polishing (CBP) machine [137] for acid-free surface-polishing, an ultrasonic bath with ultrapure-water for cavity washing and a cryocooler system for studies on Niobium samples, offering cooling down to 10 K. The development and assembly of the cryocooler system and cavity optical inspections with the OBACHT system are described below.
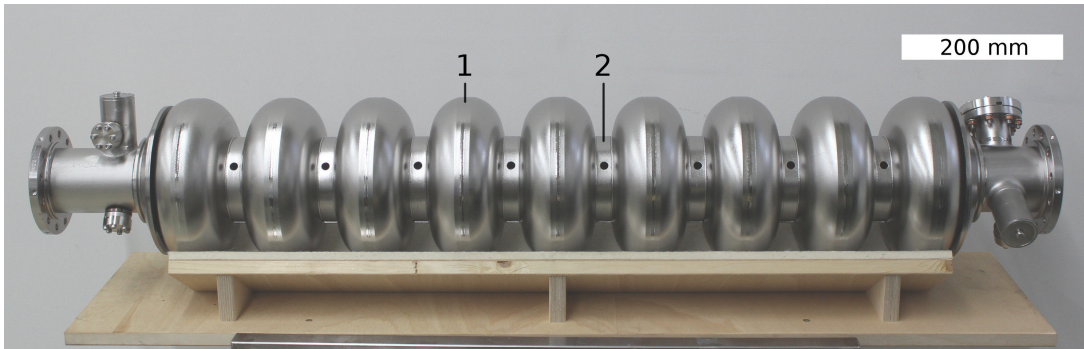
Figure 7.1: Superconducting 1.3 GHz 9-cell Niobium cavity CAV00532. Labelled are welding seams on the equator (1) and iris (2). Picture taken at the ILC-HiGrade laboratory.

7.1.1   Quality factor

One of the most important parameters of RF cavities is the quality factor, Q_0, which can be defined as [138]:

$$Q_0 = \frac{\omega W}{P_c} \quad , \tag{7.1}$$

where ω is the RF frequency, W is the energy stored in the cavity and P_c represents the power dissipated at the cavity surface. In the ideal case, the cavity quality factor should not depend on the accelerating field E_{acc} until some maximum value E_{Max}, at which the RF magnetic field at the inner cavity surface reaches the superheating field of the superconductor (200–240 mT for Niobium). This leads to a local phase transition

from the superconducting to the normal-conducting phase and global thermal breakdown, called a "quench". For TESLA-shape (Fig. 7.1) cavities, E_{Max} should be around 50-60 MV/m [129].

In practice Q_0 depends on E_{acc} and this dependence is influenced by a lot of factors (see proceedings by J. Norem and M. Pellin [139] for more details), two of which are hydrogen Q-disease and surface defects described in detail below.

7.2 Cooling system for studies of hydrogen Q disease

7.2.1 Hydrogen Q disease

Hydrogen Q-disease is a reduction of the quality factor caused by hydrogen contamination in the Niobium lattice. Hydrogen can penetrate the cavity surface during surface treatments if the natural oxide layer Nb_2O_5 which acts as a barrier is damaged. This can happen during buffered chemical polishing (BCP) [140], mechanical polishing such as centrifugal barrel polishing (CBP) or in earlier steps of the cavity production process.

At room temperature, hydrogen atoms are distributed on random tetrahedral interstitial sites in the Niobium lattice [141] forming a solid solution (α phase). This solution has solubility limit ~ 4 atomic percent of hydrogen at room temperature. During the cool down the solubility limit is reduced significantly, and as soon as it becomes lower than the bulk hydrogen concentration, Niobium and hydrogen start to form hydrides. While Niobium is a conventional superconductor with critical temperature $T_c = 9.25$ K, Niobium hydrides are non-superconducting at $T > 1.3$ K [141] and lead to quality factors about two orders of magnitude lower than the nominal.

Two solutions are known for overcoming hydrogen Q-disease: high-temperature annealing in an ultra-high vacuum (UHV) furnace [142] and fast cooling. The first method uses baking of Niobium cavities at 800-1000°C for 1-3 hours in order to reduce the bulk hydrogen concentration and prevent the formation of hydrides during cavity cooling. Hydride precipitation strictly depends on the time a cavity spent in the temperature range between about 70 and 170 K. Approximately 30 minutes in this temperature range are needed for the hydrides to start forming, and fast cooling also can be an effective method to decrease hydride precipitation. This second method is hard to use in practice due to limitations of the cooling systems in which Niobium cavities are cooled down to the operating temperature.

7.2.2 Cryocooler system setup

The test cryocooler system for cooling Niobium samples to super-low temperatures is displayed in Fig. 7.2. It consist of cold head 1 connected to helium compressor 2 and

placed in a chamber 4 with ultra-high vacuum, achieved through the use of a vacuum pump 3.
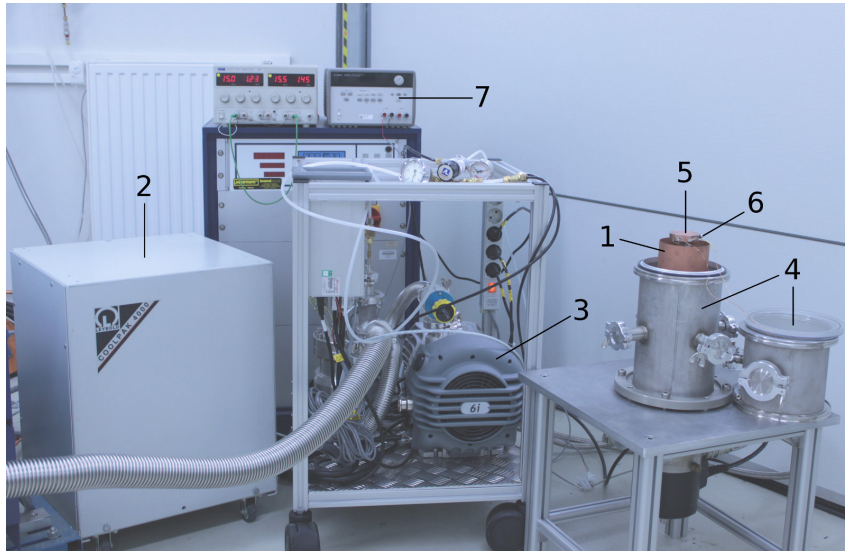
Figure 7.2: Cryocooler system setup. Labelled elements are: 1 - cold head (in shielding), 2 - helium compressor, 3 - vacuum pump, 4 - vacuum chamber, 5 - heating table, 6 - temperature sensor, 7 - power supply. Picture taken at the ILC-HiGrade laboratory.

Cold Head

Cold heads are parts of cryocooler systems at which cryogenic temperatures, i.e. temperatures below 120 K, are achieved. They are used in conjunction with compressor units to refrigerate small samples of test material for different analyses. The cold head system used for these studies is CoolPower 2/10 [143] manufactured by Leybold Vacuum. It is a double-stage cold head which can achieve temperatures down to 10 K; its schematic diagram is shown in Fig. 7.3 and main parameters are listed in Table 7.1.

The cold head is connected to the compressor unit with a pair of flexlines and operates in a closed helium gas cycle according to the Gifford-McMahon principle [144]. During this process, helium gas is compressed in a compressor and afterwards its pressure is decreased in the expansion volumes 1 and 13 (Fig. 7.3) of the cold head to generate low temperatures on cold stages 2 and 12. For this, a synchronous motor 6, supplied with electric power from the compressor unit, rotates a control valve 7 which controls the movement of the displacer piston 11. The displacer piston 11 of the first stage is mechanically interconnected with piston 3 of the second stage. Helium returns to the compressor from expansion volumes 1 and 13 through displacers 3 and 11. The refrigerating capacity of the two refrigeration stages depends on their temperature and the characteristic curves for these dependencies

Key

1 Expansion volume
2 Cold stage, copper flange } of the
3 Displacer   2nd stage
4 Regenerator

5 Helium fittings
6 Cold-head motor
7 Control valve
8 Control disc
9 Control piston

10 Regenerator
11 Displacer   } of the
12 Cold stage, copper flange   1st stage
13 Expansion volume
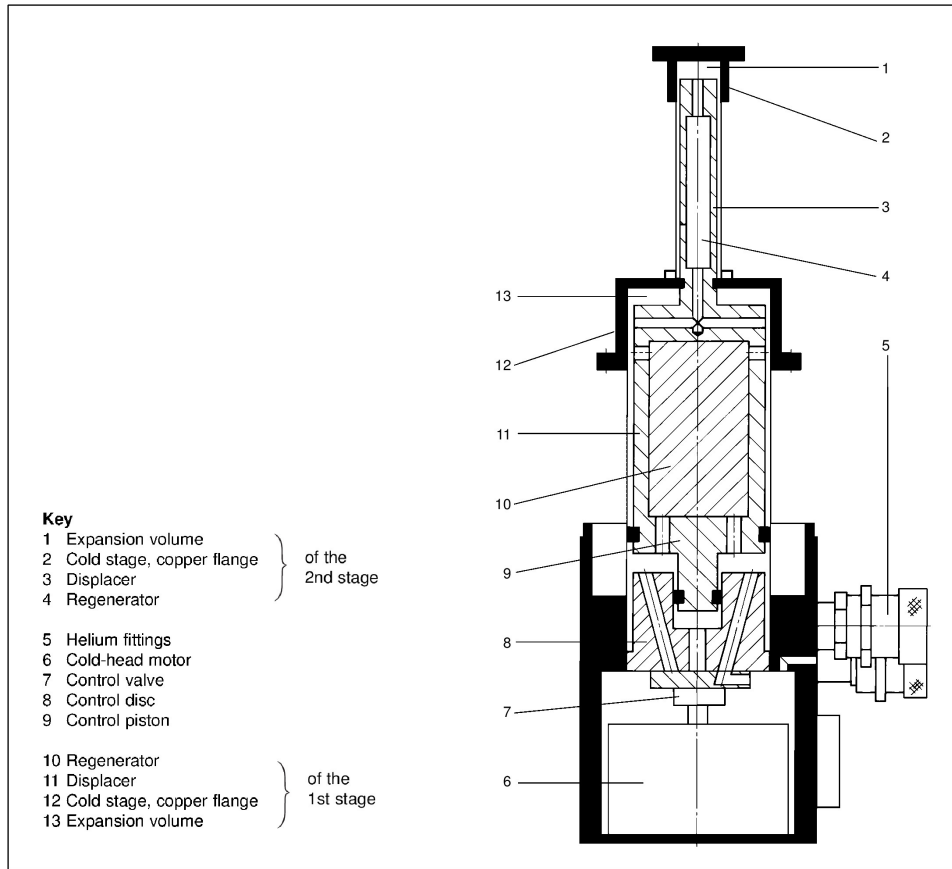
Figure 7.3: Schematic diagram of two-stage cold head CoolPower 2/10.

Cold head	CoolPower 2/10
Refrigerating capacity	
1st stage at $\sim$ 80 K	12 W
2nd stage at $\sim$ 20 K	2 W
Lowest achievable temperature	
1st stage	$\leq$ 35 K
2nd stage	$\leq$ 10 K
Cooldown time	
1st stage to $\sim$ 80 K	40 min
2nd stage to $\sim$ 20 K	35 min

Table 7.1: Technical data on CoolPower 2/10 system.

provided by the manufacturer are shown in Fig. 7.4.
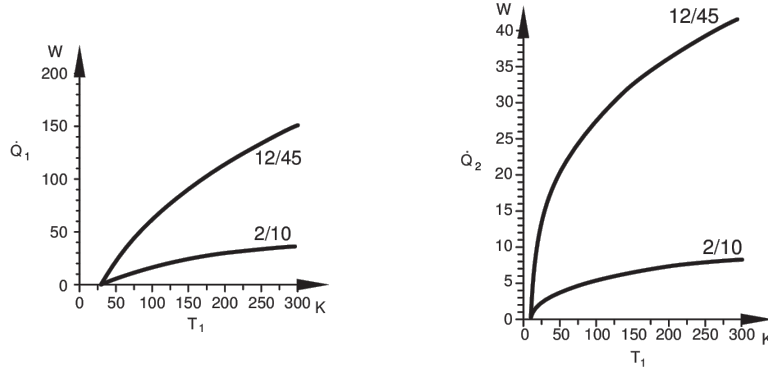
Figure 7.4: Refrigerating capacities as a function of the temperature for first (left) and second (right) stages. Curves marked with 2/10 correspond to CoolPower 2/10.

Helium compressor

A compressor unit CoolPak 4000 [145] from Leybold Vacuum is used in the laboratory to compress helium gas for the cold head. Main parts of the CoolPak and helium circuit are schematically presented in Fig. 7.5. After compression at compressor 1, the helium gas is cooled in the heat exchanger 2 in a helium/water counterflow and passed through a two-stage oil separator 3. The helium gas exiting the second oil separator will still contain small quantities of oil vapor, and in order to prevent it from entering the cold head and freezing there, helium gas is additionaly passed through an adsorber 4.

Vacuum pump

To reduce heat transfer to the cold head, it has to be used in a chamber with an insulating vacuum. An insulating vacuum suitable for normal operation of the cryocooler during long tests which may last for a few days is achieved with a turbopumping station. The pumping station operated in the ILC-HiGrade laboratory consists of a backing pump nXDS6i [146] and turbomolecular pump nEXT240 [147], both produced by Edwards Vacuum. The minimum pressure in the vacuum chamber achievable with this pumping station for the temperature on the second stage $T_{CH} \approx 300$ K is $2 \cdot 10^{-5}$ mbar, while for $T_{CH} \approx 10$ K pressures down to $2 \cdot 10^{-7}$ mbar can be achieved.

7.2.3 Heating-table for Cold Head

The main disadvantage of the described cryocooler system is that it does not provide any control over the temperature of the sample during the cooling process. Some hydride
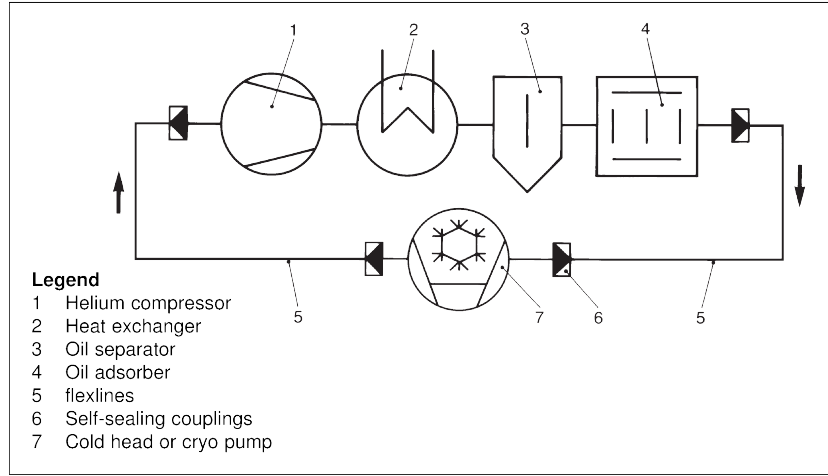
Figure 7.5: Schematic for the helium circuit.

analyses require keeping the samples at certain temperatures for some time, or cooling them with different cooling rates. To fulfill these requirements, a special heating table has been developed, produced and mounted on top of the second cold stage (label 2 in Fig. 7.3). A temperature sensor (T-sensor) is connected to the side of the table, and samples are placed on top of it.

Model of heat distribution

The heating table was made of copper with four $10\,\Omega$ resistors mounted inside. The table configuration with the most homogeneous temperature distribution on the top plane while also being simple to manufacture was chosen using the simulation. For this purpose a model of heat distribution was programmed in C++ using the explicit finite-difference method [148]. The table body was divided into equivalent cubic grid cells with side Δx. The temperature distribution was simulated for time starting from $t_0 = 0$ in intervals of Δt. For each grid cell, a set of three indices i, j, k was assigned such that its location can be expressed as $x = \Delta x \cdot i$, $y = \Delta x \cdot j$ and $z = \Delta x \cdot k$. At a time $t = \Delta t \cdot n$, the temperature T_{ijk}^n was calculated as

$$T_{ijk}^n = T_{ijk}^{n-1} + \mu(T_{(i+1)jk}^{n-1} + T_{i(j+1)k}^{n-1} + T_{ij(k+1)}^{n-1} - 6T_{ijk}^{n-1} + T_{(i-1)jk}^{n-1} + T_{i(j-1)k}^{n-1} + T_{ij(k-1)}^{n-1}) \ . \quad (7.2)$$

The parameter of stability, μ, is defined as

$$\mu = \frac{\lambda}{c\rho} \cdot \frac{\Delta t}{(\Delta x)^2} \ , \quad (7.3)$$

where λ is the thermal conductivity, c is the specific heat capacity and ρ is the volumetric mass density. To achieve a stable solution Δx and Δt should be chosen such that $\mu \leqslant$

$\frac{1}{2}$ [148].

This model has been used to simulate a cylindrical table with a height of 12 mm, diameter of 60 mm, starting temperature $\forall i, j, k : T_{ijk}^0 = 83$ K and total heating power from electrical resistors and cooling from the cold head set equivalent and equal to 20 W. Parameters λ, c and ρ for copper at this temperature were taken from a reference work by V. S. Chirkin [149] and are summarised in Table 7.2.

Thermal conductivity λ	480	$\frac{W}{m \cdot K}$
Specific heat capacity c	259	$\frac{J}{kg \cdot K}$
Volumetric mass density ρ	$9 \cdot 10^3$	$\frac{kg}{m^3}$

Table 7.2: Parameters of copper at the temperature of 83 K used for simulation of heating-table.

Configurations with four, six or eight resistors located equidistantly on different radii from the table axis and different height from the bottom plane were tested with $\Delta x = 0.5$ mm and $\Delta t = 1 \cdot 10^{-4}$ s, such that $\mu = 0.082$. A configuration with 4 resistors located on a radius of 13 mm and height of 4 mm was chosen for the production and modeled with $\Delta x = 0.2$ mm, $\Delta t = 1 \cdot 10^{-5}$ s ($\mu = 0.051$) for better resolution. The simulated heat distribution is shown on the left side of Fig. 7.6, while the right side displays the produced table mounted on stage 2 of the cold head.
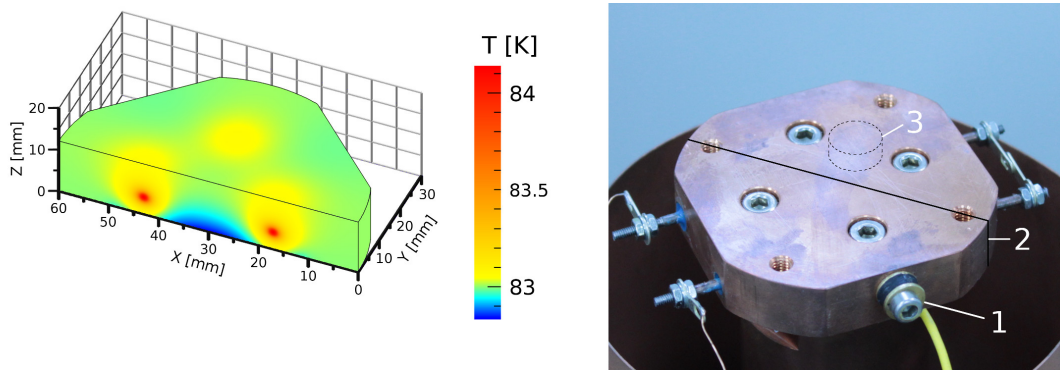
Figure 7.6: Model of heat distribution for the table cross section (left) and produced table mounted on the cold head (right). Labelled elements are: 1 - temperature sensor, 2 - plane of the cross section on the left side, 3 - possible placement of the Niobium sample.

Mathematical model of the cooling system

To approximate the cold-head and heating-table temperature dynamics in a temperature range 40 K $< T <$ 170 K, a simple mathematical model was used:

$$\frac{dT}{dt} = \frac{1}{C_p(T) \cdot M_{eff}(T)} \cdot [W_h - W_c(T) - W_{er}(T)] \quad . \tag{7.4}$$

There $C_p(T)$ is the specific heat of copper with temperature dependence taken from the Cryogenic Data Notebook by the Brookhaven National Laboratory [150], $M_{eff}(T)$ is an effective mass of the cooled system, W_h corresponds to the total heating power of the table, $W_c(T)$ represents the cooling power of the cold head plus thermal leakage to the environment and $W_{er}(T) \sim T^4$ is the heat radiation from the cold head and table surface. A set of cooling experiments with different values of W_h were performed, recording time from the start of the test, t, and temperature measured with the sensor, T. Using these data, the dependence of $M_{eff}(T)$ and $W_c(T)$ on temperature was evaluated and fitted with a third-order polynomial. Part of the temperature data from one experiment is compared to the prediction of Eq. 7.4 in Fig. 7.7.
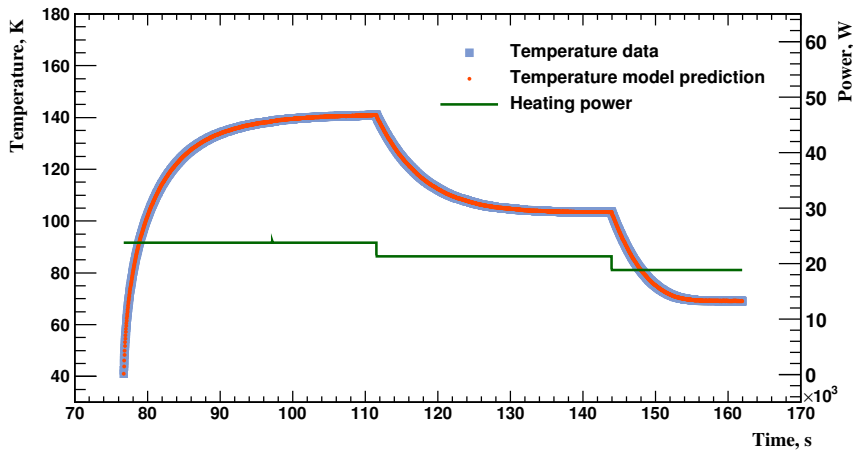
Figure 7.7: Example of the cryogenic system cooling experiment temperature data and prediction obtained from the mathematical model. The thickness of the lines is purely presentational.

Control over the cooling process

Using the mathematical model described above, a system to control the heating-table power was implemented into a cryosystem LabView interface, as shown in Fig. 7.8. The

interface for the cryosystem records the measured values of the temperature of the heating table, labelled as 3 in Fig. 7.8, pressure in the vacuum chamber 4 and power on the heating resistors 6 at the time intervals labelled as 1. The control system evaluates and sets a power on the heating table 5 such that cooling or heating rates correspond to the ones set by the user in the fields 7 and 8 and the temperature reaches the value set in the field 9.
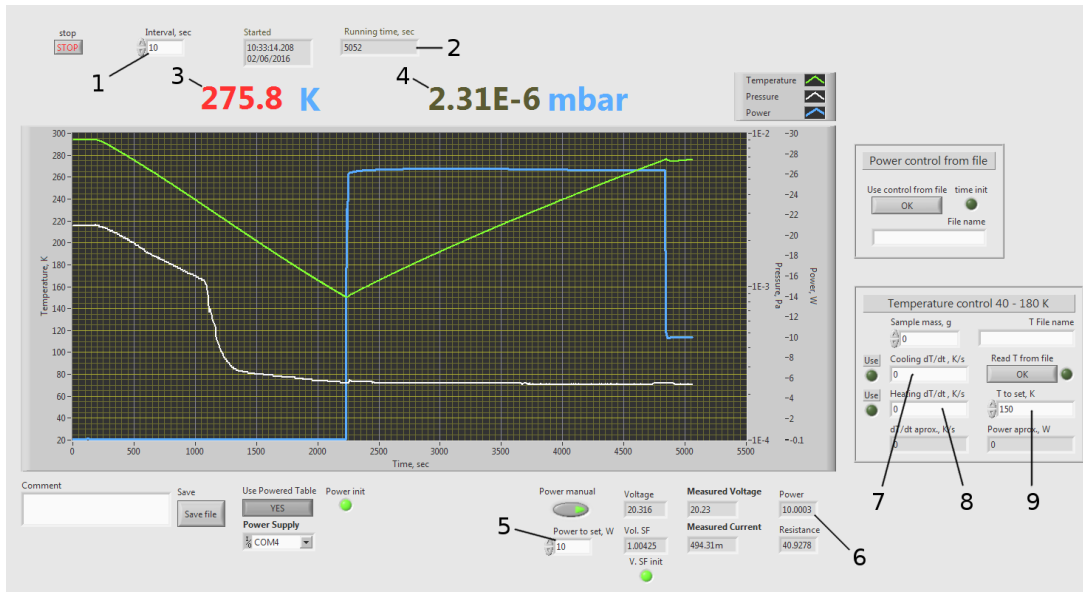
Figure 7.8: LabView interface for the cryosystem readout and heating-table controls: 1 - interval of time between readouts, 2 - time from the start of the data recording, 3 - current temperature measured by the temperature sensor, 4 - pressure in the vacuum chamber, 5 - heating power to be set, 6 - measured power of the heating resistors, 7 and 8 - required cooling and heating rates, respectively, and 9 - temperature to be set.

7.2.4 Results for hydrogen-enriched Niobium cooling

A Niobium sample from the same material which was used in the cavity production had been enriched with hydrogen by removing a surface layer of 95 μm with electro-chemical polishing. A differential interference contrast (DIC) image of the prepared sample surface is shown in Fig. 7.9 (a). The current cryocooler system and the laser scanning microscope at the ILC-HiGrade laboratory does not allow the sample surface to be scanned during cooling and surface images can be taken only after heating up, when all hydrides have disappeared. However, the formation of hydrides makes an irreversible change to the Niobium lattice structure that can be observed on the surface even after the hydrides disappear.

A set of cooling experiments was made to check the surface profile left by hydride growth under different cooling conditions. Sample surface images after four such experiments with recorded temperature and heating power data are presented in Fig. 7.9 (b) - (e). For test (b), the sample was cooled to 100 K, for (c) it was held at 140 K for $\sim$ 4 hours, cooling (d) was done without use of the heating table, while for (e) a cooling rate of -0.0024 K/s was set. After cooling in tests (b), (c) and (e), the sample was heated rapidly using the heating table, and in test (d) it was left in the vacuum chamber to heat steadily. On the DIC image after test (b), only small transformations of the sample surface can be seen, which almost had not changed after test (c). On image (d), hydride marks are clearly visible, and after test (e) they are large enough to distinguish different orientation of the hydrides. These results show that the heating table together with the control system can be effectively used for experiments on hydride growth.
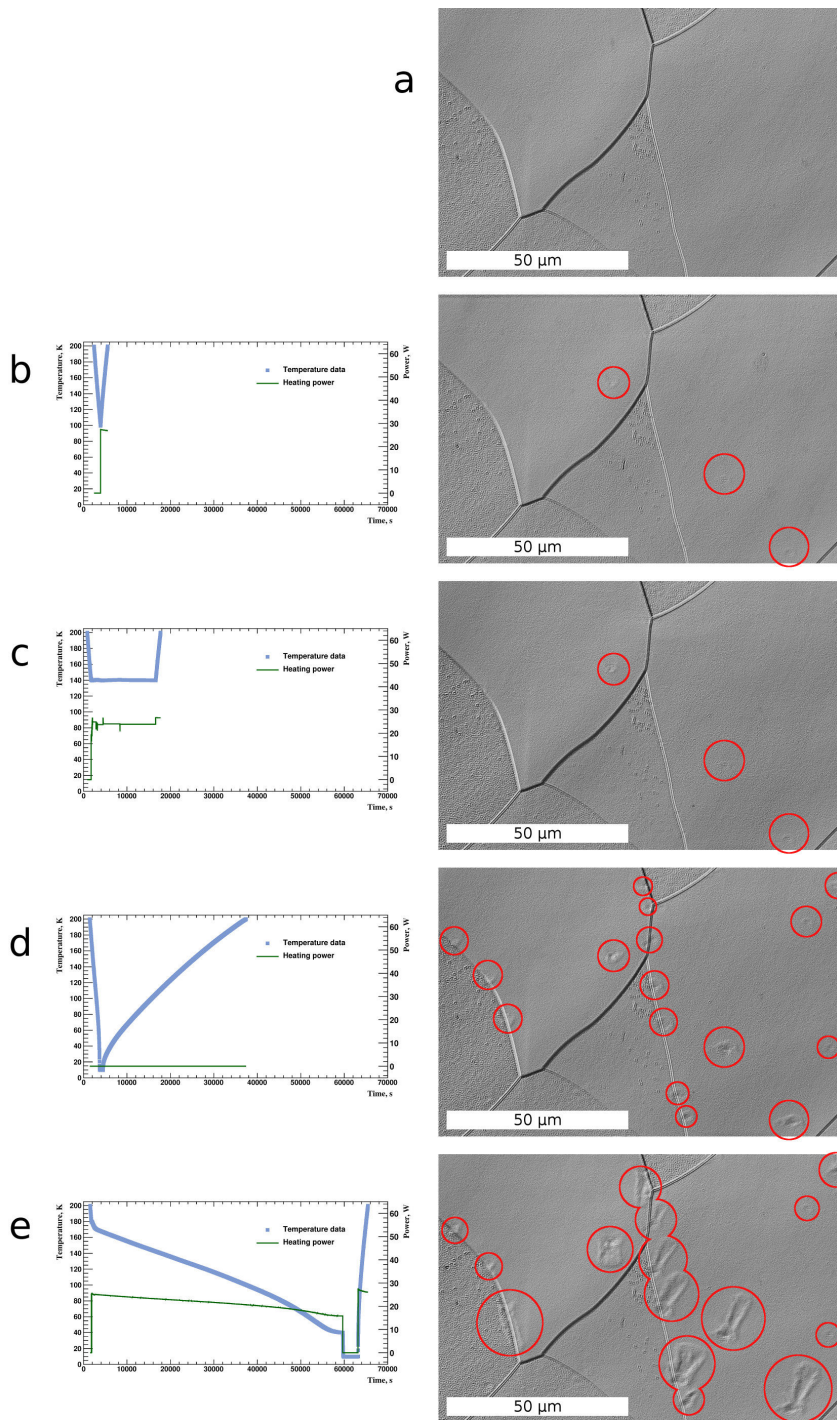
Figure 7.9: Surface relief of hydrogen-enriched Niobium after different cooling tests: a - initial sample, b - cooling to 100 K, c - holding at 140 K for 247 minutes, d - cooling without use of the heating-table, e - slow cooling with an average rate of -0.0024 K/s. Circles represent the features referred to in the text.

7.3 Optical inspection of cavity defects

When cavity fabrication conditions deviate from the ideal ones, defects or foreign material inclusions may occur on the inner cavity surface. This may happen if some dust is present on the welding seam, if the welding was not deep enough or if some foreign material is present on the inner surface during chemical or electric polishing. Geometrical defects of the Niobium surface can lead to a local rise of the magnetic field above the critical value during cavity operation, an effect called a magnetic quench. Inclusions of foreign materials that are not superconducting cause Joule heating and thus a thermal quench. In both cases, a local transition to the normal-conducting phase occurs, followed by a global thermal breakdown. If a cavity shows such behaviour during a cold radio-frequency test, its inner surface can be inspected by an optical system, which is the most inexpensive and useful option of surface diagnosis [151]. An example of the equator welding seam and cell surface near a good-quality equator are displayed in Fig. 7.10 and the types of observed defects are described in section 7.3.2.
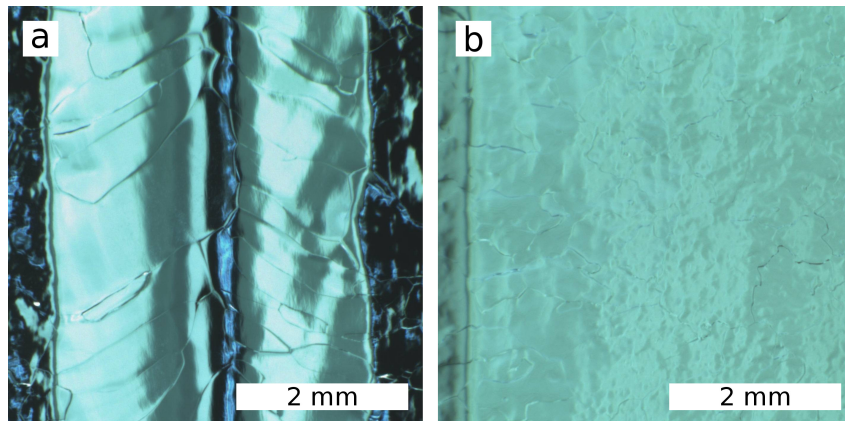
Figure 7.10: The OBACHT images of equator (a) and cell (b) surface without defects.

7.3.1 OBACHT system

The OBACHT system [135] based on the Kyoto camera system [151] has been developed at the ILC-HiGrade laboratory. It is a semi-automated tool for optical inspection of cavity inner surfaces with a graphical user interface (GUI) based on LabView. The OBACHT with a cavity prepared for inspection is displayed in Fig. 7.11. It consists of a moveable sled (labelled as 2) for cavity (1) movement during inspection and a high-resolution camera with special illumination system mounted in a cylinder rod (3) which is rotated by a torque motor (4). A standard cavity inspection [151] concentrates on the welding seams at the equators and irises (labelled 1 and 2 in Fig. 7.1, correspondingly) plus the areas to the left and right of the equator welding seams. After installation of the cavity and

measuring the exact positions of all nine equator welding seams, which are different for each cavity, the OBACHT system automatically takes approximately 3000 images in 8 hours, each covering a cavity area of 12x9 mm with better than 10 μm resolution.
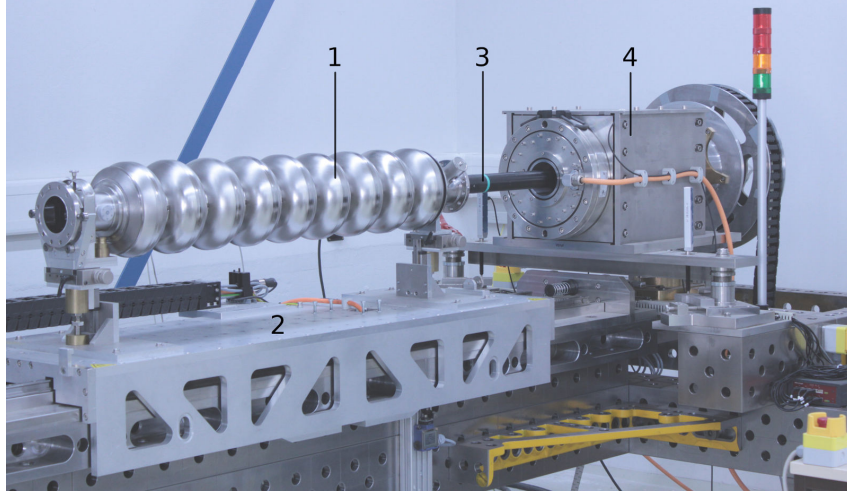
Figure 7.11: The OBACHT system with cavity CAV00707 (labelled 1) mounted on the moveable sled (2) and prepared for the optical inspection. During inspection, camera rod (3) rotates with the torque motor (4). Picture taken at the ILC-HiGrade laboratory.

7.3.2   Surface defects

In the scope of this work 28 optical inspections of SCRF cavities were done. Six main groups of defects were observed: scratches, surface erosion, "cat eyes", etching pits, rough surface and dust. Typical examples of these defects are shown in Fig 7.12.

Scratches

Scratches (labelled as "a" in Fig 7.12) are usually an indication of some error during cavity production or handling that resulted in mechanical damage of the Niobium surface. The sharp edges of the scratches enhance the electron field emission during cavity RF tests or operation, resulting in excessive X-ray radiation [151]. The repair of such a defect requires local grinding, heavy chemical polishing, retuning of the cavity (mechanical change of the cavity shape to achieve the required resonance frequency) and repetition of the whole surface preparation procedure. This cannot be done at the ILC-HiGrade laboratory and requires other DESY facilities.
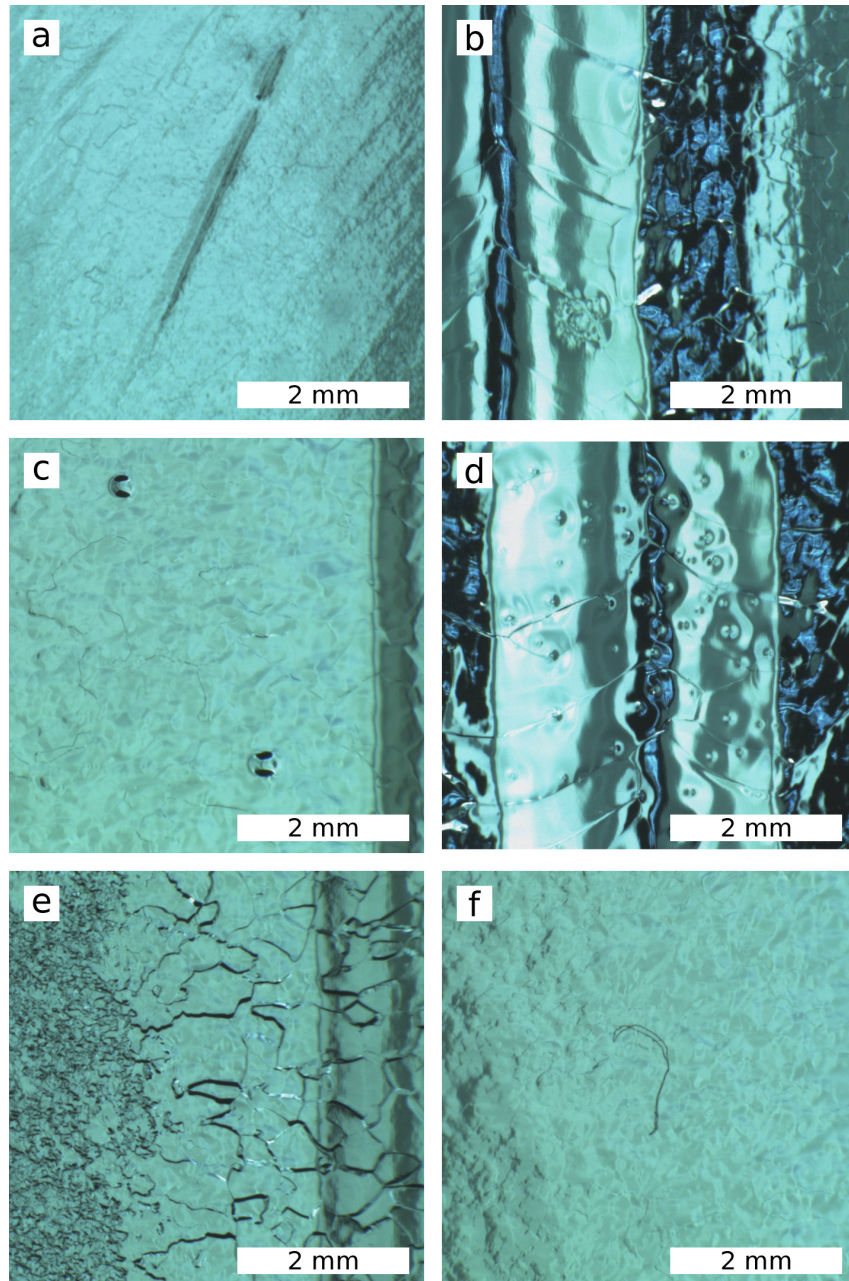
Figure 7.12: Six types of defects observed on SCRF cavities inner surface during OBACHT inspections: a - scratch, b - surface erosion, c - "cat eyes", d - etching pits, e - rough surface and f - dust.

Surface erosion

The local surface erosion ("b") can happen on the equator welding seam due to the presence of a foreign inclusion on the Niobium surface before welding. It limits the cavity performance by producing thermal breakdown without any radiation. Efforts to remove foreign material by mechanically removing a 150 μm thick layer of Niobium with a CBP machine in the laboratory ended in failure and showed that pollution goes deep into the Niobium layer. A successful repair procedure has not yet been developed.

"Cat eyes" and etching pits

The reason for the defects called "cat eyes" ("c") is still under investigations. Surface shape studies indicate that these are rounded etching holes [134] created during the chemical polishing and most probably originate from local material defects or inclusions. Removal of these defects requires a procedure similar to the repair of surface erosion, making it expensive and time-consuming. Since several cavities with these type of defects showed excellent results, even exceeding ILC specifications, they are usually left untreated.

The etching pits ("d") are most likely also created during the etching process, but because of hydrogen bubbles sticking to the Niobium surface. Similarly to the "cat eyes" they do not seem to affect cavity performance and are believed to be harmless.

Rough surface

The rough surface ("e") artefact appears as the result of improper chemical polishing parameters like acid temperature, current density etc. It appears during the chemical polishing because of different polishing rates at different grains in the Niobium lattice orientation and leads to steps between the grains. Cavities with a rough surface usually show a very low quality factor Q_0 and achievable accelerating gradient E_{acc}. Chemical or mechanical polishing is required to smooth the sharp edges between the grains. Mechanical polishing can be applied in the ILC-HiGrade laboratory but afterwards the cavity will need baking to remove hydrogen from the Niobium lattice and high-pressure ultra-pure water rinsing to remove contaminations on the surface, which can be done at other DESY facilities.

Dust

The contamination of the cavity surface with dust ("f") can happen if the cavity is stored with opened flanges outside the cleanroom. The OBACHT inspection is performed with both flanges removed and can lead to some pollution, so it is hard to judge if the observed particles or fibers were present before the inspection. Dust particles on the iris regions can lead to enhanced X-ray radiation, and dust at the equators may cause low Q_0 or early

quenches [151]. Only one high-pressure ultra-pure water rinsing applied to a polluted cavity in the cleanroom is usually enough to fully recover its performance.

Summary

All of the defects observed during 28 optical inspections were classified and divided into six main groups. For each group a relation between the presence of the defect and performance in the cold RF tests was studied and a treatment for the types of defects with significant influence was sought. These studies have contributed to the understanding of the accelerating-field gradient limitations for SCRF cavities due to surface defects and treatments which can recover their performance.

Summary

Final measurements of the inclusive neutral and charged current unpolarised electron-proton inelastic scattering, performed by the ZEUS and H1 collaborations from 1994 to 2007, corresponding to an integrated luminosity of 1 fb^{-1}, have been combined. The data from two different experiments and two different beam configurations, called HERA I and HERA II, have proven to be consistent with a χ^2 per degree of freedom being 1.04 for the combination. The combined cross sections span the values of negative four-momentum-transfer squared, Q^2, from $Q^2 = 0.045$ GeV^2 to $Q^2 = 50000$ GeV^2 and values of Bjorken x from $x_{\mathrm{Bj}} = 6 \times 10^{-7}$ to $x_{\mathrm{Bj}} = 0.65$. All correlations of systematic uncertainties and global normalisations were taken into account, resulting in their significant reduction and providing a coherent set of data. The obtained cross sections are so far the most precise measurements of the ep inelastic scattering ever published and constitute a legacy of HERA.

The combined data were used as an input to a QCD analysis within the DGLAP formalism, providing the parton density functions (PDFs) ZCIPDF. The inclusive cross sections were also used in the beyond-the-Standard-Model analyses employing simultaneous fits of PDFs and BSM parameters on sets of Monte Carlo replicas. To reduce the calculation time of the combined fits of MC replicas, a simplified approach was developed. It allowed the computation time for the limits to be reduced by about a factor of 50. The combined analysis of PDFs and quark form factor yield the 95% C.L. limits of the effective quark radius of

$$-(0.47 \cdot 10^{-16} \text{ cm})^2 < R_{\mathrm{q}}^2 < (0.43 \cdot 10^{-16} \text{ cm})^2 \quad .$$

These limits are significantly stronger than previously published ZEUS limits [118] of $-(1.06 \cdot 10^{-16}\text{cm})^2 < R_{\mathrm{q}}^2 < (0.85 \cdot 10^{-16}\text{cm})^2$ and the H1 limit [119] of $R_q < 0.65 \cdot 10^{-16}$ cm. The upper limit is comparable to the limit evaluated by the L3 collaboration [120], $R_q < 0.42 \cdot 10^{-16}$ cm. The possible BSM physics processes parameterised by the fermion form factor at LEP and HERA might be different and therefore the presented limits are to a great extent complementary.

The analysis within the context of contact interactions provided the 95% C.L. limits on compositeness scale Λ^- (Λ^+) for the LL model of 22.0 (4.5) TeV. The HERA combined data have shown the highest sensitivity to the VV model with the measured 95% C.L. limits of 14.7 (9.5) TeV. These limits are weaker than limits evaluated by the Atlas [123] and

CMS [124] collaborations, and are comparable to the limits obtained by the ALEPH [125] and DELPHI [127] experiments. The VA, X1 and X2 contact-interaction models were not considered in the LHC or LEP2 analyses and the obtained limits are the strongest limits currently available.

The analysis has shown that taking into account the possible influence of quark radii or general-contact interaction parameters on the PDF parameters is essential since the limits that would be obtained using the PDF parameters obtained in a fit assuming only QCD effects are too strong by about 10 %.

As a technical task, an optical inspection of 28 superconducting radio-frequency cavities was performed and observed defects were classified and their effect on the accelerating gradient studied. A controllable cooling system for studies of hydride formation on Niobium samples was developed and successfully tested.

Bibliography

[1] *A few holes to fill, Nature Physics* **4** (Apr, 2008) 257–257.

[2] TASSO Collaboration, R. Brandelik et al., *Evidence for Planar Events in e+ e-Annihilation at High-Energies, Phys. Lett.* **B86** (1979) 243–249.

[3] JADE Collaboration, W. Bartel et al., *Observation of Planar Three Jet Events in e+ e- Annihilation and Evidence for Gluon Bremsstrahlung, Phys. Lett.* **B91** (1980) 142–147.

[4] D. P. Barber et al., *Discovery of Three Jet Events and a Test of Quantum Chromodynamics at PETRA Energies, Phys. Rev. Lett.* **43** (1979) 830.

[5] PLUTO Collaboration, C. Berger et al., *Evidence for Gluon Bremsstrahlung in e+ e- Annihilations at High-Energies, Phys. Lett.* **B86** (1979) 418–425.

[6] UA1 Collaboration, G. Arnison et al., *Experimental Observation of Isolated Large Transverse Energy Electrons with Associated Missing Energy at $\sqrt{s} = 540$ GeV, Phys. Lett.* **B122** (1983) 103–116.

[7] UA2 Collaboration, M. Banner et al., *Observation of Single Isolated Electrons of High Transverse Momentum in Events with Missing Transverse Energy at the CERN anti-p p Collider, Phys. Lett.* **B122** (1983) 476–485.

[8] CDF Collaboration, F. Abe et al., *Observation of top quark production in $\bar{p}p$ collisions, Phys. Rev. Lett.* **74** (1995) 2626–2631, [`hep-ex/9503002`].

[9] D0 Collaboration, S. Abachi et al., *Observation of the top quark, Phys. Rev. Lett.* **74** (1995) 2632–2637, [`hep-ex/9503003`].

[10] CMS Collaboration, S. Chatrchyan et al., *Observation of a new boson at a mass of 125 GeV with the CMS experiment at the LHC, Phys. Lett.* **B716** (2012) 30–61, [`arXiv:1207.7235`].

[11] ATLAS Collaboration, G. Aad et al., *Observation of a new particle in the search for the Standard Model Higgs boson with the ATLAS detector at the LHC*, Phys. Lett. **B716** (2012) 1–29, [`arXiv:1207.7214`].

[12] M. Thomson, *Modern particle physics.* Cambridge University Press, New York (2013).

[13] C. P. Burgess and G. D. Moore, *The standard model: A primer.* Cambridge University Press (2006).

[14] H. Abramowicz et al., *Combination of measurements of inclusive deep inelastic $e\pm p$ scattering cross sections and QCD analysis of HERA data*, Eur. Phys. J. **C75** (2015), No. 12, 1–98.

[15] Particle Data Group Collaboration, C. Patrignani et al., *Review of Particle Physics*, Chin. Phys. **C40** (2016), No. 10, 100001.

[16] R. Devenish and A. Cooper-Sarkar, *Deep Inelastic Scattering.* Oxford University Press (2004).

[17] ZEUS Collaboration, S. Chekanov et al., *Search for contact interactions, large extra dimensions and finite quark radius in ep collisions at HERA*, Phys. Lett. **B591** (2004) 23–41, [`hep-ex/0401009`].

[18] G. 't Hooft and M. Veltman, *Regularization and Renormalization of Gauge Fields*, Nucl. Phys. **B44** (1972) 189–213.

[19] S. Fanchiotti, B. A. Kniehl, and A. Sirlin, *Incorporation of QCD effects in basic corrections of the electroweak theory*, Phys. Rev. **D48** (1993) 307–331, [`hep-ph/9212285`].

[20] Particle Data Group Collaboration, K. A. Olive et al., *Review of Particle Physics*, Chin. Phys. **C38** (2014) 090001.

[21] V. N. Gribov and L. N. Lipatov, *Deep inelastic e p scattering in perturbation theory*, Sov. J. Nucl. Phys. **15** (1972) 438–450. [Yad. Fiz.15,781(1972)].

[22] V. N. Gribov and L. N. Lipatov, *e+ e- pair annihilation and deep inelastic e p scattering in perturbation theory*, Sov. J. Nucl. Phys. **15** (1972) 675–684. [Yad. Fiz.15,1218(1972)].

[23] L. N. Lipatov, *The parton model and perturbation theory*, Sov. J. Nucl. Phys. **20** (1975) 94–102. [Yad. Fiz.20,181(1974)].

[24] Y. L. Dokshitzer, *Calculation of the Structure Functions for Deep Inelastic Scattering and e+ e- Annihilation by Perturbation Theory in Quantum Chromodynamics.*, *Sov. Phys. JETP* **46** (1977) 641–653. [Zh. Eksp. Teor. Fiz.73,1216(1977)].

[25] G. Altarelli and G. Parisi, *Asymptotic Freedom in Parton Language*, *Nucl. Phys.* **B126** (1977) 298–318.

[26] R. S. Thorne and R. G. Roberts, *An Ordered analysis of heavy flavor production in deep inelastic scattering*, *Phys. Rev.* **D57** (1998) 6871–6898, [hep-ph/9709442].

[27] R. S. Thorne, *A Variable-flavor number scheme for NNLO*, *Phys. Rev.* **D73** (2006) 054019, [hep-ph/0601245].

[28] R. S. Thorne, *Effect of changes of variable flavor number scheme on parton distribution functions and predicted cross sections*, *Phys. Rev.* **D86** (2012) 074017, [arXiv:1201.6180].

[29] P. Haberl, F. Schrempp, and H. U. Martyn, *Contact interactions and new heavy bosons at HERA: A Model independent analysis*, in *Workshop on Physics at HERA Hamburg, Germany, October 29-30, 1991* (W. Buchmuller and G. Ingelman, eds.), pp. 1133–1148, 1991.

[30] W. J. Marciano and A. Sirlin, *Radiative corrections to pi(lepton 2) decays*, *Phys. Rev. Lett.* **71** (1993) 3629–3632.

[31] G. Köpp et al., *Bounds on radii and magnetic dipole moments of quarks and leptons from LEP, SLC and HERA*, *Z. Phys.* **C65** (1995) 545–550, [hep-ph/9409457].

[32] *HERA - A Proposal for a Large Electron Proton Colliding Beam Facility at DESY* (1981).

[33] P. Schmüser, *The electron-proton colliding beam facility HERA*, *Nucl. Instrum. Meth.* **A235** (1985), No. 2, 201 – 208.

[34] H1 Collaboration, I. Abt et al., *The H1 detector at HERA*, *Nucl. Instrum. Meth.* **A386** (1997), No. 2, 310 – 347.

[35] H1 Collaboration, I. Abt et al., *The tracking, calorimeter and muon detectors of the H1 experiment at HERA*, *Nucl. Instrum. Meth.* **A386** (1997), No. 23, 348 – 396.

[36] HERMES Collaboration, K. Ackerstaff et al., *The HERMES spectrometer*, *Nucl. Instrum. Meth.* **A417** (1998) 230–265, [hep-ex/9806008].

[37] ZEUS Collaboration, "The ZEUS Detector. Status Report 1993." http://www-zeus.desy.de/bluebook/bluebook.html (February 1993).

[38] HERA-B Collaboration, E. P. Hartouni et al., *HERA-B: An experiment to study CP violation in the B system using an internal target at the HERA proton ring. Design report* (1995).

[39] HERA-B Collaboration, *HERA-B: Report on status and prospects October 2000. Executive summary* (2000).

[40] ZEUS Collaboration, S. Chekanov et al., *Measurement of the Longitudinal Proton Structure Function at HERA*, Phys. Lett. **B682** (2009) 8–22, [arXiv:0904.1092].

[41] H1 Collaboration, V. Andreev et al., *Measurement of inclusive ep cross sections at high Q^2 at $\sqrt{s} = 225$ and 252 GeV and of the longitudinal proton structure function F_L at HERA*, Eur. Phys. J. **C74** (2014), No. 4, 2814, [arXiv:1312.4821].

[42] U. Schneekloth, *The HERA luminosity upgrade* (1998).

[43] ZEUS Collaboration, A. Caldwell et al., *On the New Beam Pipe Calorimeter*, ZEUS-94-129, internal ZEUS note (1994).

[44] ZEUS Collaboration, A. Caldwell et al., *A Silicon Tracker for BPC and a Possible Upgrade to BPCIII*, ZEUS-96-044, internal ZEUS note (1996).

[45] N. Cartiglia and R. Sacchi, *The Leading Proton Spectrometer of ZEUS*, Nucl. Instrum. Meth. **A579** (2007), No. 2, 572 – 574. Proceedings of the 6th "Hiroshima" Symposium on the Development and Application of Semiconductor Detectors.

[46] ZEUS Collaboration, B. Foster et al., *The design and construction of the ZEUS central tracking detector*, Nucl. Instrum. Meth. **A338** (1994), No. 23, 254 – 283.

[47] ZEUS Collaboration, B. Foster et al., *The Performance of the Zeus central tracking detector z-by-timing electronics in a transputer based data acquisition system*, Nucl. Phys. Proc. Suppl. **32** (1993) 181–188.

[48] D. Bailey and R. Hall-Wilton, *Experience with the ZEUS central tracking detector*, Nucl. Instrum. Meth. **A515** (2003), No. 12, 37 – 42. Proceedings of the International Workshop on Aging Phenomena in Gaseous Detectors.

[49] ZEUS Collaboration, C. Alvisi et al., *The ZEUS vertex detector: design and prototype*, Nucl. Instrum. Meth. **A305** (1991), No. 1, 30 – 38.

[50] ZEUS Collaboration, A. Polini et al., *The design and performance of the ZEUS micro vertex detector*, Nucl. Instrum. Meth. **A581** (2007), No. 3, 656 – 686.

[51] ZEUS Collaboration, H. Abramowicz et al., *Search for a narrow baryonic state decaying to pK_S^0 and $\bar{p}K_S^0$ in deep inelastic scattering at HERA*, Phys. Lett. **B759** (2016) 446–453, [arXiv:1604.02220].

[52] J. Krüger, *The Uranium scintillator calorimeter for the ZEUS detector at the electron - proton collider HERA: The Heart of ZEUS*, Ph.D. thesis, Hamburg U. (1992).

[53] ZEUS, ZEUS Calorimeter Group Collaboration, A. Andresen et al., *Construction and beam test of the ZEUS forward and rear calorimeter*, Nucl. Instrum. Meth. **A309** (1991) 101–142.

[54] ZEUS Luminosity Group Collaboration, J. Andruszkow et al., *Luminosity measurement in the ZEUS experiment*, Acta Phys. Polon. **B32** (2001) 2025–2058.

[55] ZEUS Collaboration, L. Adamczyk et al., *Measurement of the Luminosity in the ZEUS Experiment at HERA II*, Nucl. Instrum. Meth. **A744** (2014) 80–90, [`arXiv:1306.1391`].

[56] H. Bethe and W. Heitler, *On the stopping of fast particles and on the creation of positive electrons*, Proceedings of the Royal Society of London A: Mathematical, Physical and Engineering Sciences **146** (1934), No. 856, 83–112, [`http://rspa.royalsocietypublishing.org/content/146/856/83.full.pdf`].

[57] W. H. Smith, K. Tokushuku, and L. W. Wiggers, *The ZEUS trigger system*, in *6th International Conference on Computing in High-Energy and Nuclear Physics (CHEP 1992) Annecy, France, Sept 21-25, 1992*, pp. 222–225, 1992.

[58] ZEUS Collaboration, R. Carlin et al., *Experience with the ZEUS trigger system*, Nucl. Phys. Proc. Suppl. **44** (1995) 430–434.

[59] C. Kleinwort, *H1 Alignment Experience*, in *Proceedings of the First LHC Detector Alignment Workshop* (S. Blusk et al., eds.), pp. 41–48, 2007.

[60] H1 Collaboration, D. Pitzl et al., *The H1 silicon vertex detector*, Nucl. Instrum. Meth. **A454** (2000) 334–349, [`hep-ex/0002044`].

[61] M. Nozicka, *The forward and backward silicon trackers of H1*, Nucl. Instrum. Meth. **A501** (2003), No. 1, 54 – 59. Proceedings of the 10th International Workshop on Vertex Detectors.

[62] H1 Collaboration, B. Andrieu et al., *Results from pion calibration runs for the H1 liquid argon calorimeter and comparisons with simulations*, Nucl. Instrum. Meth. **A336** (1993), No. 3, 499 – 509.

[63] H1 Collaboration, T. Nicholls et al., *Performance of an electromagnetic lead/scintillating-fibre calorimeter for the H1 detector*, Nucl. Instrum. Meth. **A374** (1996), No. 2, 149 – 156.

[64] H1 Collaboration, R. D. Appuhn et al., *The H1 lead/scintillating-fibre calorimeter*, *Nucl. Instrum. Meth.* **A386** (1997), No. 2, 397 – 408.

[65] H1 Collaboration, T. Ahmed et al., *Experimental study of hard photon radiation processes at HERA*, *Z. Phys.* **C66** (1995) 529–542.

[66] H1 Collaboration, F. D. Aaron et al., *Determination of the Integrated Luminosity at HERA using Elastic QED Compton Events*, *Eur. Phys. J.* **C72** (2012) 2163, [`arXiv:1205.2448`]. [Erratum: Eur. Phys. J.C74,2733(2012)].

[67] H1 Collaboration, F. D. Aaron et al., *Inclusive Deep Inelastic Scattering at High Q^2 with Longitudinally Polarised Lepton Beams at HERA*, *JHEP* **09** (2012) 061, [`arXiv:1206.7007`].

[68] H1 Collaboration, "H1 Trigger System." https://www-h1.desy.de/trigger/ [Online; accessed 07-January-2017].

[69] H1 Collaboration, A. Schöning, *A fast track trigger for the H1 collaboration*, *Nucl. Instrum. Meth.* **A518** (2004) 542–543.

[70] H1 Collaboration, A. Schöning, *The Fast Track Trigger at the H1 experiment design concepts and algorithms*, *Nucl. Instrum. Meth.* **A566** (2006) 130–132.

[71] H1 Collaboration, F. D. Aaron et al., *Measurement of the Inclusive ep Scattering Cross Section at Low Q^2 and x at HERA*, *Eur. Phys. J.* **C63** (2009) 625–678, [`arXiv:0904.0929`].

[72] H1 Collaboration, F. D. Aaron et al., *A Precision Measurement of the Inclusive ep Scattering Cross Section at HERA*, *Eur. Phys. J.* **C64** (2009) 561–587, [`arXiv:0904.3513`].

[73] H1 Collaboration, C. Adloff et al., *Measurement of neutral and charged current cross-sections in positron proton collisions at large momentum transfer*, *Eur. Phys. J.* **C13** (2000) 609–639, [`hep-ex/9908059`].

[74] H1 Collaboration, C. Adloff et al., *Measurement of neutral and charged current cross-sections in electron - proton collisions at high Q^2*, *Eur. Phys. J.* **C19** (2001) 269–288, [`hep-ex/0012052`].

[75] H1 Collaboration, C. Adloff et al., *Measurement and QCD analysis of neutral and charged current cross-sections at HERA*, *Eur. Phys. J.* **C30** (2003) 1–32, [`hep-ex/0304003`].

[76] ZEUS Collaboration, J. Breitweg et al., *Measurement of the proton structure function F_2 and $\sigma_{tot}^{\gamma^* p}$ at low Q^2 and very low x at HERA, Phys. Lett.* **B407** (1997) 432–448, [`hep-ex/9707025`].

[77] ZEUS Collaboration, J. Breitweg et al., *Measurement of the proton structure function F_2 at very low Q^2 at HERA, Phys. Lett.* **B487** (2000) 53–73, [`hep-ex/0005018`].

[78] ZEUS Collaboration, J. Breitweg et al., *ZEUS results on the measurement and phenomenology of F_2 at low x and low Q^2, Eur. Phys. J.* **C7** (1999) 609–630, [`hep-ex/9809005`].

[79] ZEUS Collaboration, S. Chekanov et al., *Measurement of the neutral current cross-section and F_2 structure function for deep inelastic $e^+ p$ scattering at HERA, Eur. Phys. J.* **C21** (2001) 443–471, [`hep-ex/0105090`].

[80] ZEUS Collaboration, J. Breitweg et al., *Measurement of high Q^2 charged current $e^+ p$ deep inelastic scattering cross-sections at HERA, Eur. Phys. J.* **C12** (2000) 411–428, [`hep-ex/9907010`]. [Erratum: Eur. Phys. J.C27,305(2003)].

[81] ZEUS Collaboration, S. Chekanov et al., *Measurement of high Q^2 $e^- p$ neutral current cross-sections at HERA and the extraction of xF_3, Eur. Phys. J.* **C28** (2003) 175–201, [`hep-ex/0208040`].

[82] ZEUS Collaboration, S. Chekanov et al., *Measurement of high Q^2 charged current cross-sections in $e^- p$ deep inelastic scattering at HERA, Phys. Lett.* **B539** (2002) 197–217, [`hep-ex/0205091`]. [Erratum: Phys. Lett.B552,308(2003)].

[83] ZEUS Collaboration, S. Chekanov et al., *High Q^2 neutral current cross-sections in $e^+ p$ deep inelastic scattering at $\sqrt{s} = 318$ GeV, Phys. Rev.* **D70** (2004) 052001, [`hep-ex/0401003`].

[84] ZEUS Collaboration, S. Chekanov et al., *Measurement of high Q^2 charged current cross-sections in $e^+ p$ deep inelastic scattering at HERA, Eur. Phys. J.* **C32** (2003), No. 1, 1–16, [`hep-ex/0307043`].

[85] H1 Collaboration, F. D. Aaron et al., *Measurement of the Inclusive $e^{\pm} p$ Scattering Cross Section at High Inelasticity y and of the Structure Function F_L, Eur. Phys. J.* **C71** (2011) 1579, [`arXiv:1012.4355`].

[86] ZEUS Collaboration, H. Abramowicz et al., *Measurement of high-Q^2 neutral current deep inelastic $e^+ p$ scattering cross sections with a longitudinally polarized positron beam at HERA, Phys. Rev.* **D87** (2013), No. 5, 052014, [`arXiv:1208.6138`].

[87] ZEUS Collaboration, H. Abramowicz et al., *Measurement of high-Q^2 charged current deep inelastic scattering cross sections with a longitudinally polarised positron beam at HERA*, Eur. Phys. J. **C70** (2010) 945–963, [`arXiv:1008.3493`].

[88] ZEUS Collaboration, S. Chekanov et al., *Measurement of high-Q^2 neutral current deep inelastic e^-p scattering cross sections with a longitudinally polarised electron beam at HERA*, Eur. Phys. J. **C62** (2009) 625–658, [`arXiv:0901.2385`].

[89] ZEUS Collaboration, S. Chekanov et al., *Measurement of charged current deep inelastic scattering cross sections with a longitudinally polarised electron beam at HERA*, Eur. Phys. J. **C61** (2009) 223–235, [`arXiv:0812.4620`].

[90] ZEUS Collaboration, H. Abramowicz et al., *Deep inelastic cross-section measurements at large y with the ZEUS detector at HERA*, Phys. Rev. **D90** (2014), No. 7, 072002, [`arXiv:1404.6376`].

[91] S. Bentvelsen, J. Engelen, and P. Kooijman, *Reconstruction of (x, Q^2) and extraction of structure functions in neutral current scattering at HERA*, in *Workshop on Physics at HERA Hamburg, Germany, October 29-30, 1991* (W. Buchmller and G. Ingelman, eds.), pp. 23–42, 1992.

[92] U. Bassler and G. Bernardi, *On the kinematic reconstruction of deep inelastic scattering at HERA: The Sigma method*, Nucl. Instrum. Meth. **A361** (1995) 197–208, [`hep-ex/9412004`].

[93] F. Jacquet and A. Blondel in *The Study of an ep Facility for Europe, Amsterdam, 1979* (U. Amaldi, ed.), pp. 391–396, DESY 79/48, 1979.

[94] K. Hoeger, *Measurement of x, y, Q^2 in Neutral Current events*, in *Workshop on Physics at HERA Hamburg, Germany, October 29-30, 1991* (W. Buchmller and G. Ingelman, eds.), pp. 43–55, 1992.

[95] ZEUS Collaboration, M. Derrick et al., *Measurement of the F2 structure function in deep inelastic e+ p scattering using 1994 data from the ZEUS detector at HERA*, Z. Phys. **C72** (1996) 399–424, [`hep-ex/9607002`].

[96] S. Alekhin et al., *HERAFitter, Open Source QCD Fit Project*, Eur. Phys. J. **C75** (2015), No. 7, 304, [`arXiv:1410.4412`].

[97] "HERAFitter." https://wiki-zeuthen.desy.de/HERAFitter   [Online; accessed 26-July-2016].

[98] T. Lastovicka, *Selfsimilar properties of the proton structure at low x*, Eur. Phys. J. **C24** (2002) 529–533, [`hep-ph/0203260`].

[99] "HERAverager." https://wiki-zeuthen.desy.de/HERAverager [Online; accessed 14-October-2016].

[100] ZEUS Collaboration, "ZEUS data table of F_2 values at low x and low Q^2." http://www-zeus.desy.de/physics/sfew/PUBLIC/sfew_results/published/lowq2_f2_paper/f2svx95sys.dat [Online; accessed 4-November-2016].

[101] ZEUS Luminosity Monitor Group Collaboration, J. Andruszkow et al., *First measurement of HERA luminosity by ZEUS lumi monitor* (1992).

[102] ZEUS, H1 Collaboration, F. D. Aaron et al., *Combined Measurement and QCD Analysis of the Inclusive e+- p Scattering Cross Sections at HERA*, *JHEP* **01** (2010) 109, [arXiv:0911.0884].

[103] "The combined data together with the full correlation information and the grids for HERAPDF2.0." https://www.desy.de/h1zeus/herapdf20 [Online; accessed 14-October-2016].

[104] BCDMS Collaboration, A. C. Benvenuti et al., *A High Statistics Measurement of the Proton Structure Functions F(2) (x, Q^2) and R from Deep Inelastic Muon Scattering at High Q^2*, *Phys. Lett.* **B223** (1989) 485–489.

[105] New Muon Collaboration, M. Arneodo et al., *Measurement of the proton and deuteron structure functions, F2(p) and F2(d), and of the ratio sigma-L / sigma-T*, *Nucl. Phys.* **B483** (1997) 3–43, [hep-ph/9610231].

[106] ZEUS Collaboration, M. Derrick et al., *Measurement of the proton structure function F_2 in ep scattering at HERA*, *Phys. Lett.* **B316** (1993), No. 23, 412 – 426.

[107] H1 Collaboration, I. Abt et al., *Measurement of the proton structure function F2 (x, Q^2) in the low-x region at HERA*, *Nucl. Phys.* **B407** (1993), No. 3, 515 – 535.

[108] M. Botje, *QCDNUM: Fast QCD Evolution and Convolution*, *Comput. Phys. Commun.* **182** (2011) 490–532, [arXiv:1005.1481].

[109] A. D. Martin et al., *Parton distributions for the LHC*, *Eur. Phys. J.* **C63** (2009) 189–285, [arXiv:0901.0002].

[110] F. James, *Statistical methods in experimental physics* (2006).

[111] ZEUS Collaboration, H. Abramowicz et al., *Limits on the effective quark radius from inclusive ep scattering at HERA*, *Phys. Lett.* **B757** (2016) 468–472, [arXiv:1604.01280].

[112] J. Pumplin et al., *Uncertainties of predictions from parton distribution functions. 2. The Hessian method*, Phys. Rev. **D65** (2001) 014013, [`hep-ph/0101032`].

[113] R. D. Cousins, *Why isn't every physicist a Bayesian?*, Am. J. Phys. **63** (1995) 398.

[114] S. Dulat et al., *New parton distribution functions from a global analysis of quantum chromodynamics*, Phys. Rev. **D93** (2016), No. 3, 033006, [`arXiv:1506.07443`].

[115] P. Jimenez-Delgado and E. Reya, *Delineating parton distributions and the strong coupling*, Phys. Rev. **D89** (2014), No. 7, 074049, [`arXiv:1403.1852`].

[116] L. A. Harland-Lang et al., *The impact of the final HERA combined data on PDFs obtained from a global fit*, Eur. Phys. J. **C76** (2016), No. 4, 186, [`arXiv:1601.03413`].

[117] NNPDF Collaboration, R. D. Ball et al., *Parton distributions for the LHC Run II*, JHEP **04** (2015) 040, [`arXiv:1410.8849`].

[118] ZEUS Collaboration, S. Chekanov et al., *Search for contact interactions, large extra dimensions and finite quark radius in ep collisions at HERA*, Phys. Lett. **B591** (2004), No. 12, 23 – 41.

[119] H1 Collaboration, F. Aaron et al., *Search for contact interactions in collisions at HERA*, Phys. Lett. **B705** (2011), No. 12, 52 – 58.

[120] L3 Collaboration, M. Acciarri et al., *Search for manifestations of new physics in fermion-pair production at LEP*, Phys. Lett. **B489** (2000), No. 12, 81 – 92.

[121] O. Turkot, K. Wichmann, and A. F. Zarnecki, *Simplified QCD fit method for BSM analysis of HERA data*, `arXiv:1606.06670`.

[122] A. F. Zarnecki, *Limits on the effective quark radius from inclusive ep scattering & contact interactions at HERA*, in *Proceedings of Science ICHEP2016*, in press.

[123] ATLAS Collaboration, G. Aad et al., *Search for contact interactions and large extra dimensions in the dilepton channel using proton-proton collisions at $\sqrt{s}$ = 8 TeV with the ATLAS detector*, Eur. Phys. J. **C74** (2014), No. 12, 3134, [`arXiv:1407.2410`].

[124] CMS Collaboration, V. Khachatryan et al., *Search for physics beyond the standard model in dilepton mass spectra in proton-proton collisions at $\sqrt{s} = 8$ TeV*, JHEP **04** (2015) 025, [`arXiv:1412.6302`].

[125] ALEPH Collaboration, S. Schael et al., *Fermion pair production in e^+e^- collisions at 189-209-GeV and constraints on physics beyond the standard model*, Eur. Phys. J. **C49** (2007) 411–437, [`hep-ex/0609051`].

[126] H1 Collaboration, F. D. Aaron et al., *Search for Contact Interactions in $e^{\pm}p$ Collisions at HERA*, *Phys. Lett.* **B705** (2011) 52–58, [`arXiv:1107.2478`].

[127] DELPHI Collaboration, J. Abdallah et al., *A Study of b anti-b Production in e+e- Collisions at s**(1/2) = 130-GeV - 207-GeV*, *Eur. Phys. J.* **C60** (2009) 1–15, [`arXiv:0901.4461`].

[128] J. Reuter, *The BSM Physics Case of the ILC*, in *Proceedings, International Workshop on Future Linear Colliders (LCWS15): Whistler, B.C., Canada, November 02-06, 2015*, 2016. `arXiv:1602.08352`.

[129] B. Aune et al., *The superconducting TESLA cavities*, *Phys. Rev. ST Accel. Beams* **3** (2000) 092001, [`physics/0003011`].

[130] C. Adolphsen et al., *The International Linear Collider Technical Design Report - Volume 3.I: Accelerator & in the Technical Design Phase*, `arXiv:1306.6353`.

[131] M. Vogt et al., *The Free-Electron Laser FLASH at DESY*, in *Proceedings of IPAC13, Shanghai, China*, (Geneva), 4th International Particle Accelerator Conference, Shanghai (China), 12 May 2013 - 17 May 2013, JACOW Collaboration, May, 2013.

[132] R. Abela et al., *XFEL: The European X-Ray Free-Electron Laser - Technical Design Report*. DESY, Hamburg (2006).

[133] CORDIS, "ILC HiGrade Project." Project reference: 206711, 2008.

[134] A. Navitski, A. Prudnikava, and Y. Tamashevich, *Progress of R&D on SRF cavities at DESY towards ILC performance goal*, (Geneve), 5th International Particle Accelerator Conference, Dresden (Germany), 15 Jun 2014 - 20 Jun 2014, JACoW, Jun, 2014.

[135] A. Navitski et al., *R&D on cavity treatments at DESY towards the ILC performance goal*, (Geneva), 16th International Conference on RF Superconductivity, Paris (France), 23 Sep 2013 - 27 Sep 2013, JACOW, Sep, 2013.

[136] A. Navitski et al., *ILC-HIGRADE Cavities as a Tool of the Quality Control for European XFEL*, (Geneva), 16th International Conference on RF Superconductivity, Paris (France), 23 Sep 2013 - 27 Sep 2013, JACoW, Sep, 2014. OA.

[137] A. Navitski et al., *Surface analyses and optimization of centrifugal barrel polishing of Nb cavities*, p. 5, 17th International Conference on RF Superconductivity, Whistler (Canada), 13 Sep 2015 - 18 Sep 2015, Sep, 2015. prepress release.

[138] H. Podlech, *Superconducting versus normal conducting cavities*, in *Proceedings, CERN Accelerator School on High Power Hadron Machines (CAS 2011)*, 2013. `arXiv:1303.6552`.

[139] J. Norem and M. Pellin, *Gradient Limits and SCRF Performance*, Conf. Proc. **C0710141** (2007) 119–121.

[140] V. Palmieri et al., *Besides the standard niobium bath chemical polishing*, 2001.

[141] F. Barkov et al., *Precipitation of hydrides in high purity niobium after different treatments*, Journal of Applied Physics **114** (2013), No. 16,.

[142] B. Roux et al., *Molecular-dynamics simulations of hydrogen diffusion in niobium : influence of imperfections*, Physical Review B : Condensed matter and materials physics **509** (1995) 4162–4170.

[143] Leybold Vakuum, Bonner Strasse 498, Köln, *CoolPower 2/10, 12/45, RGS 20*, 11, 2000.

[144] W. E. Gifford, *The Gifford-McMahon Cycle*, pp. 152–159. Springer US, Boston, MA, 1966.

[145] Leybold Vakuum, Bonner Strasse 498, Köln, *CoolPak 4000, 4200, 4000 D, 6000, 6200, 6000 D*, 5, 2002.

[146] Edwards Vakuum, West Sussex, RH10 9LW, Crawley, *nXDS Scroll Pump*, 3, 2013.

[147] Edwards Vakuum, West Sussex, RH10 9LW, Crawley, *nEXT Turbomolecular Pumps nEXT240, nEXT300 and nEXT400*, 11, 2013.

[148] K. W. Morton and D. F. Mayers, *Numerical Solution of Partial Differential Equations: An Introduction.* Cambridge University Press, New York, NY, USA (2005).

[149] V. S. Chirkin, *Thermophysical Properties of Materials for Nuclear Engineering.* Atomizdat, Moscow, Russia (1968).

[150] J. E. Jensen et al., *Selected Cryogenic Data Notebook.* Brookhaven National Laboratory, Upton, NY, USA (1980). BNL 10200-R.

[151] A. Navitski et al., *Characterization of Surface Defects on EXFEL Series and ILC-Higrade Cavities*, in *Proceedings, 17th International Conference on RF Superconductivity (SRF2015): Whistler, Canada, September 13-18, 2015*, p. MOPB072, 2015.

Acknowledgements

The completion of this dissertation could not have been possible without the participation and assistance of so many people whose names may not all be enumerated. I sincerely appreciate their contributions and support. It is not sufficient to express my gratitude with only a few words.

I feel to acknowledge my deep sense of thanks and gratitude to my supervisor Katarzyna Wichmann, whose valuable guidence, personal contribution and scientific vision of the analysis direction shaped the present work as it is now. She was always available or reachable when I had scientific questions and she also had time and interest when I needed or felt like talking about non-scientific issues. Her enthusiasm, dynamism and kindness have encouraged me throughout my research period. I could not have hoped for a better supervisor.

I pay my deep sense of gratitude to Brian Foster for sparing his valuable time and his keen interest on my achievements at every stage of my research. His timely advice, suggestions and corrections provided the constant progress of the analysis. I am also very much thankful to Brian for the patronage and funding of the conference trips and summer schools which allowed me to present the results to the world scientific comunity and to broaden my field of knowledge.

My profound thanks to Aleksander Filip Żarnecki for an immense contribution to the analysis code and development of the procedure for faster calculations. I am much obliged for his very constructive criticism and comments that have significantly contributed to the evolution of my ideas and clarified my doubts during my project work.

I acknowledge the sincere and untiring efforts of Aliaksandr Navitski, Yegor Tamashevich and Alena Prudnikava, who assisted me during all stages of my work in the ILC-HiGrade laboratory and helped me in preparing the cooling system for Niobium samples.

For this dissertation I would like to thank my reading committee members, Brian Foster and Katarzyna Wichmann, for reading and evaluating the thesis as well as their valuable comments in improving the manuscript. I would also like to thank the other members of my oral defense committee, Dieter Horns, Gudrid Moortgat-Pick and Aleksander Filip Żarnecki, for their time and insightful questions. I feel proud and honoured that you have accepted to be on my committee.

I am very grateful to Matthew Wing, Iris Abt, Achim Geiser, Olaf Behnke, Allen Caldwell and all active ZEUS members who participated on the physics meetings and on the editorial board for the quark-radius paper for their enthusiasm for providing valuable comments and inputs to the research. I always get inspired after discussions with them at various occasions.

Special thanks are given to Volodymyr Aushev. He is the one who believed in me and gave me an opportunity to participate in the analyses at ZEUS and D0 experiments during my undergraduate study and to acquire priceless experience that was very helpful during my Ph.D. He also helped me to find a supervisor when I expressed the desire to pursue my Ph.D. research on a HERA related topic.

I would like to give my gratitude to all current and former members of the ZEUS and

Eidesstattliche Versicherung

Hiermit erkläre ich an Eides statt, dass ich die vorliegende Dissertationsschrift selbst verfasst und keine anderen als die angegebenen Quellen und Hilfsmittel benutzt habe.

Declaration on oath

I hereby declare, on oath, that I have written the present dissertation by my own and have not used other than the acknowledged resources and aids.

Hamburg,